



**HAL**  
open science

# Synthesis and study of functional oxides based on earth-abundant elements

Hongjun Liu

► **To cite this version:**

Hongjun Liu. Synthesis and study of functional oxides based on earth-abundant elements. Material chemistry. Université Grenoble Alpes, 2017. English. NNT : 2017GREAI049 . tel-02342594

**HAL Id: tel-02342594**

**<https://theses.hal.science/tel-02342594>**

Submitted on 1 Nov 2019

**HAL** is a multi-disciplinary open access archive for the deposit and dissemination of scientific research documents, whether they are published or not. The documents may come from teaching and research institutions in France or abroad, or from public or private research centers.

L'archive ouverte pluridisciplinaire **HAL**, est destinée au dépôt et à la diffusion de documents scientifiques de niveau recherche, publiés ou non, émanant des établissements d'enseignement et de recherche français ou étrangers, des laboratoires publics ou privés.

## **THÈSE**

Pour obtenir le grade de

### **DOCTEUR DE LA COMMUNAUTE UNIVERSITE GRENOBLE ALPES**

Spécialité : **2MGE: Matériaux, Mécanique, Génie civil,  
Electrochimie**

Arrêté ministériel : 30 Sept 2017

Présentée par

**Hongjun LIU (刘红均)**

Thèse dirigée par David MUÑOZ-ROJAS, Chargé de  
Recherches, CNRS

préparée au sein du Laboratoire des Matériaux et du Génie  
Physique (LMGP)  
dans l'École Doctorale I - MEP2 - Ingénierie - Matériaux,  
Mécanique, Environnement, Énergétique, Procédés,  
Production

### **Synthesis and study of functional oxides based on earth-abundant elements**

Thèse soutenue publiquement le **31 Octobre 2017**,  
devant le jury composé de :

**Madame Nieves CASAÑ PASTOR**

Professeur des Universités, Institut de Ciencia de Materials de Barcelona,  
CSIC, Examineur

**Monsieur Hubert RENEVIER**

Professeur des Universités, Université Grenoble Alpes, Président

**Monsieur Jean-francois PIERSON**

Professeur des Universités, Institut Jean Lamour (UMR CNRS 7198)  
Département CP2S, Rapporteur

**Monsieur Naoufal BAHLOWANE**

Directeur de Recherche, Luxembourg Institute of Science and Technology  
(LIST), Rapporteur

**Monsieur David MUÑOZ-ROJAS**

CR1, Université Grenoble Alpes, Directeur de these





*For those beautiful things in my life.*

## *Acknowledgements*

At this very ending of my PhD life, I am looking back to the three years of thesis and feeling so complicated. There were exciting moments and stressful period, but at this moment I feel so grateful for those people walked with me through it. Thus, I want to give my most sincere thanks to all of them.

First of all, I am so grateful for my family that they always supported me for what I want to do. They are the harbours of my mind which helps me keep peaceful mind. Even though they miss me a lot, they always encourage me to see the world. Then, I was able to come to France to continue the study. I can still remember the first time I visited LMGP and had the interview with my thesis director David Muñoz-Rojas. I was so amazed by his kindness and gentleness to the students. In the past three years, I got along with him really well and he was always available to discuss with me for the problems I've met or the ideas I had. Meanwhile, he has the ability to cheer me up and encouraged me when I feel defeated for another experimental failure. We are a team to share the exciting results and analysing the reasons for the failure. Therefore, here I want to tell him again thank you.

In addition, I also want to give my gratitude to the researchers in LMGP, especially Daniel Bellet, Jean-Luc Deschanvres and Carmen Jiménez, they gave me lots of valuable suggestions during my thesis work. As well, I also want to thanks the characterization researchers in LMGP such as Hervé Roussel, Laetitia Rapenne, Isabelle Paintrand and Odette Chaix, they are so knowledgeable for the characterization techniques and by discussion with them for those samples characterized I have learnt a lot. Furthermore, I also appreciate for the dedicated technician support team in our lab, such as Serge Quessada, Matthieu Jouvert and Dominique De Barros, thanks to them I was able to proceed my work efficiently. Speaking about supporting team, I also want to give my gratitude to our human resources ladies, they have helped with me dealing lots of paper work I even didn't know where to start.

Also, I give many thanks to the Ministère de education nationale, de l'Enseignement supérieur et de la Recherche in France and I-MEP2 doctor school for the thesis funding, which allowed me to continue my research during past three years. Besides, CHEMABEL project is thanked for supporting my research expenses. In addition, I am very appreciate for the KIC Innoenergy program. Through this program, they helped me a lot on future career preparation and they provided financial support to allow me have exchange opportunities in other research institutes.

Lastly, but with most warming hearts and greetings to my LMGP colleagues. They are not only really helpful during the science work but also we had lots of fun when I still had the chance. I have learnt a lot from them, both from work and life. I wish all of you guys and girls get what you want in the thesis work and in the future life.

## *Résumé*

Au cours des dernières années, l'électronique à base d'oxydes métalliques a attiré de plus en plus d'attention au sein de la recherche, principalement grâce à leur potentiel en termes de réduction de coûts ainsi que la possibilité de développer une électronique transparente. Il existe plusieurs applications potentielles concernant les oxydes métalliques : le photovoltaïque, les transistors à couche mince et la photo-électrochimie. Il existe plusieurs oxydes métalliques de type n avec d'excellentes propriétés électroniques, telles que l'oxyde de zinc dopé à Al. Mais la mise au point de dispositifs entièrement à base d'oxydes métalliques est largement entravée par les mauvaises propriétés électroniques des oxydes de type p jusqu'à présent étudiés. Par conséquent, il est nécessaire de développer des matériaux semi-conducteurs d'oxyde métallique de type p présentant de meilleures propriétés électriques.

Dans cette thèse, l'optimisation du dépôt de films minces de  $\text{Cu}_2\text{O}$  a été effectuée par MOCVD assisté par aérosol (AA-MOCVD). Par conséquent, des films de  $\text{Cu}_2\text{O}$  homogènes et de très forte cristallinité ont été déposés à basse température (environ  $335\text{ }^\circ\text{C}$ ) sans contamination détectable de carbone. De plus, grâce à l'incorporation de l'humidité durant les dépôts, la taille des grains et l'orientation des films  $\text{Cu}_2\text{O}$  peuvent être modulées, ainsi des films de  $\text{Cu}_2\text{O}$  avec une texturation (111) et une taille de grains  $> 300\text{ nm}$  ont été obtenus. Pour les films  $\text{Cu}_2\text{O}$  optimisés, la mobilité peut atteindre un maximum de  $15\text{ cm}^2/\text{V.s}$  avec une concentration de porteur de l'ordre de  $10^{15}\text{ cm}^{-3}$ . Enfin, un excellent comportement diode a été observé en combinant les films de  $\text{Cu}_2\text{O}$  optimisés avec du  $\text{ZnO}$ , obtenant un rapport on/off supérieur à  $10^4$ .

Outre l'optimisation de  $\text{Cu}_2\text{O}$ , le dépôt d' $\text{AgCuO}_2$  par MOCVD a également été abordé. Pour ce faire, le dépôt de films minces d'oxyde d'argent et d'argent a été préalablement optimisé. Pour cela, deux nouveaux précurseurs d'argent, à savoir les triglymes Ag (hfac) phénanthroline et Ag (hfac) ont été synthétisés et complètement caractérisés. On peut obtenir des revêtements Ag de haute qualité avec les deux précurseurs. Les films d'oxyde d'argent ont été obtenus par oxydation électrochimique et traitement par plasma à l'oxygène des revêtements pré-déposés Ag.

En raison de l'incompatibilité entre la fenêtre de stabilité thermique associée à  $\text{AgCuO}_2$  et les températures nécessaires pour déposer des composés Ag et Cu par CVD avec les précurseurs utilisés, le dépôt direct d' $\text{AgCuO}_2$  n'a pas pu être obtenu. Ainsi, des techniques de revêtement couche mince à base de solution ont été adoptées pour le dépôt de film

AgCuO<sub>2</sub>. En particulier, la méthode SILAR a permis le dépôt de films minces d'AgCuO<sub>2</sub>. Grâce à une couche d'amorce sur substrat de verre appropriée, des couches d'AgCuO<sub>2</sub> denses et continues ont été revêtues, avec une valeur RMS minimale de 8 nm. Les films d'AgCuO<sub>2</sub> déposés avaient une phase presque pure. Les propriétés optiques et de transport des films minces AgCuO<sub>2</sub> ont donc été analysées pour la première fois. Les mesures de transmittance ont confirmé la faible largeur de bande interdite prédite d'AgCuO<sub>2</sub> (1.2 eV), tandis que grâce à l'utilisation de la formule de Tauc, nous avons constaté que ce matériau est plus susceptible d'avoir une bande interdite directe, en accord avec les calculs DFT publiés. Grâce aux mesures de l'effet Hall, les films AgCuO<sub>2</sub> déposés ont été confirmés comme étant de type p. La plus faible résistivité atteinte est de 0.2 Ω.cm. En outre, ces films avaient une densité de porteurs de charge de l'ordre de 10<sup>17</sup> cm<sup>-3</sup> et la meilleure mobilité atteinte était de 24 cm<sup>2</sup> / V.s. En comparaison avec les composés de type p de delafossite précédemment rapportés (M, Al, Cr, Ga, etc.), ce matériau présente la plus petite largeur de bande interdite (intéressant notamment pour l'application photovoltaïque) et une conductivité assez élevée. La caractéristique la plus intéressante est que le problème général de la faible mobilité des transporteurs dans ces composés delafossite a été résolu dans cet AgCuO<sub>2</sub>, grâce à sa structure électronique mixte et à la délocalisation des charges. Ainsi, ces résultats de caractérisation sans précédent ouvrent la voie à l'utilisation de films AgCuO<sub>2</sub> dans des dispositifs fonctionnels.

## *Abstract*

In recent years, metal oxide electronics has attracted more and more attention in research, mainly thanks to their potential lower cost and the possibility they offer to develop transparent electronics. There are several potential applications concerned with metal oxides including photovoltaics, thin film transistors and photo-electrochemistry. There are several n-type metal oxides with excellent electronic properties being well developed, such as Al doped zinc oxide. But the fabrication of devices fully made with metal oxides is largely impeded by the poor electronic properties of the p-type oxides so far studied. Therefore, there is the need for developing p-type metal oxide semiconducting materials with better electrical properties.

In this thesis, the optimization of pure Cu<sub>2</sub>O thin film deposition was conducted using Aerosol Assisted MOCVD (AA-MOCVD). As a result, homogenous Cu<sub>2</sub>O films were deposited at low temperature (about 335 °C) without detectable amount of carbon

contamination with high crystallinity. In addition, by incorporation of humidity during the deposition, particle size and the orientation of the Cu<sub>2</sub>O films could be tuned, thus Cu<sub>2</sub>O films with (111) textured large grain sizes (> 300 nm) were achieved. For optimized Cu<sub>2</sub>O films, the mobility can reach a maximum of 15 cm<sup>2</sup>/V.s with carrier concentration in the order of 10<sup>15</sup> cm<sup>-3</sup>. Lastly, an excellent diode behavior was observed by combining the optimized Cu<sub>2</sub>O films with ZnO, obtaining an on-off ratio exceeding 10<sup>4</sup>.

Besides the Cu<sub>2</sub>O optimization, the deposition of AgCuO<sub>2</sub> by MOCVD was also tackled. In order to do so, the deposition of silver and silver oxide thin films was previously optimized. For that, two new silver precursors, namely, Ag(hfac)phenanthroline and Ag(hfac)triglyme were synthesized and fully characterized. High quality Ag coatings could be obtained with both precursors. Silver oxide films were obtained through electrochemical oxidation and oxygen plasma treatment of pre-deposited Ag coatings.

Due to the incompatibility between the thermal AgCuO<sub>2</sub> stability window and the temperatures needed to deposit Ag and Cu compounds by CVD with the precursors used, the direct deposition of AgCuO<sub>2</sub> could not be obtained. Thus, solution based thin film coating techniques were adopted for AgCuO<sub>2</sub> film deposition. In particular, Successive Ionic Layer Adsorption and Reaction (SILAR) allowed the deposition of AgCuO<sub>2</sub> thin films. Using a proper seed layer on glass, dense and continuous AgCuO<sub>2</sub> films were coated, with minimum RMS value of 8 nm. The deposited AgCuO<sub>2</sub> films had almost pure phase. The optical and transport properties of AgCuO<sub>2</sub> thin films were thus carried out for the first time. Transmittance measurements confirmed the predicted low bandgap of AgCuO<sub>2</sub> (1.2 eV), while by using the Tauc formula, we found that this material is more likely to have a direct bandgap, in agreement with published DFT calculations. Thanks to Hall Effect measurements, the deposited AgCuO<sub>2</sub> films were confirmed to be p-type. The lowest resistivity achieved was 0.2 Ω.cm. In addition, those films had carrier density in the order of 10<sup>17</sup> cm<sup>-3</sup> and the best mobility achieved was 24 cm<sup>2</sup>/V.s. Comparing with the previously reported CuMO<sub>2</sub> (M= Al, Cr, Ga etc) delafossite p-type compounds, this material has shown the lowest bandgap (appropriate for photovoltaic application) and rather high conductivity. The most interesting characteristic is that the general problem of low carrier mobility in those delafossite compounds has been solved in this AgCuO<sub>2</sub>, thanks to its mixed-valence electronic structure and charges delocalization. Thus, those unprecedented characterization results pave the way for using AgCuO<sub>2</sub> films in functional devices.





## Table of content

A. List of abbreviations	i
B. Symbol and physical quantities	iii
C. Preface	v
Chapter I Introduction	- 1 -
I.1 Electrical properties of existing p type metal oxides	- 3 -
I.2 New emerging potential Ag-Cu oxide family for photovoltaic application: AgCuO <sub>2</sub> and Ag <sub>2</sub> Cu <sub>2</sub> O <sub>3</sub> .	- 5 -
I.2.1 Crystal and electronic structures of Ag-Cu oxides family	- 5 -
I.2.2 Transport properties of new Ag-Cu oxides	- 8 -
I.2.3 Thin film deposition of Ag-Cu mixed oxides	- 10 -
I.3 Cu <sub>2</sub> O structures and electronic properties	- 14 -
I.3.1 Application of Cu <sub>2</sub> O in thin film transistor	- 18 -
I.3.2 Application Cu <sub>2</sub> O in water splitting	- 19 -
I.3.3 Application of Cu <sub>2</sub> O in photovoltaics	- 24 -
I.4 Objective of PhD thesis	- 28 -
I.5 References	- 29 -
Chapter II Experimental setup	- 36 -
II.1 Deposition of Ag and Cu <sub>2</sub> O thin films by Metal Organic Chemical Vapor Deposition (MOCVD).	- 36 -
II.1.1 Pulsed Injection MOCVD	- 37 -
II.1.2 Aerosol Assisted MOCVD	- 38 -
II.1.3 Film deposition	- 40 -
II.1.3.1 Preparation of starting precursor solutions:	- 40 -
II.1.3.2 Substrate cleaning	- 42 -
II.1.3.3 Preparation of the MOCVD systems	- 42 -
II.2 Oxidation techniques: electrochemical oxidation and oxidation with atmospheric oxygen plasma	- 43 -
II.2.1 Electrochemical deposition and oxidation	- 43 -
II.2.2 Oxygen plasma oxidation	- 46 -
II.2.3 Deposition of AgCuO <sub>2</sub> films by the SILAR method	- 47 -

## *Table of content*

<i>II.3 Characterization techniques</i>	<i>- 48 -</i>
<i>II.3.1 Thin film crystallinity: RAMAN spectroscopy, XRD</i>	<i>- 48 -</i>
<i>II.3.1.1 Raman Spectroscopy</i>	<i>- 48 -</i>
<i>II.3.1.2 X-Ray diffraction (XRD): Bragg-Brentano and Grazing Incidence.</i>	<i>- 49 -</i>
<i>II.3.2 Morphological characterization: SEM: EDS, EBSD, AFM</i>	<i>- 53 -</i>
<i>II.3.2.1 Scanning Electron Microscopy (SEM)</i>	<i>- 53 -</i>
<i>II.3.2.2 Atomic Force Microscopy (AFM)</i>	<i>- 55 -</i>
<i>II.3.2.3 Transmission Electron Microscopy (TEM)</i>	<i>- 57 -</i>
<i>II.3.3 Ultraviolet-Visible (UV-Vis) spectroscopy</i>	<i>- 58 -</i>
<i>II.3.4 Electrical characterization</i>	<i>- 59 -</i>
<i>II.3.4.1 Four probe measurements</i>	<i>- 59 -</i>
<i>II.3.4.2 Hall Effect measurements</i>	<i>- 61 -</i>
<i>II.4 References</i>	<i>- 63 -</i>
<i>Chapter III Thin film deposition of silver and silver oxides</i>	<i>- 66 -</i>
<i>III.1 Ag Precursor design, synthesis and characterization</i>	<i>- 67 -</i>
<i>III.1.1 Synthesis and characterization of new silver metalorganic precursor</i>	<i>- 69 -</i>
<i>III.1.2 XRD analysis and structure elucidation</i>	<i>- 71 -</i>
<i>III.1.3 New Ag metalorganic precursor molecular structures and characterizations</i>	<i>- 76 -</i>
<i>III.2 Deposition of silver coatings via MOCVD.</i>	<i>- 82 -</i>
<i>III.2.1 Ag coatings via PI-MOCVD.</i>	<i>- 83 -</i>
<i>III.2.2 Ag coatings by Aerosol Assisted MOCVD.</i>	<i>- 86 -</i>
<i>III.3 Oxidation of Ag coatings</i>	<i>- 93 -</i>
<i>III.3.1 Electrochemical oxidation of Ag coatings</i>	<i>- 93 -</i>
<i>III.3.2 Oxidation of Ag film by Oxygen Plasma</i>	<i>- 96 -</i>
<i>III.4 Chapter summary</i>	<i>- 99 -</i>
<i>III.5 Appendix</i>	<i>- 101 -</i>
<i>III.6 References</i>	<i>- 104 -</i>
<i>Chapter IV Deposition of Highly crystalline Cu<sub>2</sub>O films via AA-MOCVD</i>	<i>- 110 -</i>
<i>IV.1 Optimization of deposition system and reaction parameters</i>	<i>- 111 -</i>
<i>IV.1.1 Deposition system configuration</i>	<i>- 111 -</i>
<i>IV.1.2 Choice of precursors</i>	<i>- 114 -</i>
<i>IV.1.2.1 Effects of oxygen ratio during deposition with Cu(AcAc)<sub>2</sub> precursor</i>	<i>- 114 -</i>

<i>IV.1.2.2 Deposition under oxidizing conditions using plasma with Cu(AcAc)<sub>2</sub> precursor</i>	<i>- 116 -</i>
<i>IV.1.3 Depositions of Cu<sub>2</sub>O films using CuF as precursor</i>	<i>- 118 -</i>
<i>IV.1.3.1 Optimization of uniformity</i>	<i>- 118 -</i>
<i>IV.1.3.2 Optimization for oxygen ratio</i>	<i>- 119 -</i>
<i>IV.2 Tuning the texture of Cu<sub>2</sub>O thin films</i>	<i>- 121 -</i>
<i>IV.2.1 Effect of the presence of Ag particles on film growth and morphology</i>	<i>- 122 -</i>
<i>IV.2.2 Effects of humidity on thin film orientation, morphology and electronic properties</i>	<i>- 125 -</i>
<i>IV.3 Studies on the reaction mechanism</i>	<i>- 140 -</i>
<i>IV.3.1 Study of the initial stages of thin film growth.</i>	<i>- 140 -</i>
<i>IV.3.2 Thermodynamic explanation</i>	<i>- 142 -</i>
<i>IV.4 Chapter IV conclusions</i>	<i>- 145 -</i>
<i>IV.5 References</i>	<i>- 147 -</i>
<i>Chapter V Deposition and characterization of AgCuO<sub>2</sub> thin films</i>	<i>- 151 -</i>
<i>V.1 Co-deposition of silver copper oxide via Plasma Enhanced AA-MOCVD</i>	<i>- 152 -</i>
<i>V.2 Oxidation of Ag-Cu metal alloy film</i>	<i>- 156 -</i>
<i>V.2.1 Deposition of Ag<sub>0.5</sub>Cu<sub>0.5</sub> alloy films</i>	<i>- 156 -</i>
<i>V.2.2 Electrochemical oxidation</i>	<i>- 158 -</i>
<i>V.2.3 Oxygen plasma treatment</i>	<i>- 164 -</i>
<i>V.3 Deposition of AgCuO<sub>2</sub> thin films by Successive Ionic Layer Adsorption and Reaction (SILAR)</i>	<i>- 166 -</i>
<i>V.3.1 Experimental setup and parameters</i>	<i>- 167 -</i>
<i>V.3.2 Substrate preparation</i>	<i>- 168 -</i>
<i>D. Cu<sub>2</sub>O/glass substrate preparation:</i>	<i>- 168 -</i>
<i>E. ZnO/glass substrate preparation:</i>	<i>- 168 -</i>
<i>F. TiO<sub>2</sub>/glass substrate preparation:</i>	<i>- 168 -</i>
<i>V.3.3 SILAR deposition parameters</i>	<i>- 169 -</i>
<i>V.3.4 Optimization of deposition condition</i>	<i>- 169 -</i>
<i>V.3.5 Understanding the mechanism of AgCuO<sub>2</sub> thin film coating by SILAR process.</i>	<i>- 177 -</i>
<i>V.3.6 Optical and electronic property of AgCuO<sub>2</sub> films obtained by SILAR</i>	<i>- 182 -</i>
<i>V.4 Chapter VI conclusions</i>	<i>- 185 -</i>
<i>V.5 References</i>	<i>- 187 -</i>
<i>Chapter VI In situ XRD characterization of formation mechanism of AgCuO<sub>2</sub> phase in hydrothermal reaction</i>	<i>- 190 -</i>

*Table of content*

<i>VI.1 Experimental setup</i>	<i>- 191 -</i>
<i>VI.2 Effects of solution pH and reaction mechanism</i>	<i>- 192 -</i>
<i>VI.3 Effects of temperature and calculation of the reaction activation energy</i>	<i>- 203 -</i>
<i>VI.4 Chapter VI conclusions</i>	<i>- 205 -</i>
<i>VI.5 Appendix V: In situ XRD of hydrothermal reactions at different temperatures.</i>	<i>- 206 -</i>
<i>VI.6 References</i>	<i>- 209 -</i>
<i>Conclusions and perspectives</i>	<i>- 211 -</i>





*A. List of abbreviations*

a-Si: H: amorphous-Si  
OLED: organic light emitting device  
TCOs: transparent conducting oxides  
AZO: Al doped ZnO  
ITO: Indium doped Tin oxide  
CBM: conduction band minimum  
VBM: valence band maximum  
PLD: Pulsed Laser Deposition  
ALD: Atomic Layer Deposition  
MOCVD: Metal Organic Chemical Vapor Deposition  
EHTB: Extended Hückel Tight Binding  
DOS: density of states  
TGA: Thermal Gravimetric Analysis  
PL: Photoluminescence  
SAED: Selected Area Electron Diffraction  
FE: Faradaic efficiency  
EDS: Energy-dispersive X-ray  
HR TEM: High resolution Transmission Electron Microscope  
TFT: thin film transistor  
PEC: photo electrochemical  
r-DPPC: repeated double-potential pulse chronoamperometric  
SALD: Spatial Atomic Layer Deposition  
DFT: Density of function theory  
PDOS: partial density of state  
PI-MOCVD: Pulsed Injection MOCVD  
AA-MOCVD: Aerosol Assisted MOCVD  
WE: working electrode  
CE: counter electrode  
RE: reference electrode  
LSV: sweep voltammetry  
CV: cyclic voltammetry



*List of abbreviations*

CA: chronoamperometry  
CP: chronopotentiometry  
SILAR: Successive Ionic Layer Adsorption and Reaction  
FTIR: Fourier Transfer Infrared Red  
CCD: charge-coupled device  
XRD: X-Ray diffraction  
FWHM: Full Width at Half Maximum  
EBSD: Electron Back Scatter Diffraction  
FEG: Field Emission Gun  
AFM: Atomic Force Microscopy  
ARTA: reflectance transmittance analyser  
H-hfac: 1,1,1,5,5,5-hexafluoro-2,4-pentanedione;  
H-tfac: 1,1,1-trifluoro-2,4-pentanedione;  
Hfod: 6,6,7,7,8,8,8-heptafluoro-2,2-dimethyl-3,5-octanedione  
BTMSA: bis(trimethylsilyl)acetylene;  
SEt<sub>2</sub>: Ethyl sulphide;  
VTES: vinyltriethylsilane;  
PEt<sub>3</sub>: triethylphosphine;  
P(OEt)<sub>3</sub>: triethylphosphite;  
PMe<sub>3</sub>: Trimethylphosphine;  
PPh<sub>3</sub>: Triphenylphosphine;  
O<sub>2</sub>CtBu: 2,2,6,6-tetramethyl-3,5-heptanedionate  
NMR: Nuclear magnetic resonance  
ICP-OES: ICP-coupled Optical Emission Spectrometry  
AgP: [Ag(hfac)phen]  
AgT: [Ag(triglyme)<sub>2</sub>]<sup>+</sup>[Ag(hfac)<sub>2</sub>]<sup>-</sup>  
CG: Carrier gas  
XPS: X-ray photoelectron spectroscopy  
RMS: Root Mean Squared

*B. Symbol and physical quantities*

$V_{Cu^0}$ : copper vacancy

$E_A$ : acceptor level

$W_{ph}$ : photon energy

$\mu_{FE}$ : field-effect mobility

TS: threshold slope

$V_{th}$ : threshold voltage

$\mu_H$ : carrier mobility

$V_{DS}$ : source voltage

$V_{GS}$ : gate-to-source voltage

$x_p$ : the depletion length in p type

$x_n$ : the depletion length in n type

$V_{bi}$ : built in potential

$J_{sc}$ : short circuit current density

$V_{oc}$ : open circuit voltage

FF: fill factor

$N_A$ : acceptor concentration

$N_D$ : donor concentration

$q$ : unit electron charge

$E_g$ : bandgap

$d_{hkl}$ : distance between two crystal planes with Miller index (hkl)

$\theta$ : incident angle between the X-Ray and the (hkl) crystal plane

$T_c(h_i k_i l_i)$ : the texture coefficient of the specific  $(h_i k_i l_i)$  plane

$\beta_L$ : the peak width, obtained by subtracting the width associated to the instrument

$T_a$ : absorption

$T_t$ : transmittance

$T_r$ : reflectance

$R_s$ : sheet resistance

$V_H$ : Hall voltage

$E$ : electrical field

$B_Z$ : magnetic field in the Z axis

$N_s$ : nucleation rate

*Symbols and physical quantities*

**k**: Plank constant

**P<sub>O2</sub>**: oxygen ratio in deposition chamber

**P<sub>O2</sub>\***: oxygen ratio regarding to copper atoms

**E<sub>a</sub>**: activation energy

## C. Preface

This thesis work is supported by Ecole Doctorale for Industrial, Materials, Mechanical and Process Engineering (I-MEP2) and Ministère de l'Education nationale, de l'Enseignement supérieur et de la Recherche in France. As well, KIC Innoenergy PhD program has provided financial support for the motilities during the PhD thesis. This PhD thesis work was supervised by Dr. David Muñoz-Rojas from Laboratoire des matériaux et du génie physique (LMGP), CNRS, France. The majority of the thin film synthesis and characterizations were conducted in LMGP.

The thesis structure is organized in the following way:

In Chapter I, the promising applications of metal oxides electronics are introduced. The main challenge for the development of metal oxide based electronics is point out, which is the lack of p type metal oxides with good electronic properties. Then, common p type metals oxides are introduced and their electrical properties are compared. Among those, copper oxides and its ternary compounds  $\text{CuMO}_2$  ( $M = \text{Al, Cr, Sr, etc}$ ) with delafossite structure have drawn much attention. The basic characteristics of  $\text{Cu}_2\text{O}$ , a very promising material, are then introduced. Especially, we illustrate how the electronic properties of such material are very dependent on the synthetic approach used. The main challenge in the case of  $\text{Cu}_2\text{O}$  is to achieve high quality films using chemical methods at low temperature. After that, the new Ag-Cu mixed oxide family is introduced, in particular  $\text{AgCuO}_2$ . The crystal structure and previously reported synthesis methods are discussed. It is pointed out that due to the lack of proper thin film coating techniques for this material, no detailed electronic or optical properties were reported. However, there are several works that have shown the potential of such material as a p type, small bandgap and highly conductive semiconductor material. To conclude, some potential applications of  $\text{Cu}_2\text{O}$  are briefly discussed. The chapter finishes stating the objectives of the work.

In Chapter II, different characterization tools used in this thesis work are introduced. For morphological characterizations, Scanning Electron Microscopy (SEM), Atomic Force Microscopy (AFM) and Transmission Electron Microscopy (TEM) were used in this thesis work. For crystal information acquisition, X-ray diffraction in Bragg-Brentano and Grazing Incidence configurations were both introduced. In addition, the working principle of Raman Spectroscopy was also explained. Furthermore, the electron diffraction in TEM and Electron Back Scattering Diffraction (EBSD) technique in SEM were also introduced. For optical

characterizations, UV-Vis spectroscopy was used. Lastly, for electronic property measurements, the working principles of four point probe and Hall Effect measurements were illustrated.

To achieve AgCuO<sub>2</sub> thin films, the initial plan was to conduct such depositions in Aerosol Assisted MOCVD (AA-MOCVD) coupling with an oxygen plasma system to generate O<sub>3</sub>. However, due to the large quantity of precursor consumption in AA-MOCVD, the current commercial silver precursors are too costly. Therefore, lower cost silver precursors were designed through a collaboration with Prof. Graziella Malandrino from University of Catania. Two new precursors have been obtained as a result, namely, Ag(hfac)phenanthroline (AgP) and Ag(hfac)triglyme (AgT), as presented in Chapter III. The synthesis process and molecule structures of the newly designed precursors were then introduced. The deposition results from both precursors were also compared. With AgT precursor, silver coatings with better quality were achieved. In addition to the new synthesized precursors, we also obtained coatings in MOCVD using Ag acetate (AgAc) by using ethanolamine as dispersant. Nevertheless, films quality was lower with AgAc than with the two new precursors. After optimization of silver coatings, the work about silver oxide films was also introduced. Through different after treatment techniques, electrochemical oxidation and oxygen plasma, AgO films were achieved.

In Chapter IV, the work involving the deposition of copper oxides is presented. Given that the deposition of CuO has been already studied in LMGP, we focussed on Cu<sub>2</sub>O. During this chapter, the optimization of the AA-MOCVD system is presented. With the optimized configuration, high crystalline and carbon free Cu<sub>2</sub>O films were deposited using Cu(II) trifluoro acetylacetonate. A study of the effect of i) the oxygen ratio, ii) the presence Ag nanoparticles or ii) the use humid carrier was also performed and is detailed. The effects of those factors during deposition were elaborated from the point view of morphology, crystal orientation and electronic properties. Lastly, through a classical thermodynamic model, we propose a rationalisation of the Cu<sub>2</sub>O deposition process.

In Chapter V, the work about AgCuO<sub>2</sub> thin film deposition will be introduced. Firstly the results of co-depositions using both silver and copper precursor solutions in AA-MOCVD is introduced. Due to the incompatibility between the precursor decomposition temperature and the AgCuO<sub>2</sub> phase, no AgCuO<sub>2</sub> was obtained. Then, to deposit AgCuO<sub>2</sub> films, alternative low-cost and low temperature deposition techniques were adopted, namely, solution based Successive Ionic Layer Adsorption and Reaction (SILAR). With this technique, 100 nm thick continuous and dense AgCuO<sub>2</sub> was coated on Cu<sub>2</sub>O seed layers.

The optimization of such deposition process is detailed. Then, the UV-Vis characterization of AgCuO<sub>2</sub> films are reported for the first time, implying a direct 1.2 eV bandgap. Furthermore, Hall Effect measurements were also conducted on those samples. Comparing with the previously reported CuMO<sub>2</sub> ternary compounds, the AgCuO<sub>2</sub> films presented a low resistivity down to 0.2 Ω.cm, higher carrier density in the order of 10<sup>17</sup> cm<sup>-3</sup>~ 10<sup>18</sup> cm<sup>-3</sup> and high carrier mobility as high as 24 cm<sup>2</sup>/V.s.

Lastly, in Chapter VI, through the collaboration with Prof. Mari-Ann Einarsrud from NTNU, Norway, the in-situ XRD characterizations of the hydrothermal synthesis of AgCuO<sub>2</sub> was conducted in ESRF synchrotron. The results of the characterizations of different reactions with different pH solution, reaction temperatures are presented and discussed. As a result, the hydrothermal reaction mechanism of AgCuO<sub>2</sub> formation in this case will be revealed, and an activation energy of 67 kJ/mol was obtained.



<i>Chapter I Introduction</i>	- 1 -
<i>I.1 Electrical properties of existing p type metal oxides</i>	- 3 -
<i>I.2 New emerging potential Ag-Cu oxide family for photovoltaic application: AgCuO<sub>2</sub> and Ag<sub>2</sub>Cu<sub>2</sub>O<sub>3</sub>.</i>	- 5 -
<i>I.2.1 Crystal and electronic structures of Ag-Cu oxides family</i>	- 5 -
<i>I.2.2 Transport properties of new Ag-Cu oxides</i>	- 8 -
<i>I.2.3 Thin film deposition of Ag-Cu mixed oxides</i>	- 10 -
<i>I.3 Cu<sub>2</sub>O structures and electronic properties</i>	- 14 -
<i>I.3.1 Application of Cu<sub>2</sub>O in thin film transistor</i>	- 18 -
<i>I.3.2 Application Cu<sub>2</sub>O in water splitting</i>	- 19 -
<i>I.3.3 Application of Cu<sub>2</sub>O in photovoltaics</i>	- 24 -
<i>I.4 Objective of PhD thesis</i>	- 28 -
<i>I.5 Chapter I- References</i>	- 29 -

## *Chapter I Introduction*

As it is known, Si based semiconductor materials are one of the most important foundations for the modern electronic industry. However, due to a high melting point of Si/SiO<sub>2</sub>, high purity crystalline Si wafer production is always a heavily energy demanding process, which is one of the major reasons for its high cost.<sup>1</sup> Also, Si based photovoltaic technologies are the most widespread nowadays, but due to the indirect bandgap of crystalline Si, thus much thicker absorber layers are required in solar cells. This imposes a higher degree of purity and crystallinity of the Si used and thus high cost of material fabrication is one of the hurdles for photovoltaic energy to compete with fossil fuels. With the development of new Si based materials such as amorphous-Si (a-Si: H), the production cost is largely reduced with much lower processing temperature. However, such a-Si layers suffer from low carrier mobility (~0.5 - 1 cm<sup>2</sup>/V.s), which limits its potential for wider type of applications, such as transistors.<sup>2,3</sup> In addition, crystalline Si has very poor mechanical resistance. And even when using a-Si thin layers, applying Si crystalline/amorphous layers with low-cost coating techniques for electronics on flexible substrates is still rather challenging.



To find an alternative solution, researchers have turned their interests in metal oxide semiconductors. Comparing with tradition Si based semiconductor materials, metal oxide semiconductors have several merits. First of all, many metal oxides are earth abundant and can be processed through lower cost chemical approaches at low temperature. Thus, a much cheaper cost of the semiconductor material fabrication can be achieved. The application of metal oxides layers in solar cells can thus increase the competence of the solar energy in the market. Furthermore, with a lower thermal budget and better mechanical resistance in some cases, some metal oxide materials still showed excellent carrier mobility (e.g. mobility exceeding  $100 \text{ cm}^2/\text{V}\cdot\text{s}$  was reported for  $\text{Cu}_2\text{O}$  films deposited at  $200 \text{ }^\circ\text{C}$  by radio frequency Magnetron Sputtering (rf-MS) method <sup>4</sup>). Thus metal oxide semiconductors have great potential in flexible electronics as well, such as flexible circuits for organic light emitting devices (OLED).<sup>5-7</sup> Besides the promising applications with metal oxide semiconductors, since there are several metal oxide semiconductors that have a wide bandgap (such as ZnO, over 3 eV), thus the combination of both transparency or semitransparency with conductivity is possible with metal oxides. Those type of metal oxide materials are called transparent conductive oxides (TCOs), and typical ones are Al doped ZnO (AZO), Indium doped Tin oxide (ITO) and Fluorine doped Tin Oxide (FTO). Combining all characteristics of low cost, transparency and conductivity, metal oxides have even brought new possibilities in several fancy applications such as smart windows and transparent electronic devices.<sup>8-11</sup>

However, the current situation for metal oxide electronics is still facing lots of challenges, one of which is the lack of p type oxides with identical excellent electronic properties as the n type counterparts.<sup>12,13</sup> As a result, the performance of electronic devices requiring p and n metal oxides are dragged down. Only unipolar n type metal oxide based electronic devices have shown a promising future for commercialization. Therefore, developing new p type metal oxides with better electrical properties is urgently needed.

Meanwhile, from the point view of electronic structure configurations, there are several difficulties to achieve a p type metal oxide with similar performance to n type oxides. As stated from the work of Z. Wang *et al.*,<sup>12</sup> in n type metal oxides, the electrons are created by oxygen vacancies and the pathway conduction band minimum (CBM) is composed of widely dispersed metal s orbitals. Thus, there is sufficient hybridization and delocalized CBM in n type oxide, which allows the electrons to travel through the material with high mobility. However, in p type metal oxides, since the origin of the hole is from metal ion vacancies and the valence band maximum (VBM) is made up with the anisotropic and localized O 2p orbitals, thus low carrier mobility is rather commonly observed in p type metal oxides.<sup>14,15</sup>

In addition to the low mobility, due to the high formation energy of metal ion vacancies and low formation energy of oxygen vacancies, the native generation of hole carriers is limited. Combining both aspects, finding new p type metal oxide material with proper electrical structure for hole conduction is essential to achieve a good performance of metal oxide based electronic devices.

## I.1 Electrical properties of existing p type metal oxides

So far several types of p type metal oxides have been reported. With a rough classification, there are SnO, NiO, ZnM<sub>2</sub>O<sub>4</sub> (M= Ir, Rh and Co) spinel type oxide, copper oxide and its ternary oxide compounds.<sup>12</sup> Table I-1 presents the optical and electronic properties of common p type metal oxides (we have also include n type semiconductors for the sake of comparison). Among the binary compounds, NiO has rather high bandgap more than 3.6 eV and the lowest resistivity, merely about 0.4 Ω.cm. Meanwhile, Cu<sub>2</sub>O has a smaller bandgap transition in those TCOs, between 2 and 2.7 eV. The resistivity of Cu<sub>2</sub>O films are also generally high, normally more than 100 Ω.cm.<sup>16-18</sup> Even though the optical and electronic properties of Cu<sub>2</sub>O films can be tuned by doping with other metal ions or anion doping (N mainly)<sup>19-23</sup>, they normally suffer from reduced carrier mobility. The optical bandgap of other binary oxides, such as SnO are between those two values and the reported SnO has relatively low mobility as well. Thus, NiO seems to be promising for transparent electronic with its high bandgap and low resistivity.

Concerning the ternary metal oxide compounds, recently there are reports about ZnM<sub>2</sub>O<sub>4</sub> (M= Ir, Rh and Co) spinel type compounds that have presented p type conductivity combined with a large bandgap reaching almost 3 eV as well. Thus, those type of metal oxide compounds are also attracting more and more interests for their promising applications in transparent electronics. On the other hand, due to a cheaper cost and low toxicity with copper oxide, there are several works focusing on developing copper based ternary metal oxide compounds. In fact, the largest family of p type ternary metal oxides are copper based, usually with delafossite structure CuMO<sub>2</sub> (M= Al, Ga, Cr, etc) or the spinel compound SrCu<sub>2</sub>O<sub>2</sub>, as shown in Table I-1.

Table I-1. Optical and electronic properties of reported commonly seen p and n type metal oxide materials.

p type metal oxides	deposition/ synthesis technique	resistivity ( $\Omega\cdot\text{cm}$ )	carrier density ( $\text{cm}^{-3}$ )	mobility ( $\text{cm}^2/\text{V}\cdot\text{s}$ )	bandgap (eV)	refs
SnO	PLD	n.a	$2.5 \times 10^{17}$	2.4	2.7	24,25
NiO	rf-MS	0.1~0.45	$10^{17} \sim 10^{18}$	5~28	3.6~4	26
Li doped NiO	spray pyrolysis	0.4~1.98	$1.9 \times 10^{17} \sim 1.2 \times 10^{18}$	2.2~12	~2.9	27
ZnIr <sub>2</sub> O <sub>4</sub> spinel type oxide	PLD	~25	n.a	n.a	2.97	28
Cu <sub>2</sub> O	rf-MS	~100	~ $10^{15}$	60	2.7	16
SrCu <sub>2</sub> O <sub>2</sub>	PLD	20	$6.1 \times 10^{17}$	0.46	3.3	29
CuGaO <sub>2</sub>	PLD	16.7	$1.7 \times 10^{18}$	0.23	3.6	30
CuCrO <sub>2</sub>	ALD	0.1~2.2	n.a	n.a	3.09	31
CuCr <sub>0.93</sub> Mg <sub>0.07</sub> O <sub>2</sub>	spray pyrolysis	~1	$2 \times 10^{19}$	0.2~0.3	3.1	32
CuAlO <sub>2</sub>	thermal heating	1~10	$1 \times 10^{17}$	10	3.5	33,34
CuAlO <sub>2</sub>	MOCVD	0.5	$1.8 \times 10^{19}$	0.16	3.75	35
AgCuO <sub>2</sub>	Hydrothermal (single crystal)	0.01~0.05	n.a	n.a	n.a (~1 eV)	36
n type metal oxides						
ZnO	AP-SALD	$5 \times 10^{-2}$	$10^{19} \sim 10^{20}$	5.5	3.3 ~ 3.5	37
Hydrogenated ZnO	rf-MS	$2.8 \times 10^{-3}$	$4.4 \times 10^{19}$	47.1	3.3 ~ 3.5	38
Al doped ZnO (AZO)	rf-MS	$1.4 \times 10^{-4}$	~ $10^{21}$	36.8	3.5 ~ 3.7	39
Indium doped Tin Oxide (ITO)	Reactive ion plating	~ $10^{-4}$	~ $10^{26}$	~10	~ 3.9	40
Fluorine doped Tin Oxide (FTO)	MS	$6.71 \times 10^{-3}$	$1.46 \times 10^{20}$	15	3.8	41

Note: Pulsed Laser Deposition (PLD), Atomic Layer Deposition (ALD), Metal Organic Chemical Vapor Deposition (MOCVD) and radio frequency Magnetron Sputtering (rf-MS).

They generally have shown enlarged optical bandgap, up to 3.75 eV with CuAlO<sub>2</sub>, and reduced resistivity in the range of 0.1~20  $\Omega\cdot\text{cm}$ . However, due to the presence of high VBM tail states in the electronic structure, most of the reported copper ternary oxide compounds have improper high carrier concentration and low mobility<sup>29-35</sup>. Those characteristics largely limit their applications, such as in transistors. In addition, by reviewing the listed p type metal oxides in Table I-1, p type metal oxides with small bandgap are rarely reported, which adds up to the difficulty of achieving full metal oxide composed solar cells with good performance. To use the p type metal oxide as absorber layer in solar cell, smaller bandgap around 1.5 eV is required.

## **I.2 New emerging potential Ag-Cu oxide family for photovoltaic application: $\text{AgCuO}_2$ and $\text{Ag}_2\text{Cu}_2\text{O}_3$ .**

In addition to our interests on optimization of pure  $\text{Cu}_2\text{O}$  phase, the recent family of silver copper mixed oxides family attracts our attention.<sup>36,42,43</sup> The very origin of the birth of Ag-Cu oxides family is from the attempts so seek alternatives for toxic element Hg in superconductive materials.<sup>36</sup> Until now, two types of ternary Ag-Cu mixed oxides have been reported, namely,  $\text{Ag}_2\text{Cu}_2\text{O}_3$  and  $\text{AgCuO}_2$ . With more recent study of their crystal structure and electronic and optical properties, Ag-Cu oxides compound have shown fascinating features for photovoltaic application. In this section, we introduce the crystal structures of  $\text{Ag}_2\text{Cu}_2\text{O}_3$  and  $\text{AgCuO}_2$ , the electronic and optical properties and the synthesis techniques used so far to obtain them.

### **I.2.1 Crystal and electronic structures of Ag-Cu oxides family**

The origin of the silver-copper mixed oxide family was actually from the research for copper based superconductors. Among those, the cuprates containing mercury presented the highest  $T_c$  points, however Hg is severely toxic and non-environmentally friendly.<sup>44</sup> Thus, there was a lot of work attempted to replace this element in the structure. The electronic structure of  $\text{Ag}^{1+}$  and  $\text{Hg}^{2+}$  are similar, therefore there was lots of efforts involved and attempted to substitute the Hg element in the superconductor, and this was the initial motivation of synthesizing Ag-Cu oxides. The first Ag-Cu oxide compound reported was  $\text{Ag}_2\text{Cu}_2\text{O}_3$  from the work of P.Gómez-Romero *et al.* in 1999 by using acid bath chemistry or molten hydroxide fluxes to precipitate the precursor and the crystal structure was proposed.<sup>45</sup> In another work from this group, the  $\text{Ag}_2\text{Cu}_2\text{O}_3$  phase was obtained by reacting  $\text{Cu}(\text{NO}_3)_2$  and  $\text{AgNO}_3$  in 3 M NaOH solution for 6 hours at room temperature. From that, more detailed studies on this material were investigated including thermal, magnetic and electronic properties.<sup>46</sup>

As shown in Figure I-1 a), the crystal structure of  $\text{Ag}_2\text{Cu}_2\text{O}_3$  contains Cu-4O structure and zigzag shaped linear arranged Ag atoms. Such as structure is very similar to PdO except that there is Cu-4O and Ag zigzag shaped coordinated alternatively. While in Figure I-1 b), in a reducing environment (Ar with  $\text{H}_2$ ),  $\text{Ag}_2\text{Cu}_2\text{O}_3$  rapidly decomposed to Ag and Cu metallic around 270 °C. While with more oxidation environments, like in air or oxygen, such phase can be stable up to 320 °C and then rapidly decomposes to Ag plus CuO. While in Figure I-1 c), the band structure of  $\text{Ag}_2\text{Cu}_2\text{O}_3$  is given along the symmetry lines of Brillouin Zone

calculated by *Extended Hückel Tight Binding* (EHTB) method which exhibits about 1 eV bandgap along the  $\Gamma$ X and  $\Gamma$ Z directions in Brillouin Zone. Unlike the  $\text{Cu}_3\text{O}_4$  case (isostructural with  $\text{Ag}_2\text{Cu}_2\text{O}_3$ ), the minimum of conduction band is mainly contributed from Ag ions and the valence band maximum is established mainly from Cu ions, as shown in Figure I-1 d), which shows the density of states (DOS) for both  $\text{Ag}_2\text{Cu}_2\text{O}_3$  and  $\text{Cu}_3\text{O}_4$ .

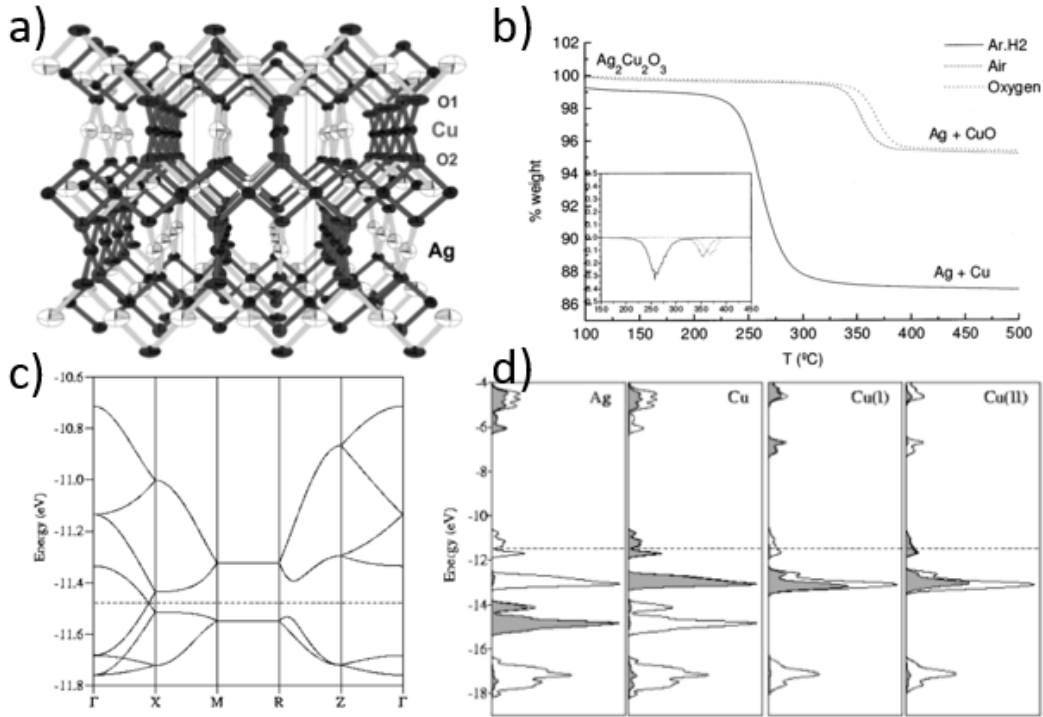


Figure I-1. Details about  $\text{Ag}_2\text{Cu}_2\text{O}_3$  phase. a) Schematic illustration of crystal structure. b) Thermal Gravimetric Analysis (TGA) shows rapid decomposition at 250 °C in reducing atmospheres. c) Band structure of  $\text{Ag}_2\text{Cu}_2\text{O}_3$  obtained by Extended Hückel Tight Binding (EHTB) calculation. d) Density of States (DOS) for  $\text{Ag}_2\text{Cu}_2\text{O}_3$  (left) and  $\text{Cu}_3\text{O}_4$  (right) obtained from EHTB calculation. The shading areas refer to the contribution of the metal ions marked on the top corner. In both c) and d), dash line represents position of the Fermi level.<sup>46</sup>

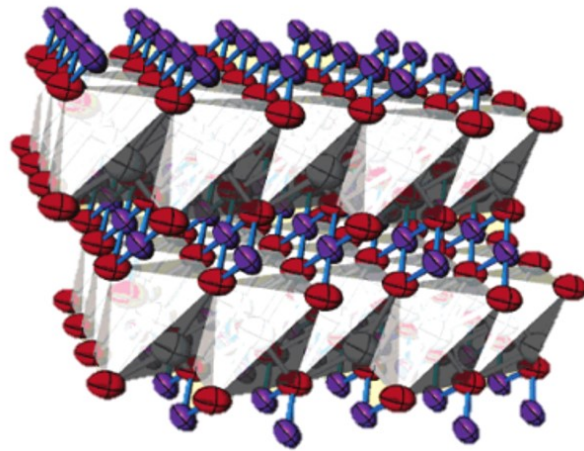


Figure I-2. Schematic illustration of  $\text{Ag}_2\text{Cu}_2\text{O}_4$  crystal structure with octahedral  $\text{Ag-O}_6$  (2+4), in which red atom represents oxygen, blue for copper and grey for silver atom (inside octahedral)<sup>47</sup>

Besides the  $\text{Ag}_2\text{Cu}_2\text{O}_3$  phase, in a work from D. Muñoz-Rojas *et al.*, a new Ag-Cu oxide phase  $\text{AgCuO}_2$ , was synthesized based on electrochemical oxidation of  $\text{Ag}_2\text{Cu}_2\text{O}_3$ .<sup>48</sup> The crystal structure is schematically illustrated in Figure I-2,<sup>47</sup> in which the copper atoms (blue) are surrounded by 4 oxygen atoms (red) each, while silver atoms (grey) are inside a distorted octahedral structure formed by six oxygen atoms. The crystal structure of  $\text{Ag}_2\text{Cu}_2\text{O}_4$  resembles a lot that of  $\text{AgO}$  ( $\text{Ag(I)Ag(III)O}_2$ )<sup>49</sup>, therefore there is a tendency to view the oxidation state of Ag and Cu in the silver copper oxide as  $1+$  and  $3+$ .

To explore the charges thus the electronic structure of the  $\text{AgCuO}_2$ , XPS characterization of such compound was carried out and the full spectra is shown in Figure I-3. As it is shown in Figure I-3 b), the Ag 3d range contains a spin-orbit coupling doublet, Ag  $3d_{3/2}$  and Ag  $3d_{5/2}$ . For  $\text{Ag}_2\text{Cu}_2\text{O}_3$  XPS spectra, the positions of the two peaks, locating at 367.9 eV and 373.9 eV, corresponding to  $\text{Ag}^{1+}$  oxidation state in this compound.<sup>47</sup>

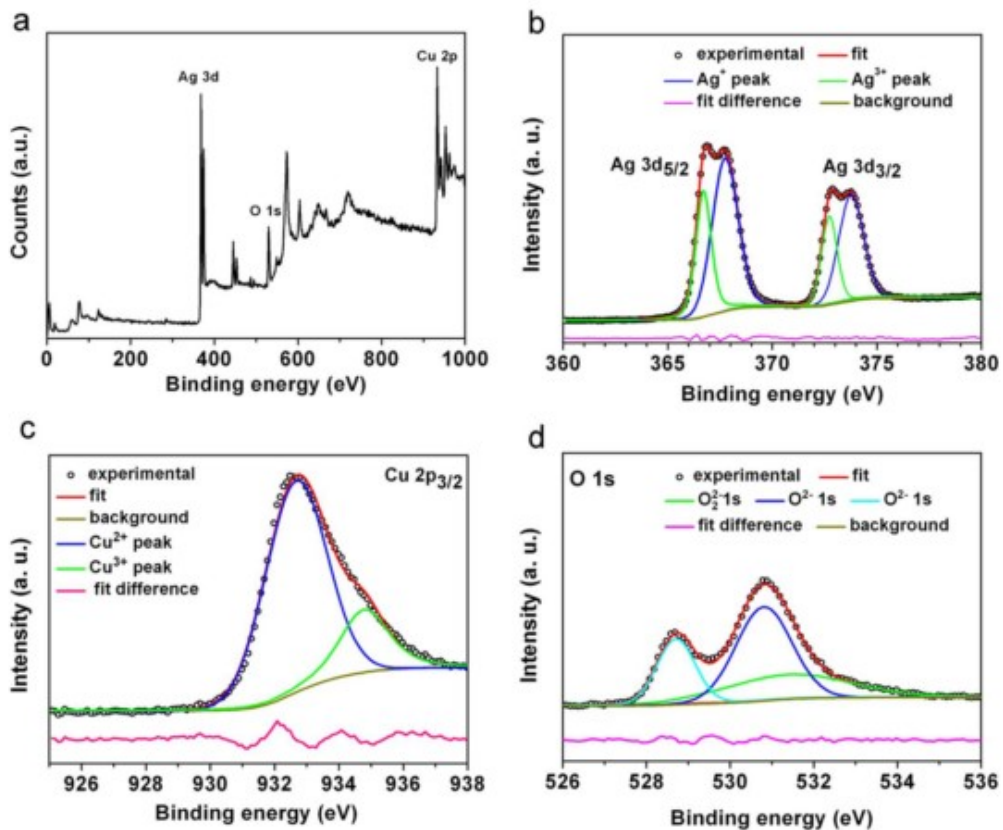


Figure I-3. XPS characterization of electrodeposited  $\text{AgCuO}_2$  ( $\text{Ag}_2\text{Cu}_2\text{O}_4$ ) phase. a) the full XPS spectra and the detailed spectra at a) Ag 3d, c) Cu 2p and d) O 1s regions. Open circles represent experimental data and solid and dashed lines are fittings.<sup>50</sup>

While in the case of electrochemically deposited  $\text{Ag}_2\text{Cu}_2\text{O}_4$ , each originally single peak at Ag  $3d_{3/2}$  and Ag  $3d_{5/2}$  is splitted into two peaks. By fitting, they were ascribed to a coexistence of  $\text{Ag}^{1+}$  and  $\text{Ag}^{3+}$  charge states, a mixed valence state classified as type II (fast hopping between  $\text{Ag}^{1+}$  and  $\text{Ag}^{3+}$ ) or type III, totally delocalized.<sup>47,50</sup> Similar mix valence charging

states can be also found in Figure I-3 c), implying that Cu ions in this oxide compound could carry both 2+ and unusual 3+ oxidation state. Lastly, the peaks corresponding to O 1s are presented in Figure I-3 d). The fitted lines showed three components corresponding to three binding energies, 528.9, 530.6 and 532.3 eV. Binding energies at 528.9 and 530.6 eV refer to oxide species ( $O^{2-}$ ) and binding energy 523.3 eV would correspond to peroxide species ( $O_2^{2-}$ ). This implies that the extra charges from Ag and Cu are delocalized onto oxygen atoms. After the discovery of the Ag-Cu oxide tertiary family, other derivatives from this family were also reported. Such as the discovery of  $Ag_2MnCuO_4$ , by substitution of one Cu atom in the structure with Mn atom.<sup>51</sup> The SEM image of such phase is shown in Figure I-4 a), in which a layered structure with large surface area is presented. In Figure I-4 b), the diffraction pattern and crystal structure are presented.

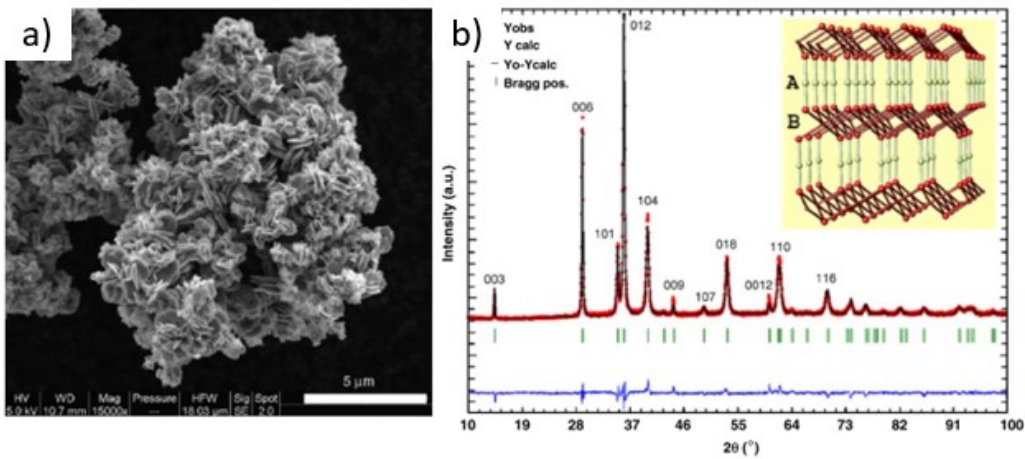


Figure I-4. a) SEM image of  $Ag_2MnCuO_4$  crystals. b) the XRD pattern and inserted schematic crystal structure.<sup>51</sup>

## I.2.2 Transport properties of new Ag-Cu oxides

Since the initially synthesized  $AgCuO_2$  was in powder form, to investigate the transport properties of the new phase, low density pellets were pressed, as reported in the work by F. Sauvage *et al.*<sup>43</sup> In this work, both  $AgCuO_2$  and  $AgCu_{0.5}Mn_{0.5}O_2$  pellets were prepared and conductivity and Seebeck coefficients were measured. The electrical conductivity was measured by standard four probe Pt tip device and the Seebeck coefficient was characterized by thermopower. High electrical conductivity  $3.2 \times 10^{-1}$  S/cm was obtained for  $AgCuO_2$ , while  $AgCu_{0.5}Mn_{0.5}O_2$  presented much lower (3 orders of magnitude) conductivity, as shown in Figure I-5.

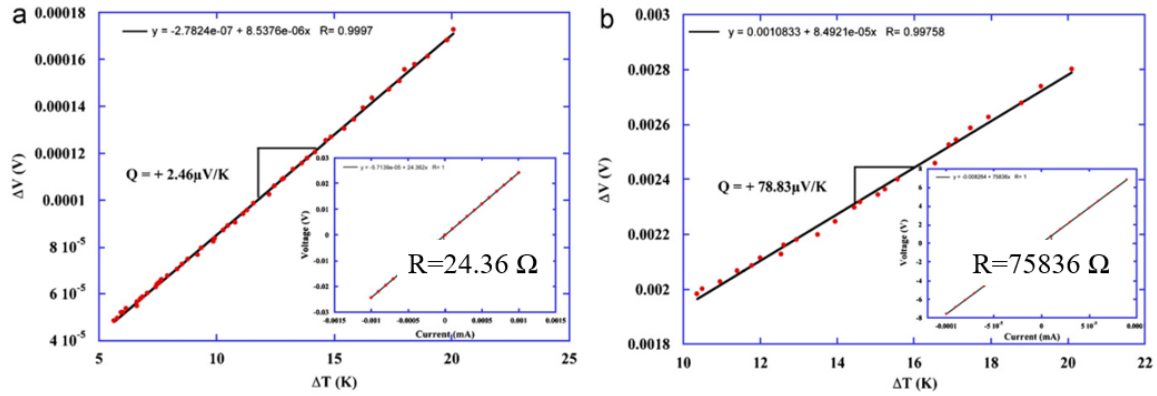


Figure I-5. Thermopower characterization  $\Delta V = f(\Delta T)$  for: a)  $\text{AgCuO}_2$  and b)  $\text{Ag}_2\text{MnCuO}_4$ . Four probes DC conductivity measurements conducted in room temperature as inserted images.<sup>43</sup>

During the thermal power measurement, thermovoltage  $\Delta V$  and temperature gradient  $\Delta T$  were followed simultaneously from the decay of short pulse to 100 °C. Therefore, the Seebeck coefficient was extracted, as shown in Figure I-5. The thermopower measurements show that the nature of conductivity is hole-type (p) with positive Seebeck coefficient of value +2.46 for  $\text{AgCuO}_2$  and +78.83  $\mu\text{V/K}$  for  $\text{AgCu}_{0.5}\text{Mn}_{0.5}\text{O}_2$ . Such a high conductivity and low Seebeck coefficient for  $\text{AgCuO}_2$  (3 orders of magnitude higher conductivity than  $\text{AgCu}_{0.5}\text{Mn}_{0.5}\text{O}_2$ ) can be attributed to the charge delocalization in its mix-valence bands.

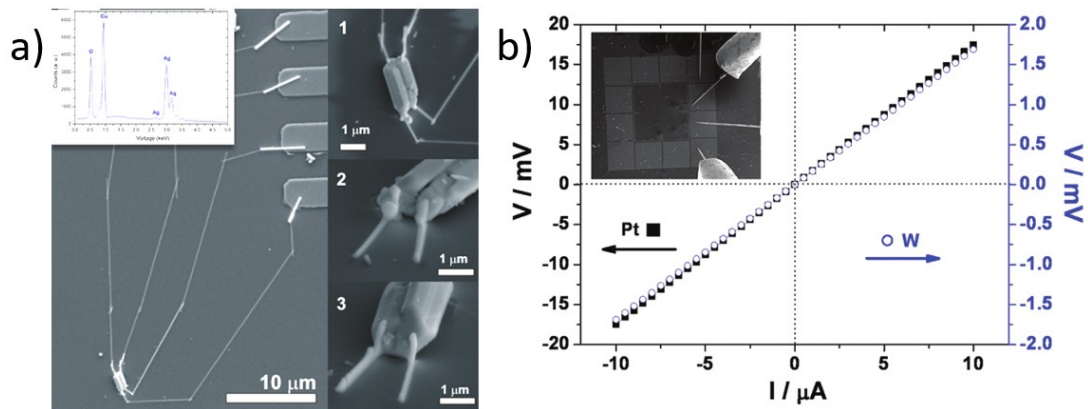


Figure I-6. a) SEM image of a  $\text{AgCuO}_2$  particle from hydrothermal reaction contacted using ion assisted deposition of Pt. The insets show a close-up of the particle from different perspectives, as well as an EDX spectrum of the contacted particle showing the corresponding peaks for Ag and Cu. b)  $V$  versus  $I$  plots obtained for contacted particles using FIB-Pt nanocontacts. The inset shows the 4 probes contacting the patterned Al microelectrodes in the wafer, to which the metallic nano-wires, Pt in this case, are connected.<sup>36</sup>

However, due to the porosity and weak connections in the low density pellets (the presence of Ag prevents a high temperature sintering of the pellets), the reported conductivity was an underestimation. Therefore, a more precise conductivity study of  $\text{AgCuO}_2$  single crystals was reported by D. Muñoz-Rojas *et al.*,<sup>36</sup> as shown in Figure I-6.  $\text{AgCuO}_2$  particles with size about 2  $\mu\text{m}$  were synthesized through hydrothermal reaction and Pt nano contacts were deposited on the particles by Focused Ion Beam, as shown in Figure I-6 a).



Thus, current versus voltage characterization was performed. Initially, with the measured data by 2-probes, linear fitting of the lines showed comparable resistance of 250.6 and 235 k $\Omega$  with different sets of nanocontacts, thus implying good electrical contacts. Then 4-probe conductivity measurements were also conducted, linear fitting were also found and shown in Figure I-6 b). In this case, much lower resistance value of 1.75 k $\Omega$  was discovered. Considering the size and shape of the particles, a conductivity of 17 S.cm<sup>-1</sup> was estimated (one order of magnitude higher than for the low density pellets reported previously).

### I.2.3 Thin film deposition of Ag-Cu mixed oxides

The Ag-Cu oxides reported above were all initially synthesized as powder. For Ag<sub>2</sub>Cu<sub>2</sub>O<sub>3</sub> compound, since it has less limitation to be synthesized in less oxidizing environment, there are several works already reported for its deposition as thin films. Most of the Ag<sub>2</sub>Cu<sub>2</sub>O<sub>3</sub> thin films were deposited by sputtering or PLD<sup>52-54</sup>. In the work from J.F. Pierson *et al.*,<sup>55</sup> the possibility of tuning the Ag-Cu ratio in the compound films by Reactive Sputtering technique was reported.

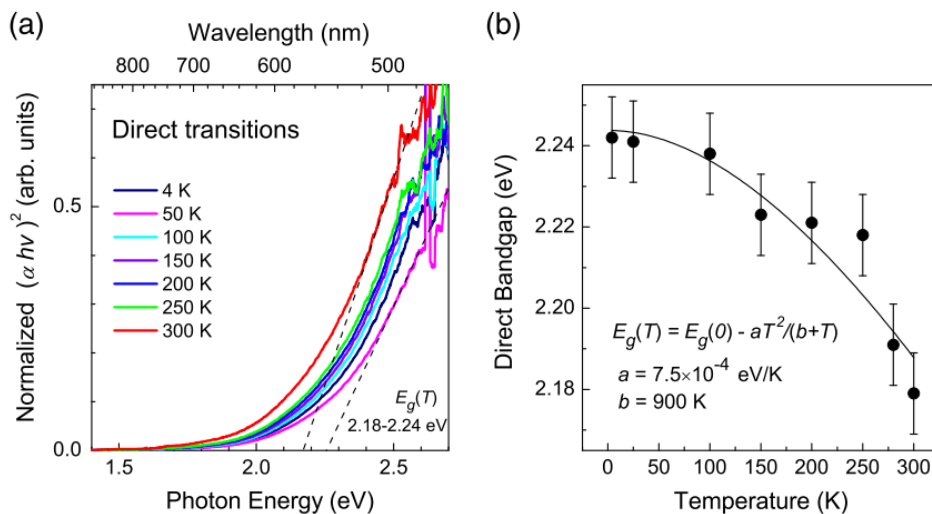


Figure I-7. a) Tauc plot using direct bandgap formula from transmittance data of a 460 nm thick Ag<sub>2</sub>Cu<sub>2</sub>O<sub>3</sub> thin film at temperatures ranging from 4 K to 300 K and b) the corresponding Varshni fitting of the bandgap versus temperature.<sup>53</sup>

In addition, from the work of E.Lund *et al.*,<sup>53</sup> the Ag<sub>2</sub>Cu<sub>2</sub>O<sub>3</sub> thin film electronic and optical properties were comprehensively studied. As shown in Figure I-7 a), presenting transmittance data of 460 nm thick Ag<sub>2</sub>Cu<sub>2</sub>O<sub>3</sub> film, a bandgap about 2.2 eV was obtained. While in Figure I-7 b), a decreasing bandgap with increasing temperature was observed.

In addition for bandgap determination, Photoluminescence (PL) characterizations were conducted at various temperatures ranging from 10 to 300 K and results are shown in Figure I-8 a). As it is shown, the PL curves of Ag<sub>2</sub>Cu<sub>2</sub>O<sub>3</sub> demonstrate a low luminescence yields.

Also, the emission spectra present two peaks at about 2.2 and 2.7 eV. The former can be related to the intra band transition as plotted in Figure I-7 a) with bandgap 2.2 eV.

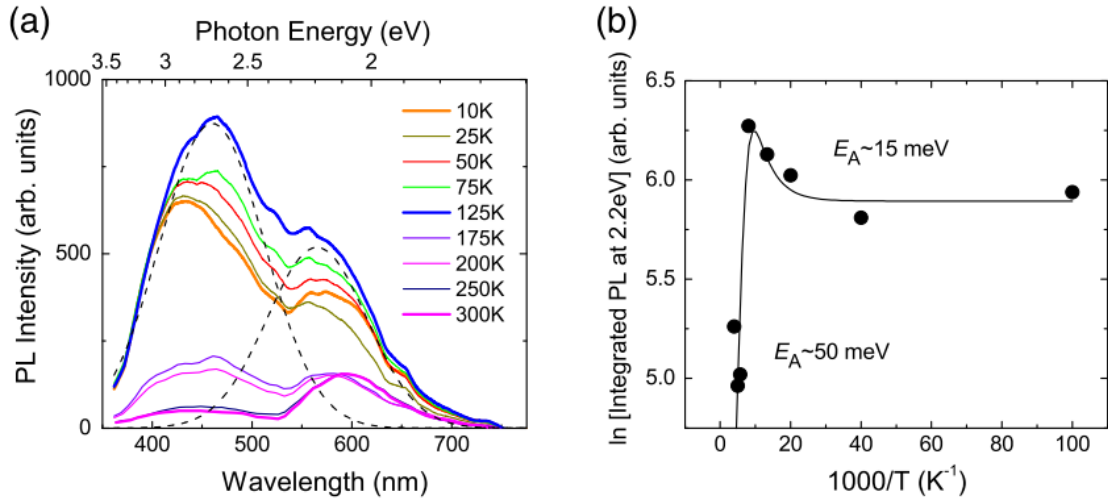


Figure I-8. Photoluminescence (PL) characterization of a 460 nm  $Ag_2Cu_2O_3$  thin film. a) Full PL curve between temperature 10 and 300 K using 325 nm as excitation line. b) Arrhenius plot of integrated PL intensity at 2.2 eV.<sup>53</sup>

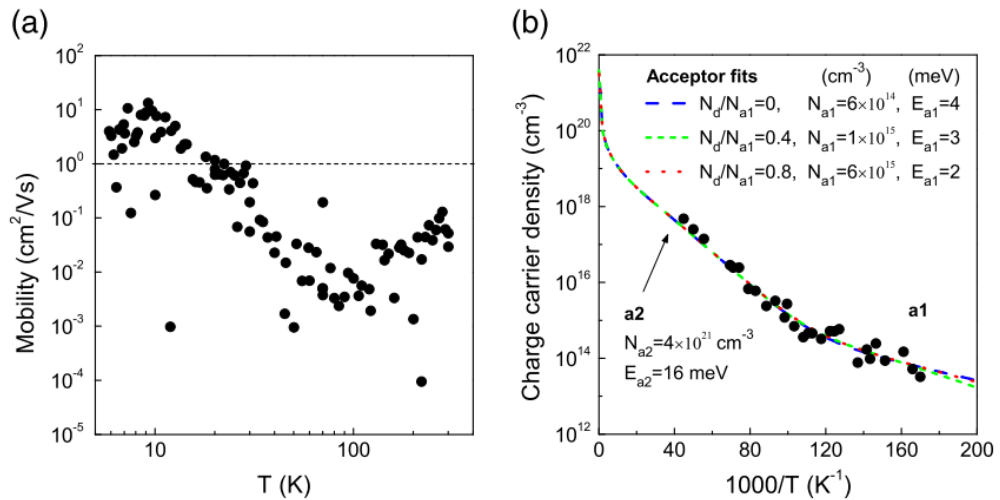


Figure I-9. Hall effect measurements of 90 nm thick  $Ag_2Cu_2O_3$  thin film deposited at various temperatures. a) Mobility and b) carrier concentration versus the deposition temperature.<sup>53</sup>

While the other emission center at 2.7 eV can be attributed to a higher band emission but it was not confirmed. Lastly, Hall Effect measurements revealed the low mobility and high carrier density nature as shown in Figure I-9. With higher deposition temperature, the charge mobility tends to decrease from 10 to  $10^{-2}$   $cm^2/V.s$ , while carrier concentration increases from the order of  $10^{14}$  to  $10^{19}$   $cm^{-3}$ . Both the optical and electronic properties were confirmed in another work.<sup>54</sup>

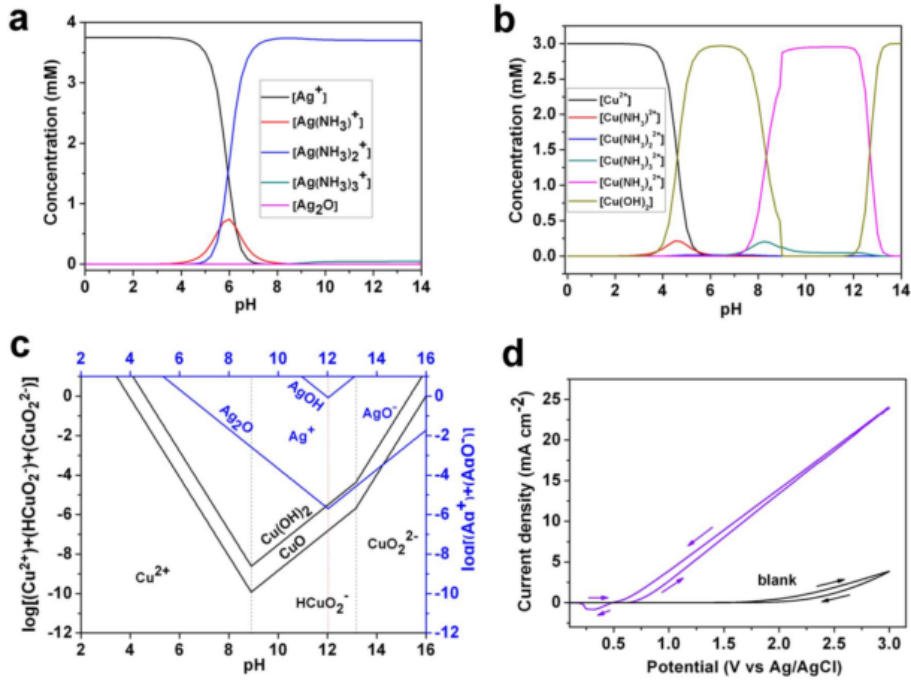


Figure I-10. Calculated species distribution versus pH in solution contains 3.75 mM  $\text{AgNO}_3$ , 3 mM  $\text{Cu}(\text{NO}_3)_2$ , 0.5 M  $\text{NH}_3 \cdot \text{H}_2\text{O}$  at room temperature for a) Ag (I) and b) Cu (II) species. c) Influence of pH on solubility of  $\text{Ag}_2\text{O}$ ,  $\text{AgOH}$ ,  $\text{CuO}$  and  $\text{Cu}(\text{OH})_2$  in solution. d) Cyclic voltammograms (CVs) measured with ITO electrode ( $1.5 \text{ cm}^2$ ) in such solution with scanning speed  $10 \text{ mV/s}$ .

Even though  $\text{Ag}_2\text{Cu}_2\text{O}_3$  in thin film was reported by sputtering technique at low temperature (no more than  $100 \text{ }^\circ\text{C}$ ), due to the critical requirements for high oxidation environment to form  $\text{AgCuO}_2$  phase plus its thermal instability, currently there is no dense and continuous thin films reported. But, recently from a work of *Q. Lu et al.*,<sup>50</sup>  $\text{AgCuO}_2$  nano plates were successfully deposited by electrochemical deposition on ITO substrate with incorporation of ammonia in the process as electron pair donor ligand. In order to chose a proper pH for an easier control of the stoichiometry of the final product, the influence of solution pH on Ag(I) and Cu(II) species were investigated and calculated in a solution with 3.75 mM  $\text{AgNO}_3$ , 3 mM  $\text{Cu}(\text{NO}_3)_2$  and 0.5 M  $\text{NH}_3 \cdot \text{H}_2\text{O}$  at room temperature, as shown in Figure I-10 a) and b). The concentration of  $\text{Ag}^{1+}$  species decreases for pH values exceeding 5 and the  $\text{Ag}(\text{NH}_3)^{2+}$  species concentration keep increasing until pH reaches 8 and stabilizes. While the  $\text{Ag}(\text{NH}_3)^+$  only exists when pH is between 5 and 8. In the case of Cu(II), due to the strong bonding between Cu ions and ammonia group, the ammonia ligand keeps increasing in the Copper ammonia complex when pH increases, therefore we see several plateaus at different pH ranges. Figure I-10 c) demonstrates the solubility evolution of both Ag and Cu oxide/hydroxide by the influence of pH in such solution. The silver species presents higher solubility in a general view, therefore to maintain the correct stoichiometry in  $\text{AgCuO}_2$  compound, slightly more Ag precursor should be added. Lastly, with  $10 \text{ mV} \cdot \text{s}^{-1}$  scanning

rate, the cyclic voltammograms with and without the mixture solution on ITO substrate are shown in Figure I-10 d). In the forward scan, the current rose for potential higher than 0.58 V. In the backward scan, the current decreased down to even lower potential than 0.58 V. This implies reduced slight irreversibility of the electrochemical oxidation reaction.

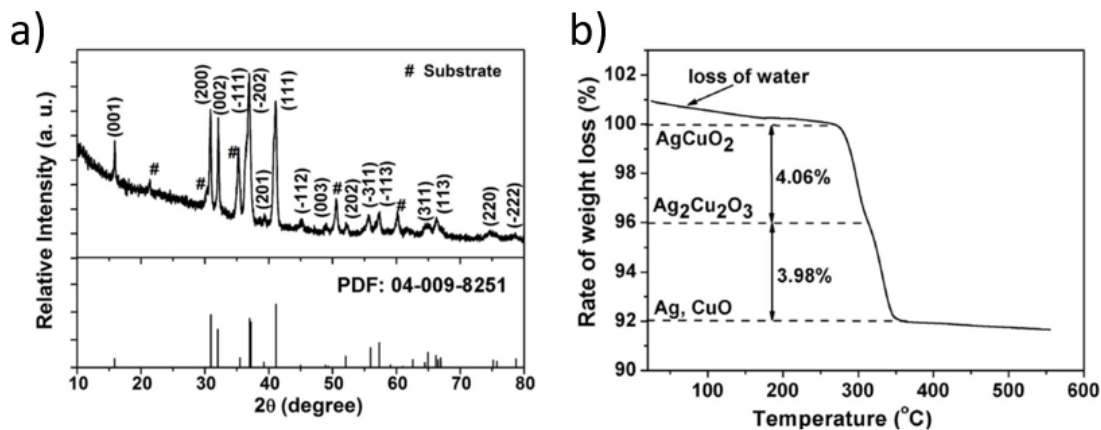


Figure I-11. a) XRD pattern of electrodeposited on ITO substrate. b) TGA analysis of  $\text{AgCuO}_2$  nano plates under  $\text{N}_2$  atmosphere.

Within the 0.25 M NaOH solution, by applying potential in the range of  $\text{H}_2\text{O}$  and  $\text{NH}_3$  oxidation,  $\text{AgCuO}_2$  nanoplates were coated on ITO electrode. The XRD pattern in Figure I-11 a) presents a rather pure  $\text{AgCuO}_2$  compound phase and the TGA analysis in figure b) shows a rapid decomposition over 250 °C of this compound.

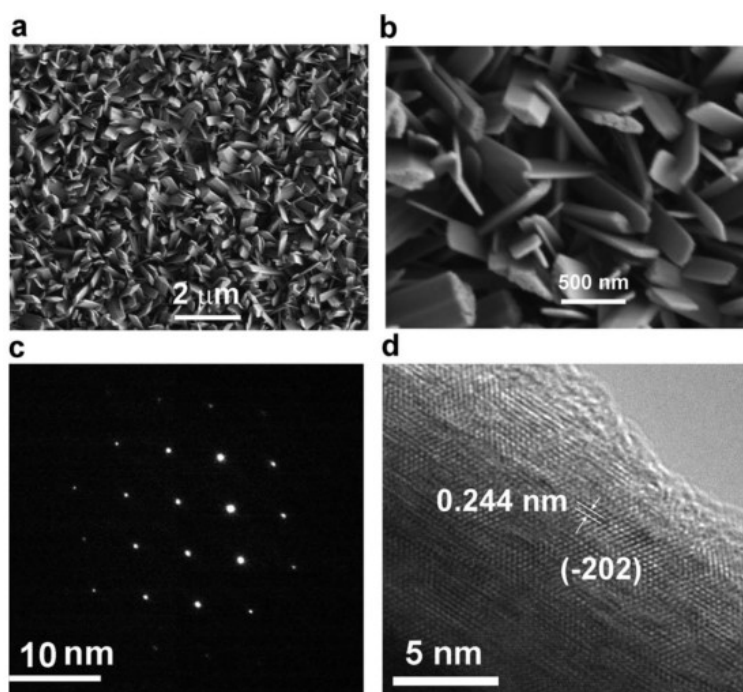


Figure I-12. a) and b) morphology of  $\text{AgCuO}_2$  nanoplates by SEM. c) is the SAED pattern of  $\text{AgCuO}_2$  plate and d) is the HRTEM image of a nanoplate.<sup>50</sup>

The morphology of the nano plates shown in Figure I-12 a) and b) have thickness about 50 nm and length 1  $\mu\text{m}$ , in which the EDS also suggests a Ag/Cu ratio 1:1 in accordance with the stoichiometry. With the TEM characterization of one single nanoplate, the SEAD pattern (Figure I-12 c) and HR TEM image (Figure I-12 d) suggest that each nano plate is a single crystal of  $\text{AgCuO}_2$ . Even though  $\text{AgCuO}_2$  phase was achieved from the report, further optimization with this technique is required to obtain continuous and dense films.

Thus, among all the Ag-Cu oxides family, currently only  $\text{Ag}_2\text{Cu}_2\text{O}_3$  phase can be sputtered as a thin film, thus its electronic and optical properties have been evaluated and confirmed that it has direct optical bandgap of 2.2 eV. The mobility can reach maximum 10  $\text{cm}^2/\text{V}\cdot\text{s}$  and carrier density can get maximum  $10^{19} \text{ cm}^{-3}$ . In the case of  $\text{AgCuO}_2$ , due to a more critical oxidation environment required during its formation, currently no dense films are reported except nanoplates electrodeposited on ITO, therefore it requires more optimization or new thin film coating techniques in order to evaluate its electronic and optical properties.

### I.3 $\text{Cu}_2\text{O}$ structures and electronic properties

Among the p type metal oxides previously introduced,  $\text{Cu}_2\text{O}$  has drawn our attention, this is so since copper element is earth abundant, non-toxic and it can be processed through low cost chemical approaches.  $\text{Cu}_2\text{O}$  has a direct bandgap around 2 eV, depending on the synthetic technique. Thus, it has a wide range of applications, especially for application in photovoltaics, the calculated theoretical efficiency for  $\text{Cu}_2\text{O}$  based solar cells can reach an astonishing 20%.<sup>56</sup>

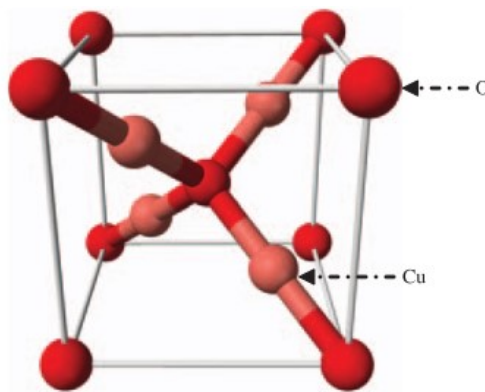


Figure I-13. Cubic crystal structure of  $\text{Cu}_2\text{O}$ .<sup>7</sup>

The crystal structure of  $\text{Cu}_2\text{O}$  is shown in Figure I-13.  $\text{Cu}_2\text{O}$  crystallizes in a cubic structure ( $a = 4.2696 \text{ \AA}$ ,  $Pn\bar{3}m$ ), with unit cell containing 4 copper atoms inside, 1 oxygen atom at center and 8 more oxygen atoms at each corner, shared with 8 other unit cells, and thus giving 2 oxygen atoms per unit cell.

The bandgap of  $\text{Cu}_2\text{O}$  is formed by interaction of outer shell orbitals between  $\text{Cu}^{1+}$  and  $\text{O}^{2-}$ . As shown in Figure I-14 a), the minimum of the conduction band (CB) is created by the empty 4s shell of  $\text{Cu}^{1+}$  cations while the maximum of the valence band (VB) is formed due to the hybridization between  $3d^{10}$  orbital of  $\text{Cu}^{1+}$  and  $2p^6$  orbital of  $\text{O}^{2-}$ . There are several acceptor levels within the gap, as have been described in the work of D. O. Scanlon *et al.*<sup>57</sup>, as shown in Figure I-14 b). The acceptor level is formed by copper vacancies just about 0.52 eV above the valence band, while there are other deep trap levels around 1 eV on top of the VBM.

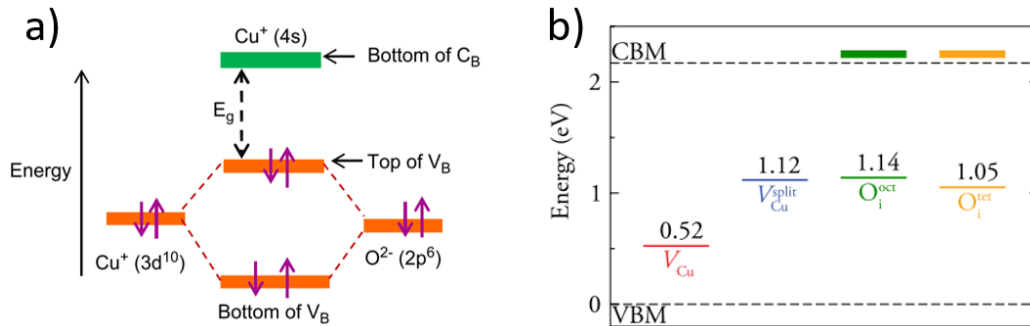
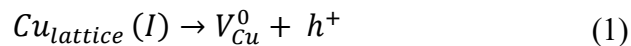


Figure I-14. Diagram of a) Conduction band and valence band formation in  $\text{Cu}_2\text{O}$ . b) Acceptor levels in  $\text{Cu}_2\text{O}$ .  
23,57

As it is known, pure  $\text{Cu}_2\text{O}$  without any doping is an intrinsic p type semiconductor oxide. To further understand the origin of the p type conductivity, the work of H. Raebiger *et al.*<sup>58</sup> gave an explanation from the point view of formation energy. They pointed out that such intrinsic p type conductivity arises from the non-stoichiometry of the  $\text{Cu}_2\text{O}$  lattice, by removing copper atoms and leaving an ionized copper vacancy  $V_{\text{Cu}}^0$ , as described in Equation 1.



To confirm the origin of p type conduction in  $\text{Cu}_2\text{O}$ , the formation enthalpies of different types of defects and vacancies were calculated and compared in copper rich/oxygen poor and copper poor/oxygen rich conditions, as presented in Figure I-15. As it is shown, in the Cu-rich/O-poor system (Figure I-15 a)), the overall lowest formation enthalpy is from formation of copper vacancy  $\Delta H(V_{\text{Cu}}^0) = 0.7 \text{ eV}$ . Another type of vacancy creation mechanism, i.e. neutral split vacancy, can be generated with higher formation energy  $\Delta H(V_{\text{split}}^0) = 1 \text{ eV}$ . Meanwhile, the oxygen interstitials have formation energy 1.3 eV and 1.8 eV, separately. In the other case (Figure I-15 b)), the Cu-poor/O-rich diagram has also shown that the overall lowest formation energy corresponds to copper vacancies.<sup>58</sup>

Therefore, in either deposition conditions, copper vacancy formation has always the lowest formation energy, thus it explains the origin of p type conductivity of intrinsic  $\text{Cu}_2\text{O}$ .

Another important principle of  $\text{Cu}_2\text{O}$  p type conductivity is the self-compensation mechanism. As shown in Figure I-15, the formation energy of charged defects changes with regard to the Fermi level. When the Fermi level is over 1 eV, the formation energy of  $V_{\text{Cu}}^0$  decreased to zero or even negative, implying that to compensate the increasing Fermi level, the crystal lattice produces positively charged copper vacancy. Such compensation mechanism is called self-compensation. Therefore, it explains the difficulty of doping  $\text{Cu}_2\text{O}$  into n type semiconductor (the same principle is behind the difficulty to have intrinsic p type  $\text{ZnO}$  for example).<sup>58</sup>

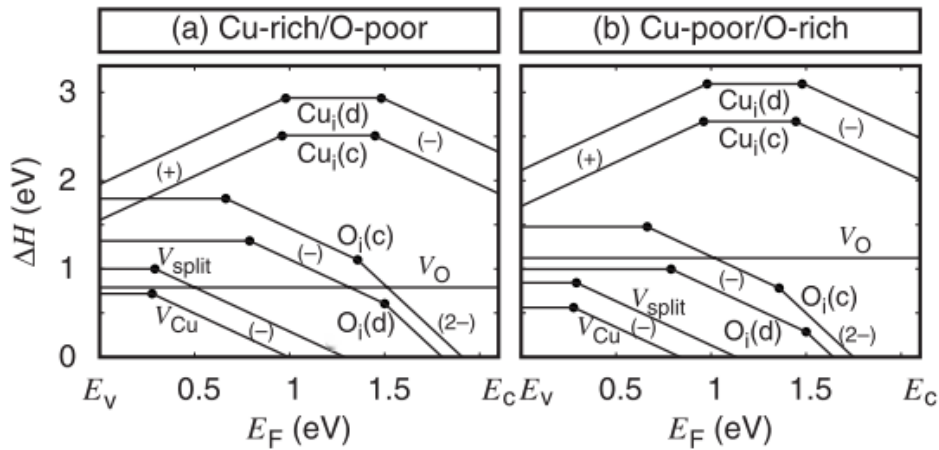


Figure I-15. Formation energy of different vacancies in copper rich a) and copper poor b) conditions. The signal c, d represents different interstitial sites inside the unit cell.<sup>58</sup>

Lastly, one significant characteristic of  $\text{Cu}_2\text{O}$  films is that the electronic properties, including even the bandgap, heavily rely on the synthesis technique used. As shown in Table I-2,  $\text{Cu}_2\text{O}$  films can be fabricated through almost all major thin film coating techniques. Meanwhile the electronic properties obtained with the different techniques varies a lot. Among those different synthesis techniques, the best quality  $\text{Cu}_2\text{O}$  films were produced through thermal oxidation of copper sheets and they presented high mobility over  $100 \text{ cm}^2/\text{V}\cdot\text{s}$ , thanks to the enormous grains size obtained (tens of microns). However, the daunting high temperature (above  $1000 \text{ }^\circ\text{C}$ ) for such oxidation process is very energy demanding. As well, with such high processing temperature, it's inconvenient and expensive for scalable production, and not well suited to device fabrication. On the other hand,  $\text{Cu}_2\text{O}$  film with good electronic properties can be also synthesized through several physical deposition techniques, like Pulsed Laser Deposition (PLD) or radio frequency Magnetron Sputtering (rf-MS).<sup>4, 16, 59</sup> But, long deposition duration and critical high vacuum are usually required with these physical

deposition techniques, making them still rather expensive and difficult to achieve scalable production.

Comparing with those techniques mentioned, chemical thin film coating techniques have shown their advantages in terms of low cost and scalability, especially with chemical solution based techniques. But, unfortunately, , due to the existence of higher density of defects in the grains boundaries, Cu<sub>2</sub>O films synthesized through solution approaches commonly have low electrical performance. For example, electrodeposited Cu<sub>2</sub>O films generally only reach carrier concentration about 10<sup>14</sup> cm<sup>-3</sup> and very low mobility around 1 cm<sup>2</sup>/(V.s) .<sup>60</sup> Applying those types of Cu<sub>2</sub>O films in devices can severely damage the final performance. Considering both cost, scalability and thin film quality, Metal Organic Chemical Vapor Deposition (MOCVD) and related techniques seem like an optimal option. We will discuss more in details about MOCVD synthesis and optimization of Cu<sub>2</sub>O in Aerosol Assisted MOCVD in Chapter IV.

Table I-2. Electronic and optical properties of Cu<sub>2</sub>O synthesized through different techniques.

Deposition techniques	Carrier Concentration (cm <sup>-3</sup> )	Mobility (cm <sup>2</sup> /V.s)	Resistivity (Ω. cm)	Bandgap (eV)	References
AP-SALD	~ 8.5 × 10 <sup>15</sup>	~ 7	~190	2.47	61,62
MOCVD	~ 3.3 × 10 <sup>15</sup>	~ 5	~ 1000	2.5	63
PLD	~ 1 × 10 <sup>15</sup>	~ 20	~ 200	n.a	22
rf-MS	~ 1 × 10 <sup>15</sup>	~ 60	~ 100	2.7	16, 66
Electrochemical deposition	~ 10 <sup>14</sup>	~ 1	~ 10 <sup>4</sup>	1.99	64
Spin coating	~ 1–2 × 10 <sup>15</sup>	~ 18 to 5	n.a	2	65
Thermal Oxidation	10 <sup>13</sup>	>100	n.a	2	17

This difference of electronic properties can be partly attributed to the synthesis temperature. In the work from E.Fortunato *et al.*,<sup>66</sup> by fitting the resistivity of Cu<sub>2</sub>O films sputtered at different temperatures, two conduction path models were found. As shown in Figure I-16, at higher deposition temperatures the conductivity is mainly controlled by the acceptor level E<sub>A</sub> (V<sub>Cu</sub>) with activation energy 0.15 eV, while at lower deposition temperatures, photon energy W<sub>ph</sub> with activation energy 0.03 eV becomes the dominant factor. It indicates that for Cu<sub>2</sub>O films deposited at lower temperatures, the hopping mechanism induced from the activation of phonon energy level is the major mechanism for Cu<sub>2</sub>O conductivity, while at higher temperatures the conductivity is determined by the acceptor level. Besides the reason of deposition temperature, there are other factors that can largely affect the produced Cu<sub>2</sub>O films, such as morphology, grain size and defects, etc.



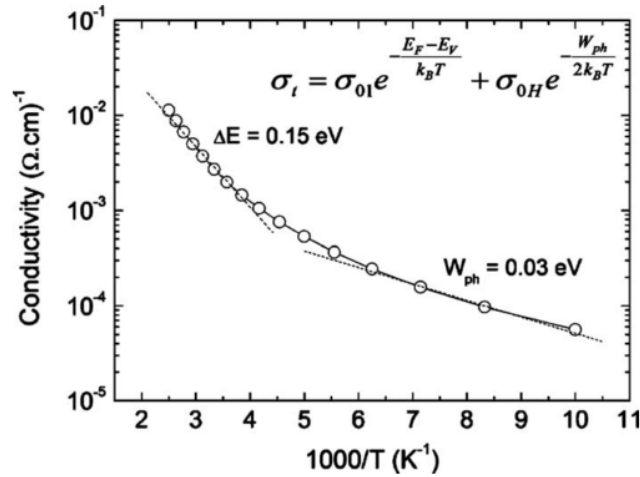


Figure I-16. Temperature dependency of dark conductivity of a 270 nm thick  $\text{Cu}_2\text{O}$  film. With higher deposition temperature, the conductivity is mainly controlled by the copper vacancy  $V_{\text{Cu}}$  0.3 eV above the VBM while at lower temperature, the conductivity is limited by the hopping mechanism. <sup>66</sup>

### I.3.1 Application of $\text{Cu}_2\text{O}$ in thin film transistor

First of all, with the semi-transparency of  $\text{Cu}_2\text{O}$ , it's widely studied for transparent electronic applications.  $\text{Cu}_2\text{O}$  as a p type oxide, it's normally used as the channel layer (active layer) in the p type thin film transistor (TFT) device. In the work of D.W. Nam *et al.*,<sup>67</sup> different thickness of  $\text{Cu}_2\text{O}$  films deposited by rf-MS were used as the active layer, Ni was used for the drain and source metal contacts. The width and length of the device are 1000  $\mu\text{m}$  and 100  $\mu\text{m}$  separately, as schematically presented in Figure I-17 a).

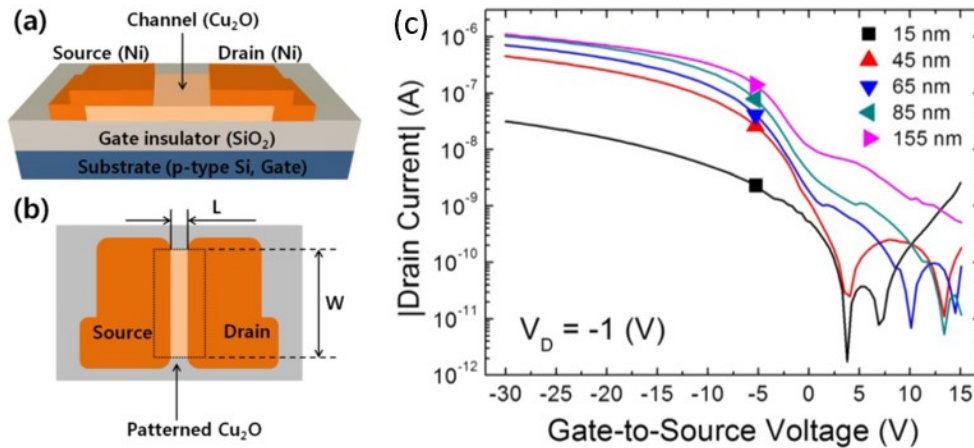


Figure I-17. Diagram of  $\text{Cu}_2\text{O}$  transistor a) top view and b) cross section view. c) the transfer curves of the fabricated  $\text{Cu}_2\text{O}$  TFT with different active layer thickness and drain voltage  $V_D$  -1 V.  $W$  and  $L$  are the width and length of the fabricated device ( $W$ : 1000  $\mu\text{m}$ ,  $L$ : 100  $\mu\text{m}$ ). <sup>67</sup>

By fixing the drain to source voltage to -1 V, the drain current vs Gate voltage curves were measured and are presented in Figure I-17 b). As it's shown, with a 45 nm thick  $\text{Cu}_2\text{O}$  film as the active layer, it shows a clean transfer function with low threshold slope (TS) around 1.6 V/dec. Furthermore, it reported the field-effect mobility ( $\mu_{\text{FE}}$ )  $\sim$  0.06  $\text{cm}^2/(\text{V}\cdot\text{s})$ , on-off

ratio exceeding  $10^4$  and threshold voltage ( $V_{th}$ ) about  $-6.7$  V. With even thicker active layer, the on-off ratio keeps increasing which can be explained by less boundary scattering in thicker  $\text{Cu}_2\text{O}$  films.

In addition, from a work of E. Fortunato *et al.*,<sup>66</sup> a p type  $\text{Cu}_2\text{O}$  based TFT was synthesized through sputtering technique at room temperature and followed with annealing at  $200^\circ\text{C}$  in air for 10 h. They showed the possibility of enhancing the carrier mobility ( $\mu_H$ ) from  $0.65$  to  $18.5$   $\text{cm}^2/\text{V}\cdot\text{s}$  thus the performance of the TFTs, which had a transmittance about 85%. The device output  $I_{DS} - V_{DS}$  curve is shown in Figure I-18 a), as it is shown, the drain to source voltage ( $V_{DS}$ ) is swept from  $+10$  to  $-60$  V and gate-to-source voltage ( $V_{GS}$ ) varies between  $+5$  and  $-55$  V. The output curves present a linear to saturation transition and no obvious charge accumulation at low  $V_{DS}$ , implying a low series resistance in source-drain contacts. By checking Figure I-18 b), the overall on off ratio is about  $2 \times 10^2$  and  $\mu_{FE}$  is up to  $3.9$   $\text{cm}^2/\text{V}\cdot\text{s}$ . Such low temperature fabricated TFTs opens new possibilities for flexible electronics as well.

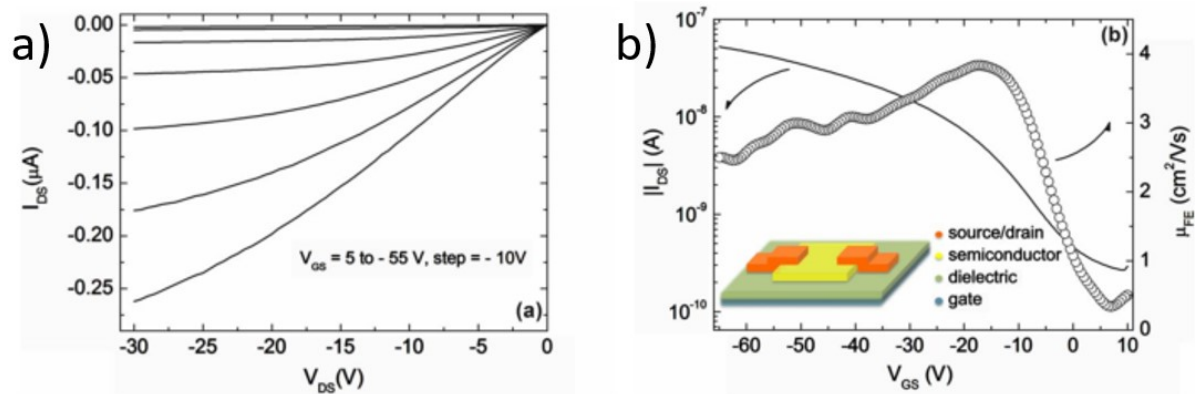


Figure I-18. Electrical characterizations of  $\text{Cu}_2\text{O}$  based TFT fabricated at room temperature and annealed at  $200^\circ\text{C}$ . a)  $I_{DS} - V_{DS}$  output curve; b) Transfer curve characterization  $I_{DS} - V_{GS}$  with drain voltage  $V_D = -5$  V and field effect mobility  $\mu_{EF}$  VS gate voltage  $V_{GS}$ .<sup>66</sup>

There are other reports about fabricating  $\text{Cu}_2\text{O}$  p type channel TFTs through other fabrication techniques like spin coating<sup>65</sup>, spray pyrolysis<sup>68</sup>, etc. But due to the undermined electronic property of synthesized  $\text{Cu}_2\text{O}$ , on off ratio only reach  $10^2$  and field effect mobility just reaches  $0.01$   $\text{cm}^2/\text{V}\cdot\text{s}$ . Therefore, due to a higher mobility of  $\text{Cu}_2\text{O}$  produced through several physical deposition techniques, including rf-MS and PLD, the final devices generally have better performance. However, those physical deposition process are rather expensive and time demanding, thus lower cost and more rapid chemical deposition approaches should be optimized.

### I.3.2 Application Cu<sub>2</sub>O in water splitting

Besides applying Cu<sub>2</sub>O layers for transistors, Cu<sub>2</sub>O is also very interesting for water splitting via photocatalysis, also called photo electrochemical (PEC) cell. It's a technique which combines solar energy collection and water electrolysis onto a single photoelectrode. The PEC cell relies on minority carriers generated by light absorption of the electrode and then being pumped into the liquid, thus a potential difference is created between the junction of semiconductor electrode and liquid, as shown in Figure I-19 a).<sup>69</sup> Thus, a redox reaction can be conducted at the vicinity of the electrode and one of the most studied reaction is for reducing H<sup>+</sup> into H<sub>2</sub>, namely, hydrogen generation. To achieve that, the energy band position of the semiconductor material should be carefully chosen. For an ideal semiconductor material for water electrolysis, its energy band should have negative potential versus hydrogen reduction and positive potential regarding to oxygen generation. With a comprehensive review of the energy band diagram of different semiconductors, Cu<sub>2</sub>O offers features. As shown in Figure I-19 b), Cu<sub>2</sub>O has an ideal energy band position for PCE cell hydrogen generation. Comparing to hydrogen reducing reaction potential, conduction band of Cu<sub>2</sub>O lies 0.7 V below while the valence band stays above the potential for oxidation reaction to produce O<sub>2</sub>.<sup>69</sup> Thus, it's an attractive material for H<sub>2</sub> generation without external voltage bias or low voltage bias. But Cu<sub>2</sub>O as the photoelectrode has problems of stability in solution and tends to be reduced into metallic Cu. Thus, finding a proper protection method for the Cu<sub>2</sub>O from reduction or oxidation in solution is required.

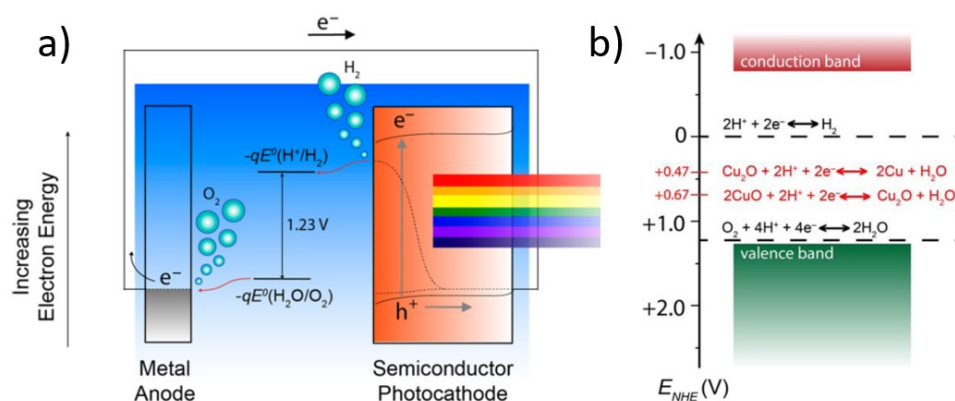


Figure I-19. a) working principle of a PEC cell. b) Energy diagram of Cu<sub>2</sub>O versus the potential of redox reactions of H<sub>2</sub>O.<sup>69</sup>

In the work of A. Paracchino *et al.*<sup>70</sup>, on top of electrodeposited Cu<sub>2</sub>O, different combinations of protection layers were tested and bilayers of n type Al doped ZnO and TiO<sub>2</sub> are confirmed for an effective prevention of the surface from oxidation. Pt was electrodeposited functioning as a catalyst, as shown in Figure I-20 a).

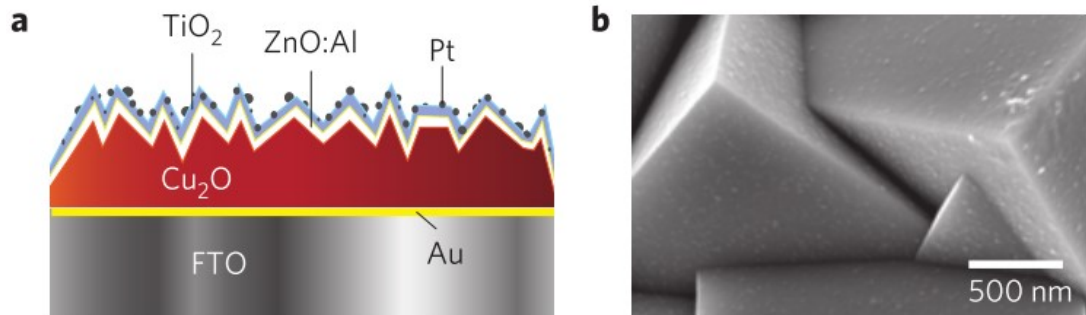


Figure I-20. PCE cells made from 1.3  $\mu\text{m}$  electrodeposited  $\text{Cu}_2\text{O}$  layer, bilayers of Al doped ZnO and  $\text{TiO}_2$  as the protective layers and Pt nanoparticles as catalyst. a) schematic presentation of the cross section and b) SEM image of the top-view.<sup>70</sup>

With (111) oriented  $\text{Cu}_2\text{O}$  surface, the photo electrochemical responses were characterized with bare  $\text{Cu}_2\text{O}$  electrode and with the bilayer protection, the results are shown in Figure I-21. With bared  $\text{Cu}_2\text{O}$  as the electrode, a photocurrent of  $-2.4 \text{ mA cm}^{-2}$  was generated at 0.25 V regarding to the reversible hydrogen electrode (RHE), in a 1 M  $\text{Na}_2\text{SO}_4$  electrolyte at pH 4.9. The corresponding J-V curve is presented in Figure I-21 a), which shows a rapid decay of photocurrent. The major reason for this rapid photocurrent decrease can be attribute to the reduction of  $\text{Cu}_2\text{O}$  electrode in solution, shown in Equation 2,

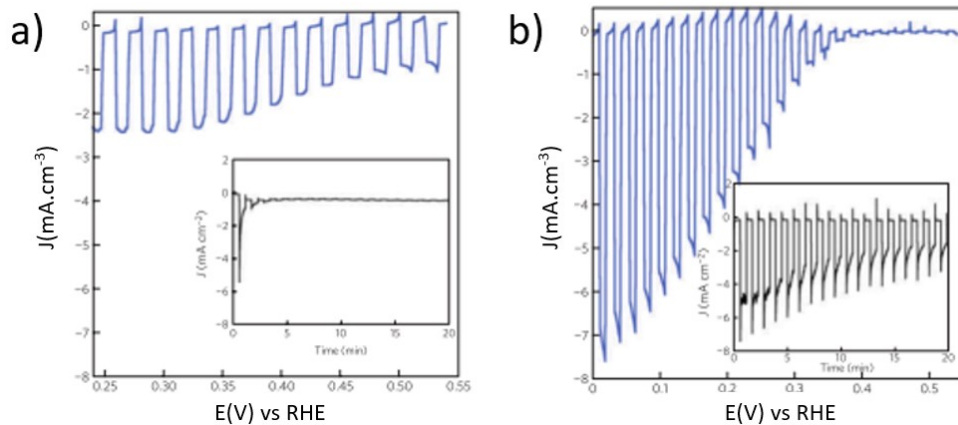
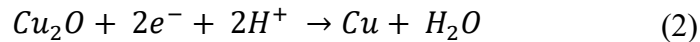


Figure I-21. Photo electrochemical response for bare a) and surface bilayer AZO/ $\text{TiO}_2$  coated b)  $\text{Cu}_2\text{O}$  electrode in 1 M  $\text{Na}_2\text{SO}_4$  solution. For the characterization a pulsed AM 1.5 light source was used.<sup>70</sup>

Therefore, to suppress such reaction, the bilayer made up of AZO and  $\text{TiO}_2$  was coated on top of  $\text{Cu}_2\text{O}$  as the protection layer with the Pt nanoparticles as catalyst. Meanwhile, the energy band bending was maintained to enable electrons flowing into liquid. The J-V curve with the protection is shown in Figure I-21 b), a maximum  $-7.6 \text{ mA cm}^{-2}$  was achieved at 0 V versus RHE in this case. The  $\text{Cu}_2\text{O}$  electrode has been kept active during 1 hour of test,

thus it confirmed a better stability during the water electrolysis process. The final Faradaic efficiency was evaluated to be close to 100%.

In addition to using  $\text{Cu}_2\text{O}$  as photoelectrode and solving its stability issues, in the work of Y.F. Lim *et al.*,<sup>71</sup>  $\text{CuO}$  was also under study for PECs cells with comparison of  $\text{Cu}_2\text{O}$ . Both phases were achieved through sol gel spin coating and followed with annealing in different atmosphere under  $500\text{ }^\circ\text{C}$ . Although  $\text{CuO}$  has an indirect bandgap about  $1.2\text{ eV}$ , it has shown a higher photocurrent of  $-0.35\text{ mA cm}^{-2}$  ( $\text{Cu}_2\text{O}$   $-0.28\text{ mA cm}^{-2}$ ) and better stability in liquid. But due to the preferable energy band position of  $\text{Cu}_2\text{O}$ , with the catalyst  $\text{NiO}$ , the photocurrent of PEC cells with  $\text{Cu}_2\text{O}$  can be enhanced up to  $-0.47\text{ mA cm}^{-2}$ . The energy band position of  $\text{Cu}_2\text{O}$  and  $\text{CuO}$  with respect to  $\text{NiO}$  is shown in Figure I-22. Therefore, even though both  $\text{Cu}_2\text{O}$  and  $\text{CuO}$  are suffering from instability in solution,  $\text{CuO}$  seems to be more stable and this can inspire new choices or structures for PEC cells to solve the stability issue and meanwhile obtaining higher photocurrent.

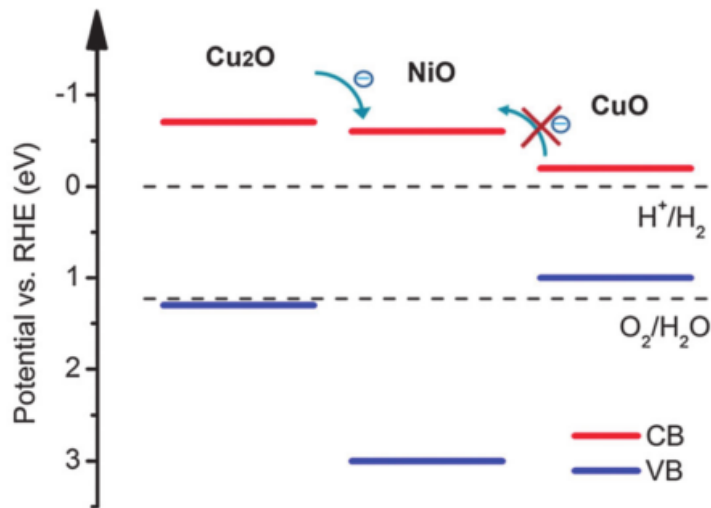


Figure I-22. Energy band diagram of  $\text{Cu}_2\text{O}$  and  $\text{CuO}$  versus  $\text{NiO}$  as the catalyst.

Therefore, in the work of Y. Yang *et al.*,<sup>72</sup> bilayer of  $\text{Cu}_2\text{O}/\text{CuO}$  was used at the photo electrode,  $\text{CuO}$  as the outside layer in contact with solution. The  $\text{Cu}_2\text{O}$  layer is synthesized through a repeated double-potential pulse chronoamperometric (r-DPPC) deposition method.  $\text{Cu}_2\text{O}/\text{CuO}$  bilayers were acquired through thermal oxidation of the  $\text{Cu}_2\text{O}$ . The PEC cell structure is shown in Figure I-23. With such combined bilayer structure, the light spectrum able to be absorbed was broadened, longer electrical field for efficient charge separation was obtained and the overall electrode could have better stability than a single  $\text{Cu}_2\text{O}$  phase.

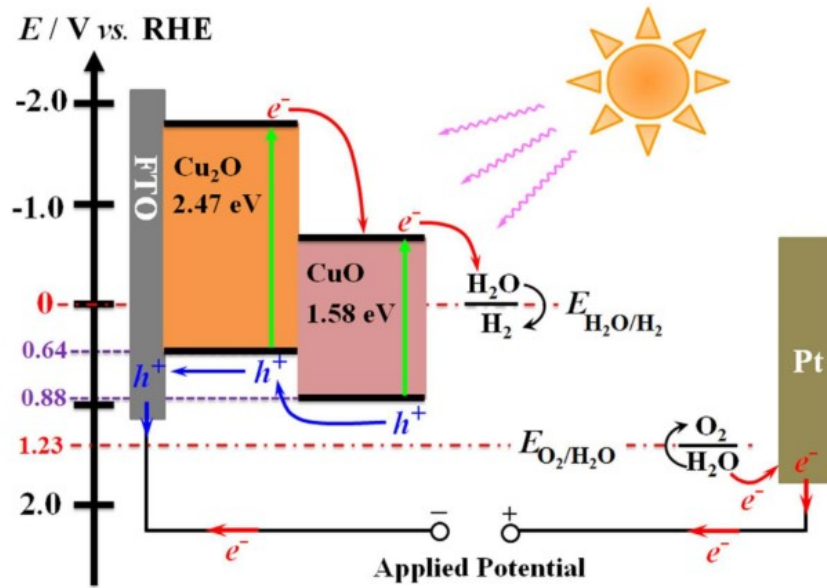


Figure I-23. Schematic presentation of energy diagram of  $\text{Cu}_2\text{O}/\text{CuO}$  bilayer photo electrode.

The photocurrent density with regarding to RHE is shown in Figure I-24 a), in which the pure  $\text{Cu}_2\text{O}$  photoelectrode (red line) has much lower current density ( $-0.21 \text{ mA cm}^{-2}$ ) and decaying much faster than the other two. Due to a smaller bandgap of  $\text{CuO}$  and better stability in solution, as previously mentioned, the current density with  $\text{CuO}$  electrode delivers much higher current density and more stable performance. But with the  $\text{Cu}_2\text{O}/\text{CuO}$  as electrode, as expected the photon current was largely enhanced up to  $-2.47 \text{ mA cm}^{-2}$ . In addition, the stability of the composite electrode is largely improved as well. Moreover, with such composite structure more light absorption and larger charge separation space, the conversion efficiency is largely improved than  $\text{Cu}_2\text{O}$  as electrode and better than pure  $\text{CuO}$ , as shown in Figure I-24 b).

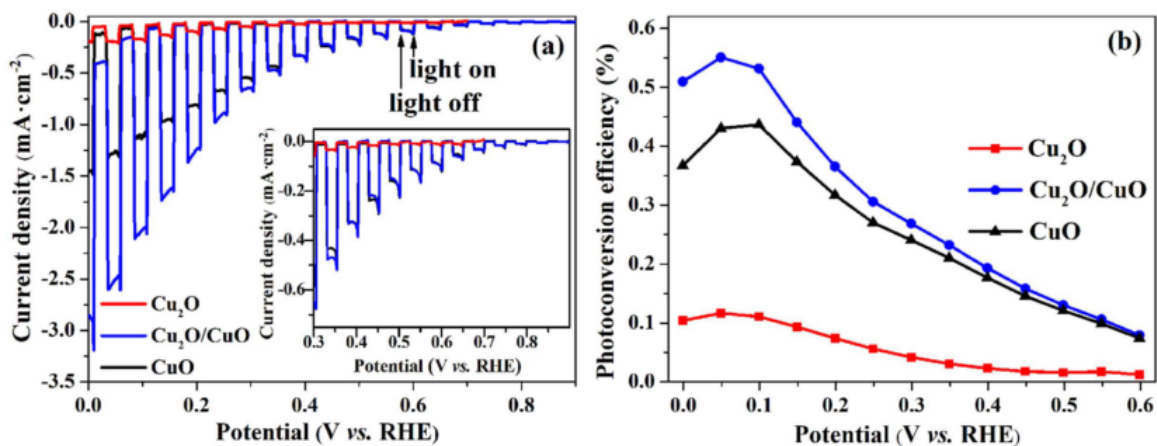


Figure I-24. Comparison of the performance of photoelectrode made from  $\text{Cu}_2\text{O}$  (red line),  $\text{CuO}$  (dark line) and  $\text{Cu}_2\text{O}/\text{CuO}$  bilayer (blue line). a) comparison of the current density versus potential and b) photo conversion efficiency of different photo electrode versus potential.

In addition to the works on Cu<sub>2</sub>O stability through using composite layers, in the work of Q.B. Ma *et al.*,<sup>73</sup> the facet preferential orientation of Cu<sub>2</sub>O could be tuned between (200) plane and (111) plane during the process of electrochemical deposition thus obtaining a different performance of Cu<sub>2</sub>O as photo electrode. Cu<sub>2</sub>O films with (111) texture exhibits a better stability without corrosion in PEC test. Besides using Cu<sub>2</sub>O films as PEC cell electrode, using Cu<sub>2</sub>O nanowires as electrodes was also reported.<sup>74,75</sup> In those works, unprecedentedly high photon current of 10 mA cm<sup>-2</sup> was reported. At the same time with an excellent stable performance over 50 h test. Thus, even though Cu<sub>2</sub>O has shown great potential in photo electrochemical cells for hydrogen generation, stability of such electrodes need to be carefully tackled.

### I.3.3 Application of Cu<sub>2</sub>O in photovoltaics

In addition to the water splitting, by forming heterojunction normally with ZnO or AZO (Al doped ZnO), Cu<sub>2</sub>O is also applied as the absorber layer in ultra low-cost all oxide solar cells. With AZO (or ZO)/ Cu<sub>2</sub>O structure, the highest efficiency reached so far is merely 3.83% using thermally oxidized Cu<sub>2</sub>O by T. Minami *et al.*<sup>18</sup> Other work from the same group, by using thermally oxidized Cu<sub>2</sub>O film coupled with ZnO/Ga<sub>2</sub>O<sub>3</sub> as the n layer, the highest efficiency achieved was 5.38%, with structure ZnO/Ga<sub>2</sub>O<sub>3</sub>/Cu<sub>2</sub>O. There are several reasons leading to the poor performance of the Cu<sub>2</sub>O based photovoltaic devices (as said before, maximum theoretical efficiency of Cu<sub>2</sub>O based cells is 20%<sup>76-78</sup>). To understand the actual problems with those devices, we will elaborate those issues from the point view of Cu<sub>2</sub>O materials itself.

First of all, the effects from the electronic properties of Cu<sub>2</sub>O on the final solar cell performance are discussed. As has been stated above, the properties of Cu<sub>2</sub>O are very dependent on the deposition method and conditions. With electrodeposited Cu<sub>2</sub>O layers in solar cells, for example, the incompatibility between charge collection length and depletion zone is reported by K. Mussleman *et al.*<sup>79</sup>

As shown in Figure I-25 a) and b), they illustrate planar Cu<sub>2</sub>O/ZnO and Cu<sub>2</sub>O/ZnO nanorods solar cell structures. Figure c) is the energy diagram of such Cu<sub>2</sub>O/ZnO p-n junction, in which  $x_p$  represents the full depletion length in the p part,  $x_n$  is defined as the depletion length in ZnO and  $V_{bi}$  is built in potential in such photovoltaic devices.

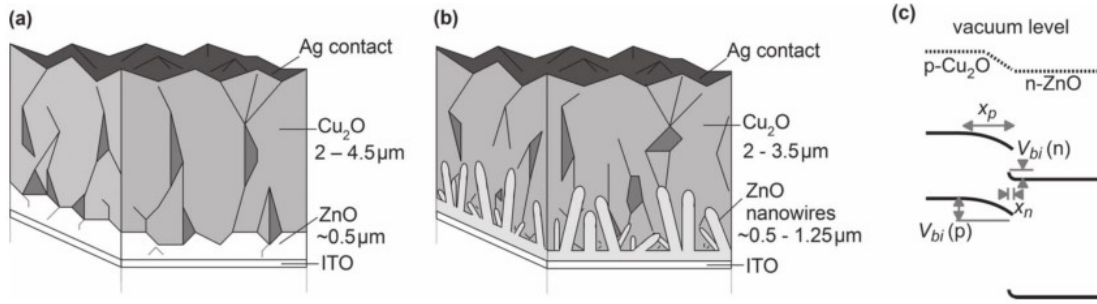


Figure I-25. Schematic presentation of a)  $\text{Cu}_2\text{O}/\text{ZnO}$  bilayer structure, b)  $\text{Cu}_2\text{O}/\text{ZnO}$  nanorods structure and c) energy diagram. <sup>79</sup>

During this study, by varying the  $\text{Cu}_2\text{O}$  layer thickness deposited by electrochemical deposition, the short circuit current  $J_{sc}$ , open circuit voltage  $V_{oc}$  and fill factor  $FF$  were evaluated. The depletion length  $x$  in both p and n parts can be calculated by applying Poisson's Equation at the p-n junction interface and giving the build in potential ratio relation following Equation 3:

$$\frac{V_{bi(n)}}{V_{bi(p)}} = \frac{N_A \epsilon_{\text{Cu}_2\text{O}}}{N_D \epsilon_{\text{ZnO}}} \quad (3)$$

In which,  $N_A$  and  $N_D$  represent the acceptor and donor concentration in p and n type semiconductors, respectively.  $\epsilon$  with different subscript are the absolute permittivity with values 6.2 for ZnO and 8 for  $\text{Cu}_2\text{O}$ . Due to the fact that most electrodeposited  $\text{Cu}_2\text{O}$  has poor carrier mobility ( $\sim 1 \text{ cm}^2/\text{V.s}$ ), effective charge collection length in such material is less than  $1 \mu\text{m}$ .<sup>79</sup> On the other hand, such  $\text{Cu}_2\text{O}$  has relatively lower carrier concentration (in the range of  $10^{13} - 10^{14} \text{ cm}^{-3}$ ). By comparing the general ZnO carrier density in the range of  $10^{18} - 10^{20} \text{ cm}^{-3}$ , the relation between build in potential in this type of  $\text{Cu}_2\text{O}$  and full depletion length can be expressed in Equation 4:

$$V_{bi(p)} = \frac{q N_A x_p^2}{2 \epsilon_{\text{Cu}_2\text{O}}} \quad (4)$$

Where  $q$  is the unit electron charge and  $x_p$  is the full depletion length in  $\text{Cu}_2\text{O}$ . Therefore, according to Equation 4, in order to obtain a build-in potential in the range of 0.4 to 0.7 V, the full depletion length is estimated to be about 2.3 to 3  $\mu\text{m}$ . For bilayer solar cell structures, the open circuit voltage evolution is clearly presented in Figure I-26 a). Before reaching the required thickness 2.7  $\mu\text{m}$  to form a full depletion layer, the  $V_{oc}$  increased rapidly with regarding to a thicker film, in accordance with the theory prediction. While in Figure I-26 b), the short circuit current with bilayer structure showed a peak. The increase of current could be attributed to more absorbed light thanks to a thicker absorber layer. On the other hand, the decrease of the current can be explained by that  $\text{Cu}_2\text{O}$  layer was thicker than the



effective charge collection length. Thus, even though more excitons were generated in the active layer, there was less possibility for the excitons to be separated and collected. Meanwhile, in figure c) the evolution of the solar cell efficiency presented a similar trend.

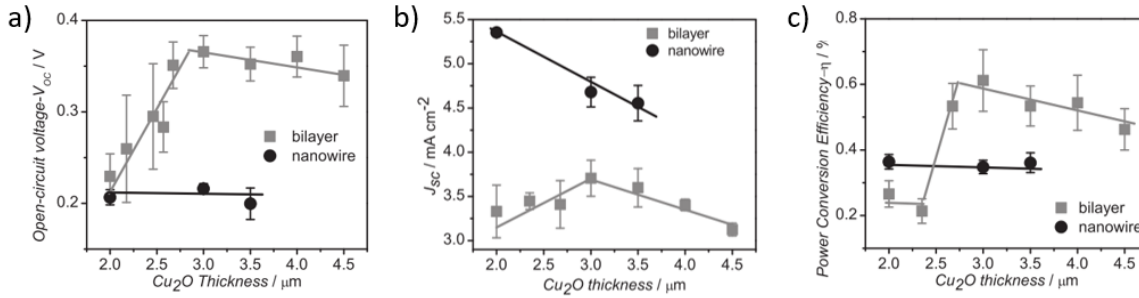


Figure I-26. Evaluation of Cu<sub>2</sub>O/ZnO bilayer and Cu<sub>2</sub>O/ZnO nanowires solar cell performance depending on the absorber layer Cu<sub>2</sub>O thickness. a) open circuit voltage  $V_{oc}$ , b) short circuit current  $J_{sc}$  and c) fill factor FF evolution with regarding to Cu<sub>2</sub>O thickness change.<sup>79</sup>

On the other hand, in the Cu<sub>2</sub>O/ZnO nanorods structure, the  $V_{oc}$  remained stable and  $J_{sc}$  decreased with thicker Cu<sub>2</sub>O layer. The stable voltage value implied that the distance between the rods plays an important role in the depletion zone formation. In another words, if the distance between the rods is smaller than the required full depletion length, the final Cu<sub>2</sub>O/ZnO rods structure couldn't form a p-n junction with a complete depletion zone, regardless the thickness of the top layer. While the decrease of the short circuit current in Figure I-26 b) could be due to inefficient charge collection with much thicker Cu<sub>2</sub>O top layer. To solve this incompatibility between charge collection and full depletion length, better thin film coating techniques could be helpful. From the work of A.T.Marin *et al.*,<sup>61</sup> by applying the new Spatial Atomic Layer Deposition (SALD) technique<sup>62</sup>, Cu<sub>2</sub>O layer with higher carrier concentration was coated on top of electrodeposited Cu<sub>2</sub>O. Thanks to such deposition technique, the carrier concentration of deposited Cu<sub>2</sub>O layers were two orders of magnitude higher than the electrodeposited ones, which reduced the required thickness to achieve full depletion zone.

With another thin film coating technique, Spray Pyrolysis, the electronic properties of deposited Cu<sub>2</sub>O films show mobility of 1.3 cm<sup>2</sup>/(V.s) and carrier concentration of  $4.17 \times 10^{15} \text{ cm}^{-3}$ , as reported in the work of S.Panigrahi *et al.*<sup>80</sup> To systematically study the effect of layer thickness in Cu<sub>2</sub>O/ZnO bilayer structures, solar cells with gradient thickness were fabricated and studied as schematically presented in Figure I-27. As it's shown, by applying thickness gradients of Cu<sub>2</sub>O and ZnO in a perpendicular manner, bilayer structures with Cu<sub>2</sub>O thickness ranging from 200 nm to 800 nm and ZnO thickness varying from 50 nm to 320 nm were fabricated. With such configuration, by applying separate Au contacts on top,

a mapping of the performance for  $\text{Cu}_2\text{O}/\text{ZnO}$  bilayer cell with various thickness parameters was established, as shown in Figure I-28.

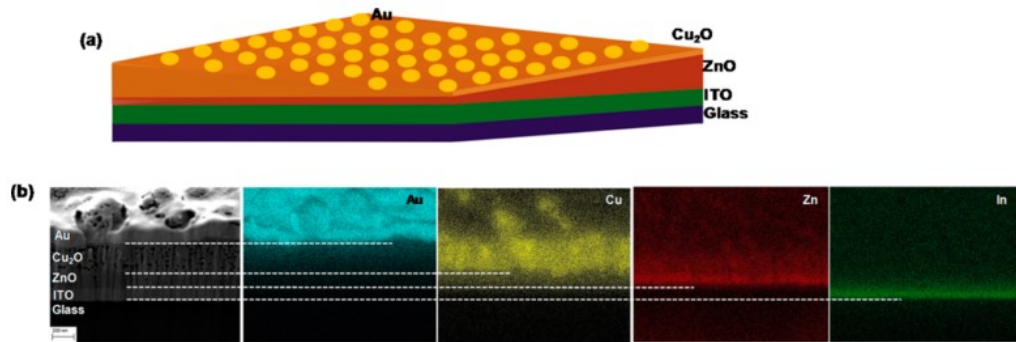


Figure I-27. a) scheme of  $\text{Cu}_2\text{O}/\text{ZnO}$  bilayer solar cell structure with gradient layer thickness. b) the cross section view of bilayer structure and corresponding elemental analysis by EDS.<sup>80</sup>

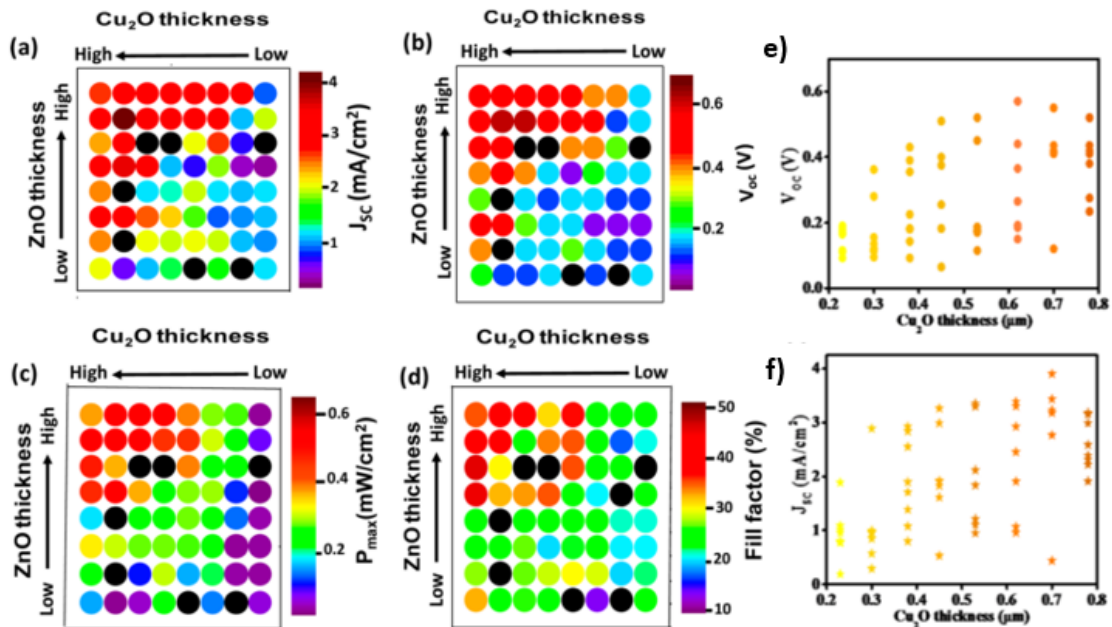


Figure I-28. Mapping of  $\text{Cu}_2\text{O}/\text{ZnO}$  bilayer solar cell performance with gradient thickness. a)  $J_{sc}$ , b)  $V_{oc}$ , c) Maximum output power ( $P_{max}$ ) and d) fill factor (FF). e) summary of  $V_{oc}$  and f)  $J_{sc}$  versus  $\text{Cu}_2\text{O}$  thickness evolution.<sup>80</sup>

Comparing with electrodeposited  $\text{Cu}_2\text{O}$ ,  $\text{Cu}_2\text{O}$  used in this work has higher carrier concentration (2 orders higher than electrodeposited). Thus, to achieve 0.7 V build-in potential, by calculation using Equation 3 and 4, the full depletion length in this case was estimated about merely 250~ 300 nm. In Figure I-28, a) presents the  $J_{sc}$  mapping of the gradient structure. Figure b) shows the trend of  $V_{oc}$  on the gradient surface. In both cases, solar cells with thicker ZnO and  $\text{Cu}_2\text{O}$  layers at the top-left corner have generally better performance, which can be confirmed by figure c) and d). However by checking the color bar, it's easy to find that the optimal performance point was not the ones with the thickest layers. This result are presented with a clear view in figure e) and f). In figure e), the optimal

$V_{oc}$  0.6 V achieved was with about 250 nm ZnO and 600 nm thick  $Cu_2O$ . With even thicker  $Cu_2O$  layer, the  $V_{oc}$  decreased slightly, which is in accordance with the previous results shown Figure I-27. Thus, since the electronic properties of  $Cu_2O$  films deposited by Spray Pyrolysis and by MOCVD are rather similar, those thickness versus performance maps is also a good indication for  $Cu_2O$  based solar cell devices fabricated by MOCVD.

Besides the work on  $Cu_2O$  material its self, other works are focusing on the ZnO or AZO layer. Such as in the work of T.S.Gershon *et al.*,<sup>81</sup> the fill factor of  $Cu_2O/ZnO$  bilayer solar cell was improved up to 54% through optimizing ZnO surface morphology with larger grains. With application of new deposition techniques such as atomic layer deposition, electronic property of ZnO/AZO can be also largely improved<sup>82,37</sup>. Therefore,  $Cu_2O$  thin films have shown a wide range of potential applications. For either application of TFT, water splitting or solar cells, with a better quality  $Cu_2O$  film, the device performance can be always improved by tuning the deposition of  $Cu_2O$ . Thus, concerning both cost and deposition quality, a proper thin film deposition technique for  $Cu_2O$  should be chosen carefully. Although the great potential presented with  $Cu_2O$ , the material has its own limitations. Especially for photovoltaic applications, the bandgap of  $Cu_2O$  is not ideal enough as an absorber. For the sun light spectrum, absorber layers with a lower bandgap (about 1.5 eV) are more efficient to convert the majority of the photon energy into electricity. From this point of view, new emerging silver copper mixed oxides have much lower bandgaps, thus they might be more suitable for photovoltaic applications.

#### **I.4 Objective of PhD thesis**

With the rising demands for p type metal oxides with better performance, the main objective of this paper work is using low temperature, chemical approaches to deposit p type metal oxides with improved electronic properties. The new  $AgCuO_2$  phase has shown p type transport nature with low resistivity. As well, from the DFT calculation, low bandgap about 1 eV was predicted. Given the promising characteristics of  $AgCuO_2$ , this work will focus on the synthesis of  $AgCuO_2$  thin films. To achieve that, several approaches, namely MOCVD,  $AgCu$  alloy film oxidation and solution coating method, will be evaluated.

For the deposition of  $AgCuO_2$  by MOCVD, first the deposition of silver and silver oxide films, on the one hand, and of copper oxides, on the other hand, will have to be optimized. Then, the co-deposition of mixed oxide phases will be parallel, given the relevance of  $Cu_2O$ , the deposition conditions of  $Cu_2O$  thin films by MOCVD will also be optimized.

For the oxidation of AgCu foam films, electrochemical and ozone oxidation will be adopted. Finally, the Successive Ionic Layer Adsorption and Reaction (SILAR) method will be evaluated for the direct deposition of AgCuO<sub>2</sub> thin films. The governing condition will be optimized to achieve continuous and dense AgCuO<sub>2</sub> coatings. The synthetic AgCuO<sub>2</sub> thin films, will allow to determine the electronic properties and optical bandgap of AgCuO<sub>2</sub>.

## I.5 References

1. Aberle, A. G. Thin-film solar cells. *Thin Solid Films* **517**, 4706–4710 (2009).
2. Oda, S., Adachi, N., Katoh, S. & Matsumura, M. p-Channel Amorphous Silicon Thin-Film Transistors with High Hole Mobility. *Jpn. J. Appl. Phys.* **27**, L1955 (1988).
3. Schiff, E. A. Low-mobility solar cells: A device physics primer with application to amorphous silicon. *Sol. Energy Mater. Sol. Cells* **78**, 567–595 (2003).
4. Li, B. S., Akimoto, K. & Shen, a. Growth of Cu<sub>2</sub>O thin films with high hole mobility by introducing a low-temperature buffer layer. *J. Cryst. Growth* **311**, 1102–1105 (2009).
5. Yu, X., Marks, T. J. & Facchetti, A. Metal oxides for optoelectronic applications. *Nat. Mater.* **15**, 383–396 (2016).
6. Fortunato, E., Barquinha, P. & Martins, R. Oxide semiconductor thin-film transistors: a review of recent advances. *Adv. Mater.* **24**, 2945–86 (2012).
7. Nandy, S., Banerjee, A., Fortunato, E. & Martins, R. A Review on Cu<sub>2</sub>O and Cu(I)-Based p Type Semiconducting Transparent Oxide Materials: Promising Candidates for New Generation Oxide Based Electronics. *Rev. Adv. Sci. Eng.* **2**, 273–304 (2013).
8. Arora, A. K., Jaswal, V. S., Singh, K. & Singh, R. Applications of metal/mixed metal oxides as photocatalyst: A review. *Orient. J. Chem.* **32**, 2035–2042 (2016).
9. Ray, C. & Pal, T. Recent advances of metal–metal oxide nanocomposites and their tailored nanostructures in numerous catalytic applications. *J. Mater. Chem. A* **5**, 9465–9487 (2017).
10. Sun, Y.-F., Liu, S.-B., Meng, F.-L., Liu, J.-Y., Jin, Z., Kong, L.-T. & Liu, J.-H. Metal Oxide Nanostructures and Their Gas Sensing Properties: A Review. *Sensors* **12**, 2610–2631 (2012).
11. Intrater, J. A Review of Synthesis, Properties, and Applications of Oxide Nanomaterials. *Mater. Manuf. Process.* **23**, 114–115 (2007).
12. Wang, Z., Nayak, P. K., Caraveo-Frescas, J. A. & Alshareef, H. N. Recent Developments in p-Type Oxide Semiconductor Materials and Devices. *Adv. Mater.* **28**, 3831–3892 (2016).
13. Al-Jawhari, H. A review of recent advances in transparent p-type Cu<sub>2</sub>O-based thin film transistors. *Mater. Sci. Semicond. Process.* **40**, 241–252 (2015).
14. Lorenz, M., Ramachandra Rao, M. S., Venkatesan, T., Fortunato, E., Barquinha, P., Branquinho, R., Salgueiro, D., Martins, R., Carlos, E., Liu, A., Shan, F. K., Grundmann, M., Boschker, H., Mukherjee, J., Priyadarshini, M., DasGupta, N., Rogers, D. J., Teherani, F. H.,

- Sandana, E. V, Bove, P., Rietwyk, K., Zaban, A., Veziridis, A., Weidenkaff, A., Muralidhar, M., Murakami, M., Abel, S., Fompeyrine, J., Zuniga-Perez, J., Ramesh, R., Spaldin, N. A., Ostanin, S., Borisov, V., Mertig, I., Lazenka, V., Srinivasan, G., Prellier, W., Uchida, M., Kawasaki, M., Pentcheva, R., Gegenwart, P., Miletto Granozio, F., Fontcuberta, J. & Pryds, N. The 2016 oxide electronic materials and oxide interfaces roadmap. *J. Phys. D. Appl. Phys.* **49**, 433001 (2016).
15. Robertson, J. & Falabretti, B. *Handbook of Transparent Conductors*. (2011). doi:10.1007/978-1-4419-1638-9
  16. Ishizuka, S., Maruyama, T. & Akimoto, K. Thin-film deposition of Cu<sub>2</sub>O by reactive radio-frequency magnetron sputtering. *Japanese J. Appl. Physics, Part 2 Lett.* **39**, L786–L788 (2000).
  17. Musa, a. ., Akomolafe, T. & Carter, M. . Production of cuprous oxide, a solar cell material, by thermal oxidation and a study of its physical and electrical properties. *Sol. Energy Mater. Sol. Cells* **51**, 305–316 (1998).
  18. Minami, T., Nishi, Y., Miyata, T. & Nomoto, J. I. High-efficiency oxide solar cells with ZnO/Cu<sub>2</sub>O heterojunction fabricated on thermally oxidized Cu<sub>2</sub>O sheets. *Appl. Phys. Express* **4**, 1–4 (2011).
  19. Resende, J., Jiménez, C., Nguyen, N. D. & Deschanvres, J.-L. Magnesium-doped cuprous oxide (Mg:Cu<sub>2</sub>O) thin films as a transparent p-type semiconductor. *Phys. Status Solidi* **7**, 1–7 (2016).
  20. Li, J., Mei, Z., Liu, L., Liang, H., Azarov, A., Kuznetsov, A., Liu, Y., Ji, A., Meng, Q. & Du, X. Probing defects in nitrogen-doped Cu<sub>2</sub>O. *Sci. Rep.* **4**, 7240 (2014).
  21. Yu, L., Xiong, L. & Yu, Y. Cu<sub>2</sub>O Homojunction Solar Cells: F-Doped N-type Thin Film and Highly Improved Efficiency. *J. Phys. Chem. C* **119**, 22803–22811 (2015).
  22. Kikuchi, N. & Tonooka, K. Electrical and structural properties of Ni-doped Cu<sub>2</sub>O films prepared by pulsed laser deposition. *Thin Solid Films* **486**, 33–37 (2005).
  23. Zhang, L., McMillon, L. & McNatt, J. Gas-dependent bandgap and electrical conductivity of Cu<sub>2</sub>O thin films. *Sol. Energy Mater. Sol. Cells* **108**, 230–234 (2013).
  24. Ogo, Y., Hiramatsu, H., Nomura, K., Yanagi, H., Kamiya, T., Kimura, M., Hirano, M. & Hosono, H. Tin monoxide as an s-orbital-based p-type oxide semiconductor: Electronic structures and TFT application. *Phys. Status Solidi Appl. Mater. Sci.* **206**, 2187–2191 (2009).
  25. Ogo, Y., Hiramatsu, H., Nomura, K., Yanagi, H., Kamiya, T., Hirano, M. & Hosono, H. p-channel thin-film transistor using p-type oxide semiconductor, SnO. *Appl. Phys. Lett.* **93**, 32113 (2008).
  26. Chen, S. C., Wen, C. K., Kuo, T. Y., Peng, W. C. & Lin, H. C. Characterization and properties of NiO films produced by rf magnetron sputtering with oxygen ion source assistance. *Thin Solid Films* **572**, 51–55 (2014).

27. Wu, C. C. & Yang, C. F. Fabricate heterojunction diode by using the modified spray pyrolysis method to deposit nickel-lithium oxide on indium tin oxide substrate. *ACS Appl. Mater. Interfaces* **5**, 4996–5001 (2013).
28. Dekkers, M., Rijnders, G. & Blank, D. H. A. ZnIr<sub>2</sub>O<sub>4</sub>, a p-type transparent oxide semiconductor in the class of spinel zinc-d<sub>6</sub>-transition metal oxide. *Appl. Phys. Lett.* **90**, 89–91 (2007).
29. Kudo, A., Yanagi, H., Hosono, H. & Kawazoe, H. SrCu<sub>2</sub>O<sub>2</sub>: A p-type conductive oxide with wide band gap. *Appl. Phys. Lett.* **73**, 220–222 (1998).
30. Ueda, K., Hase, T., Yanagi, H., Kawazoe, H., Hosono, H., Ohta, H., Orita, M. & Hirano, M. Epitaxial growth of transparent p-type conducting CuGaO<sub>2</sub> thin films on sapphire (001) substrates by pulsed laser deposition. *J. Appl. Phys.* **89**, 1790–1793 (2001).
31. Tripathi, T. S., Niemelä, J.-P. & Karppinen, M. Atomic layer deposition of transparent semiconducting oxide CuCrO<sub>2</sub> thin films. *J. Mater. Chem. C* **3**, 8364–8371 (2015).
32. Lim, S. H., Desu, S. & Rastogi, A. C. Chemical spray pyrolysis deposition and characterization of p-type CuCr<sub>1-x</sub>Mg<sub>x</sub>O<sub>2</sub> transparent oxide semiconductor thin films. *Journal of Physics and Chemistry of Solids* **69**, 2047–2056 (2008).
33. Kawazoe, H., Yasukawa, M., Hyodo, H. & Kurita, M. P-type electrical conduction in transparent thin films of CuAlO<sub>2</sub>. *Nature* **389**, 939–942 (1997).
34. Bandara, J. & Yasomane, J. P. P-Type Oxide Semiconductors As Hole Collectors in Dye-Sensitized Solid-State Solar Cells. *Semicond. Sci. Technol.* **22**, 20–24 (2007).
35. Gong, H., Wang, Y. & Luo, Y. Nanocrystalline p -type transparent Cu–Al–O semiconductor prepared by chemical-vapor deposition with Cu(acac)<sub>2</sub> and Al(acac)<sub>3</sub> precursors. *Appl. Phys. Lett.* **76**, 3959–3961 (2000).
36. Muñoz-Rojas, D., Córdoba, R., Fernández-Pacheco, A., De Teresa, J. M., Sauthier, G., Fraxedas, J., Walton, R. I. & Casañ-Pastor, N. High conductivity in hydrothermally grown AgCuO<sub>2</sub> single crystals verified using focused-ion-beam-deposited nanocontacts. *Inorg. Chem.* **49**, 10977–10983 (2010).
37. Nguyen, V. H., Resende, J., Jiménez, C., Deschanvres, J.-L., Carroy, P., Muñoz, D., Bellet, D. & Muñoz-Rojas, D. Deposition of ZnO based thin films by atmospheric pressure spatial atomic layer deposition for application in solar cells. *J. Renew. Sustain. Energy* **9**, 21203 (2017).
38. Gaspar, D., Pereira, L., Gehrke, K., Galler, B., Fortunato, E. & Martins, R. High mobility hydrogenated zinc oxide thin films. *Sol. Energy Mater. Sol. Cells* **163**, 255–262 (2017).
39. Zhan, Z., Zhang, J., Zheng, Q., Pan, D., Huang, J., Huang, F. & Lin, Z. Strategy for Preparing Al-Doped ZnO Thin Film with High Mobility and High Stability. *Cryst. Growth Des.* **11**, 21–25 (2011).
40. Le, Y., Shao, Y., Xiao, X., Xu, X. & Zhang, S. Indium–Tin–Oxide Thin-Film Transistors

- With In Situ Anodized Ta<sub>2</sub>O<sub>5</sub> Passivation Layer. *IEEE Electron Device Lett.* **37**, 603–606 (2016).
41. Banyamin, Z., Kelly, P., West, G. & Boardman, J. Electrical and Optical Properties of Fluorine Doped Tin Oxide Thin Films Prepared by Magnetron Sputtering. *Coatings* **4**, 732–746 (2014).
  42. Muñoz-Rojas, D. Silver-copper mixed oxides. *Mater. Today* **14**, 119 (2011).
  43. Sauvage, F., Muñoz-Rojas, D., Poeppelmeier, K. R. & Casañ-Pastor, N. Transport properties and lithium insertion study in the p-type semi-conductors AgCuO<sub>2</sub> and AgCu<sub>0.5</sub>Mn<sub>0.5</sub>O<sub>2</sub>. *J. Solid State Chem.* **182**, 374–380 (2009).
  44. Zhao, X. D., Yu, G. C., Cho, Y. C., Chabot-Couture, G., Barisic, N., Bourges, P., Kaneko, N., Li, Y., Lu, L., Motoyama, E. M., Vajk, O. P. & Greven, M. Crystal growth and characterization of the model high-temperature superconductor HgBa<sub>2</sub>CuO<sub>4+δ</sub>. *Adv. Mater.* **18**, 3243–3247 (2006).
  45. Tejada-rosales, E. M. & Palacín, M. R. Ag<sub>2</sub>Cu<sub>2</sub>O<sub>3</sub>: The First Silver Copper Oxide. *Angew. Chem. Int. Ed* **13**, 524–525 (1999).
  46. Tejada-rosales, E. M., Rodri, J., Casan, N., Bellaterra, E., Brillouin, L. L. & Etudes, C. Room-Temperature Synthesis and Crystal, Magnetic, and Electronic Structure of the First Silver Copper Oxide. *Society* **41**, 103–108 (2002).
  47. Muñoz-Rojas, D., G.Subias, J.Fraxedas, P.Gomez-Romero & N.Casañ-Pastor. Electronic Structure of Ag<sub>2</sub>Cu<sub>2</sub>O<sub>4</sub>. Evidence of Oxidized Silver and Copper and Internal Charge Delocalization. *J. Phys. Chem. B* **109**, 6193–6203 (2005).
  48. Munoz-Rojas, D., Fraxedas, J., Oró, J., Gómez-Romero, P. & Casañ-Pastor, N. Structural study of electrochemically-synthesized Ag<sub>2</sub>Cu<sub>2</sub>O<sub>4</sub>. A novel oxide sensitive to irradiation. *Cryst. Eng.* **5**, 459–467 (2002).
  49. Curda, J., Klein, W. & Jansen, M. AgCuO<sub>2</sub>—Synthesis, Crystal Structure, and Structural Relationships with CuO and AgI<sub>3</sub>Ag<sub>2</sub>O<sub>2</sub>. *J. Solid State Chem.* **162**, 220–224 (2001).
  50. Lu, Q., Lu, K., Zhang, L., Gong, J. & Liu, R. Electrodeposition of AgCuO<sub>2</sub> Nanoplates. *J. Electrochem. Soc.* **164**, D130–D134 (2017).
  51. Muñoz-Rojas, D., Subías, G., Oró-Solé, J., Fraxedas, J., Martínez, B., Casas-Cabanas, M., Canales-Vázquez, J., Gonzalez-Calbet, J., García-González, E., Walton, R. I. & Casañ-Pastor, N. Ag<sub>2</sub>CuMnO<sub>4</sub>: A new silver copper oxide with delafossite structure. *J. Solid State Chem.* **179**, 3883–3892 (2006).
  52. Petitjean, C., Horwat, D. & Pierson, J. F. Effect of annealing temperature on the decomposition of reactively sputtered Ag<sub>2</sub>Cu<sub>2</sub>O<sub>3</sub> films. *Appl. Surf. Sci.* **255**, 7700–7702 (2009).
  53. Lund, E., Galeckas, A., Monakhov, E. V. & Svensson, B. G. Basic optical and electronic properties of Ag<sub>2</sub>Cu<sub>2</sub>O<sub>3</sub> crystalline films. *Thin Solid Films* **531**, 185–188 (2013).

54. Lund, E., Galeckas, a., Monakhov, E. V. & Svensson, B. G. Structural, optical and electrical properties of reactively sputtered Ag<sub>2</sub>Cu<sub>2</sub>O<sub>3</sub> films. *Thin Solid Films* **520**, 230–234 (2011).
55. Pierson, J. F., Wiederkehr, D., Chappé, J. M. & Martin, N. Reactive sputtering: A method to modify the metallic ratio in the novel silver-copper oxides. *Appl. Surf. Sci.* **253**, 1484–1488 (2006).
56. Meyer, B. K., Polity, a., Reppin, D., Becker, M., Hering, P., Klar, P. J., Sander, T., Reindl, C., Benz, J., Eickhoff, M., Heiliger, C., Heinemann, M., Bläsing, J., Krost, a., Shokovets, S., Müller, C. & Ronning, C. Binary copper oxide semiconductors: From materials towards devices. *Phys. Status Solidi* **249**, 1487–1509 (2012).
57. Scanlon, D., Morgan, B., Watson, G. & Walsh, A. Acceptor Levels in p-Type Cu<sub>2</sub>O: Rationalizing Theory and Experiment. *Phys. Rev. Lett.* **103**, 96405 (2009).
58. Raebiger, H., Lany, S. & Zunger, A. Origins of the p-type nature and cation deficiency in Cu<sub>2</sub>O and related materials. *Phys. Rev. B* **76**, 45209 (2007).
59. Jeong, S. & Aydil, E. S. Heteroepitaxial growth of Cu<sub>2</sub>O thin film on ZnO by metal organic chemical vapor deposition. *J. Cryst. Growth* **311**, 4188–4192 (2009).
60. Mizuno, K., Izaki, M., Murase, K., Shinagawa, T., Chigane, M., Inaba, M., Tasaka, A. & Awakura, Y. Structural and Electrical Characterizations of Electrodeposited p-Type Semiconductor Cu<sub>2</sub>O Films. *J. Electrochem. Soc.* **152**, C179 (2005).
61. Marin, A. T., Muñoz-Rojas, D., Iza, D. C., Gershon, T., Musselman, K. P. & MacManus-Driscoll, J. L. Novel Atmospheric Growth Technique to Improve Both Light Absorption and Charge Collection in ZnO/Cu<sub>2</sub>O Thin Film Solar Cells. *Adv. Funct. Mater.* **23**, 3413–3419 (2013).
62. Muñoz-Rojas, D. & MacManus-Driscoll, J. Spatial atmospheric atomic layer deposition: a new laboratory and industrial tool for low-cost photovoltaics. *Mater. Horizons* **1**, 314 (2014).
63. Ikenoue, T., Sakamoto, S. & Inui, Y. Fabrication and characteristics of p-type Cu<sub>2</sub>O thin films by ultrasonic spray-assisted mist CVD method. *Jpn. J. Appl. Phys.* **53**, 4–7 (2014).
64. Fortunato, E., Figueiredo, V., Barquinha, P., Elamurugu, E., Barros, R., Gonçalves, G., Park, S.-H. K., Hwang, C.-S. & Martins, R. Thin-film transistors based on p-type Cu<sub>2</sub>O thin films produced at room temperature. *Appl. Phys. Lett.* **96**, 192102 (2010).
65. Mahalingam, T., Chitra, J. S. ., Rajendran, S., Jayachandran, M. & Chockalingam, M. J. Galvanostatic deposition and characterization of cuprous oxide thin films. *J. Cryst. Growth* **216**, 304–310 (2000).
66. Kim, S. Y., Addis, F. W., Lee, J. H., Kwon, Y. H., Hwang, S., Lee, J. Y. & Cho, H. K. p-Channel oxide thin film transistors using solution-processed copper oxide. *ACS Appl. Mater. Interfaces* **5**, 2417–21 (2013).
67. Nam, D.-W., Cho, I.-T., Lee, J.-H., Cho, E.-S., Sohn, J., Song, S.-H. & Kwon, H.-I. Active layer thickness effects on the structural and electrical properties of p-type Cu<sub>2</sub>O thin-film



- transistors. *J. Vac. Sci. Technol. B Microelectron. Nanom. Struct.* **30**, 60605 (2012).
68. Pattanasattayavong, P., Thomas, S., Adamopoulos, G., McLachlan, M. a. & Anthopoulos, T. D. P-channel thin-film transistors based on spray-coated Cu<sub>2</sub>O films. *Appl. Phys. Lett.* **102**, 163505 (2013).
69. Wick, R. & Tilley, S. D. Photovoltaic and Photoelectrochemical Solar Energy Conversion with Cu<sub>2</sub>O. *J. Phys. Chem. C* 26243–26257 (2015). doi:10.1021/acs.jpcc.5b08397
70. Paracchino, A., Laporte, V., Sivula, K., Grätzel, M. & Thimsen, E. Highly active oxide photocathode for photoelectrochemical water reduction. *Nat. Mater.* **10**, 456–461 (2011).
71. Lim, Y.-F., Chua, C. S., Lee, C. J. J. & Chi, D. Sol-gel deposited Cu<sub>2</sub>O and CuO thin films for photocatalytic water splitting. *Phys. Chem. Chem. Phys.* **16**, 25928–34 (2014).
72. Yang, Y., Xu, D., Wu, Q. & Diao, P. Cu<sub>2</sub>O/CuO Bilayered Composite as a High-Efficiency Photocathode for Photoelectrochemical Hydrogen Evolution Reaction. *Sci. Rep.* **6**, 35158 (2016).
73. Ma, Q.-B., Hofmann, J. P., Litke, A. & Hensen, E. J. M. Cu<sub>2</sub>O photoelectrodes for solar water splitting: Tuning photoelectrochemical performance by controlled faceting. *Sol. Energy Mater. Sol. Cells* **141**, 178–186 (2015).
74. Luo, J., Steier, L., Son, M. K., Schreier, M., Mayer, M. T. & Grätzel, M. Cu<sub>2</sub>O Nanowire Photocathodes for Efficient and Durable Solar Water Splitting. *Nano Lett.* **16**, 1848–1857 (2016).
75. Shi, W., Zhang, X., Li, S., Zhang, B., Wang, M. & Shen, Y. Carbon coated Cu<sub>2</sub>O nanowires for photo-electrochemical water splitting with enhanced activity. *Appl. Surf. Sci.* **358**, 404–411 (2015).
76. Ievskaya, Y., Hoyer, R. L. Z., Sadhanala, A., Musselman, K. P. & MacManus-Driscoll, J. L. Fabrication of ZnO/Cu<sub>2</sub>O heterojunctions in atmospheric conditions: Improved interface quality and solar cell performance. *Sol. Energy Mater. Sol. Cells* **135**, 43–48 (2015).
77. Lee, Y. S., Winkler, M. T., Siah, S. C., Brandt, R. & Buonassisi, T. Hall mobility of cuprous oxide thin films deposited by reactive direct-current magnetron sputtering. *Appl. Phys. Lett.* **98**, 192115 (2011).
78. Chen, Y., Yan, H., Yang, B., Lv, Y., Wen, M., Xu, J., Wu, M., Zhu, X. & Fu, Z. Fabrication and optical properties of Cu<sub>2</sub>O--ZnO composite opal. *Appl. Phys. A* **98**, 467 (2009).
79. Musselman, K. P., Marin, A., Schmidt-Mende, L. & MacManus-Driscoll, J. L. Incompatible Length Scales in Nanostructured Cu<sub>2</sub>O Solar Cells. *Adv. Funct. Mater.* **22**, 2202–2208 (2012).
80. Panigrahi, S., Nunes, D., Calmeiro, T., Kardarian, K., Martins, R. & Fortunato, E. Oxide-Based Solar Cell: Impact of Layer Thicknesses on the Device Performance. *ACS Comb. Sci.* **19**, 113–120 (2017).
81. Gershon, T. S., Sigdel, A. K., Marin, A. T., van Hest, M. F. a. M., Ginley, D. S., Friend, R.

- H., MacManus-Driscoll, J. L. & Berry, J. J. Improved fill factors in solution-processed ZnO/Cu<sub>2</sub>O photovoltaics. *Thin Solid Films* **536**, 280–285 (2013).
82. Illiberi, A., Scherpenborg, R., Wu, Y., Roozeboom, F. & Poodt, P. Spatial atmospheric atomic layer deposition of al<sub>x</sub>zn<sub>1-x</sub>o. *ACS Appl. Mater. Interfaces* **5**, 13124–13128 (2013).

Chapter II Experimental setup	- 36 -
II.1 Deposition of Ag and Cu <sub>2</sub> O thin films by Metal Organic Chemical Vapor Deposition (MOCVD).	- 36 -
II.1.1 Pulsed Injection MOCVD	- 37 -
II.1.2 Aerosol Assisted MOCVD	- 38 -
II.1.3 Film deposition	- 40 -
II.1.3.1 Preparation of starting precursor solutions:	- 40 -
II.1.3.2 Substrate cleaning	- 42 -
II.1.3.3 Preparation of the MOCVD systems	- 42 -
II.2 Oxidation techniques: electrochemical oxidation and oxidation with atmospheric oxygen plasma	- 43 -
II.2.1 Electrochemical deposition and oxidation	- 43 -
II.2.2 Oxygen plasma oxidation	- 46 -
II.2.3 Deposition of AgCuO <sub>2</sub> films by the SILAR method	- 47 -
II.3 Characterization techniques	- 48 -
II.3.1 Thin film crystallinity: RAMAN spectroscopy, XRD	- 48 -
II.3.1.1 Raman Spectroscopy	- 48 -
II.3.1.2 X-Ray diffraction (XRD): Bragg-Brentano and Grazing Incidence.	- 49 -
II.3.2 Morphological characterization: SEM: EDS, EBSD, AFM	- 53 -
II.3.2.1 Scanning Electron Microscopy (SEM)	- 53 -
II.3.2.2 Atomic Force Microscopy (AFM)	- 55 -
II.3.2.3 Transmission Electron Microscopy (TEM)	- 57 -
II.3.3 Ultraviolet-Visible (UV-Vis) spectroscopy	- 58 -
II.3.4 Electrical characterization	- 59 -
II.3.4.1 Four probe measurements	- 59 -
II.3.4.2 Hall Effect measurements	- 61 -
II.4 References	- 63 -

## *Chapter II Experimental setup*

In this chapter, an introduction to the experimental techniques and equipment will be presented. This introduction is mainly composed of four parts, including Metal Organic Chemical Vapor deposition techniques, thin film oxidation setups, solution approaches to thin film deposition and different types of characterization techniques used in this thesis work. The thin film deposition/oxidation techniques aim to the synthesis of  $\text{AgCuO}_2$  thin films, as introduced in the thesis objective. The synthesized films have been characterized from the point view of morphology, elemental composition, phase identification, and optical and electronic properties.

### **II.1 Deposition of Ag and $\text{Cu}_2\text{O}$ thin films by Metal Organic Chemical Vapor Deposition (MOCVD).**

As one of the most widely used thin film deposition techniques, MOCVD can be used to deposit a wide range of metallic or metal oxide coatings. In general, the MOCVD deposition process relies on the delivering of precursor in vapor phase onto the reaction zone where a substrate is placed. With enough heating temperature or other means of reaction activation (i.e. plasma, light), metalorganic precursors can be decomposed and thus deposition takes place. Depending on the property of the metal atom and the oxidation atmosphere in the deposition chamber, either metallic or metal oxide films can be coated with high quality. Such type of thin film coating technique has the advantages of being scalable, low cost and being able to yield homogeneous dense coatings. As a consequence, MOCVD is a widely applied technique in industry. After decades of developing such thin film coating technique, MOCVD has derived into several branches. Depending on how the precursor is fed into the deposition chamber, MOCVD is classified into several types, including conventional Hot Wall MOCVD (HW-MOCVD), Cold Wall MOCVD (CW-MOCVD), Aerosol Assisted MOCVD (AA-MOCVD) and Pulsed Injection MOCVD (PI-MOCVD), etc.<sup>1</sup> In this work, two types of MOCVD approaches were applied for the deposition of Ag and Cu based thin films, namely Aerosol Assisted MOCVD (AA-MOCVD) and Pulsed Injection MOCVD (PI-MOCVD). In the following section, a brief introduction to AA-MOCVD and PI-MOCVD principles, systems setups and the deposition process will be introduced.

### II.1.1 Pulsed Injection MOCVD

PI-MOCVD is based on the flash evaporation of precursors or precursor solutions. This is carried out through the pulsed injection of small droplets of the precursor solution in a chamber under vacuum. In this way, the deposition rate is not dependent on the volatility of the precursor itself, and larger range of precursors can be available when compared with other MOCVD techniques.<sup>2,3</sup> Due to the low quantity of precursor required for an efficient deposition, PI-MOCVD can allow a rapid precursor screening with small precursor consumption (about 25 ml of 0.01 M precursor solution for each test). Therefore, for the sake of convenience, depositions with more expensive or less volatile precursors were conducted via PI-MOCVD in this work.

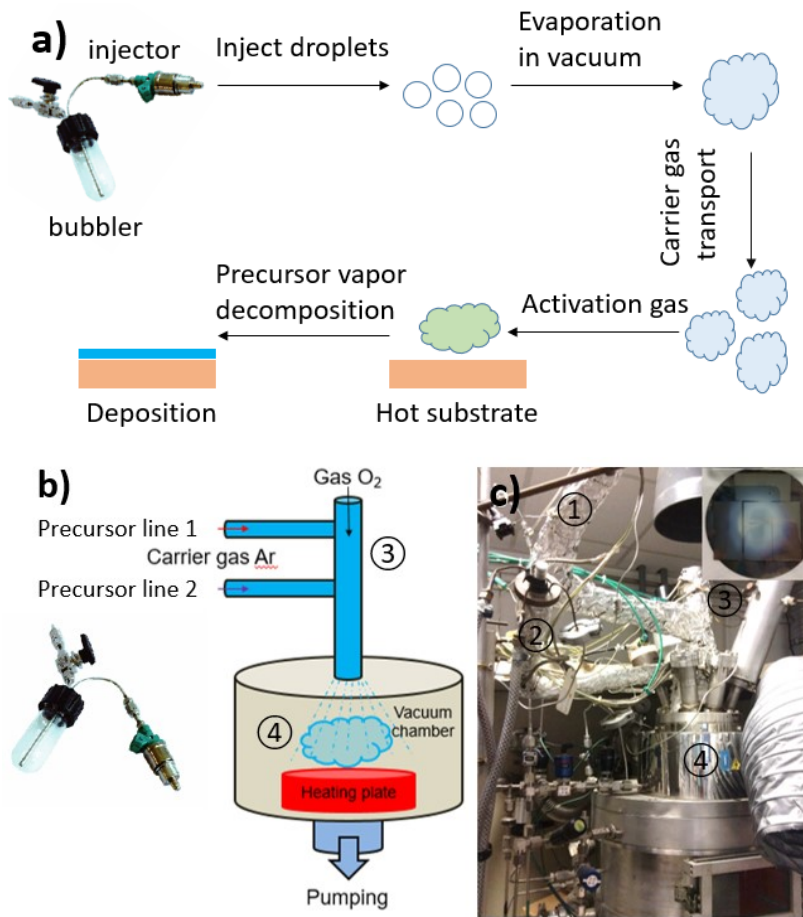


Figure II-1. a) Working principle of PI-MOCVD. b) Schematic presentation and c) photo of PI-MOCVD system. INSET: Ag coating obtained with this system in which a homogeneous 5 cm diameter coating can be observed. 1 and 2 are the injector lines, 3 is the gas line for oxygen and 4 is the deposition chamber.

The photo and schematic presentation of the PI-MOCVD system used in this work is shown in Figure II-1. Figure a) illustrates the process of deposition in PI-MOCVD, where injected droplets are immediately evaporated in vacuum injection lines, thus vapor phase precursors are transported by carrier onto the hot substrate, where deposition takes place. The PI-

MOCVD system used in this work is shown in both Figure II-1 b) and c). Two injector lines, 1 and 2, are present and Ar is used as carrier gas. Oxygen is fed via another line through the top of the reactor. The vacuum chamber can reach a minimum pressure of 0.1 mbar. The heating plate is a Si wafer with diameter about 8 cm that is illuminated by an ultra violet lamp placed below (the temperature of the lamp is controlled by adjusting the lamp power). Fast heating rates can be achieved and the temperature is monitored with an infrared detector on the right-top corner of the deposition chamber and controlled by adjusting the lamp power. As shown in Figure c) right top corner, uniform depositions over a 5 cm diameter circumference can be achieved with our setup.

### II.1.2 Aerosol Assisted MOCVD

AA-MOCVD is well known for the ability to use less volatile metal organic precursors during CVD deposition at atmospheric pressure (no vacuum).<sup>4</sup> The deposition process is shown in Figure II-2, in which the precursor solution is atomized into small droplets (diameter about several microns) by a piezoelectric ceramic and the droplets are transported by the carrier gas into deposition chamber. Before the droplets reach hot substrate, the solvent is firstly evaporated due to the temperature gradient close to the heating source and the precursor molecules are further evaporated when the flow is closer to the hot substrate. Lastly the vaporized precursors are decomposed on the hot substrate thus dense and continuous thin films can be deposited.

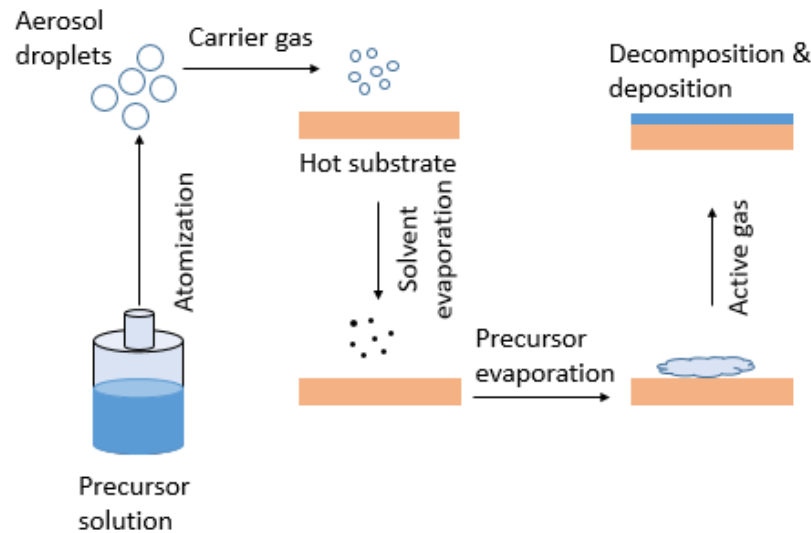


Figure II-2. Basic working principle of thin film deposition in AA-MOCVD.<sup>5</sup>

In this work, AA-MOCVD has been mostly used for the deposition of  $\text{Cu}_2\text{O}$  thin films, although Ag deposition has also been tested. Ag coating was indeed also successfully carried out by this approach but the large precursor consumption makes it less convenient than PI-

MOCVD, as stated above, when precursors are expensive. The AA-MOCVD system used during this work is presented in its initial configuration in Figure II-3. The precursor solution is subjected to ultrasounds generated by a piezoelectric ceramic and atomized droplets are formed. The mist is then carried by N<sub>2</sub> carrier gas (CG#1) from the bottom. For the sake of security, oxygen or air are only introduced from the middle part, accelerating the precursor onto the top heating plate, where the reaction takes place. The decomposed precursor byproducts and evaporated solvent are ventilated from the top, going through a solvent trap cooled with liquid nitrogen.

It has to be noticed that, in our AA-MOCVD systems, in order to ensure the same amount of precursor consumption throughout the deposition process, the precursor solution level in the chamber has to be kept stable. In our case, this was realized by connecting the solution chamber with a specially designed small reservoir as shown in Figure II-3. Due to the balance of the pressure, the solution level in the mist chamber was the same as the level in the small reservoir. By shifting the position of the reservoir up and down, the level of precursor solution in the mist chamber was adjusted and maintained stable.

Lastly, an atmospheric plasma system was connected with the deposition chamber in the AA-MOCVD, which was used for providing highly oxidizing species in this work. The working principle of the atmospheric plasma system is introduced in section II.2.2.

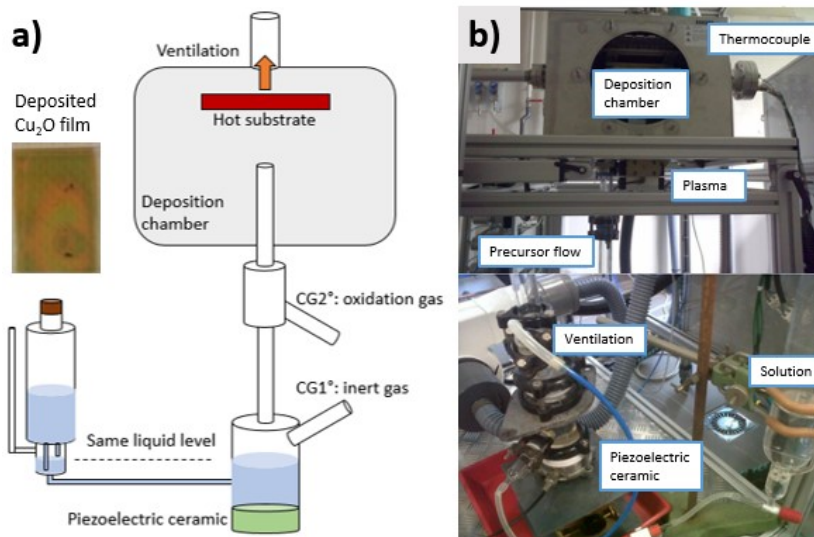


Figure II-3. Original configuration of the AA-MOCVD system used.

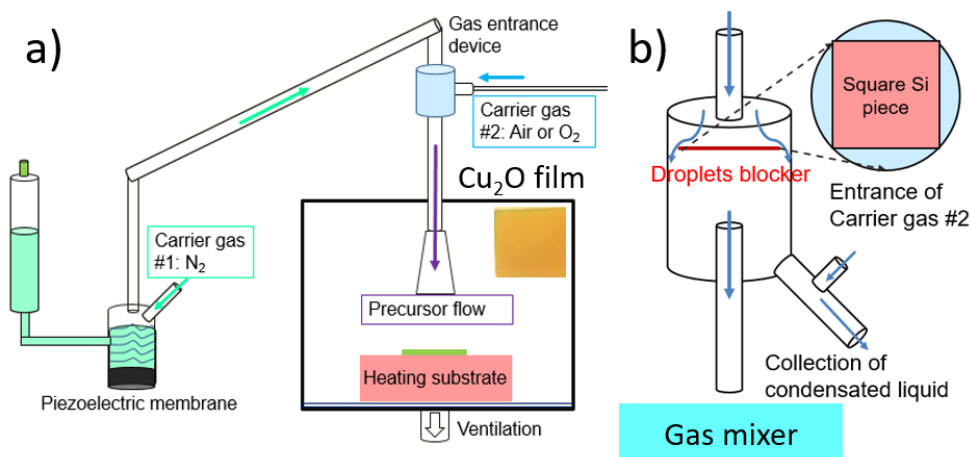


Figure II-4. Details of the final optimized AA-MOCVD configuration.

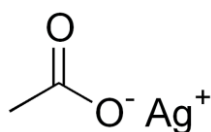
The AA-CVD system went through several modifications in order to improve the  $\text{Cu}_2\text{O}$  thin film deposition quality, which will be discussed in details in Chapter IV. The schematic illustration of the final configuration of our AA-MOCVD system is shown in Figure II-4 a). In this configuration, the hot plate is placed below the precursor flow. Figure II-4 b) presents a close up view of the carrier gas mixer, which has been designed to avoid big droplets in the precursor flow and condensation on the tube to have direct impact on deposition quality. The big and fast droplets in flow are mostly removed by hitting the Si substrate that acts as a filter and the condensations above are collected through the tube at the bottom side while smaller droplets are introduced in the reaction chamber.

## II.1.3 Film deposition

### II.1.3.1 Preparation of starting precursor solutions:

In the case of Ag, several different precursors were evaluated:

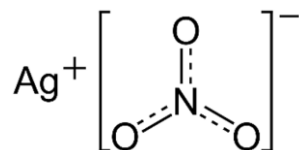
a). **Ag acetate** ( $\text{AgAc}$ , 99%, Sigma Aldrich). 0.02 M solutions were prepared by adding 1.67 g (0.01 mol) of  $\text{AgAc}$  in 500 ml of butanol-01 or ethanol, with continuous magnetic stirring with a speed of 300 cycle/min.  $\text{AgAc}$  can slowly be dissolved in alcohol solvents, but a long stirring duration is required. To facilitate this dissolving process, both ethanolamine and ethylene diamine can be added as dispersants. The solution presented a clear transparent color. The molecular structure of silver acetate is presented:



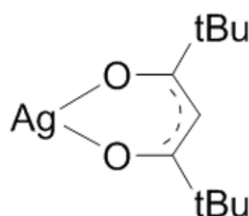
b). **Ag nitrate** (99.5%, Sigma Aldrich). Solutions with 0.02 M concentration were prepared by mixing 1.7 g (0.01 mol) of  $\text{AgNO}_3$  in 500 ml of ethanol. The mixture was stirred with



magnetic bar with speed 300 cycles/min for 30 min. The fully dissolved solution was clear yellow. The structure of the precursor is shown as below:



c). **2,2,6,6-Tetramethyl-3,5-heptanedionato Ag(I)** [Ag(TMHD)] (99.9%, Strem Chemical). Another silver precursor solution with 0.01 mol/L concentration was prepared by adding 1.46 g (0.005 mol) of Ag(TMHD) in 500 ml of ethanol (or butanol-01). The mixture was stirred for more than 60 min with magnetic bar at 300 cycles/min, dispersants such as ethanolamine was needed to obtain a clear grey solution. The molecular structure of the Ag(TMHD) is shown below:



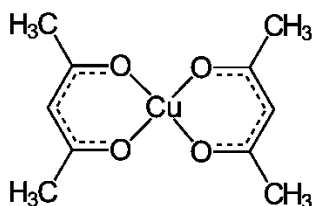
d). **Ag(hexafluoro acetylacetonate) phenanthroline** (AgP, new precursor obtained during this thesis)<sup>6</sup>. The precursor was carefully grinded in a ceramic mortar before dissolving it in alcohol solvent. 0.01 M precursor solutions were prepared by adding 2.45 g (0.005 mol) of precursor AgP in 500 ml ethanol solvent with magnetic bar stirring at a speed of 300 cycle/min for 60 min. Again, to speed up the process, dispersants as mentioned above can be added. The structure of the precursor is presented in Chapter III.

e). **Ag(hexafluoro acetylacetonate) triglyme** (AgT, new precursor obtained during this thesis)<sup>6</sup>. Compared with the previous two precursors, better solubility was found during the process of solution preparation. 0.01 M of precursor solution could be rapidly prepared by adding 2.45 g (0.005 mol) of AgT in 500 ml of ethanol with magnetic stirring for only 5 min, a clear grey colored solution being obtained. The molecular structure is presented in Chapter III.

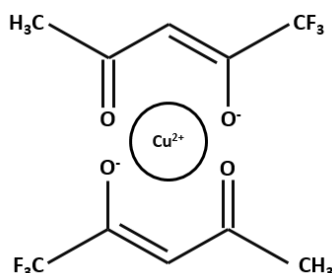
As for copper, two different copper precursors were used in this work:

a) **Cu(II) acetylacetonate (Cu(AcAc)<sub>2</sub>)** (98%, STREM Chemicals). Starting solutions with a concentration of 0.01 M were prepared by adding 1.3 g (0.005 mol) of precursor in 500 ml of alcohol solvent (butanol-01 or ethanol). The mixture was stirred until complete dissolution using a magnetic bar with speed 300 cycle/min. Since Cu(AcAc)<sub>2</sub> has low solubility in alcohol solvents, at least 0.01 M ethylene diamine (99%, Sigma Aldrich) was added as

dispersant (for 500 ml of 0.01 M solution, 2.5 ml of ethylene diamine). The solution became clear blue right after the dispersant was introduced. After 10 mins of further stirring, the solution was ready for deposition. The precursor molecule structure is shown below:



b) **Cu(II) trifluoro acetylacetonate (CuF)** (97%, STREM Chemical). The precursor solutions with 0.01 mol/L concentration were prepared by adding 1.85 g (0.005 mol) of CuF into 500 ml alcohol solvent (ethanol in this case) with magnetic bar stirring for 10 min with a speed of 300 cycle/min. The precursor rapidly dissolved in alcohol solvent and the solution presented a crystal clear green blue color after 2~3 minutes. The molecule structure is shown below:



### II.1.3.2 Substrate cleaning

Glass or Si substrates were cut with a diamond pen into squares with size of about 2.5 x 5 cm<sup>2</sup>. The substrates were washed in a soap solution with ultrasounds for 10 mins, rinsed with deionized water and dried with a N<sub>2</sub> flow. They were then washed in an ultrasonic bath again with acetone and isopropanol solvents in sequence, each for 10 mins at 40 °C. Lastly, they were dried with a N<sub>2</sub> flow and kept in a clean plastic box.

### II.1.3.3 Preparation of the MOCVD systems

**PI-MOCVD:** First of all, the injector was cleaned with the same solvent to be used, in this case ethanol or butanol-01. The injector was filled with 50 ml of precursor solution and fixed onto the precursor line. The temperature of the vacuum precursor line was adjusted to prevent the condensation of precursor before reaching the deposition chamber. The particular deposition conditions for each sample are detailed and discussed in the following chapters.

**AA-MOCVD:** In MOCVD, the distribution of temperature on the heating plate has a huge impact on thin film homogeneity. To ensure a homogeneous heat distribution on the substrate, a Si wafer with a diameter of 10 cm was placed between the substrate and heating plate. The water cooling on the atmospheric plasma head needs to be always on during deposition, even when not using it, to avoid overheating. Meanwhile, before starting the deposition, the precursor solution in the atomization chamber is pre-warmed by switching on the piezoelectric ceramic and applying a power of 6 W, with frequency 5 Hz. Since the mist formation is dependent on temperature, this ensures that the mist is the same during the whole reaction.

The ventilation of the system is monitored by the pressure gauge, as shown in Figure II-5, connecting with the deposition chamber on one side and the other exposed to atmospheric pressure. By changing the value of the gauge between 0 and 300 (maximum), the ventilation can be adjusted. Without ventilation the pressure gauge is at zero and the higher the ventilation power is, the higher the value on the pressure gauge. The ventilation used in this work was adjusted by setting the pressure gauge to about 3 cm with 10 L/min of carrier gas entering the deposition chamber. At least during 5 minutes before the deposition actual start, the gases with the correct ratio for the deposition need to be pre-introduced in the deposition chamber.

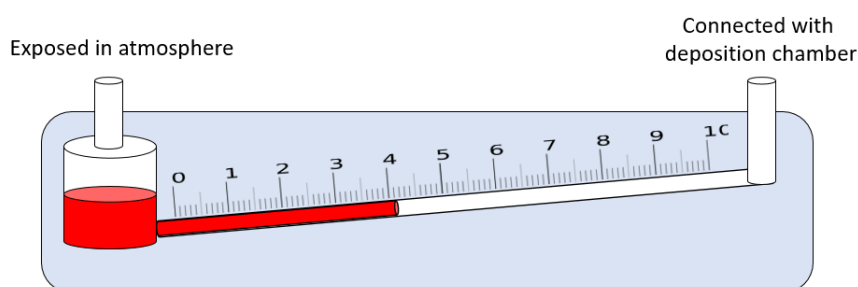


Figure II-5. Scheme of the pressure gauge used in the system with a 5 ° tilted capillary filled with red liquid.

## II.2 Oxidation techniques: electrochemical oxidation and oxidation with atmospheric oxygen plasma

### II.2.1 Electrochemical deposition and oxidation

In the majority of cases, as illustrated in Figure II-6, an electrochemistry system is made up of a potentiostat, and a cell containing the electrolyte and three electrodes, namely, working electrode (WE), counter electrode (CE) and reference electrode (RE). Among those electrodes, WE is where the expected reaction happens and RE is the electrode to fix the

reference potential for the WE independent from the change of the solutions.<sup>7</sup> During the electrochemical reaction process, voltage or current can be applied on the WE with the potentiostat. If the potential on the WE is positive, then WE acts as the anode, where electrons are removed and oxidation takes place. Conversely, the CE is the cathode. Where electrons are supplied and thus reduction takes place.

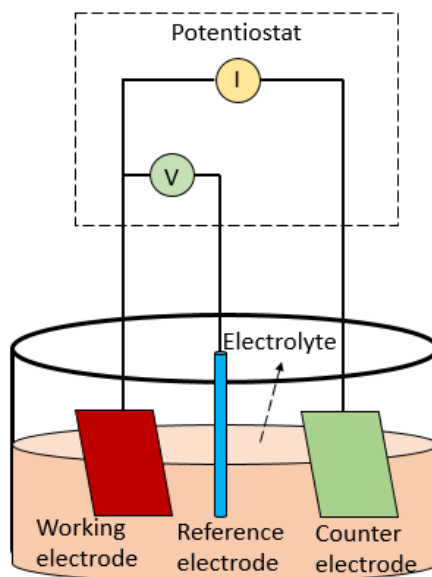


Figure II-6. Scheme of the electrochemical setup with a potentiostat and the electrochemical cell with the working, counter and reference electrodes.<sup>7</sup>

There are several protocols that are currently used when performing electrochemistry. The most commonly used modes are linear sweep voltammetry (LSV), cyclic voltammetry (CV), chronoamperometry (CA) and chronopotentiometry (CP). Among those different working modes, the LSV and CV modes are normally used to identify electrochemical processes. In LSV mode, as shown in Figure II-7 a), the potential linearly increases from potential  $E_0$  to  $E_1$  (forward scan) and back to  $E_0$  (backward scan),  $E_0$  normally representing the open circuit voltage. Through recording the current versus voltage, the oxidation and/or reduction potential at which electrochemical processes occur can be identified. Conversely, in CV mode the potential is linearly increased from  $E_0$  up to  $E_1$  and then falls back to negative potential  $E_2$  and finally returns to  $E_0$ , as presented in Figure II-7 b). Through the full cycle characterization, not only the oxidation/ reduction potentials can be distinguished, but also the reversibility of the reactions can be evaluated, as shown in Figure II-7 c). Each peak on the forward curve represents an oxidation process at bias  $E_p^a$ . For reversible reactions, the backward curve shows a reduction reaction at potential  $E_p^c$ . The degree of reversibility of the electrochemical process is described by the difference between  $E_p^a$  and  $E_p^c$ , the bigger

the difference the less reversible the reaction is. In addition, the ratio of intensity  $i_p^a$  and  $i_p^c$  should be close to 1:1 for a reversible reaction. In the case of oxide deposition or oxidation, after identifying reaction potentials with LSV or CV, a particular oxidation state of the metal ions can be achieved by applying the necessary voltage (i.e. by performing a CA, where current is monitored). Reactions can be carried out in CP mode, where the current is set to a certain value as required and the potential evolution is monitored.

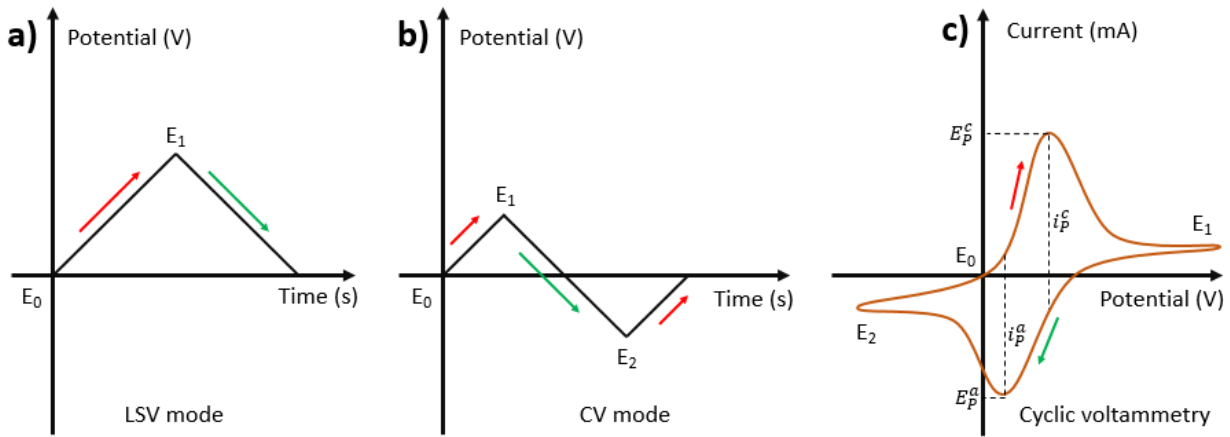


Figure II-7. a) Potential versus time in LVS mode. b) Potential versus time in CV mode and c) is the correspondent CV curve (voltammogram) with single electron transfer, current versus potential.

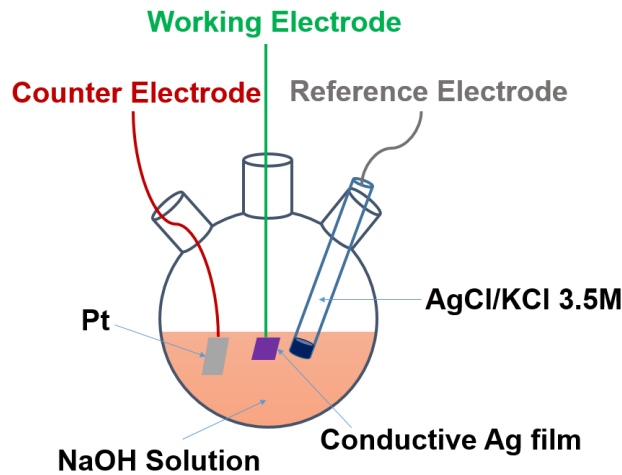


Figure II-8. Experimental setup for electrochemical oxidation of Ag/AgCu films.

In this work, electrochemistry was used for oxidizing conductive metallic Ag or Ag-Cu films and for the direct deposition of  $\text{AgCuO}_2$  thin films from solution. For the oxidation purpose, a typical three-electrode cell configuration was used, as shown in Figure II-8, in which the Ag/Cu films deposited by MOCVD were the working electrode and Pt was used as counter electrode (left), with a AgCl/KCl 3.5 M reference electrode (right). The three electrodes were placed in a three neck flask containing a 1 M NaOH solution as the electrolyte. The

potential was controlled and swiped between -1 and +1 V using a Model 273A, Princeton Applied Research potentiostat. To find a proper potential bias for the electrochemical oxidation of AgCu films and electrochemical deposition of AgCuO<sub>2</sub>, cyclic voltammetry studies were conducted. The detailed parameters are described in Chapter V.

## II.2.2 Oxygen plasma oxidation

Another oxidation technique adopted in this work has been atmospheric oxygen plasma oxidation. The working principle of atmospheric plasma is illustrated in Figure II-9, in which the gas flow passes through the two electrodes with high voltage applied in between. The ultra-high potential between the two electrodes ionizes the gas molecules passing through. Thus, the emission plasma flow contains electrons, ions and radicals.

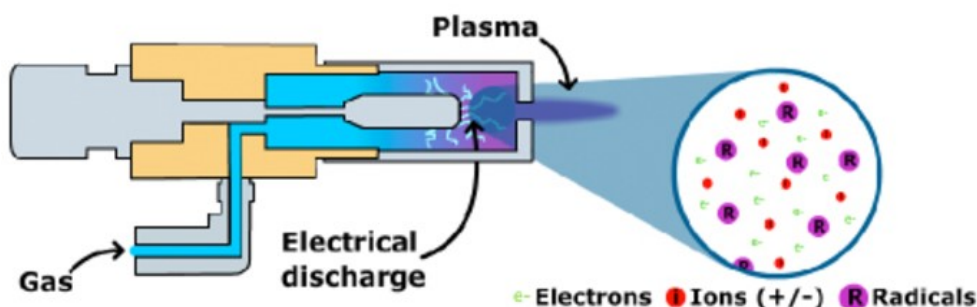


Figure II-9. Working principle of atmospheric plasma.<sup>8</sup>

In this work, the atmospheric plasma generator was used to produce a highly oxidizing atmosphere.<sup>9,10</sup> The oxygen plasma head (from AcXys technologies) is placed in the AA-MOCVD deposition chamber, as illustrated in Figure II-10.

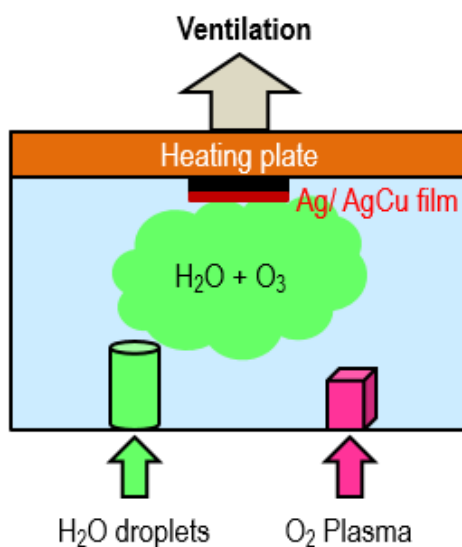
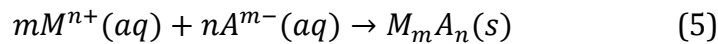


Figure II-10. Scheme of the setup used to carry out oxygen plasma oxidation of metallic Ag/Cu films.

The plasma generator is set at the bottom of the deposition chamber besides the carrier gas flow tube. As it is shown, Ag/Cu metallic films were placed on the heating plate and subjected to the plasma with different powers (up to 500 W, with an O<sub>2</sub> flow of 15 L/min). During the oxidation process, H<sub>2</sub>O mist was introduced at the same time to reduce corrosive radicals emitted from the plasma head. The effect of temperature was also studied during plasma oxidation. The results are detailed in Chapter III and Chapter V.

### II.2.3 Deposition of AgCuO<sub>2</sub> films by the SILAR method

Successive Ionic Layer Adsorption and Reaction (SILAR) deposition is a solution based technique, widely used for metal oxide and sulfide thin film coatings. Commonly, there are at least three types of solutions used in the SILAR process, namely metal ion solution, cation solution and buffer solution. The buffer solution normally consists of deionized water or a water-alcohol mixture. The deposition mechanism relies on the electric static affinity between the ions in solution and the substrate<sup>11</sup>. The thin film deposition mechanism in SILAR is illustrated in Figure II-11, the reactions between metal ions and negative cations lead to the precipitation and thus the deposition of the targeted material, as shown in Equation II 5.



Thus, theoretically SILAR deposition can be conducted in a layer-by-layer manner, yielding dense and high quality films.

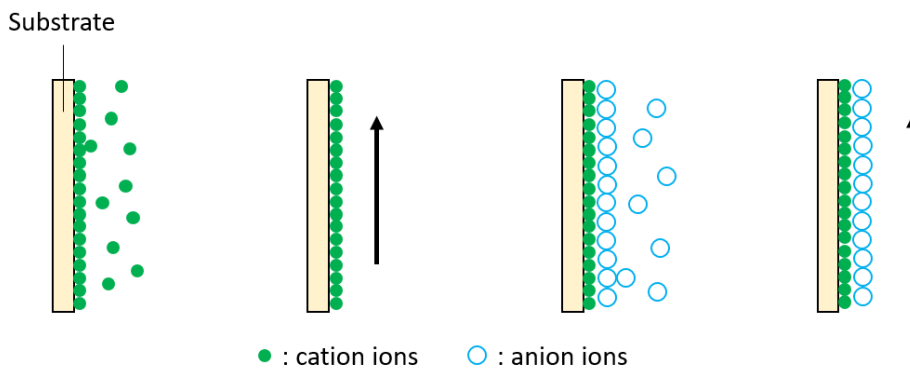


Figure II-11. Schematic illustration of thin film coating during one SILAR cycle. (a) cation adsorption; (b) rinsing; (c) anion reaction; and (d) rinsing.<sup>11</sup>

In this work, for the first time, the SILAR deposition technique had been used to synthesize AgCuO<sub>2</sub> thin films. The experimental setup used is mainly composed of a motor in the Z axis to move the substrate up and down and a rotating platform on the X-Y plane to change the position of the three solutions in a sequential order.

More detailed experimental process, parameters and results will be discussed in Chapter V.

## II.3 Characterization techniques

### II.3.1 Thin film crystallinity: RAMAN spectroscopy, XRD

#### II.3.1.1 Raman Spectroscopy

Raman spectroscopy is a spectroscopic technique to study vibrational, rotational or other low-frequency modes in a chemical system. It is based on the measurement and analysis of the signal/photons arising from the Raman effect (or Raman scattering) which is an inelastic scattering process due to the interaction of a monochromatic light used for excitation (laser) with phonons of a lattice.<sup>12</sup>

Scattering processes involve the simultaneous absorption of an incident photon and emission of another photon called the scattered photon. As illustrated in Figure II-12, they can be classified as<sup>13</sup>:

- the elastic scattering, known as the Rayleigh scattering, where the incident and scattered photons have the same energy, meaning that there is no energy transfer during the process.
- the inelastic scattering where the scattered photon has an energy different from that of the incident photon. Raman scattering is one of the most important inelastic scattering processes; it involves transitions between the vibrational/rotational levels due to the combination of an absorption of the incident photon through a transition to a higher energy level, represented as an intermediate virtual state, followed by a spontaneous emission of the scattered photon. If the scattered photon has less energy than the incident one, the molecule is excited to a higher energy level and the process is called the Stokes Raman process. It corresponds to the excitation of the molecule from the vibrational ground state ( $v=0$ ) to the first excited state ( $v=1$ ) of a vibrational mode with energy  $E_{\text{inc}}-E_{\text{scat}}$ . If the scattered photon has more energy than the incident photon, it is the anti-Stokes Raman process, and the molecule has relaxed from an excited vibrational state ( $v=1$ ) to its ground state ( $v=0$ ). The energy of the vibration is equal to  $E_{\text{scat}}-E_{\text{inc}}$ . Thus, the Stokes and anti-Stokes parts of a Raman spectrum can be symmetrically observed on both sides of the Rayleigh line but with different intensities. In practice, the more commonly measured in Raman spectroscopy is the Stokes spectrum which has a higher intensity. It is to be noted that the intensities of the Raman lines are very weak in comparison with the very intense Rayleigh line (at least  $\times 10^{-6}$ ). The energy lost (Stokes) or gained (anti-Stokes) by the photons in the scattering process is called the Raman shift. Raman shifts ( $\nu$ ) are commonly expressed in wavenumbers ( $\text{cm}^{-1}$ ) such as  $\nu = 1/\lambda$ . The Raman spectrum corresponds to the wavenumber dependence of the Raman scattered



intensity at a given incident wavelength. It is characteristic of a molecule or a material for a given crystallographic structure.

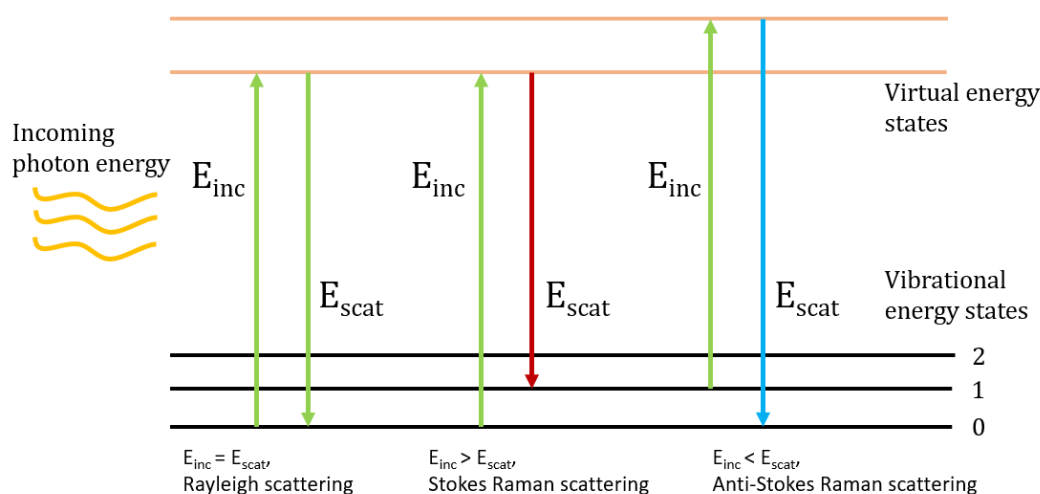


Figure II-12. Schematic representation of the Rayleigh and Raman scattering, and of the IR absorption processes.<sup>14</sup>

The main advantage of Raman spectroscopy is that it is a local probe; moreover, it is non destructive, cost-effective and doesn't need sample preparation. It gives complementary information to Infrared (IR) spectroscopy which also probes the vibrational modes through an absorption process where the molecule is excited to a higher vibrational level within a given electronic state, usually the ground state.

Raman spectroscopy has mainly been used in this work for the identification of crystal phases and detection of carbon species in the thin films. In addition, Raman intensities also gave us information about the crystallinity of the materials.

Raman spectra were recorded from the film surface using a Jobin Yvon/Horiba Labram spectrometer equipped with a charge-coupled device (CCD) detector cooled with liquid nitrogen. The experiments were conducted in the micro-Raman mode at room temperature. Among the three exciting wavelengths available in LMGP (red, blue and green), we used the blue (at 488 nm) and green (514.5 nm) ones Ar<sup>1+</sup> laser with a power as low as ranging from 60  $\mu$ W to 6  $\mu$ W (filter 1/100 to 1/1000) at the sample surface to avoid sample heating. The laser was focused to a spot size close to 1  $\mu$ m on the sample with using a  $\times 100$  or  $\times 50$  objective. Before each spectrum acquisition, the Raman line of a Si substrate was measured and used as reference for calibration (theoretical position at 520.7  $\text{cm}^{-1}$ ).

### II.3.1.2 X-Ray diffraction (XRD): Bragg-Brentano and Grazing Incidence.

X-Ray Diffraction is a widely used characterization technique for studying crystalline matter, providing information including phase identification, texture and grain size, etc. The basic

working principle of this technique relies on the Bragg diffraction. When X-Ray radiation (having wave length similar to the distances between atoms in crystals) reaches a crystalline material, it is scattered by the electrons around each atom. Depending on the angle between the incident radiation and the atomic plane, collective constructive scattering can take place. This is expressed by Bragg's equation (Shown in Equation II 6):

$$2d_{hkl} \times \sin\theta = n\lambda \quad (6)$$

Where  $d_{hkl}$  is the distance between two crystal planes with Miller index (hkl),  $\theta$  is the incident angle between the X-Ray and the (hkl) crystal plane,  $n$  is the diffraction order and  $\lambda$  is the X-Ray wavelength.

The X-Ray Bragg diffraction is schematically presented in Figure II-13. In the figure, the scattering vector is defined as  $\mathbf{K} = \mathbf{k}_e - \mathbf{k}_i$  as the difference between the wave vector  $\mathbf{k}_e$  of the scattered wave, and the wave vector  $\mathbf{k}_i$  of the incident X-ray.

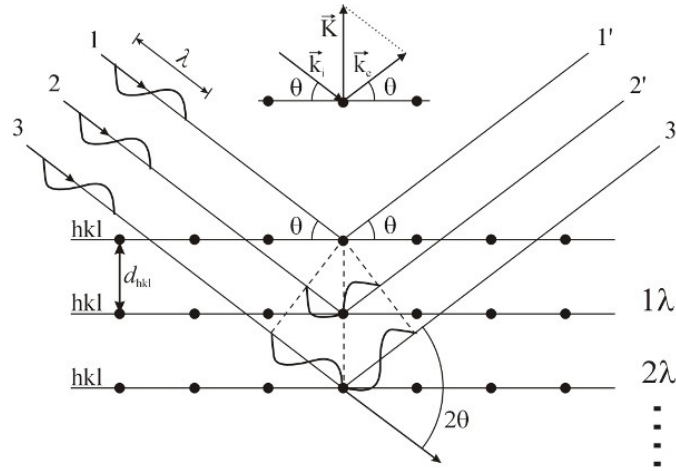


Figure II-13. Scheme of the Bragg diffraction. The two scattered X-Ray beams undergo constructive interference when  $2dhkl \sin\theta = n\lambda$ . (image from: <https://fys.kuleuven.be/iks/nvsf/experimental-facilities/x-ray-diffraction-2013-bruker-d8-discover>)

A typical X-Ray diffractometer setup is schematically presented in Figure II-14. Based on the desired information to be obtained, different XRD configurations can be applied. The Bragg-Brentano geometry (see Figure II-14) is the most typically used configuration.

In Bragg-Brentano geometry, during XRD acquisition the X-Ray source is fixed and both sample plane and detector turn along the same rotation axis.  $\theta$  is defined as the angle between incident X-Ray beam and the sample surface while  $2\theta$  is the resulting angle between incident beam and scattered beam (the detector is moved so that it keeps the same  $\theta$  angle with respect to the sample, thus  $2\theta$  with respect to the incident beam).

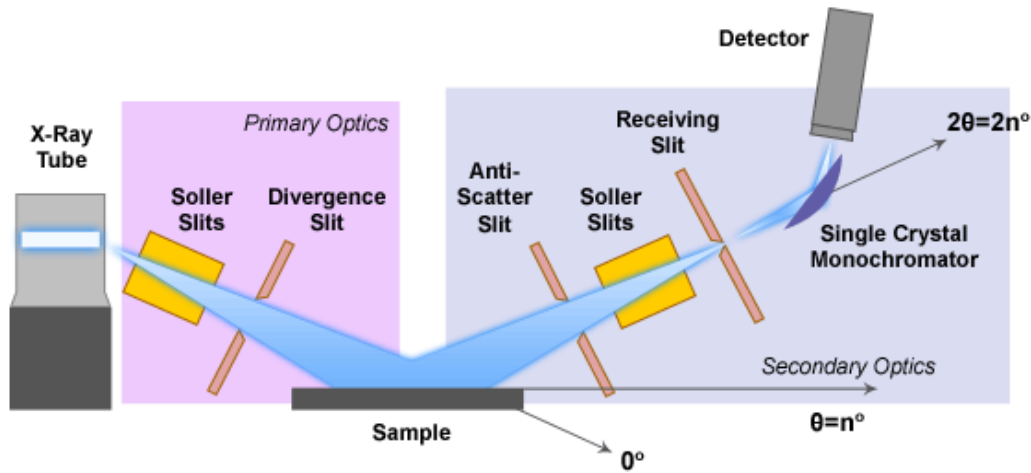


Figure II-14. Schematic illustration of the Bragg-Brentano geometry. (image from: <http://li155-94.members.linode.com/myscope/xrd/background/machine/>)

With such a setup, only the diffraction planes parallel to the sample surface can undergo constructive interference, thus resulting in diffraction peaks. As shown in Figure II-15, crystal A will diffract in Bragg-Brentano geometry while crystal B won't be able to satisfy the diffraction condition thus not appearing in the diffraction pattern.

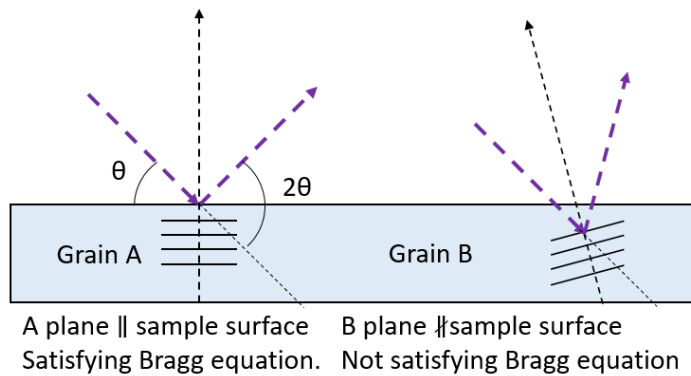


Figure II-15. Scheme to illustrate that only crystallographic planes parallel to sample surface diffract in Bragg-Brentano geometry.

In this work, a Bruker D8 Advance diffractometer was used for acquiring XRD patterns with Bragg-Brentano Geometry, with wavelength  $1.5406 \text{ \AA}$  from  $\text{Cu K}\alpha_1$  radiation. A 1D detector with resolution about  $0.05^\circ$  was used for signal collection.  $2.5^\circ$  and  $0.3^\circ$  Soller slits were used for divergent slit, while anti-scatter slits were 6.8 mm width.

For very thin films ( $< 10 \text{ nm}$ ) Grazing Incidence geometry (shown in Figure II-16) can be applied. <sup>12</sup>Grazing incidence (GI) geometry is very sensitive to phase composition even for samples with less radiation volume, like thin films. With the Bragg-Brentano geometry, the incident X-ray can easily penetrate through the thin film material, the resulting collected signal being too weak to be distinguished from the background noise, especially with an amorphous substrate. In GI geometry, the incident X-ray beam is aligned to the sample

surface with a very small incident angle, typically ranging from  $0.25^\circ - 0.5^\circ$ .<sup>15</sup> The positions of X-ray source and sample stage are fixed, only the detector scans in  $2\theta$  angle to collect the diffracted signal. With such a close to parallel beam, larger amount of thin film material can be radiated thus stronger diffraction signal can be acquired. In this way, the interference signal from the substrate can be minimized. But it has to be noticed that since the X-Ray beam is almost parallel to the sample surface, thus the crystal planes parallel to the sample surface diffract with much weaker signal. Contrarily to the Bragg-Brentano geometry, under GI geometry, the grains with crystal planes not parallel to the sample surface are the main contributors to GI diffraction signal. In this work, most GIXRD patterns were acquired with a Bruker C40 D8 with incidence and exit angles maintained around  $0.5^\circ$ . There are also part of the GIXRD patterns collected with a RIGAKU Smart lab diffractometer.

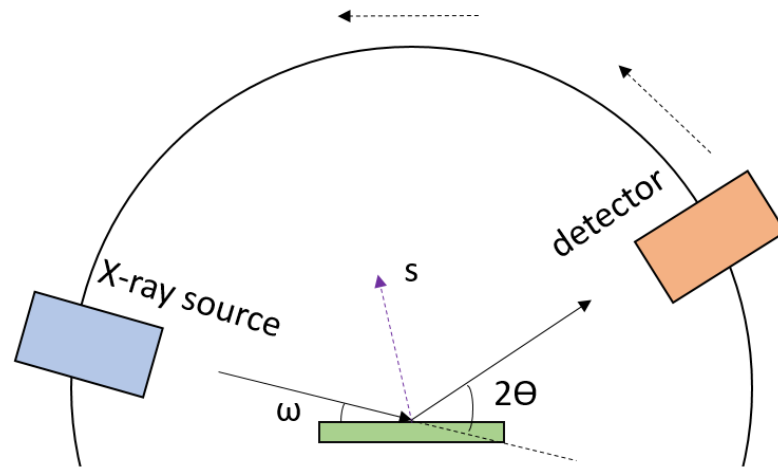


Figure II-16. Schematic illustration of Grazing Incidence XRD characterization.  $\omega$  is the incidence angle and  $s$  is the vector perpendicular to the diffraction plane.

In addition to phase identification, the XRD patterns acquired under Bragg-Brentano geometry can also give information about grain orientation in the thin film (i.e. texture). Such a preference or texture can be evaluated using a texture coefficient.<sup>16</sup> The texture coefficient  $T_c$  can be calculated with Equation II 7.

$$T_c(h_i k_i l_i) = \frac{I(h_i k_i l_i) / I_0(h_i k_i l_i)}{(1/n) [\sum_{j=1}^n \frac{I(h_j k_j l_j)}{I_0(h_j k_j l_j)}]} \quad (7)$$

Where  $T_c(h_i k_i l_i)$  is the texture coefficient of the specific  $(h_i k_i l_i)$  plane,  $I$  is the measured diffraction intensity (under Bragg Brentano geometry) for a particular Miller index,  $I_0$  is the intensity for the same index in the reference pattern and  $n$  is the number of reflections taken

into account. Indexes with  $T_c$  values bigger than 1 indicate that there is a preferred orientation along the respective direction

Besides texture, by measuring the Full Width at Half Maximum (FWHM) of the reflections, the crystallite size on each particular direction can be estimated through the Scherrer Equation,<sup>17,18</sup> as shown in Equation II 8.<sup>19</sup>

$$\beta_L = \frac{K\lambda}{L \cos\theta} \quad (8)$$

Where  $\beta_L$  is the peak width (obtained by subtracting the width associated to the instrument),  $K$  is a numerical constant to account for instrumental widening (0.9 in our case),  $\lambda$  is the wavelength of the X-Ray source,  $L$  is the average crystallite size and  $\theta$  is the incident angle.

## **II.3.2 Morphological characterization: SEM: EDS, EBSD, AFM**

### **II.3.2.1 Scanning Electron Microscopy (SEM)**

Scanning Electron Microscopy is a widely used characterization technique for acquiring topographical information on the sample surface. It is also a versatile analysis technique providing qualitative and semi-quantitative information about sample composition. Finally, it can also provide information about crystal structure and texture. In SEM, a primary electron beam is allocated towards the sample surface and causes a series of phenomena (see Figure II-17) taking place at different penetration depths and providing complementary information. As it is shown, due to the strong energy of the primary electron beam, Auger Electrons are firstly excited at the very surface of the sample, next are the secondary electrons (few nm range) which are used for imaging the sample. In a deeper penetration depth, back scattered electrons and characteristic X-Rays are also generated, both carrying information on the sample composition.

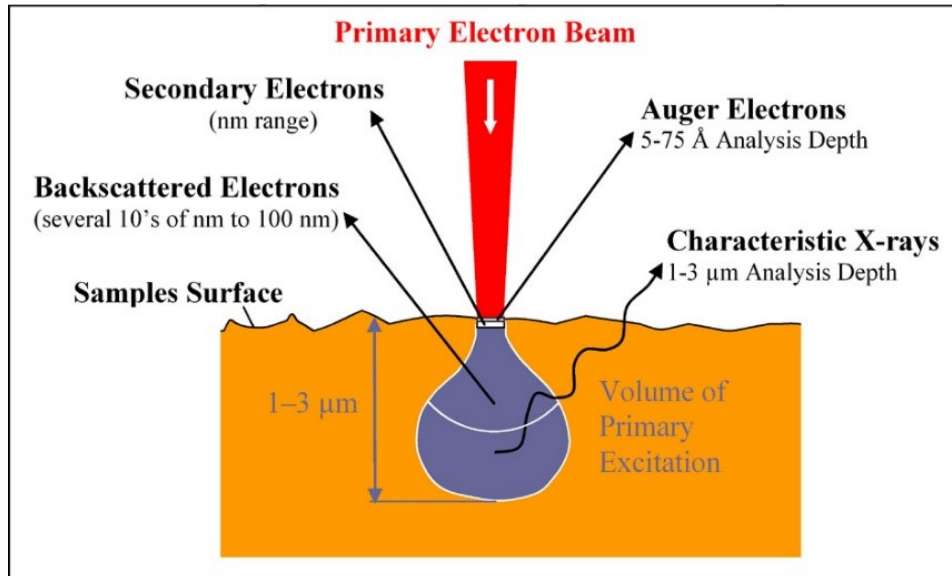


Figure II-17. Schematic illustration of the primary electron beam interacting with the surface of the sample.<sup>20</sup>

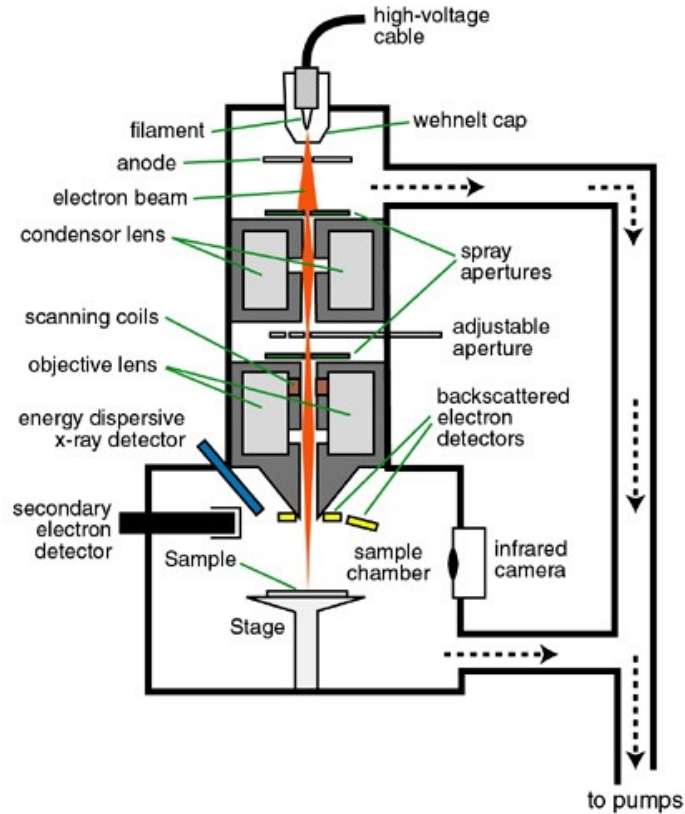


Figure II-18. Scheme of a typical Scanning electron microscope. (image from: <http://saturno.fmc.uam.es/web/superficies/instrumentacion/Instrumentation.htm>)

The scheme of a typical scanning electron microscope is shown in Figure II-18. Actually, it resembles a conventional optical microscope, but in optical microscopes light is confined and focused by optical lenses, while in SEM electrons are instead confined by a magnetic field created by surrounding coils. There are different types of electron beam generation,

namely, thermionic emission and potential caused field emission. Most of the new SEM setups adopt the Field Emission Gun (FEG) since the generated electron beam has smaller diameter, is more coherent and much more intense than with thermionic emission. In this work, a FEI QUANTA FEG 250 equipped with an OXFORD energy dispersive X-Ray detector and backscattering electron detector was used.

In addition to that, by taking advantage of the back scattered electrons, surface crystal information can also be analyzed by Electron Back Scatter Diffraction (EBSD). This technique provides crystallographic characterization for the surface of crystalline microstructures. In materials science, it is widely used in SEM for phase identification and to reveal defects and texture of the grains. A typical EBSD setup is shown in Figure II-19. The sample surface layer (about 40 nm penetration depth) is scanned under an intense electron beam aligned with highly tilted angle ( $60^\circ$  to  $80^\circ$ ) point by point. Right in front of the tilted sample surface, a CCD camera is placed to form the electron backscatter diffraction patterns. After the patterns are recorded, those bands will be transformed into points by Hough transformation, allowing peak identification. Thus, through this point by point scan, information about phases, orientations and defects on the surface of the crystalline material can be revealed.

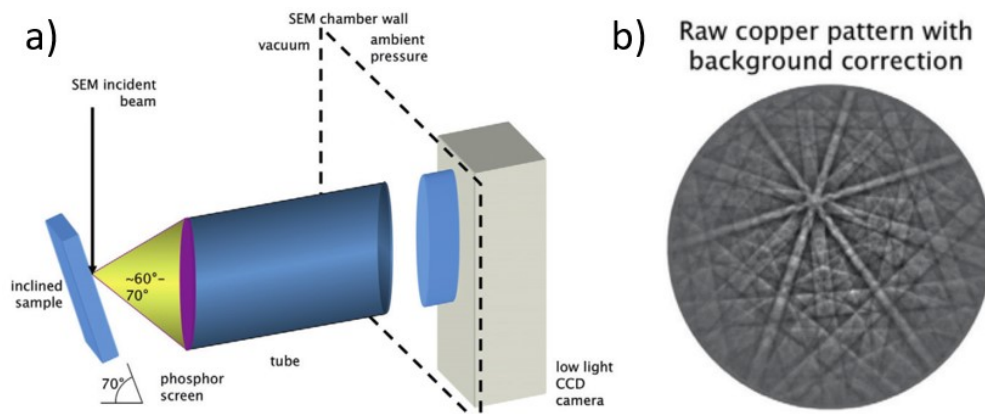


Figure II-19. Schematic presentation of the EBSD configuration and example of a Cu diffraction pattern.<sup>21</sup>

### II.3.2.2 Atomic Force Microscopy (AFM)

Atomic Force Microscopy (AFM) is a nondestructive surface probing technique. Equipped with an ultra-sharp probe (tip) of only a few atoms, it is possible to physically interact with surface atoms. The basic working principle of AFM is shown in Figure II-20. A focused laser spot is aimed at the top end of the probe and reflected into a 2D photodiode detector. When the probe tip scans across the surface, any change in the sample morphology will cause the deflection of the cantilever thus a change in the reflection of the laser spot on the

detector. To maintain the laser spot at the center of the detector, a feedback signal will be applied on the tip cantilever through a piezoelectric piece in the Z axis. Thus, the morphology change of the sample surface is converted into electrical signal and recorded to recreate the surface 2/3 D image afterwards.

There are mainly three types of AFM scanning modes, namely, contact mode, tapping mode and non-contact mode (or vibration mode). In contact mode, the AFM tip is dragged along the surface of the sample, the repulsive force between the atoms from the tip and sample causing a deflection of the cantilever. Such imaging mode shows better resolution than the other two imaging modes but some fragile or weakly attached samples are not resistant to such dragging force. Thus the other semi/non-contact modes will be more appropriate. The other imaging mode is called tapping mode or semi-contact mode, in which the cantilever is driven by the piezoelectric with a certain frequency and amplitude. With closer interaction with the surface, the amplitude of the oscillation will be affected thus recorded as the morphological information. Lastly, by taking advantage of the Van Der Waals force interaction between the tip and sample atoms, both the oscillation and amplitude modulation are the characterization approaches in non-contact mode. Since there is no physical contact between the tip and sample, non-contact mode is preferable when dealing with soft samples. In this work, the AFM system used was a Digital Instruments D3100 Nano scope, working in tapping mode. Si and Ti coated Si probes were used.

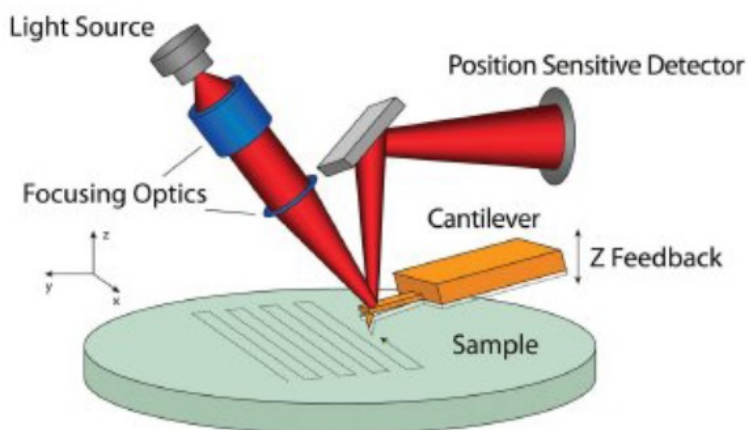


Figure II-20. Illustration of the AFM working principle.<sup>22</sup>

In addition to the normal topographical information acquisition, the conductivity mapping of the sample surface was also carried out in this work. Samples were deposited on conductive ITO/glass substrate. To ensure a good connection, a 100 nm thick Au contact was evaporated onto the ITO, as shown in Figure II-21. During the characterization, a conductive Pt coated Si tip was used under contact mode. Meanwhile, a potential was applied



between the Au contact and the AFM tip (Asylum Research PPP-CONTPt). and the current passing through was recorded. Thus, when the conductive AFM tip drags through the surface, both topographical information and conductivity mapping of the surface can be obtained simultaneously. In this characterization, a bias potential of 2 V was applied.

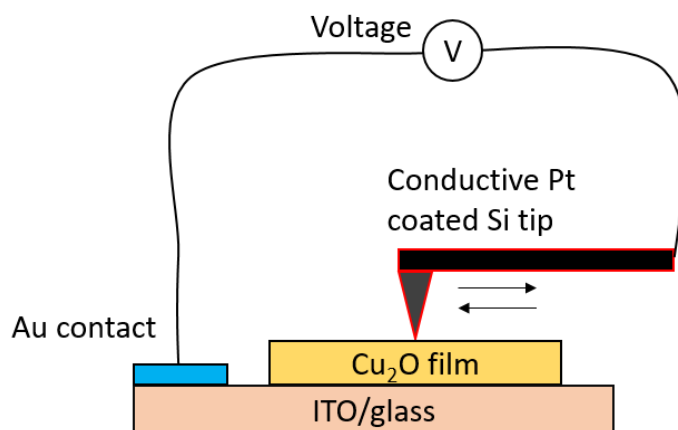


Figure II-21. Illustration of electrical Atomic Force Microscope characterization.

### II.3.2.3 Transmission Electron Microscopy (TEM)

Transmission Electron Microscopy allows both sample imaging and *in situ* crystallographic analysis. Its basic working principle is built on the interactions between the electrons in the material and the e-beam crossing the sample (thickness has to be less than 100 nm) to form images or diffraction patterns. This requires preparation of samples thin enough for characterization. Therefore TEM is a destructive characterization technique, but it can allow observing the fine details of the sample on atomic scale. In some cases, powder samples can also be studied and in this case very little amount of sample is needed.

For thin film characterization in this work, there were two ways to prepare the samples, mainly by scratching the surface to get small clusters of the thin film material or by cutting and mechanical milling followed by polishing the cross-section with an Ar<sup>+</sup> beam. The scratching methods allows rapid preparation but it may take a lot of time during the characterization process to find the parts of interest. Preparation of cross-sections can take much longer but it is much easier to find the area of interests. In a typical TEM characterization, there are two operational modes commonly used, namely imaging and diffraction mode. Their schematic configuration is shown in Figure II-22. A JEOL-2016 LaB6 working at 200 kV was used in this work.

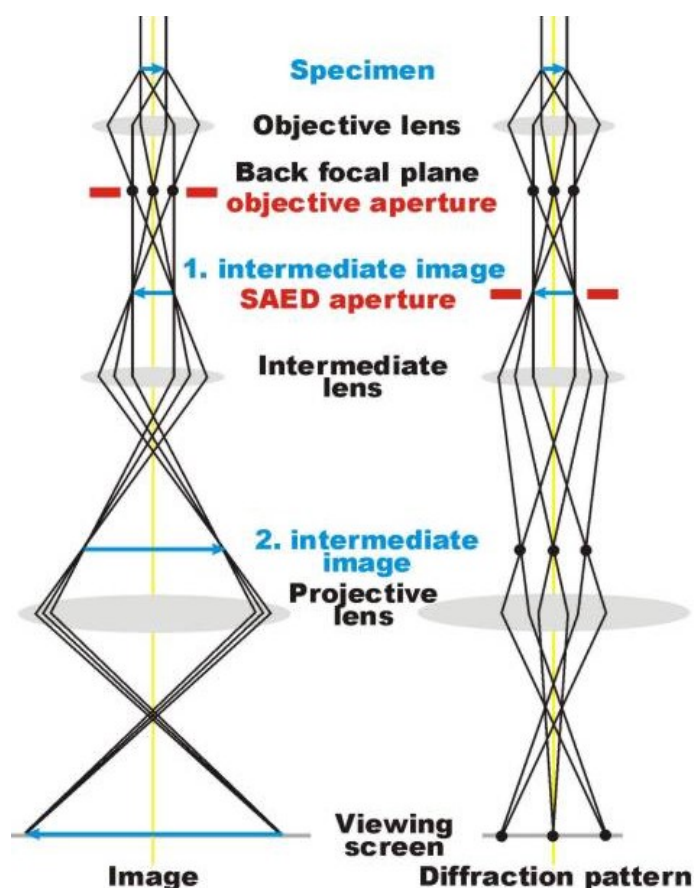


Figure II-22. Schemes of imaging and diffraction mode in TEM.<sup>23</sup>

### II.3.3 Ultraviolet-Visible (UV-Vis) spectroscopy

UV-Vis spectroscopy is mainly used for optical characterization. In this work, a Perkin Elmer Lambda 950 spectrometer was used, equipped with a deuterium and a tungsten lamps to emit light with different wavelengths ranging from 250 nm to 2500 nm. For signal collection, two photon detectors work in sequence switching at wavelength 850 nm (a photomultiplier for UV and visible light; An InGaAs sensor for infrared). The spectrometer is equipped with an integrating sphere and an automated reflectance transmittance analyser (ARTA). Therefore, transmittance, reflectance and absorbance spectra can be acquired.

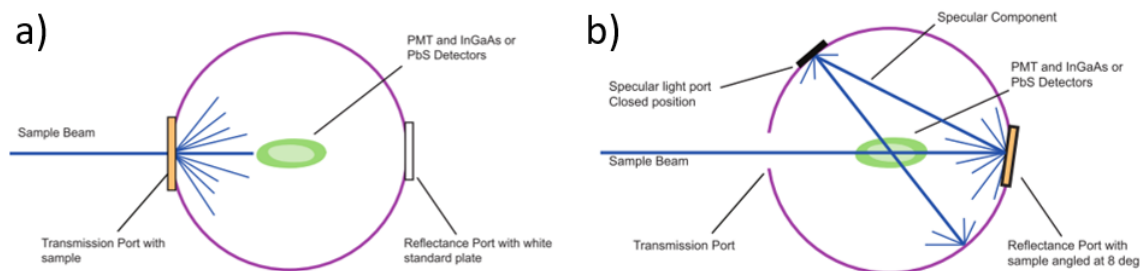


Figure II-23. Optical measurement of a) the total transmittance (TT) and b) the total reflectance (TR). (image from: <https://www.perkinelmer.com>)

Both total transmittance/reflectance or direct transmittance/reflectance can be measured. Figure II-23 presents the configurations used for the measurements in our work, figure a) total transmittance and figure b) total reflectance. Absorption can as well be measured in two different ways. The first one involves placing the sample inside the ARTA. In this method, the measurement is more accurate but extra care has to be taken not to damage the spectroscope components. The second method to obtain the absorption  $T_a$  (used in this work) is by deducting it from  $T_t$  and  $T_r$  according to Equation II 9.

$$T_a = 1 - T_t - T_r \quad (9)$$

Based on the optical measurements, the absorption coefficient can be approximately calculated following Equation II 10 and 11,<sup>24</sup>

$$T \approx (1 - R)^2 e^{-\alpha d} \quad (10)$$

$$\alpha = -\frac{1}{d} \ln\left(\frac{T}{(1 - R)^2}\right) \quad (11)$$

Thus, optical bandgap of the thin film semiconductor material can be identified using the Tauc plot as shown in Equation II 12,<sup>24</sup>

$$(\alpha h\nu)^{1/n} = A(h\nu - E_g) \quad (12)$$

in which  $\alpha$  is the absorption coefficient,  $h$  the plank constant,  $\nu$  is the photon frequency and  $E_g$  is the bandgap. The value of  $n$  depends on the nature of the bandgap<sup>25,26</sup>:

direct allowed transition,  $n=2$ ,

direct forbidden transition,  $n=3/2$ ,

indirect allowed transition,  $n=1/2$ ,

indirect forbidden transition,  $n=3$ .

## II.3.4 Electrical characterization

### II.3.4.1 Four probe measurements

Four point probe is a widely used technique to rapidly measuring the resistivity of semiconducting materials. The basic setup is illustrated in Figure II-24. By passing a current through the two outer probes (1, 4), voltage is measured between the two inner probes (2, 3)<sup>27</sup>. Thus, the resistance can be calculated as:

$$R = \frac{V}{I} = \rho \frac{L}{Wt} = \frac{\rho}{t} \frac{L}{W} \quad (13)$$

in which R is the resistivity, V is the voltage, I is the current,  $\rho$  is the conductivity, W is the width, L is the length and t is the thickness. The sheet resistance  $R_s$  (unit  $\Omega/\square$ ) for thin films can be obtained from  $\rho$  and the film thickness (t), as shown in Equation II 10.

$$R_s = \frac{\rho}{t} \quad (14)$$

Therefore,

$$\frac{V}{I} = R = R_s \frac{L}{W} \quad (15)$$

$$R_s = \frac{W}{L} \cdot \frac{V}{I} = k \cdot \frac{V}{I} \quad (16)$$

Where k is a correction factor based on sample size and space between each probe, which is taken as  $\pi/\ln 2$  in this work for thin film measurements.<sup>28,29</sup> Thus,  $R_s$  can be rewritten as in Equation II 13.

$$R_s = \frac{\pi}{\ln 2} \times \frac{V}{I} = 4.53 \frac{V}{I} \quad (17)$$

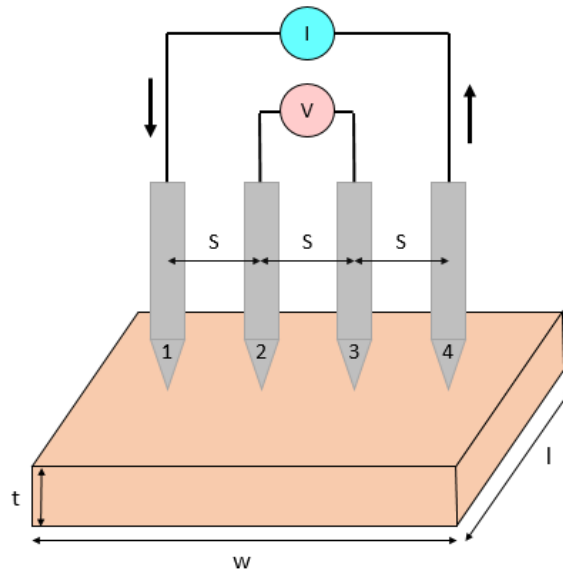


Figure II-24. Schematic illustration of four point probe measurement.

### II.3.4.2 Hall Effect measurements

In addition to the four point probe measurement, the Hall Effect measurement can allow direct measurement of more detailed electronic properties besides resistivity, including identifying the type of semiconducting material, carrier concentration and mobility.

As it is shown, the working principle of Hall effect measurement is based on the Lorentz force generated when passing charged particles (electrons in this case) through an electric field while applying a perpendicular ( $Z$  axis) magnetic field:  $q_v E \times B_Z$ , where  $q_v$  is the carried charge,  $E$  is the electrical field and  $B_Z$  is the magnetic field in the  $Z$  axis. In a semiconducting material, due to the unequal quantity of mobile charges (electrons and holes) present, when the current is applied along the  $X$  axis ( $I_X$ ), a potential difference appears in the  $Y$  axis, which is defined as the Hall voltage ( $V_H$ ), from which carrier concentration ( $n$ ) and mobility ( $\mu$ ) can be obtained from Equation II 18 and 19, provided the  $R_s$  value is known.<sup>30,31</sup>

$$n = \frac{I_X B_Z}{e V_H t} \quad (18)$$

$$\mu = \frac{1}{e R_s n t} \quad (19)$$

where  $t$  is the thin film thickness and  $e$  is the elemental charge.

The most widely used characterization configuration is called Van Der Pauw configuration, as illustrated in

Figure II-25. To measure the carrier concentration and mobility, the semiconductor sample is exposed to a magnetic field in the  $Z$  axis and a current is applied between the corners 1 and 3, namely  $I_{13}$ . Due to the Lorentz force applied on different charged particles (electrons and holes), a potential difference can be created from the corner 2 and 4, namely  $V_{24}$ .

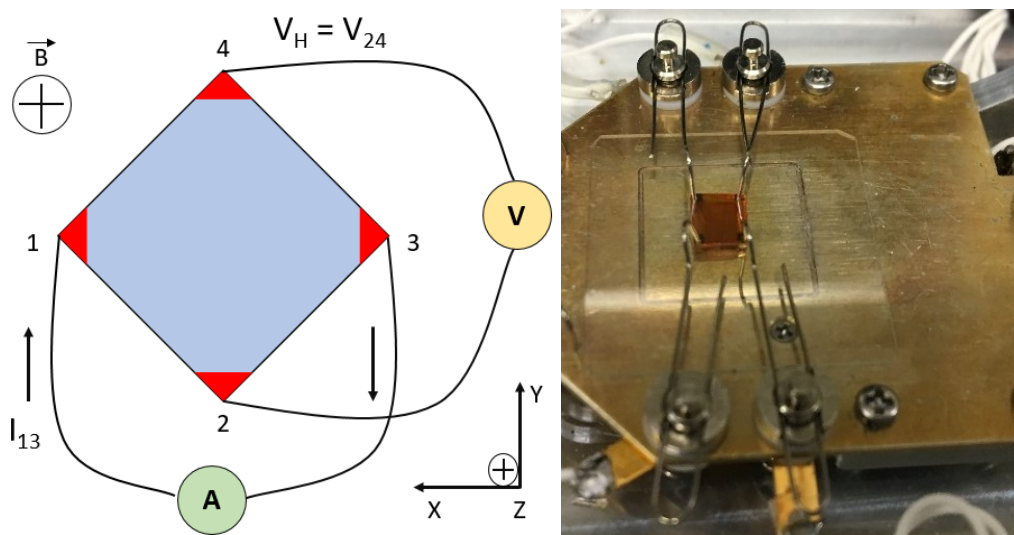


Figure II-25. Illustration of the Van Der Pauw configuration for Hall effect measurement.<sup>32</sup>

By also measuring  $I_{24}$  and  $V_{13}$ , an average value of carrier concentration and mobility can be obtained. Measurements in this study were conducted with a Nano Metrics model at room temperature by applying 0.5 T of magnetic field in such Van Der Pauw configuration. Due to the high resistivity of  $\text{Cu}_2\text{O}$  films, a current amplifier was applied for a better accuracy. To ensure an ohmic contact between the measured  $\text{Cu}_2\text{O}$  films and the Pt tips, gold contacts were evaporated on each corner on the  $0.5 \times 0.5 \text{ cm}^2$  square sample.

## II.4 References

1. S.Siveram. *Chemical Vapor Deposition-Thermal and plasma deposition of electroinic materials*. (Springer Science+Bussiness media, LLC, 1995).
2. Sénateur, J.-P., Dubourdieu, C., Weiss, F., Rosina, M. & Abrutis, A. Pulsed injection MOCVD of functional electronic oxides. *Adv. Mater. Opt. Electron.* **10**, 155–161 (2000).
3. A.V.Narlikar. *High temperature Superconductivity 1*. (Springer, 2004).
4. Marchand, P., Hassan, I. A., Parkin, I. P. & Carmalt, C. J. Aerosol-assisted delivery of precursors for chemical vapour deposition: expanding the scope of CVD for materials fabrication. *Dalton Trans.* **42**, 9406–22 (2013).
5. Hou, X. & Choy, K. L. Processing and Applications of Aerosol-Assisted Chemical Vapor Deposition. *Chem. Vap. Depos.* **12**, 583–596 (2006).
6. Liu, H., Battiato, S., Pellegrino, A. L., Paoli, P., Rossi, P., Jiménez, C., Malandrino, G. & Muñoz-Rojas, D. Deposition of metallic silver coatings by Aerosol Assisted MOCVD using two new silver  $\beta$ -diketonate adduct metalorganic precursors. *Dalt. Trans.* (2017). doi:10.1039/C7DT01647F
7. Bard, A. J. & Faulkner, L. R. *Electrochemical methods-fundamentals and applications*. (JOHN WILEY & SONS, INC, 2001).

8. Gadow, R. Development of Atmospheric Plasma Sprayed Dielectric Ceramic Coatings for High Efficiency Tubular Ozone Generators. *J. Water Resour. Prot.* **2**, 799–808 (2010).
9. Waterhouse, G. I. N., Bowmaker, G. A. & Metson, J. B. Oxidation of a polycrystalline silver foil by reaction with ozone. *Appl. Surf. Sci.* **183**, 191–204 (2001).
10. Waterhouse, G. I. N., Bowmaker, G. A. & Metson, J. B. Interaction of a polycrystalline silver powder with ozone. *Surf. Interface Anal.* **33**, 401–409 (2002).
11. Lindroos, S. & Leskelä, M. Successive Ionic Layer Adsorption and Reaction (SILAR) and Related Sequential Solution-Phase Deposition Techniques. *Solut. Process. Inorg. Mater.* 239–282 (2008). doi:10.1002/9780470407790.ch8
12. John R. Ferraro, K. N. & Brown, C. W. *Introductory Raman Spectroscopy. Introductory Raman Spectroscopy* (1994). doi:10.1016/B978-0-12-254105-6.50004-4
13. C., E., Ru, L. & Etchegoin, P. G. *Principles of Surface-Enhanced Raman Spectroscopy and related plasmonic effects*. (Elsevier, 2009).
14. Baker, M. J., Hussain, S. R., Lovergne, L., Untereiner, V., Hughes, C., Lukaszewski, R. A., Thiéfin, G. & Sockalingum, G. D. Developing and understanding biofluid vibrational spectroscopy: a critical review. *Chem. Soc. Rev.* **45**, 1803–1818 (2015).
15. B.K.Tanner, T.P.A.Hase, T.A.Lafford & M.S.Goorsky. Grazing Incidence in-plane X-Ray diffraction in the laboratory. *Int. Cent. Diffraction data 2004, Adv. X-ray Anal.* **47**, 1–7 (2004).
16. Márquez, J. A. R., Rodríguez, C. M. B., Herrera, C. M., Rosas, E. R., Angel, O. Z. & Pozos, O. T. Effect of Surface Morphology of ZnO Electrodeposited on Photocatalytic Oxidation of Methylene Blue Dye Part I: Analytical Study. *Int. J. Electrochem. Sci.* **6**, 4059–4069 (2011).
17. Patterson, A. L. The scherrer formula for X-ray particle size determination. *Phys. Rev.* **56**, 978–982 (1939).
18. Alexander, L. & Klug, H. P. Determination of crystallite size with the x-ray spectrometer. *J. Appl. Phys.* **21**, 137–142 (1950).
19. Monshi, A., Foroughi, M. R. & Monshi, M. R. Modified Scherrer equation to estimate more accurately nano-crystallite size using XRD. *World J. Nano Sci. Eng.* **2**, 154 (2012).
20. Linsmeier, C. Auger electron spectroscopy. *CAPCOAT* **45**, 673–690 (1994).
21. Wilkinson, A. J. & Britton, T. Ben. Strains, planes, and EBSD in materials science. *Mater. Today* **15**, 366–376 (2012).
22. Atomic Force Microscopy ( AFM ) - Basics and Technical Challenges of Combining Optical and Atomic Force Microscopy by Asylum Research. *Asylum Research* 1–17 (2009).
23. Ishizuka, K. & Shirota, K. Electron Microscopy. *Science* **62**, 9–13 (1996).
24. Viezbicke, B. D., Patel, S., Davis, B. E. & Birnie, D. P. Evaluation of the Tauc method for optical absorption edge determination: ZnO thin films as a model system. *Phys. Status Solidi* **252**, 1700–1710 (2015).
25. Davis, E. A. & Mott, N. F. Conduction in non-crystalline systems V. Conductivity, optical

- absorption and photoconductivity in amorphous semiconductors. *Philos. Mag.* **22**, 903–922 (1970).
26. Shore, K. A. *Electronic Processes in Non-crystalline Materials* (Second Edition), by N.F. Mott and E.A. Davis. *Contemp. Phys.* **55**, 337 (2014).
  27. F.M.SMITS. Measurements of Sheet Resistivity with the Four-Point Probe. *BSTJ* 371 (1958).
  28. Schroder, D. K. *Semiconductor Material and Device Characterization*. (John Wiley & Sons, New York, 1998).
  29. Putley, E. H. *he Hall Effect and Related Phenomena*. (Butterworths, London, 1960).
  30. Kinder, R., Mikolášek, M., Donoval, D., Kováč, J. & Tlaczala, M. Measurement system with Hall and a four point probes for characterization of semiconductors. *J. Electr. Eng.* **64**, 106–111 (2013).
  31. Green, R. Hall Effect Measurements in Materials Characterization. *Keithley White Pap.* **3111**, 1–11 (2011).
  32. Ellmer, K. Hall Effect and Conductivity Measurements in Semiconductor Crystals and Thin Films. in *Hall Effect and Conductivity Measurements in Semiconductor Crystals and Thin Films* (John Wiley & Sons, Inc., 2012). doi:10.1002/0471266965.com035.pub2



*Chapter 3. Thin film deposition of  
silver and silver oxide*

<i>Chapter III Thin film deposition of silver and silver oxides</i>	<i>- 66 -</i>
<i>III.1 Ag Precursor design, synthesis and characterization</i>	<i>- 67 -</i>
<i>III.1.1 Synthesis and characterization of new silver metalorganic precursor</i>	<i>- 69 -</i>
<i>III.1.2 XRD analysis and structure elucidation</i>	<i>- 71 -</i>
<i>III.1.3 New Ag metalorganic precursor molecular structures and characterizations</i>	<i>- 76 -</i>
<i>III.2 Deposition of silver coatings via MOCVD.</i>	<i>- 82 -</i>
<i>III.2.1 Ag coatings via PI-MOCVD.</i>	<i>- 83 -</i>
<i>III.2.2 Ag coatings by Aerosol Assisted MOCVD.</i>	<i>- 86 -</i>
<i>III.3 Oxidation of Ag coatings</i>	<i>- 93 -</i>
<i>III.3.1 Electrochemical oxidation of Ag coatings</i>	<i>- 93 -</i>
<i>III.3.2 Oxidation of Ag film by Oxygen Plasma</i>	<i>- 96 -</i>
<i>III.4 Chapter summary</i>	<i>- 99 -</i>
<i>III.5 Appendix</i>	<i>- 101 -</i>
<i>III.6 References</i>	<i>- 104 -</i>

In this chapter, first of all, the deposition of metallic silver films using different precursors in both PI-MOCVD and AA-MOCVD will be introduced. With commercialized silver precursors, a cheap cost silver precursor, silver acetate, has been firstly reported for MOCVD deposition. In addition, two brand new silver metal organic precursors, Ag(hfac)phenanthroline and Ag(hfac)triglyme, will be introduced. The deposition results from those precursors are characterized. Secondly, the process to obtain silver oxides films are also included in this part of work, two oxidation techniques are adopted and the results will be presented.

### *Chapter III Thin film deposition of silver and silver oxides*

Silver is a noble metal with unique physical properties including high conductivity and plasmonic, anti-bacterial and self-cleaning effects.<sup>1-3</sup> There are several techniques used for depositing Ag coatings, such as electroless plating, magnetron sputtering and sol gel, etc.<sup>4, 5,</sup>  
<sup>6</sup> In this work, given that the final objective was to deposit AgCuO<sub>2</sub> coatings by MOCVD,

the same method was used to optimize the deposition of Ag and silver oxides. As shown in the Chapter I, MOCVD is an industrially relevant technique for obtaining functional coatings, including metallic Ag coatings. Due to the noble nature of Ag, a high oxidation environment is required for further oxidation into silver oxide films. In this chapter, several types of silver precursors were tested including two newly designed silver metalorganic precursors. Ag depositions could be achieved with the commercially available and cost-efficient precursor silver acetate (AgAc), in specific MOCVD systems, and with the new metal organic precursors. Better quality and uniformity were achieved in both AA-MOCVD and PI-MOCVD when using the two new precursors. Finally, different approaches to oxidize silver films deposited by MOCVD are also detailed, including electrochemical oxidation and oxygen plasma treatment.

### **III.1 Ag Precursor design, synthesis and characterization**

As indicated in Chapter II, in MOCVD the process can be largely altered by the way in which precursors are designed and delivered. Thus, depending on how precursors are fed into the deposition chamber, MOCVD is classified into several branches: HW-MOCVD, CW-MOCVD, PI-MOCVD, AA-MOCVD, etc.<sup>7</sup> This big family of MOCVD systems also brings new challenges for the design of new silver precursors. In particular, AA-MOCVD is an interesting CVD approach since it operates at ambient pressure. For AA-MOCVD, alcohol solvents are preferred due to the concerns related to the use of other more hazardous solvents, thus precursors being soluble in alcohol solvents are desirable.<sup>8,9</sup> In the case of the currently known silver metalorganic precursors, solubility in alcohols is low since silver complex molecules tend to polymerize when dissolved in the solvent. This limits the number of available silver precursors suitable for AA-MOCVD systems. AgNO<sub>3</sub> has indeed been reported as precursor for Ag coatings using AA-MOCVD by Ponja et al. and also in a pulsed-spray-evaporation CVD system by N. Bahlawane et al.<sup>10,11</sup> But given the non-organometallic nature of AgNO<sub>3</sub>, the utilization of such precursor may be limited to some type of CVD reactors. In addition, the development of new organometallic Ag precursors is also interesting, for instance for application in ALD, where suitable Ag precursors are still needed, especially for thermal ALD<sup>12</sup>. As shown in Table III-1, the different silver metalorganic precursors reported to date were mostly used in conventional or PI-MOCVD systems. Few examples of ALD of Ag coatings have also been reported previously.<sup>13-16</sup> In the cases where AA-MOCVD was used, non-environmentally friendly solvents, such as THF and toluene, were used in combination with organometallic precursors.<sup>17-19</sup> Concerning the

design of Ag metalorganic precursors, previous works have introduced different systems, including  $\beta$ -diketonate adducts  $\text{Ag}(\text{hfac})(\text{L})^{20}$  or  $\text{Ag}(\text{fod})(\text{L})$ , where L were tertiary phosphines ( $\text{PPh}_3$ ), 2,5,8,11,14-pentaoxapentadecane or bis(trimethylsilyl)-acetylene) or carboxylates ( $\text{Ag}(\text{O}_2\text{C-L})$ ).<sup>19,21,22</sup> Apart from the low solubility of these precursors in alcohol solvents, other issues such as low volatility or the high toxicity of the ligands have been also reported.<sup>23, 16, 20</sup> In addition, some of the ligands are rather expensive, contributing to a higher price of the final Ag precursor. Thus, new silver precursors with less toxic ligands, good solubility in alcohol solvents and clean rapid decomposition, are still needed, ideally using less expensive ligands.

Table III-1. Reported silver metal organic precursors used in metalorganic CVD.

Metalorganic Precursor	CVD variant	Solvents	Deposition Temperature / °C	Ref
Ag(hfac)COD	Pulsed-spray-evaporation CVD	Ethanol, methanol, monoglyme	150-400	11
(hfac)Ag(BTMSA)	HW-CVD	none	~ 250	22
(hfac)Ag(SEt <sub>2</sub> )	AA-MOCVD	Toluene	n.a.	18
[Ag(O <sub>2</sub> CC <sub>3</sub> F <sub>7</sub> )(PPh <sub>3</sub> ) <sub>2</sub> ]	AA-MOCVD	THF	310	19
Ag(fod)(PEt <sub>3</sub> )	PI-MOCVD	None (Liquid precursor)	220	24
(hfac)Ag(VTES)	CW-CVD	None (Liquid precursor)	220	25
(tfac)AgP(OEt) <sub>3</sub>	CW-CVD	None (Liquid precursor)	180	23
(C <sub>2</sub> F <sub>5</sub> COO)Ag(PMe <sub>3</sub> )	HW-CVD	n.a.	200	21
Ag(hfac)(PPh <sub>3</sub> )	AA-MOCVD	THF	310	17
Ag(O <sub>2</sub> CtBu)(PMe <sub>3</sub> )	HW-CVD	n.a.	180	26
Silver carboxylates	PI-MOCVD	Mesitylene	300	27

**COD:** 1,5-cyclooctadiene; **H-hfac:** 1,1,1,5,5,5-hexafluoro-2,4-pentanedione; **H-tfac:** 1,1,1-trifluoro-2,4-pentanedione; **Hfod:** 6,6,7,7,8,8,8-heptafluoro-2,2-dimethyl-3,5-octanedione **BTMSA:** bis(trimethylsilyl)acetylene; **SEt<sub>2</sub>:** Ethyl sulphide; **VTES:** vinyltriethylsilane; **PEt<sub>3</sub>:** triethylphosphine; **P(OEt)<sub>3</sub>:** triethylphosphite; **PMe<sub>3</sub>:** Trimethylphosphine; **PPh<sub>3</sub>:** Triphenylphosphine; **O<sub>2</sub>CtBu:** 2,2,6,6-tetramethyl-3,5-heptanedionate

In this work, besides deposition tests performed with commercially available Ag precursors including AgAc, AgNO<sub>3</sub> and Ag(TMHD), two new silver metalorganic precursors were used. The new precursors were designed and synthesized thanks to a collaboration with the group of Prof. Graziella Malandrino's in the University of Catania, Sicily. The new precursors,

with general formula  $\text{Ag}(\text{hfac})\text{-L}$ , were synthesized using different ligands:  $[\text{Ag}(\text{hfac})(\text{phen})]$  (**AgP**, phen=1,10-phenanthroline) and  $[\text{Ag}(\text{triglyme})_2]^+[\text{Ag}(\text{hfac})_2]^-$  (**AgT**, triglyme = 2,5,8,11-tetraoxadodecane). In addition, all the ligands used in the new precursors, namely, Hhfac, triglyme and phenanthroline, are not very expensive, thus reducing the final precursor cost. The synthesis and characterization of these new silver complexes is described in the next sections, along with the results of their use as precursors for the deposition of Ag coatings via AA-MOCVD with alcohol solvents.

### III.1.1 Synthesis and characterization of new silver metalorganic precursor

**Starting materials:**  $\text{Ag}_2\text{O}$  (99%, Strem Chemicals), H-hfac (99%, Strem Chemicals), triglyme (99%, Sigma Aldrich), 1,10-phenanthroline (anhydrous 99%, Strem Chemicals), dichloromethane (99.8%, Sigma Aldrich), and n-pentane (99%, Sigma Aldrich) were used as received for the synthesis.

Synthesis of  $[\text{Ag}(\text{hfac})(\text{phen})]$  (**AgP**):

The synthesis was performed suspending 2.20 g of  $\text{Ag}_2\text{O}$  (9.49 mmol) in 50 ml of dichloromethane. 2.54 g of Phenanthroline (14.14 mmol) were then added to the suspension. After 10 min, 2.94 g of H-hfac (14.14 mmol) were added to the mixture, which was refluxed under stirring for 1 h as shown in Figure III-1. In order to ensure the full consumption of the ligand, excess silver oxide was added and the unreacted oxide was filtered off after the reaction. Lastly, yellow crystals were obtained after removal of the solvent upon evaporation. A pure crystalline solid was obtained after purification with small quantities of n-pentane, in which the adduct is insoluble, and then vacuum dried. The reaction yield was 72%. The melting point of the crude product was 158-164 °C (dec.) (760 Torr). Elemental analysis for **AgP** ( $\text{C}_{17}\text{H}_9\text{AgF}_6\text{N}_2\text{O}_2$ ): Calc: C, 41.23; H, 1.83; N, 5.66. Found: C, 41.35; H, 1.71; N, 5.78. The chemical reaction is shown in Equation III 20.

Synthesis of  $[\text{Ag}(\text{triglyme})_2]^+[\text{Ag}(\text{hfac})_2]^-$  (**AgT**):

The synthesis was conducted following a similar procedure to that used for **AgP** from  $\text{Ag}_2\text{O}$  (2.20 g, 9.49 mmol), triglyme (2.528 g, 14.14 mmol) and H-hfac (2.94 g, 14.14 mmol). Pure light yellow crystals were obtained after purification with n-pentane. The reaction yield was 82%. The melting point of the crude product was 62-65 °C (760 Torr). Elemental analysis for **AgT** ( $\text{C}_{26}\text{H}_{38}\text{Ag}_2\text{F}_{12}\text{O}_{12}$ ): Calc: C, 31.66; H, 3.88. Found: C, 31.52; H, 3.76. The reaction mechanism is shown in Equation III 21.

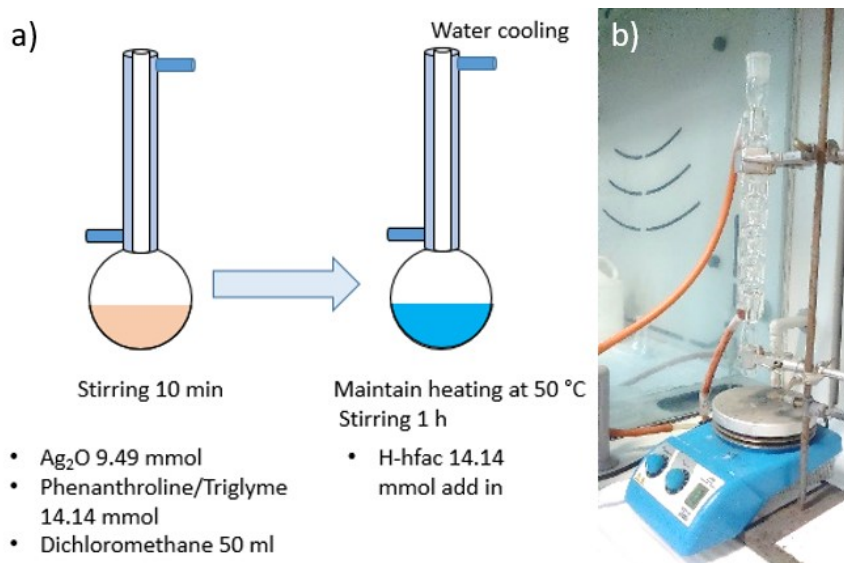
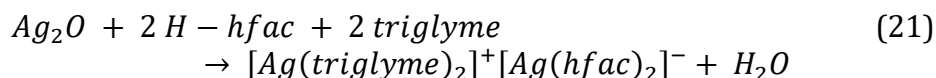
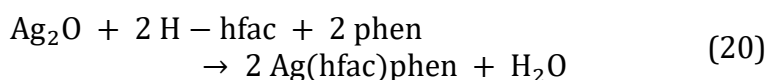


Figure III-1. Reflux system used for the synthesis of Ag metalorganic precursors.



Precursor characterizations:

Elemental microanalysis were performed using a Carlo Erba 1106 elemental analyzer. Fourier Transform Infrared Spectroscopy (FT-IR) was done using a Jasco FT/IR-430 spectrometer with nujol mulls between NaCl plates. <sup>1</sup>H NMR (400.13 MHz) and <sup>13</sup>C NMR (100.61 MHz) were acquired on a Bruker Avance™ 400 spectrometer. Chemical shifts (δ) are expressed in parts per million (ppm). Spectra were referenced to the residual proton solvent peaks; coupling constant (J) values are given in Hz. Thermogravimetric analyses were made using a Mettler Toledo TGA/SDTA 851e. Dynamic thermal analyses were carried out under purified nitrogen flow (30 sccm) at atmospheric pressure with a 5 °C/min heating rate. Weights of the samples were between 10-15 mg. Melting points were taken on very small single crystals using a Kofler hot-stage microscope.

Ag coating characterizations:

The Ag coatings were analysed using a Scanning Electron Microscope (SEM-FEG Environmental FEI QUANTA 250). Particle diameter distribution was calculated from SEM images using the Image J software.<sup>28</sup> The Ag coating were scratched for further

characterization with Transmission Electron Microscopy (TEM-JEM2010-JEOL). Carbon residues were analyzed with RAMAN Spectroscopy (Jobin Yvon/Horiba LabRam) equipped with a liquid nitrogen cooled charge coupled device detector.

### **III.1.2 XRD analysis and structure elucidation**

Through a collaboration with *Dr. Patrizia Rossi's* group from University of Florence, Italy, the molecular and crystal structures of **AgP** and **AgT** were studied by means of single crystal X-ray diffraction. Measurements were carried out with an Oxford Diffraction Excalibur diffractometer using the Cu-K $\alpha$  radiation ( $\lambda = 1.54184 \text{ \AA}$ ) for **AgP** and Mo-K $\alpha$  radiation ( $\lambda = 0.71073 \text{ \AA}$ ) for **AgT**. Data collection and data reductions were performed with the program CrysAlis Pro. Finally, absorption correction was performed with the program ABSPACK.<sup>29</sup> Structures were solved by using the SIR-2004 package<sup>30</sup> and subsequently refined on the  $F_2$  values by the full-matrix least-squares program SHELXL-2013.<sup>31</sup> Geometrical calculations were performed by PARST97<sup>32</sup> and molecular plots were produced by the program Mercury (v3.7).<sup>33</sup>

The crystal data and refinement parameters of the new Ag adducts are reported in Table III-2. Single crystals of **AgT** were twinned. Two domains were taken into account during refinement. The fluorine atoms bound to the carbon atom C5 (see Figure III-2 below) of the -hfac anion in **AgP** are disordered. Such disorder was modelled by introducing three positions for each fluorine atom (refined occupancy factors: 0.44, 0.41, 0.15). In **AgT** all the CF<sub>3</sub> moieties are disordered (see Figure III-3 below). Such a disorder was modelled by introducing two positions for each fluorine atom bonded to C4, C5 and C10 (with refined occupancy factors: 0.62/0.38 for the atoms bonded to C4; 0.83/0.17 for the atoms bonded to C5; 0.76/0.34 for the atoms bonded to C10). In addition all the atoms of the C4(F<sub>3</sub>) moiety were set in double position (refined occupancy factors: 0.55/0.45). For all the non-hydrogen atoms in **AgP** and **AgT**, anisotropic thermal parameters were used. For the hydrogen atoms in **AgP**, they were found in the Fourier difference map and their positions were freely refined, while their thermal parameters were refined accordingly to the bound atoms. The hydrogen atoms in **AgT** were introduced in calculated position and refined in agreement with the carbon atom to which they are bound.

Table III-2. Single crystal crystallographic data and refinement parameters for AgP and AgT.

	AgP	AgT
Chemical formula	[Ag(hfa)(phen)]	[Ag(triglyme) <sub>2</sub> ] <sup>+</sup> [Ag(hfa) <sub>2</sub> ]
Empirical formula	C <sub>17</sub> H <sub>9</sub> AgF <sub>6</sub> N <sub>2</sub> O <sub>2</sub>	C <sub>26</sub> H <sub>38</sub> Ag <sub>2</sub> F <sub>12</sub> O <sub>12</sub>
Formula weight	495.13	986.30
Temperature (K)	100	250
Wavelength (Å)	1.54184	0.71073
Crystal system, space group	Triclinic, P-1	Triclinic, P-1
Unit cell dimensions (Å, °)	$a = 7.4309(3)$ $b = 9.2288(4)$ $c = 13.1426(6)$ $\alpha = 102.579(4)$ $\beta = 105.172(4)$ $\gamma = 103.608(4)$	$a = 11.4965(6)$ $b = 12.9561(7)$ $c = 13.0344(9)$ $\alpha = 96.821(5)$ $\beta = 91.795(5)$ $\gamma = 92.350(4)$
Volume (Å <sup>3</sup> )	807.10(6)	1924.8(2)
Z, D <sub>c</sub> (mg/cm <sup>3</sup> )	2, 2.037	2, 1.702
$\mu$ (mm <sup>-1</sup> )	10.823	1.127
F(000)	484	984
Crystal size (mm)	0.30x0.27x0.20	0.28x0.25x0.19
$\theta$ range (°)	5.165 to 72.336	4.111 to 29.400
Reflections collected / unique	8748 / 3045	13020 / 7438
Data / parameters	3045 / 295	7438 / 519
Goodness-of-fit on F <sup>2</sup>	1.115	1.061
Final R indices [ $I > 2\sigma(I)$ ]	R1 = 0.0407, wR2 = 0.0934	R1 = 0.0637, wR2 = 0.1714
R indices (all data)	R1 = 0.0565, wR2 = 0.1169	R1 = 0.0876, wR2 = 0.1942

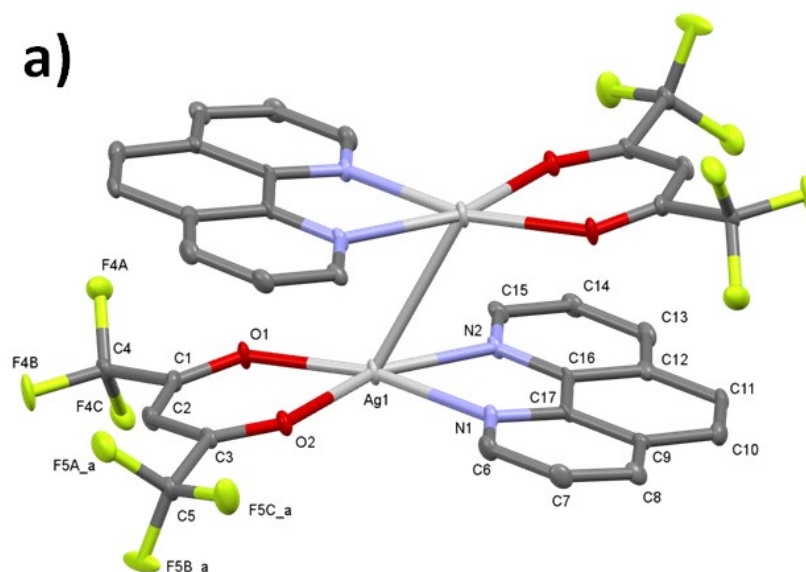


Table III-3. Selected bond distances (Å) and bond angles (°) for AgP and AgT.

AgP		Bond Angles (°)	
		N(1)-Ag-N(2)	71.4(2)
Bond distances (Å)		O(1)-Ag-O(2)	79.4(1)
Ag-N(1)	2.369(6)	N(1)-Ag-O(1)	165.4(2)
Ag-N(2)	2.327(4)	N(2)-Ag-O(2)	158.8(1)
Ag-O(1)	2.276(5)	N(1)-Ag-O(2)	87.6(2)
Ag-O(2)	2.439(3)	N(2)-Ag-O(1)	121.1(2)
AgT		Bond Angles (°)	
Bond Distance (Å)		O(5)-Ag(1)-O(10)	76.0(2)
Ag(1)-O(1)	2.329(5)	O(5)-Ag(1)-O(11)	95.5(2)
Ag(1)-O(2)	2.275(5)	O(5)-Ag(1)-O(12)	85.7(2)
Ag(1)-O(3)	2.340(5)	O(6)-Ag(1)-O(7)	64.0(2)
Ag(1)-O(4)	2.261(4)	O(6)-Ag(1)-O(8)	125.1(2)
Ag(2)-O(5)	2.662(6)	O(6)-Ag(1)-O(9)	82.8(2)
Ag(2)-O(6)	2.626(8)	O(6)-Ag(1)-O(10)	130.0(2)
Ag(2)-O(7)	2.618(7)	O(6)-Ag(1)-O(11)	145.5(2)
Ag(2)-O(8)	2.792(7)	O(6)-Ag(1)-O(12)	84.8(3)
Ag(2)-O(9)	2.550(6)	O(7)-Ag(1)-O(8)	62.7(2)
Ag(2)-O(10)	2.661(7)	O(7)-Ag(1)-O(9)	81.0(2)
Ag(2)-O(11)	2.568(8)	O(7)-Ag(1)-O(10)	138.4(2)
Ag(2)-O(12)	2.559(8)	O(7)-Ag(1)-O(11)	133.7(2)
Bond Angles (°)		O(7)-Ag(1)-O(12)	96.8(2)
O(1)-Ag(1)-O(2)	79.8(2)	O(8)-Ag(1)-O(9)	100.9(2)
O(1)-Ag(1)-O(3)	111.1(2)	O(8)-Ag(1)-O(10)	99.1(2)
O(1)-Ag(1)-O(4)	127.3(2)	O(8)-Ag(1)-O(11)	74.0(2)
O(2)-Ag(1)-O(3)	125.6(2)	O(8)-Ag(1)-O(12)	89.1(1)
O(2)-Ag(1)-O(4)	135.7(2)	O(9)-Ag(1)-O(10)	65.4(2)
O(3)-Ag(1)-O(4)	81.0(2)	O(9)-Ag(1)-O(11)	124.9(2)
O(5)-Ag(1)-O(6)	63.6(2)	O(9)-Ag(1)-O(12)	167.1(3)
O(5)-Ag(1)-O(7)	127.0(2)	O(10)-Ag(1)-O(11)	61.7(2)
O(5)-Ag(1)-O(8)	169.5(2)	O(10)-Ag(1)-O(12)	121.3(2)
O(5)-Ag(1)-O(9)	85.6(2)	O(11)-Ag(1)-O(12)	65.5(3)

The solid state molecular structure of AgP consists of dimers made up of two silver complexes related by an inversion center (-x+1, -y, -z+2), shown in Figure III-2 a). In each complex the silver ion is bound to the oxygen and nitrogen atoms provided by the -hfac and -phen ligands, respectively. The coordination sphere is a slightly distorted square planar (as provided by the angle between the AgO<sub>2</sub> and AgN<sub>2</sub> planes, 7.2(2)°, and the small displacement of the silver ion with respect to the four donor atoms, 0.1110(5) Å). Even if quite uncommon<sup>34</sup>, this kind of geometry has been observed in similar Ag(I) complexes.<sup>35,36</sup>

Bond distances and angles are within the expected range for this kind of compounds (Table III-3).<sup>37</sup> Additionally, as already found in other [Ag(hfac)-L] complexes,<sup>36,38</sup> the Ag-O bond distances are significantly different, Ag(1)-O(1) = 2.276(5) vs Ag(1)-O(2) = 2.439(3). The distance separating the two metal centres (3.0843(7) Å) is definitely longer than the silver-silver one in the metal (2.888 Å).<sup>39</sup> As a consequence, the two metal ions do not interact significantly.<sup>38,40</sup> However, given the fact that there are no bridging ligands holding together the dimer, a weak stabilizing interaction between the metal ions might be postulated.<sup>41</sup> In addition, intra-dimer  $\pi$  stacking appeared between the -hfac and -phen rings (the distances separating the centroids (CT), centroid of the hfa ring as defined by O(1)C(2)C(1)C(3)O(2), centroid of the central ring of phen as defined by C(9)C(10)C(11)C(12)C(16)C(17), is 3.60(1)Å) and the angle between the CT-CT line and the mean phen plane is 71.2(2)°. Finally, the dimers stack along the a axis in a head-to-tail arrangement (Figure III-2 b), which brings the carbon atom C(10) of a symmetry related (-x, -y, 2-z) phen molecule 3.350(8) Å apart from the silver ion, with a distance less than the sum of the Van der Waals radii (3.81 Å)<sup>42</sup>. In addition, inter-dimer  $\pi$  stacking interactions involving the phen molecules provided by two contiguous dimers are present (the mean phen planes are 3.5 Å apart). Finally, dimers propagate along the b axis (Figure III-2 c) through a weak C(7)H(7)...O(1)' intermolecular interaction (' =x, 1+y, z; D...A and H...A distances 3.628(6) and 2.75(6) Å, respectively, DHA angle 161(6)°). The check CIF reports of both precursors submitted to Cambridge structure data center are presented in the Appendix at the end of the chapter.



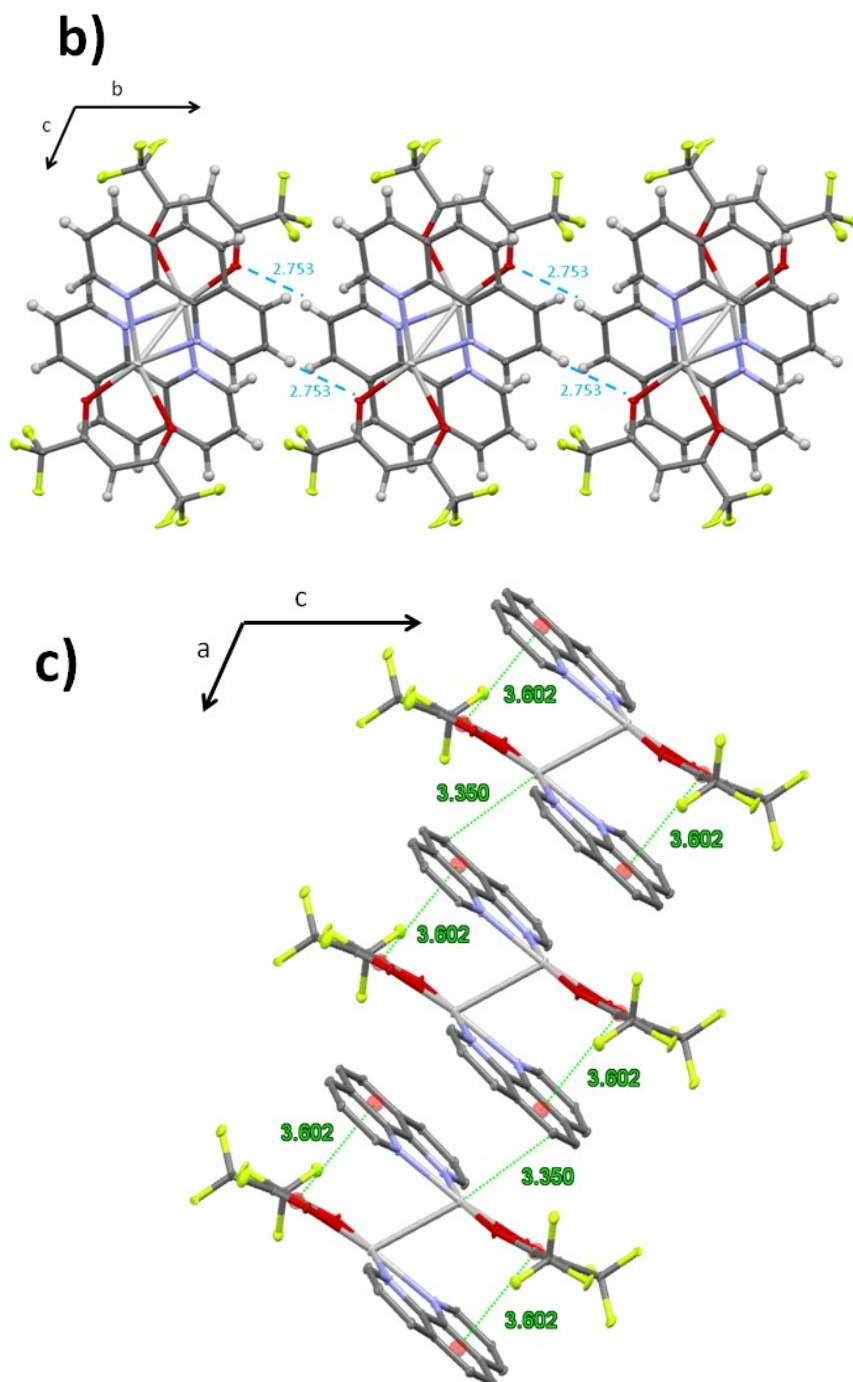


Figure III-2. a) Ellipsoid representation of the dimer found in the solid state structure of **AgP** (hydrogen atoms have been omitted for sake of clarity, for the same reason just one model of the disordered CF<sub>3</sub> moiety was shown). b) along the b axis direction showing the intra- and inter-dimer  $\pi$ -stacking interactions. Hydrogen atoms were omitted (top); c) along the a axis direction showing the CH...O intermolecular interactions. For the sake of clarity just one model of the -hfac fluorine atoms bound to C<sub>5</sub>.

The solid state structure of compound AgT was also determined by means of single crystal X-ray diffraction. In the asymmetric unit of AgT one [Ag(triglyme)<sub>2</sub>]<sup>+</sup> cation and one [Ag(hfac)<sub>2</sub>]<sup>-</sup> anion are present (Figure III-3). In the two ions, the silver atom shows different coordination spheres. In fact, in the [Ag(triglyme)<sub>2</sub>]<sup>+</sup> cation, the silver atom Ag(2) is

surrounded by two triglyme molecules and bound to all the eight oxygen atoms that those ligands provide. It is worth noting that, although one Ag-O distance [i.e. Ag(1)-O(8)] is longer than the others (see Table III-3), it is inside the Ag-O range as retrieved in the Cambridge Structural Database (CSD v. 5.37).<sup>43</sup> The two triglyme molecules are almost perpendicular to each other, the angle between the mean planes defined by the non-hydrogen atoms of the two molecules being 85.4(1)°. Finally the resulting coordination polyhedron could be described as a distorted dodecahedron.

Concerning the [Ag(hfac)<sub>2</sub>]<sup>-</sup> anion, the silver atom Ag(1) is four-coordinated by the oxygen atoms of two -hfac anions in a resulting pseudo-tetrahedral arrangement. This coordination arrangement resembles well that already found in the similar silver complex [[Ag(hmten)][Ag(hfac)<sub>2</sub>]; hmten = hexamethyl-triethylene tetra-amine].<sup>44</sup> The two -hfac anions lay in two planes nearly perpendicular to each other (the angle between the two mean planes defined by O(1), O(2), C(1), C(2), C(3) and O(3), O(4), C(6), C(7), C(8) is 84.8(2)°. Finally, no relevant intermolecular interactions are present in the crystal packing of AgT.

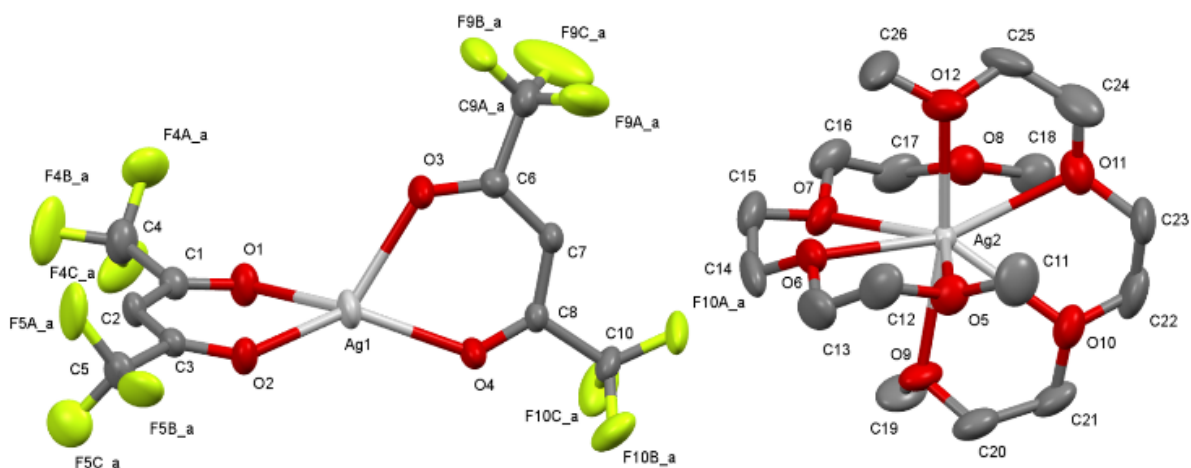


Figure III-3. View of the [Ag(triglyme)<sub>2</sub>]<sup>+</sup> cation and [Ag(hfac)<sub>2</sub>]<sup>-</sup> anion in AgT (ellipsoids are drawn at 30% probability). For the sake of clarity, just one model of all the -hfac fluorine atoms (which were disordered and refined isotropically) is shown. For the same reason the hydrogen atoms are not shown in the image.

### III.1.3 New Ag metalorganic precursor molecular structures and characterizations

In both cases, the synthesis was reproducible and yielded an anhydrous product. Adducts were soluble in dichloromethane and could be isolated as yellow crystalline powders by removal of the solvent. The silver precursors were characterized by FT-IR spectroscopy in the wave number range of 4000-500 cm<sup>-1</sup>. The results for AgP and AgT are shown in Figure

III-4 a) and b) respectively. In both cases, the FT-IR spectra do not show bands in the 3300–3600  $\text{cm}^{-1}$  interval, which indicates the absence of water coordinated to the silver cation. Peaks at 2923, 1461, and 1375  $\text{cm}^{-1}$  are associated with the nujol used to prepare the mull. In both silver complexes, the  $\beta$ -diketonate ligand can be evidenced by the presence of the C=O stretching at 1658  $\text{cm}^{-1}$ , while the C=C stretching vibration is associated with the absorptions at 1500-1550  $\text{cm}^{-1}$ .

In addition, the bands present in the interval 1050-1400  $\text{cm}^{-1}$  can be attributed to typical C-F vibrations of the -hfac ligand present in both adducts. For **AgP**, the bands observed in the 700–1100  $\text{cm}^{-1}$  range are considered fingerprints of the phenanthroline coordination to silver ion. In **AgT**, the broad band observed in the 1000-1300  $\text{cm}^{-1}$  range might be associated with absorptions from polyether C-O bending and/or stretching overlapped with the C-F stretching of the  $\beta$ -diketonate. Furthermore, bands at 700-1100  $\text{cm}^{-1}$  are related with glyme modes. The C-H glyme stretching modes, lying in the 2800-3000  $\text{cm}^{-1}$  range, overlap with nujol features.

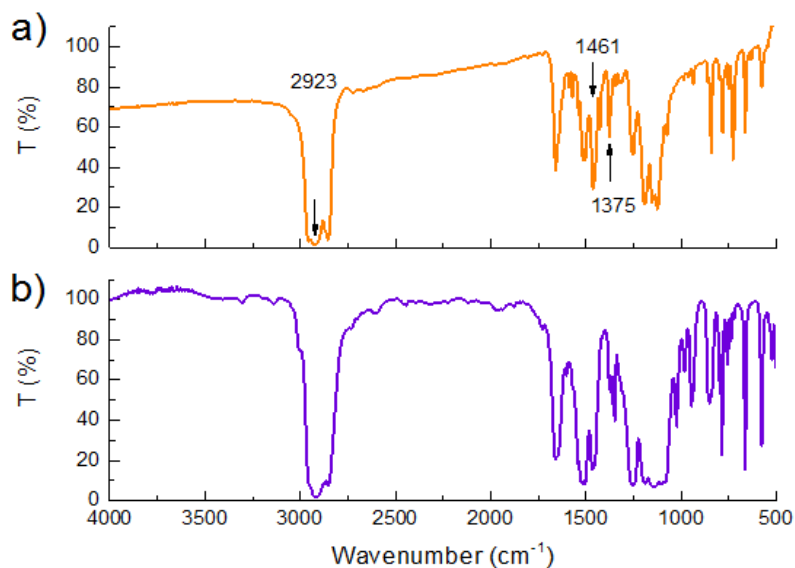


Figure III-4. FT-IR spectra of **AgP** a) and **AgT** b) in nujol (peaks from nujol marked with arrows).

$^1\text{H}$  and  $^{13}\text{C}$  NMR of **AgP** and **AgT** were recorded in  $\text{CDCl}_3$  (Table III-4). The  $^1\text{H}$  NMR spectrum of **AgP** (Figure III-5) has been attributed in accordance to the assignments of references.<sup>45,46</sup> The spectrum shows a singlet (5.79  $\delta$ ) associated with the ring proton of the hfa ligand, while the phenanthroline shows peaks in the typical range of aromatic ligand from 7.6 to 9.1  $\delta$ . The **a** protons are observed as a singlet at 9.04  $\delta$ , the **b** proton as a multiplet at 7.79  $\delta$ , the **c** protons as a doublet of doublets at 8.40  $\delta$  and, finally, the **e** protons as a doublet at 7.89  $\delta$ . The phen peaks have been assigned following the notation reported as a

note in Table III-4. The 1:1 (hfa:phen) ratio found through evaluation of intensities of pertinent resonances finds counterpart in the ratio obtained through single crystal X-ray diffraction, as shown in Figure III-5.

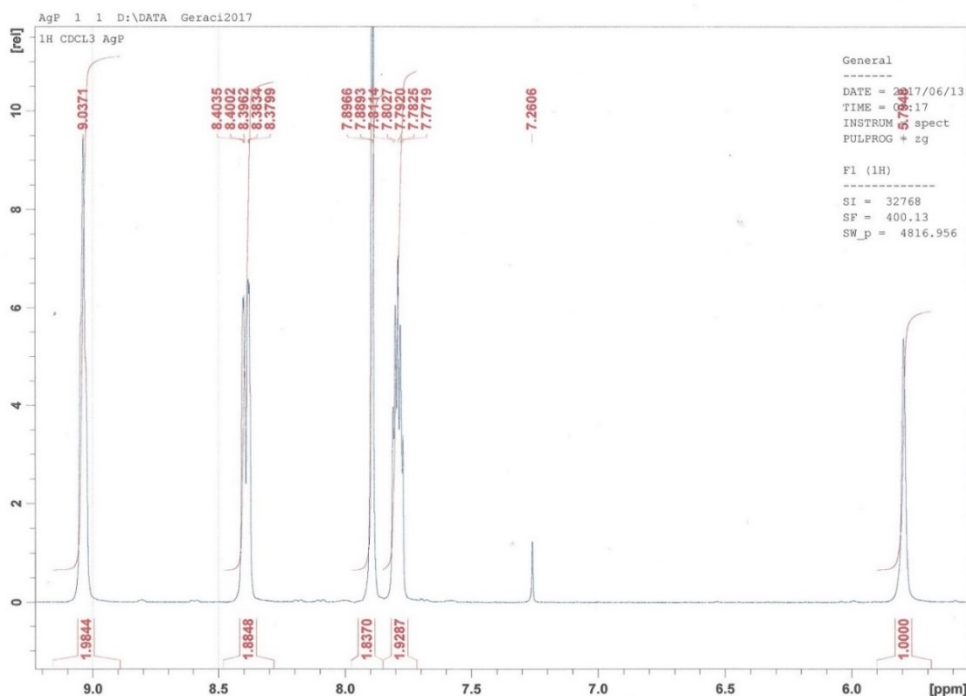


Figure III-5.  $^1\text{H}$  NMR spectrum of AgP in  $\text{CDCl}_3$ .

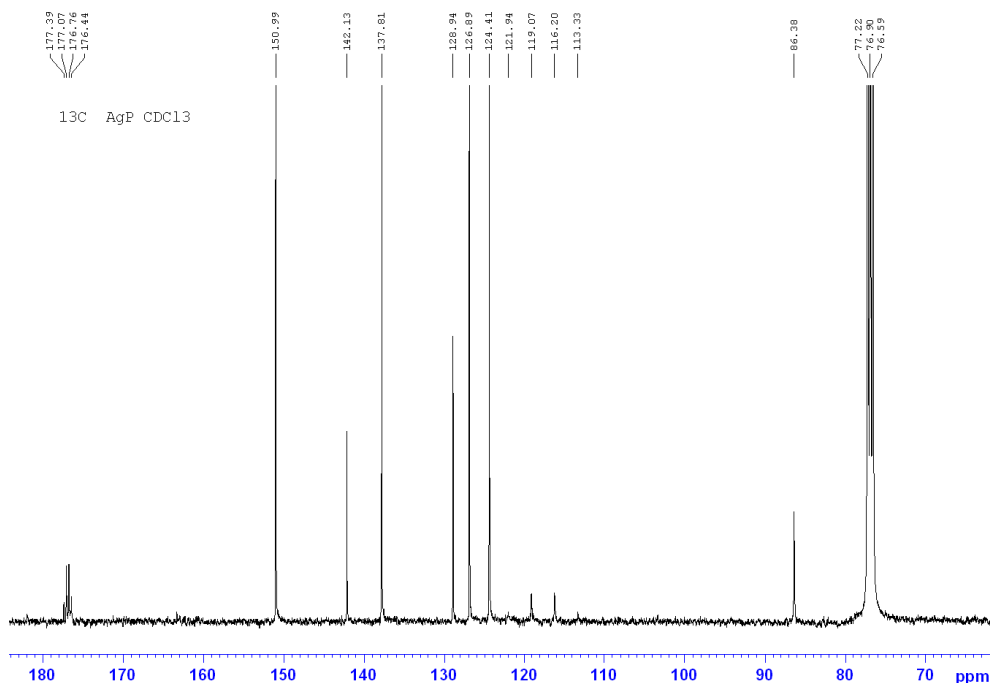


Figure III-6.  $^{13}\text{C}$  NMR spectrum of AgP in  $\text{CDCl}_3$ .

In Figure III-6, the  $^{13}\text{C}$  NMR spectrum of AgP shows resonances associated with the coordinated hfa ligand, which consist of a singlet ( $\delta \approx 86$ ) for the CH group, quartets ( $\delta \approx 118$ )

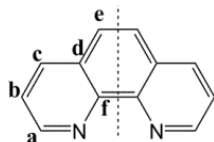
for the  $\text{CF}_3$  groups and quartets ( $\delta \approx 177$ ) for the CO groups. The quartets are due to first order ( $\text{CF}_3$ ;  $^1J = 288$  Hz) and second order (CO;  $^2J = 32$  Hz) coupling with the  $\text{CF}_3$  fluorine atoms. The coordinated phenanthroline signals are observed in the range of 127-152  $\delta$ . Assignments are reported in the Table III-4 together with the notation used for phenanthroline.

The  $^1\text{H}$  NMR spectrum of **AgT** (Table III-4) can be assigned using comparative arguments with data from the related lanthanum complex.<sup>31</sup> In Figure III-7, the spectrum shows a singlet at 5.81  $\delta$  associated with the ring proton of the hfa ligand. Different resonances are associated with the triglyme framework. The methyl groups (**a** protons) are always observed as a singlet at  $\delta = 3.60$ . The **b** and **c** protons are observed as a multiplet centered at  $\delta = 3.62$ . The protons **d** are associated with a singlet at  $\delta = 3.71$ . Evaluation of intensities of pertinent resonances points to a 1:1 (hfa: triglyme) ratio in accordance with single crystal X-ray diffraction.

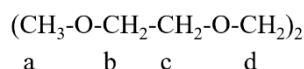
Table III-4.  $^1\text{H}$  and  $^{13}\text{C}$  NMR of **AgP** and **AgT**.

complex	$^1\text{H}$ NMR		$^{13}\text{C}$ NMR			
	-CO-CH-CO	Phen*	-CO-CH-CO	-CO-CH-CO	-CF <sub>3</sub>	Phen*
AgP	5.79 (s, 1H)	<b>a</b> 9.04 (s, 2H), <b>b</b> 7.79 (m, 2H), <b>c</b> 8.40 (dd, 2H) <b>e</b> 7.89 (d, 2H)	86.38 (s)	176.91 (q, $^2J=32\text{Hz}$ )	117.63(q, $^1J=288$ Hz)	<b>a</b> 150.99, <b>b</b> 124.40, <b>c</b> 137.81, <b>d</b> 128.94, <b>e</b> 126.89, <b>f</b> 142.13
complex	$^1\text{H}$ NMR		$^{13}\text{C}$ NMR			
	-CO-CH-CO	polyether <sup>†</sup>	-CO-CH-CO	-CO-CH-CO	-CF <sub>3</sub>	polyether <sup>†</sup>
AgT	5.81 (s, 1H)	<b>a</b> 3.60 (s, 6H), <b>b, c</b> 3.62 (m, 8H), <b>d</b> 3.71 (s, 4H)	86.12 (s)	176.84 (q, $^2J=32\text{Hz}$ )	117.56 (q, $^1J=289$ Hz)	<b>a</b> 61.21, <b>b</b> 70.11, <b>c</b> 70.58, <b>d</b> 71.42

\* The notation has been used for phenanthroline:



<sup>†</sup> The notation has been used for triglyme:



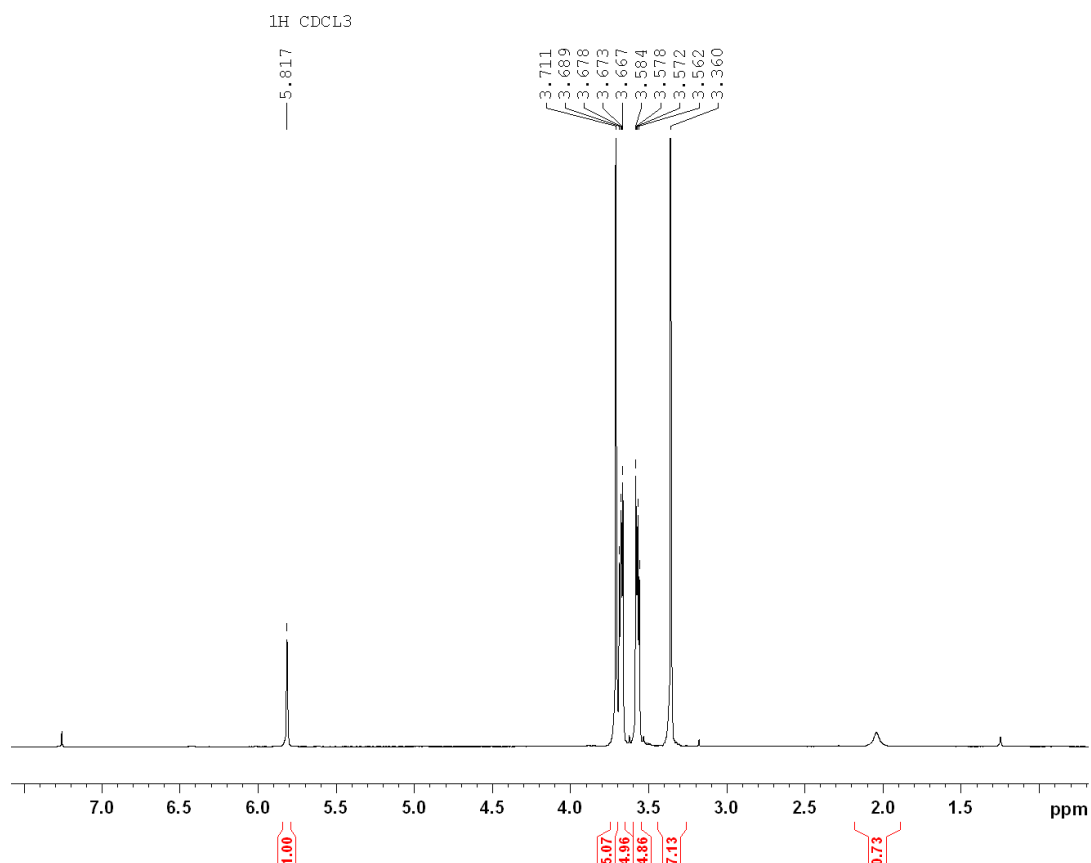


Figure III-7. <sup>1</sup>H NMR spectrum of AgT in CDCl<sub>3</sub>.

In Figure III-8, the <sup>13</sup>C NMR spectrum of AgT is similar to that found for the AgP adduct in regard to the hfa ligand. Resonances associated with the coordinated hfa ligand consist of a singlet ( $\delta \approx 86$ ) for the CH group, a quartet ( $\delta \approx 117$ ) for the CF<sub>3</sub> groups and a quartet ( $\delta \approx 177$ ) for the CO groups. The quartets are due to first order (CF<sub>3</sub>; <sup>1</sup>J = 289 Hz) and second order (CO; <sup>2</sup>J = 32 Hz) coupling with the CF<sub>3</sub> fluorine atoms. The coordinated triglyme signals are observed at  $\delta$  61.21 (s, OCH<sub>3</sub>, **a**),  $\delta$  70.11 (s, OCH<sub>2</sub>, **b**),  $\delta$  70.58 (s, OCH<sub>2</sub>, **c**) and  $\delta$  71.42 (s, OCH<sub>2</sub>, **d**).



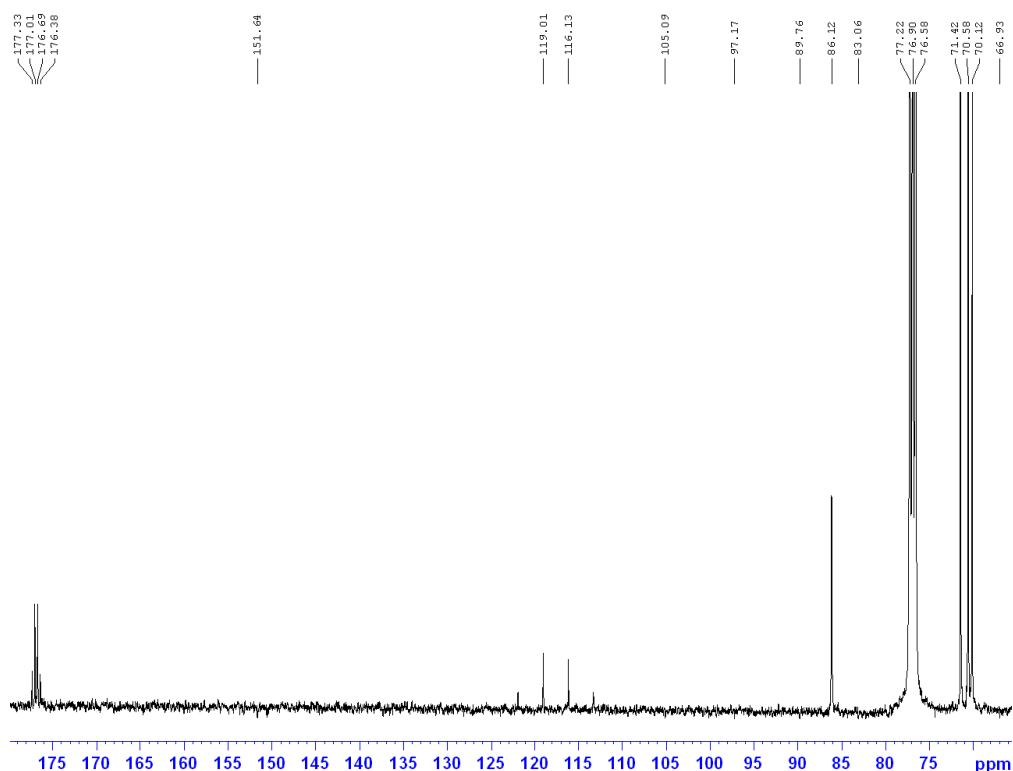


Figure III-8.  $^{13}\text{C}$  NMR spectrum of AgT in  $\text{CDCl}_3$ .

The thermal characteristics of the present adducts were evaluated by Thermogravimetric Analysis (TGA). The TGA profile of AgP (Figure III-9 a) presents a two-step weight loss (as clearly shown in the derivative curve), in the range 190-230 °C and 230 - 280 °C, respectively, with a residue of 37% up to 400 °C. This value does not match the stoichiometric Ag weight % in the precursor, namely, 21.8%.

Thus it can be concluded that the precursor does not present a clean decomposition, with some organic species still remaining at 400 °C. Conversely, the TGA curve related to AgT (Figure III-9 b) shows a single (see derivative) rapid weight loss in the range 150 - 250 °C, yielding a 22.5% residue when heating to 400 °C. The stoichiometric Ag weight portion in the precursor being 21.9%, the value obtained from TGA is thus well tuned with the expected percentage of metallic silver in the compound, implying a clean and complete decomposition of the precursor. By comparing the TGA results for those two precursors, AgT appears as a better silver metalorganic precursor.

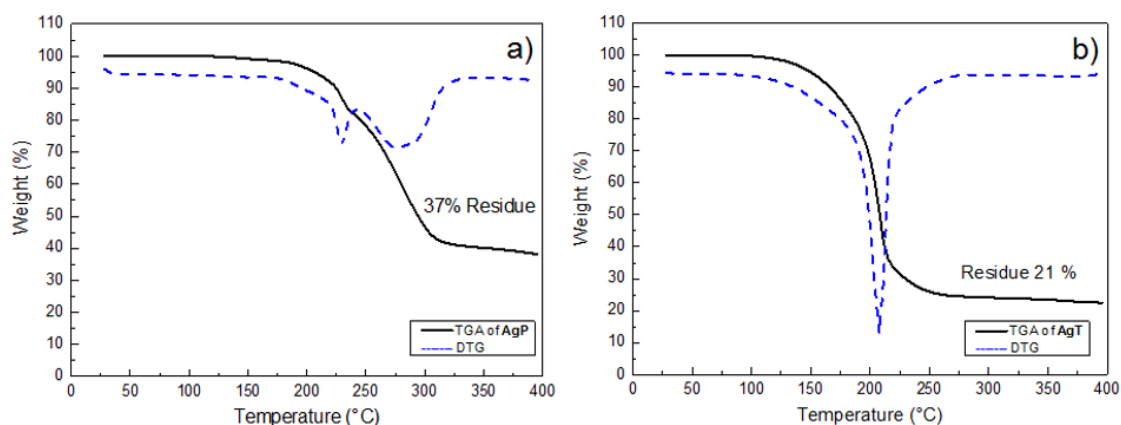


Figure III-9. Thermogravimetric Analysis (TGA) and its derivative curves (DTG) of precursors, between 30 °C and 400 °C, of a) AgP and b) AgT. TGA was conducted under N<sub>2</sub> atmosphere with heating rate 5 °C/min.

### III.2 Deposition of silver coatings via MOCVD .

In order to deposit Ag coatings by MOCVD, different types of silver precursors were tested in both PI-MOCVD and AA-MOCVD. The summary of the deposition conditions is shown in Table III-5. In this work 5 different types of Ag precursors were tested, including 3 precursor commercially available and two newly synthesized as previously described. All the precursors were tested in both MOCVD systems.

Table III-5. Ag coating deposition conditions and results summary.

Precursors tested	AgNO <sub>3</sub>	AgAc	Ag(TMHD)	AgP	AgT
tested deposition temperature (°C)	300 - 450	250 - 400	250 - 400	250 - 350	250 - 350
Need dispersant ? (In alcohol solvents)	N	Y	Y	N	N
Deposition of Ag in PI-MOCVD ?	N	Y	N	Y	Y
Deposition of Ag in AA-MOCVD ?	N	Y	N	Y	Y

Even though Ag coating deposited using AgNO<sub>3</sub> has been reported in previous works by N. Bahlawane *et al.*<sup>11</sup> and S.D.Ponja *et al.*<sup>10</sup>, in this work we were not able to obtain Ag coatings from AgNO<sub>3</sub>. For Ag(TMHD), different types of solvents were tested including M-Xylene, Toluene, butanol-01 and ethanol. With deposition temperatures between 250 and 400 °C, no Ag coating was obtained. Thus, only results of Ag coatings by **AgAc**, **AgP** and **AgT** are discussed here.

### III.2.1 Ag coatings via PI-MOCVD.

First of all, PI-MOCVD was used since less precursor solution is needed. Our PI-MOCVD reactor has been introduced in Chapter II. All the Ag precursors listed in Table III-5 have been tested. Only **AgAc**, **AgP** and **AgT** yielded Ag coatings. In this section, the results of Ag coatings deposited with the three types of Ag precursors are given.

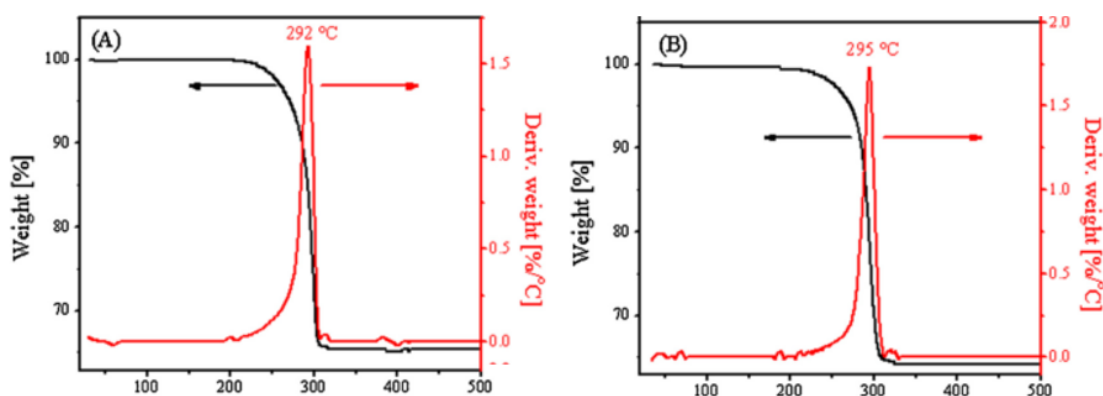
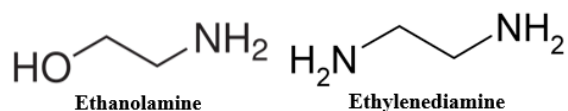


Figure III-10. TGA and DGA of **AgAc** in a) nitrogen and b) air atmosphere with heating speed 20 °C/min.<sup>47</sup>

Among all the Ag precursors, **AgAc** is reported for the first time in this work as a metal organic precursor for MOCVD deposition of Ag coatings. The thermal properties of **AgAc** have been investigated in the work of BM. Abu-Zied *et al.*<sup>47</sup> As shown in Figure III-10, **AgAc** decomposes rapidly at about 295 °C in both nitrogen and air atmosphere with a heating speed of 20 °C/min. In order to dissolve **AgAc** in alcohol solvent such as ethanol, two dispersants can be used, namely, ethylenediamine and ethanolamine (as introduced in the Chapter II).<sup>48,49</sup> We used solutions prepared with each of the dispersants. While no Ag coatings can be obtained with ethylenediamine, solutions containing ethanolamine yielded Ag coatings using similar conditions 320 °C). The hypothetical mechanism behind this different behavior is shown in Figure III-11.

As it's well known, for ammine complex there are normally 2 coordination numbers for the silver ion and they present a linear coordination (angle between N-Ag-N is 180 °).<sup>50</sup> Meanwhile, the molecule structures of the two dispersants are rather similar, except that in ethylenediamine, two ammine groups are presented at each end of the molecule while in ethanolamine, only one ammine group is present on one side of the molecule, as shown below:



When the silver acetate is mixed with the alcohol solvent, the molecule itself is difficult to be dissolved. By adding ethanolamine into the mixture, the silver precursor ammine complex is formed. As illustrated in Figure III-11 a), 1 mol of AgAc can coordinate with 2 mol of ethanolamine, thus the precursor molecule can be easily dissolved in the alcohol solvent and form a clear solution. On the other hand, with ethylenediamine added instead, due to the double ammine group, several AgAc molecules can possibly form larger linear structure as presented in Figure III-11 b).<sup>49,51</sup> Thus, with ethanolamine the silver precursor ammine complex is generally lighter and possibly more volatile than the linear complex formed with ethylenediamine. The lighter ammine complex could facilitate the precursor transport during deposition in the PI-MOCVD system, which could explain the Ag coatings using AgAc as precursor adding ethanolamine as dispersant but no deposition with ethylenediamine.

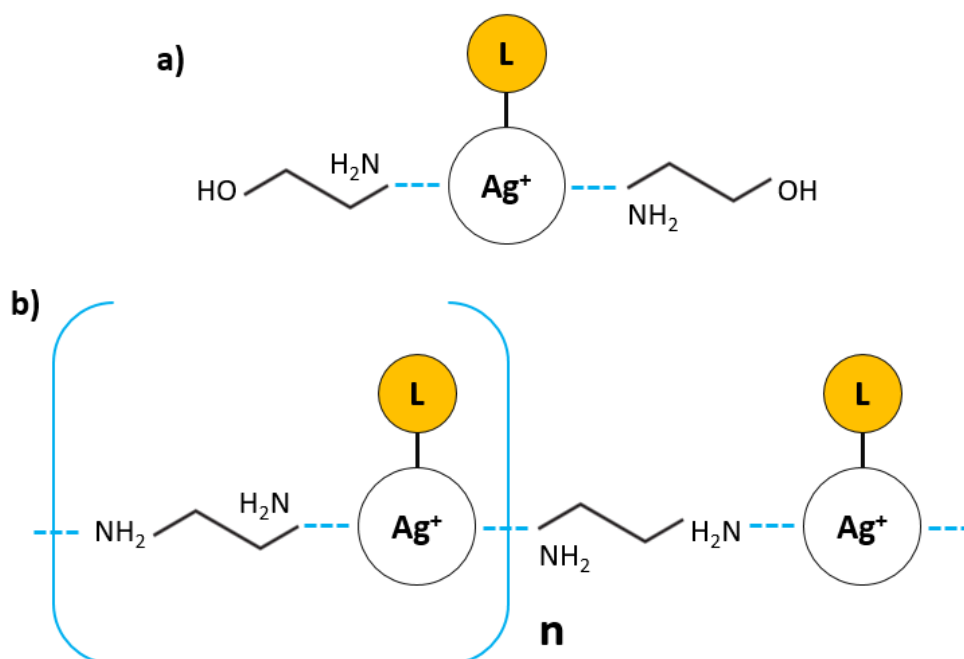


Figure III-11. Illustration of silver precursor complex group formed with a) ethanolamine, forming single silver precursor molecule containing structure, and b) with ethylenediamine, creating linear chain like complex with multiple silver precursor molecules included. "L" represents ligand in precursor.

The depositions of Ag coating using AgAc as precursor were carried out at a pressure of 0.1 mbar and at 330 °C on cleaned glass substrates. With ethanolamine as the dispersant, AgAc is able to give Ag coatings with 500 injected droplets (about 12 ml) and the SEM images of the Ag coatings with different flow rates are shown in Figure III-12. The circular shape of depositions is typically the sign of incomplete vaporization of the precursor or the precursor solution, which could be due to the low volatility of the AgAc precursor. With less carrier gas flow rate during the deposition, the size of grains in Ag coatings tends to decrease from

a) 2 L/min, b) 1 L/min to c) 0.5 L/min. The films present a dark purple color and high resistance since the coatings are not continuous films.

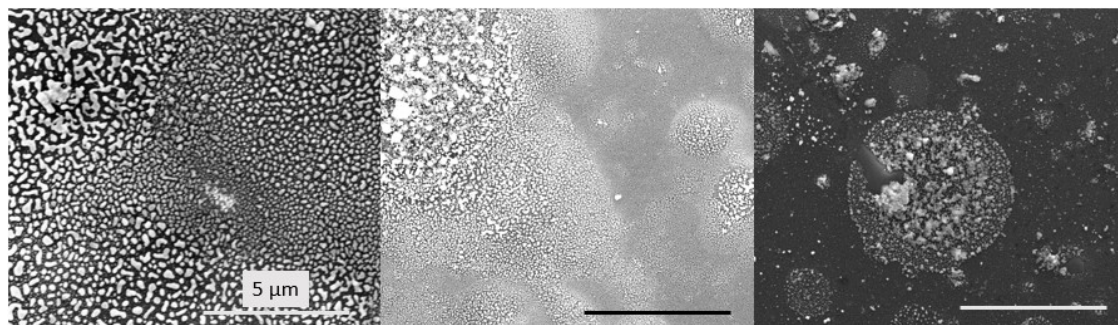


Figure III-12. SEM images of Ag coatings deposited in PI-MOCVD at 330 °C for 5 minutes, using AgAc as precursor concentration 0.02 M 12 ml, with ethanolamine as dispersant (about 0.05 M ). Coatings were deposited on glass substrate with different flow rate of carrier gas: a) 2 L/min, b) 1 L/min and 0.5 L/min.

With longer deposition duration, more continuous Ag films with 100 nm thickness could be deposited as shown in Figure III-13. These films were deposited with 0.02 M AgAc precursor solution, also at 330 °C on glass substrate. Figure a) and b) are the silver coating deposited for 8 minutes duration (20 ml solution consumption), presenting a yellow brown color and connected Ag grain networks. In Figure c) and d), the Ag film deposited for 10 minutes is presented (with 25 ml solution consumption). With a longer deposition duration, the silver grains became denser and more continuous on the substrate, and the films presented a silver white color was. The resistivity of this silver film reached down to 40  $\mu\Omega$ .cm.

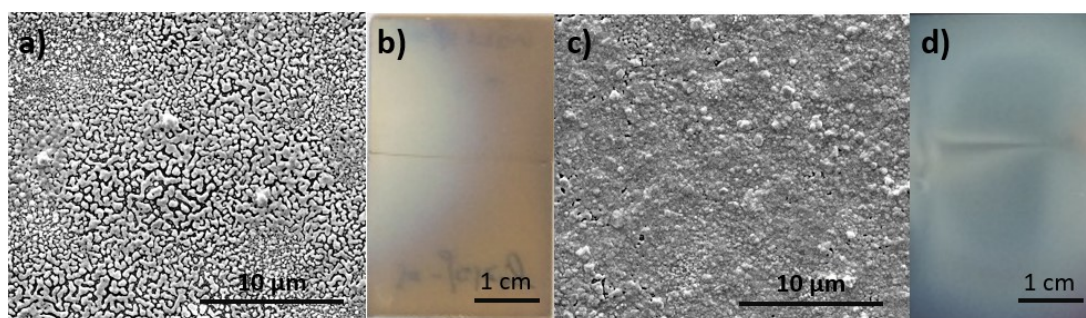


Figure III-13. Conductive Ag coatings using 0.02 M AgAc precursor in PI-MOCVD system. a), b) with 20 ml deposition duration about 8 minutes and c), d) 10 minutes deposition with 25 ml solution consumed. Image b) is the photo corresponding to coating a) and image d) is the photo of the coating in c).

Also, in all silver coatings deposited with PI-MOCVD, due to the geometry of the MOCVD system, the deposition center with diameter about 4 cm are always visible. These films were used to obtain silver oxides by oxidation, as explained in section III.3.1. In PI-MOCVD, with either ethanolamine or ethylenediamine as dispersant, no silver coatings could be achieved by using AgNO<sub>3</sub> as precursor (with concentration 0.02 M), but since previous

reports have shown the possibility of using  $\text{AgNO}_3$  as precursors, it could be worth trying again in future work with PI-MOCVD.

With the newly designed silver metal organic precursors, **AgP** and **AgT**, silver coatings could be successively deposited as well via PI-MOCVD. **AgP** can be dissolved in ethanol solvent but with a long stirring duration (more than 4 hours), thus ethanolamine was also applied here as dispersant. With 0.01 mol/L precursor concentration using ethanol as solvent, high quality Ag films were deposited at 320 °C for 5 min (1000 injection pulses, about 12 ml) at 0.1 mbar on glass substrates. The morphology of the Ag coatings are presented in Figure III-14. Similar effects of enhanced deposition by ethanolamine is shown here with precursor **AgP**, in which a) shows a pink Ag coating with small grains (size about 20 nm) without ethanolamine as the dispersant. In figure b) a darker Ag coating deposited with ethanolamine as dispersant is shown, presenting higher deposition rate and bigger grain size (averagely about 55 nm). Using **AgT** as the precursor with the same deposition conditions, thanks to a much better solubility of **AgT** in alcohol solvents, no dispersant was necessary. The deposited Ag coating is presented in figure c), which shows a blue color coating with big round silver grains on top (maximum up to 100 nm diameter). The morphology is rather different from the silver coatings shown in figure b).

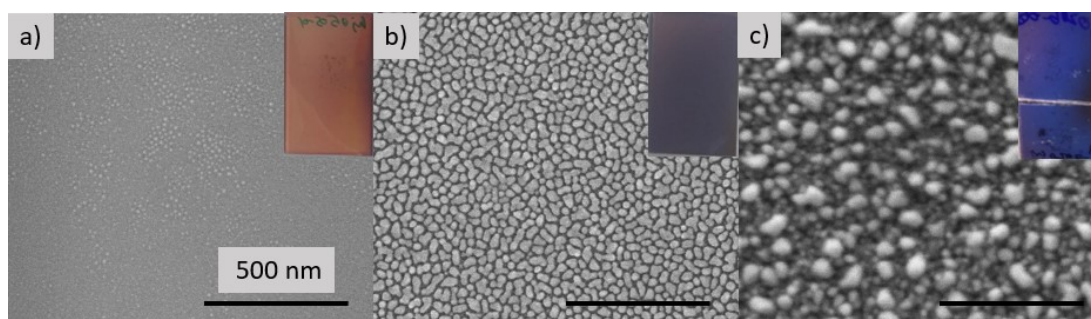


Figure III-14. SEM images of Ag coatings deposited with AgP precursor: a) without ethanolamine and b) with ethanolamine as dispersant. c) SEM image of the coating obtained with AgT (no need to add dispersant) in PI-MOCVD system at 320 °C with 1000 injection pulses (0.01 M about 12 ml solution consumption).

### III.2.2 Ag coatings by Aerosol Assisted MOCVD.

Due to that the final objective of this work was to deposit Ag and Ag-Cu oxide films, thus different precursors were also tested with our AA-MOCVD system, since it incorporates an atmospheric oxygen plasma that can be used to create highly oxidizing conditions.

As with PI-MOCVD, AgAc was tested in AA-MOCVD as precursor for Ag coating as well. At higher deposition temperature (more than 250 °C), no Ag could be deposited on the glass substrate. At lower temperatures (210 °C) a coating was obtained, mainly composed of Ag

clusters, as shown in Figure III-15 a) and b). Clusters with diameter of about 6  $\mu\text{m}$  can be seen. EDS in figure c) confirmed the existence of Ag.

Trying to get insight into the mechanism behind the different results obtained at different temperatures, we made a test with precursor solution sprayed on a hot plate at 300  $^{\circ}\text{C}$  using a sprayer. The spray droplets moved rapidly upon arriving in the hot plate, leaving practically no decomposition products on the heated glass substrate. Combined with the fact that MOCVD is a very surface sensitive technique, the absence of deposition might be due to a low adhesion between the glass substrate and the Ag particles produced, which could be carried away by the relatively high gas flow before having the chance to grow on the substrate surface. It has to be noted that the PI-MOCVD reactor had the initial configuration (see chapter II) for this tests, and thus the fact that the substrate holder was upside down could imposed an extra difficulty.

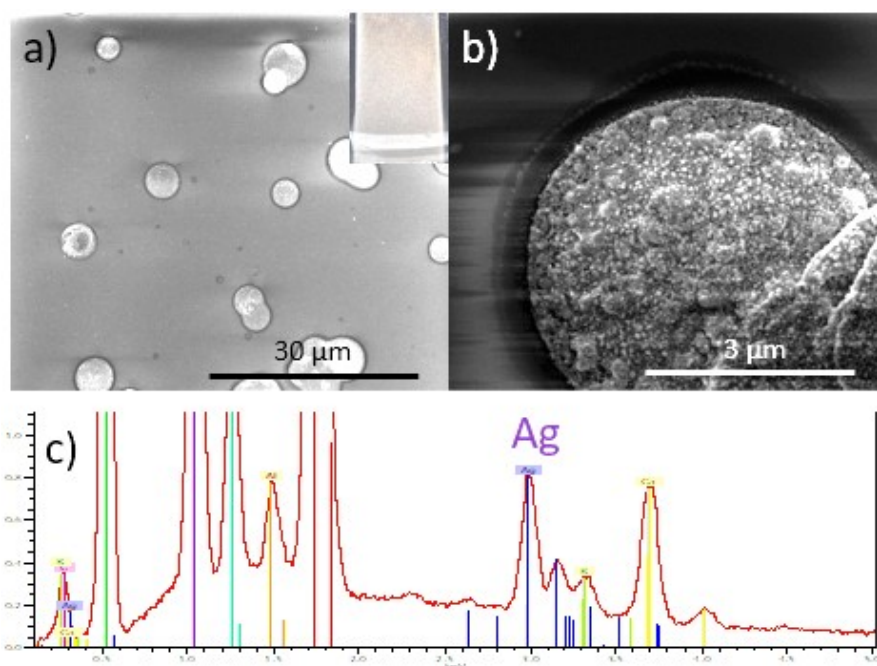


Figure III-15. Ag clusters deposited by AA-MOCVD using AgAc as precursor with concentration of 0.01 M (and including ethanolamine with a concentration of 0.02 M) at 210  $^{\circ}\text{C}$  for 1 h. a) and b) are the SEM images of the silver clusters. Inset in a) is a picture of the glass substrate. c) is the EDS for Ag element identification (the other elements are from the glass substrate).

To obtain better quality Ag coatings with AA-MOCVD, the two new silver precursors were tested as well with deposition temperatures ranging from 250  $^{\circ}\text{C}$  to 350  $^{\circ}\text{C}$ . We could obtain silver coatings with both precursors at deposition temperatures as low as 270  $^{\circ}\text{C}$ . Due to the difficulty for characterizations on glass substrate, only the results of thicker coatings deposited at 320  $^{\circ}\text{C}$  will be presented here with the deposition duration shown in Table III-6.

Both precursors were carefully grinded before being dissolved in ethanol, reaching 0.01 M concentration at room temperature.

Table III-6. Deposition parameters (all reactions carried at 320 °C) using the new Ag precursors.

Sample names	Precursor used	Deposition Duration (h)
P1	[Ag(hfac)(phen)] (AgP)	0.5
P2		1.5
T1	[Ag(triglyme) <sub>2</sub> [Ag(hfac) <sub>2</sub> ]- (AgT)	0.5
T2		1.5

Comparing the results of depositions using the different precursors, AgT showed higher deposition efficiency than AgP (see SEM images in Figure III-19). For a deposition duration of 0.5 h, AgP yielded a yellow coating while AgT gave an orange color with a higher particle density (Figure III-19 a) and c)).

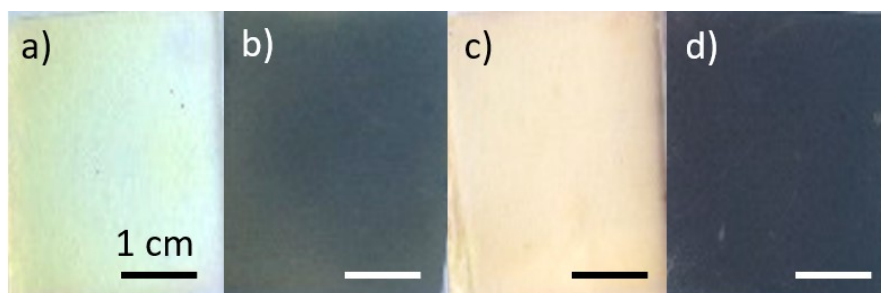


Figure III-16. Images of silver coatings: a) P1 (yellow), b) P2 (dark in the picture but with a purple hue to the naked eye), c) T1 (orange), d) T2 (as for P2, dark in the image but having a purple hue to the naked eye).

Increasing the deposition duration to 1.5 h, coatings from AgP and AgT both presented purple color but the grain density for the latter was still higher than for the former (Figure III-19 b) and d); Pictures of the films are shown in Figure III-16). The color of the films is due to both thickness, but also to particle diameter and shape, since Ag nanoparticles present plasmonic absorption at different wavelengths depending on both the size and the shape of the particles (Transmission spectra of the films are shown in Figure III-17).<sup>52,53</sup>



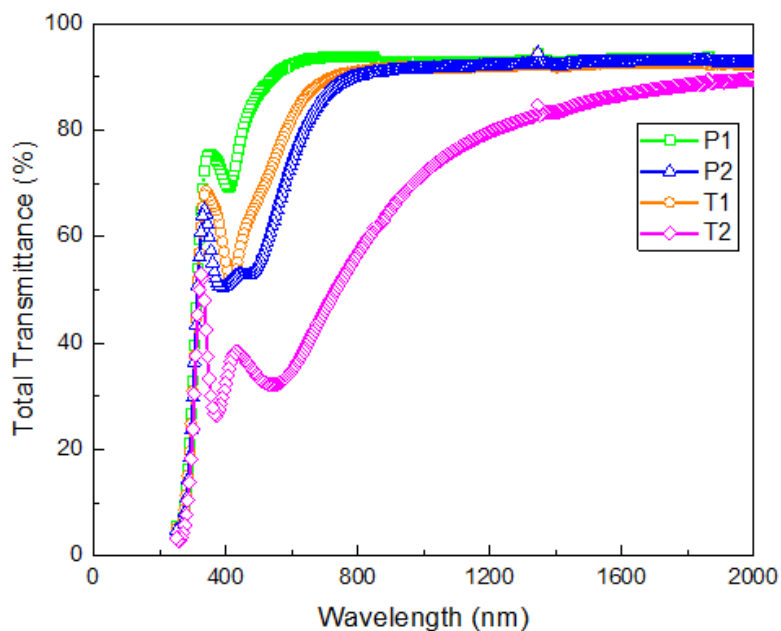


Figure III-17. Transmittance spectra of Ag films deposited with different precursors AgP and AgT with deposition duration 0.5 h (P1 and T1) and 1.5 h (P2 and T2).

For the deposition conditions used, the particles in the coating are not connected and thus the samples present high resistance values, namely a sheet resistance of  $5 \times 10^8 \Omega/\text{cm}^2$  measured by 4 probes. As well, the adhesion between the Ag coating and glass substrate is poor and the films can be easily removed. The thickness of the coatings is on average equivalent to the diameter of the nanoparticles (see Figure III-18).

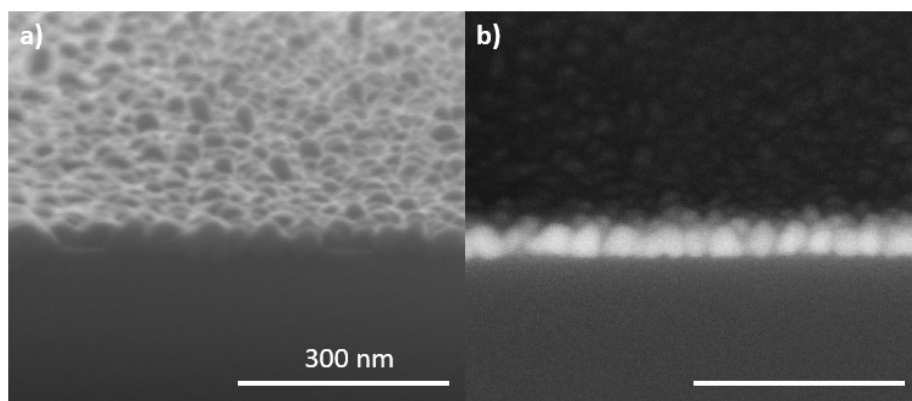


Figure III-18. SEM Crosssection of sample T2 (deposited using AgT precursor for 1.5 h). a) Secondary electrons b) Back/scattered electrons. The height of the coating is about 35 nm.

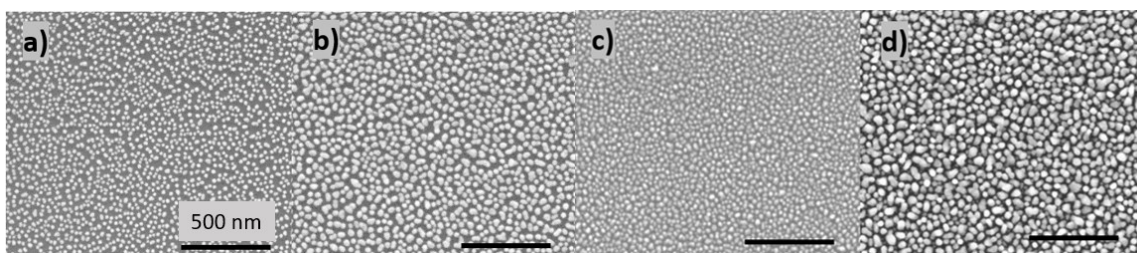


Figure III-19. SEM images of silver coatings deposited at 320 °C by AA-MOCVD using: AgP precursor with deposition duration a) 0.5 h (P1); b) 1.5 hrs (P2); and AgT precursor with deposition duration c) 0.5 h (T1); d) 1.5 hrs (T2).

By analyzing the different particle diameters, a narrower size distribution of Ag grains in P1 is revealed from comparing Figure III-20 a) and b). The size of grains in P1 is mainly located around 19 nm, while particles obtained in T1 range broadly distributed from 10 nm to 22 nm.

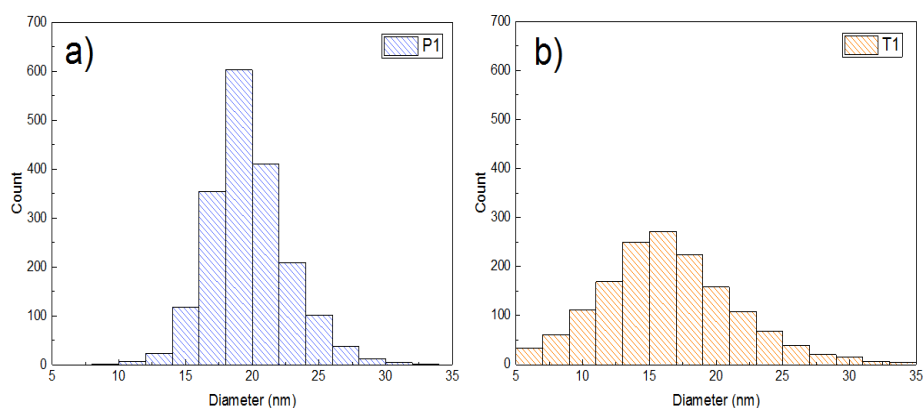


Figure III-20. Size distribution of Ag nanoparticles deposited from AgP and AgT: P1 (a) and T1 (b).

As shown in Figure III-21 a) and b), the coatings obtained with both precursors present well crystallized Ag nanoparticles, but from the sample deposited with AgP (P2), a thin shell surrounding the Ag nanoparticles was observed. Also, as already hinted by TEM images (Figure III-21 c) and d)), Ag nanoparticles obtained from AgP gave more regular round shapes than those obtained from AgT (T2), which are elongated. Electron diffraction patterns of the different particles show diffraction rings which only correspond to metallic Ag. Thus a smaller average grain size for Ag coatings with AgP precursor can be attribute to such a shell layer, which possibly limited the grain growth during the silver deposition process.

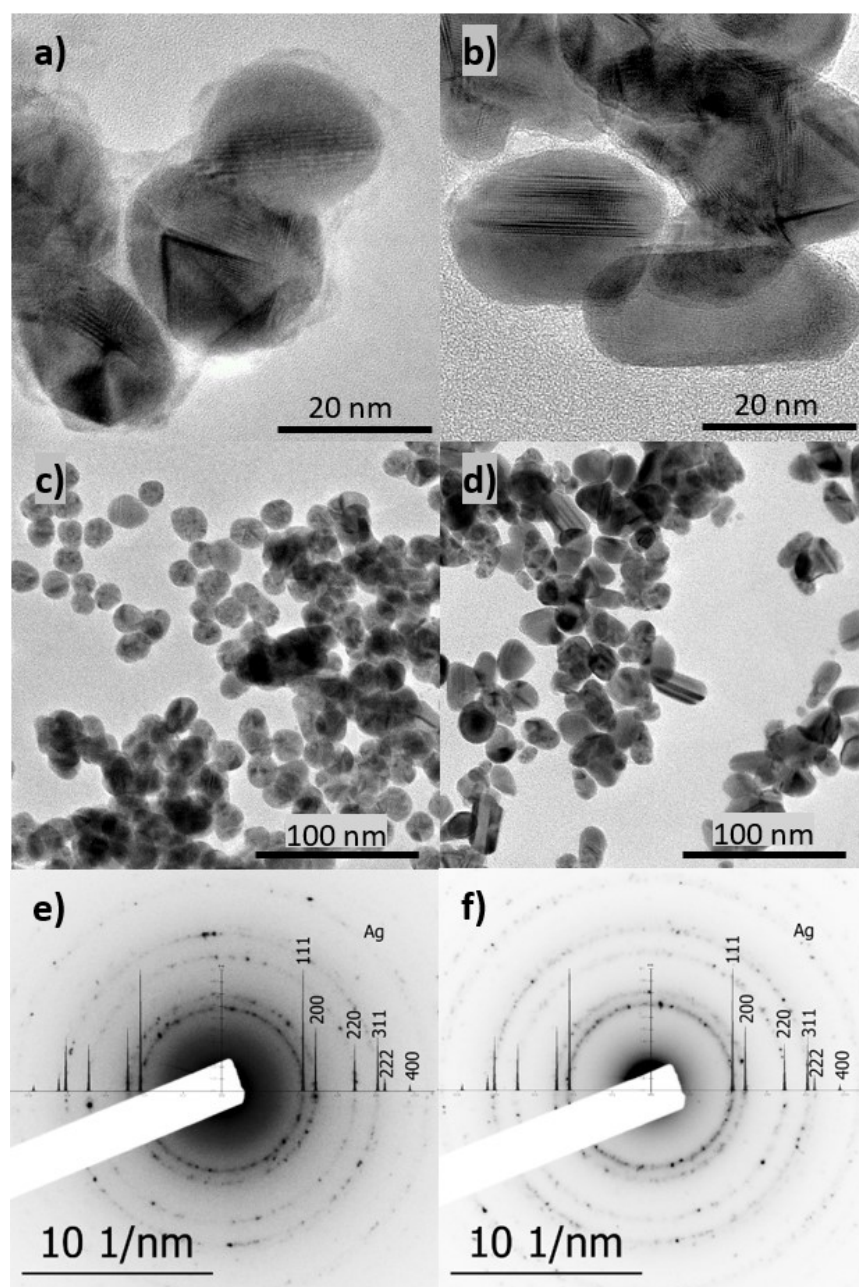


Figure III-21. Transmission Electron Microscopy images and electron diffractions for Ag particles deposited using AgP (P2), a), c), e) and AgT (T2), b), d), f).

To further evaluate the purity and crystallinity of the coatings obtained from the two precursors, Raman spectroscopy and X-Ray Diffraction were used and the results are shown in Figure III-22. Figure a) shows the Raman spectrum obtained for silver particles deposited using AgP. In this case, strong peaks related to the C-OH group in the range  $1200\text{ cm}^{-1}$  and  $1600\text{ cm}^{-1}$  can be observed, in agreement with the presence of the carbonaceous shell observed by TEM. On the other hand, coatings deposited with AgT showed a flat band curve in this high wavenumber range.

XRD patterns of the two different coatings are shown in Figure III-22 b). Comparing the XRD pattern of silver coatings from AgT (green curve) and from AgP (orange curve), in both cases the XRD patterns show the characteristic reflections of the face centered cubic Ag phase, confirming the formation of crystalline Ag coatings, and the smaller crystallite size for coatings deposited with AgP.

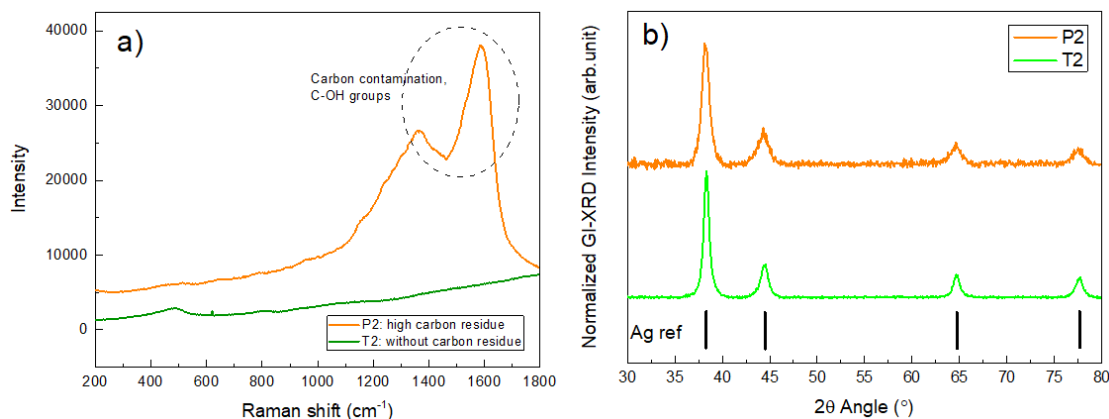


Figure III-22. Characterization of silver coatings deposited with the different precursors. a) RAMAN spectroscopy for carbon residues detection; b) Normalized GIXRD patterns of silver coatings deposited on glass substrate.

The carbon contaminations found for AgP, both by Raman and TEM, are due to the incomplete decomposition of the precursor under the deposition conditions used, and are in agreement with the TGA results shown above. Removal of the organic coating could not be obtained by annealing. For temperatures above 300 °C, the Ag nanoparticles in the coating tend to fuse together forming bigger rounded particles (See the image in Figure III-23).

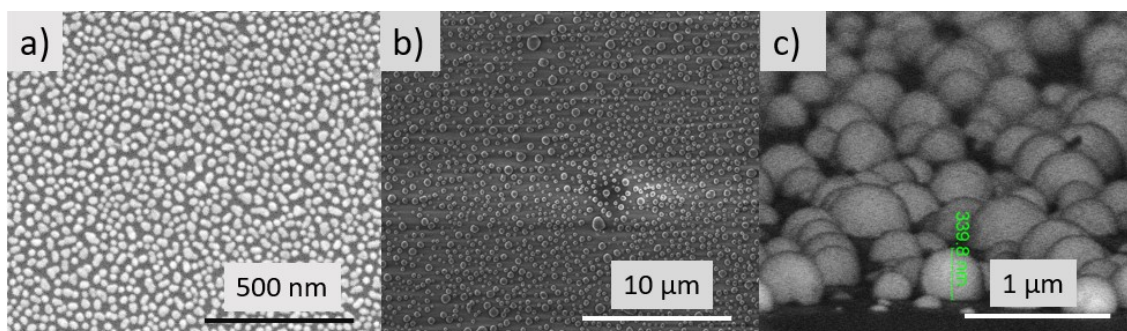


Figure III-23. a) SEM image of the as deposited Ag coating (using AgP). Images b) and c) show SEM images of the coating after annealing at 400 °C in air for 1 h.

Thus, although AgP is able to yield Ag coatings when used as precursor in AA-MOCVD, these present carbon species which are expected to affect the properties of the final coating (i.e. conductivity) and thus can be not suitable for certain applications. At the same time, the direct deposition of Ag@C core-shell nanoparticles could be indeed interesting especially for plasmonic applications.

### **III.3 Oxidation of Ag coatings**

Having optimized the deposition of Ag coatings via AA-MOCVD using the two new precursors, the deposition of silver oxides was tackled, as an optimization step for the final deposition of AgCuO<sub>2</sub>. Due to the noble nature of the Ag metal, and thus the low thermal stability of Ag oxides, obtaining a high quality silver oxide film is very challenging. In this section we describe three approaches that have been evaluated for the deposition of Ag oxides. Those are, direct deposition of oxides by using plasma assisted AA-MOCVD, and oxidation of pre-deposited Ag films by electrochemical oxidation and by oxygen plasma treatment.

Direct deposition of silver oxide in AA-MOCVD system was thus tested, but due to the high decomposition temperature of the silver precursor (above 270 °C for an efficient deposition), the silver oxides are unstable at this condition. In addition to that, the oxidation gas (mainly being ozone and radicals generated by the plasma) are highly corrosive and thus deposition rate needs to be higher than etching rate. This can be achieved by increasing the precursor concentration in the solution. Given the high cost of Ag precursors, and the rather high amounts of precursor needed in AA-MOCVD for each single deposition we decided to perform post treatment of the Ag metal coatings rather than further attempting to optimize the direct deposition of Ag oxides. The experiments performed and the results obtained are detailed next.

#### **III.3.1 Electrochemical oxidation of Ag coatings**

The setup of electrochemical oxidation has been introduced in Chapter II, Experimental part. In this section, the study of the electrochemical oxidation of metallic Ag coatings has been studied (the study of the oxidation Ag/Cu alloys will be presented in Chapter IV). As usual, cyclic voltammetry was used to evaluate the oxidation potentials of the different oxidation reactions at a certain condition. In this case, silver films (about 100 nm thick) were deposited on corning glass by PI-MOCVD at 330 °C for 10 minutes using 0.02 M AgAc as precursor solution. As it's shown in Figure III-24, a voltammogram was acquired by applying the potential sequence 0 V → 0.7 V → -0.3 V → 0 V (all the potential values in the chapter are given versus Ag/AgCl 3.5 M KCl reference electrode) and a scanning speed of 10 mV/s. This is in accordance with the reference works<sup>54,55</sup>. 1 M NaOH solution was used as the electrolyte, since several works reported for AgCuO<sub>2</sub> synthesis used such high pH (>13).<sup>56,57</sup> As it will be shown by works introduced in Chapter V, the high pH is crucial for AgCuO<sub>2</sub>

phase formation. At forward bias potential, two oxidation peaks at +0.34 V, +0.607 V are clearly visible, corresponding to  $\text{Ag} \rightarrow \text{Ag}^{1+}$  and  $\text{Ag}^{1+} \rightarrow \text{Ag}^{2+}$ , respectively. When scanning back, two reducing peaks at +0.31 V and +0.05 V appeared, corresponding to the reduction of silver following the inverse reactions with respect to the oxidation sweep.

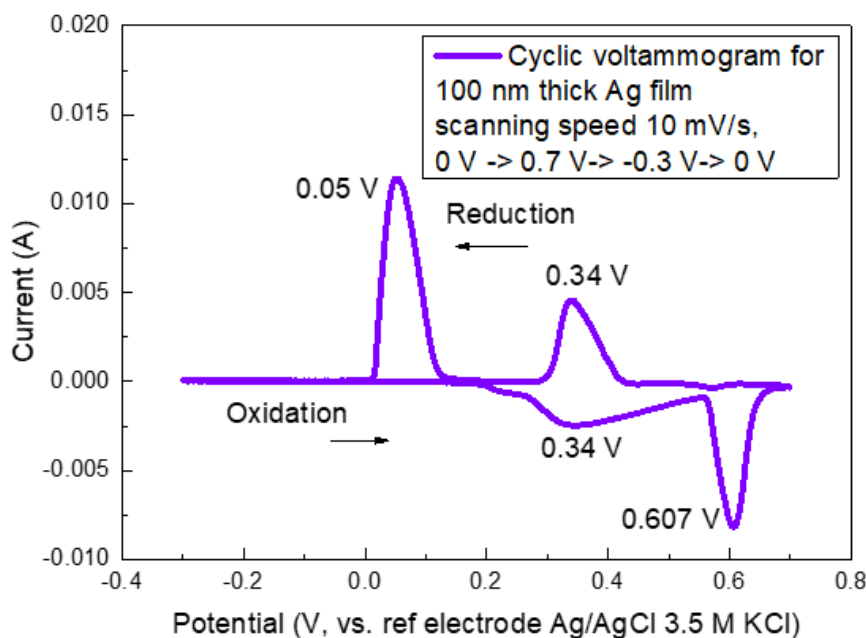


Figure III-24. Cyclic voltammetry of a conductive Ag film (100 nm thick)/ Corning glass, voltage range: 0 V  $\rightarrow$  0.7 V  $\rightarrow$  -0.3 V  $\rightarrow$  0 V, in 1 M NaOH solution with scanning speed 10 mV/s.

The silver films deposited at the same condition (as previously mentioned) were oxidized in 1 M NaOH electrolyte, by applying 0.7 V potential with different durations, as shown in Table III-7. Given the high oxidation state of Ag in  $\text{AgCuO}_2$ ,<sup>58</sup> this potential value was chosen to ensure high oxidation states for Ag. The same Ag film was cut into several pieces with roughly similar area (about 0.25 cm<sup>2</sup>), thus those Ag thin film samples were roughly identical.

Table III-7. Electrochemical oxidation of Ag films with different durations, under 0.7 V, in 1 M NaOH solution

Oxidation duration (s)	500	1000	1300
Sample names	E01	E02	E03

The morphology of the oxidized Ag films obtained with various durations are shown in Figure III-25. Figure a) shows the original as deposited Ag film (with a low resistivity of about 40  $\mu\Omega\cdot\text{cm}$ ). With electrochemical oxidation for 500 s, the morphology of the oxidized sample shows particle like and discontinuous surface in Figure III-25 b). With longer

oxidation duration, the surface contains bigger flake-like grains, while the surface becomes rougher (shown in Figure III-25 c and d).

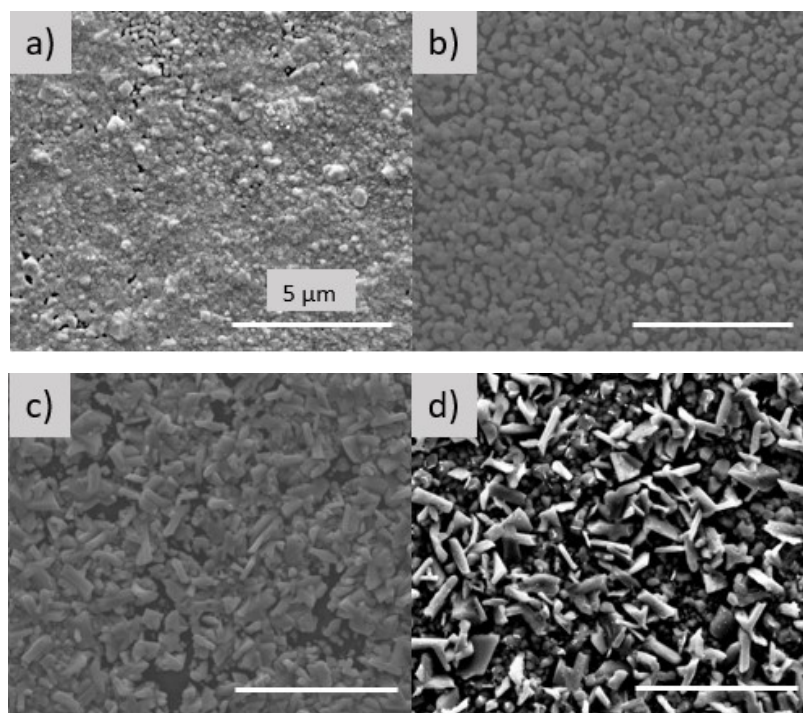


Figure III-25. Scanning Electron Images of Ag/Ag oxides film morphology evolution with oxidation duration. A). Original Ag film; b). after 500 s (E1); c). after 1000 s (E2); d). after 1300 s (E3).

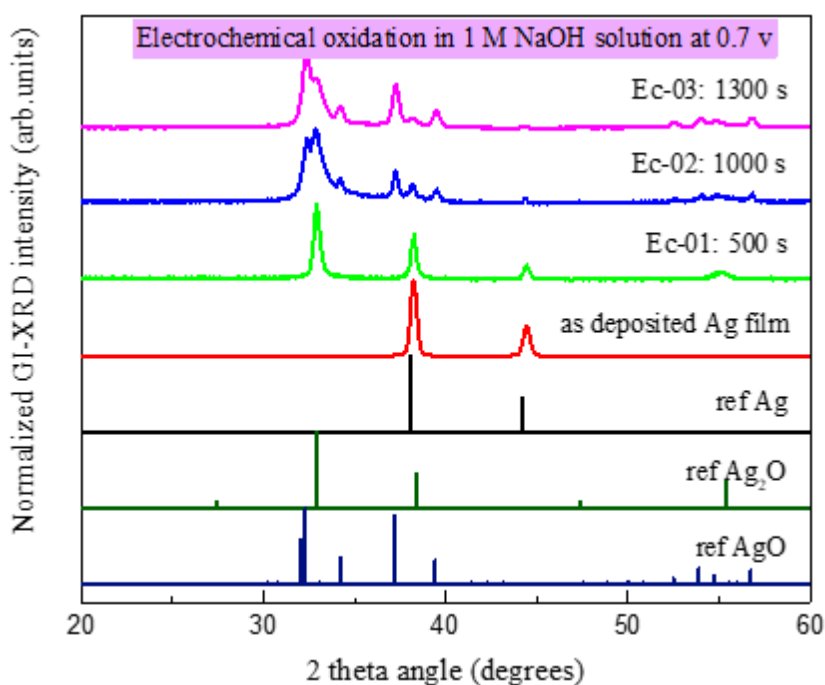


Figure III-26. GIXRD patterns of Ag film oxidized electrochemically in 1 M NaOH solution with 0.7 V potential showing the phase evolution with time. Dark curve represents Ag film as deposited in PI-MOCVD and is oxidized with duration 500 s (blue), 1000 s (pink) and 1300 s (green).

To distinguish the phase evolution carefully, GIXRD was applied to each oxidized sample and the diffraction patterns are shown in Figure III-26. Even though in GIXRD, the signal intensity cannot be used to infer the amount of each phase, nor a possible texture, the change of diffraction intensity still can tell the trend of the phase emerging or declining.

During the oxidation process, the intensity of reflections from metallic Ag decreases while reflections from the Ag<sub>2</sub>O phase are present after 500 s at 0.7 V (green curve). With longer oxidation duration, Ag<sub>2</sub>O is further oxidized into AgO, thus the intensity of reflections from AgO increase while reflections from Ag<sub>2</sub>O and Ag decrease in intensity.

Thus, we can conclude that the cubic like grains shown in Figure III-25 b) correspond mainly to Ag<sub>2</sub>O while the big flakes in figure c) and d) would correspond to AgO. Therefore, conductive silver films can be electrochemically oxidized into high oxidation state, like the AgO phase in a 1 M NaOH solution. It therefore opens the possibility for further work on synthesizing AgCuO<sub>2</sub> in thin film phase from metallic coatings. But, the morphology of the electrochemically oxidized films are rather rough and discontinuous, which is hard to avoid. In addition, in order to fully oxidize the thin film, a conductive substrate is preferred.

### III.3.2 Oxidation of Ag film by Oxygen Plasma

Apart from using an electrochemical approach, silver can also easily be oxidized with ozone. Silver oxidation by ozone has indeed been reported in the work of *G.I.N. Waterhouse et al.*, who studied the reaction of ozone with a polycrystalline silver foil.<sup>59</sup> In addition, the interaction of silver powder with ozone have been also studied.<sup>60</sup> Even AgNO<sub>3</sub> solution has been reported to react with ozone and form AgO or Ag<sub>7</sub>O<sub>8</sub>NO<sub>3</sub> depending on the solution pH.<sup>61</sup> In addition, a solid state phase transition from Ag<sub>2</sub>Cu<sub>2</sub>O<sub>3</sub> to AgCuO<sub>2</sub> in ozone atmosphere has been reported in a work by D. Muñoz-Rojas *et al.*<sup>62</sup> In general, ozone has been proven to be a very efficient oxidizer gas to achieve silver oxides with high oxidation state. In this work, by taking advantage of the atmospheric plasma head coupled with the AA-MOCVD system, ozone can be generated thus to create highly oxidizing environment. As stated above, while we tried to directly deposit silver oxide films with plasma, the precursors available to deliver silver coatings require deposition temperatures of at least 270 °C, which is too high for the existence of silver oxide phase. Thus, an alternative approach was taken by us, which is a two step process involving silver film deposition by PI-MOCVD and oxygen plasma treatment afterwards.

To choose a proper power and inlet gas for ozone generation, Air and O<sub>2</sub> were tested and the plasma was analyzed by ICP-coupled Optical Emission Spectrometry (ICP-OES) (model



iCAP 7400, in collaboration with Prof. Christophe Vallée, from the Laboratoire des technologies de la Microélectronique (LTM)). Air was primarily tested as the gas source at maximum plasma power (500 W) and the emitted plasma spectra is shown in Figure III-27 a). Surprisingly enough, with air as the inlet gas, a very weak trace of ozone signal was detected (at 774.2 nm) and the emitted spectra peaks are similar to those obtained when using pure N<sub>2</sub> as the gas source, as shown in Figure III-27 b). This absence of ozone generation with air is further studied by varying the ratio of oxygen mixed with Ar. Generation of ozone presents a quasi linear dependence with the concentration of oxygen in inlet gas, as illustrated in Figure III-27 c). Lastly, to understand the relationship between plasma power and ozone generation with pure oxygen as gas source, different powers were analyzed and the result is shown in Figure III-27 d). The figure shows that a minimum power of 300 W is needed to be able to generate measurable ozone species intensity. With higher powers, the intensity of the ozone signal increases.

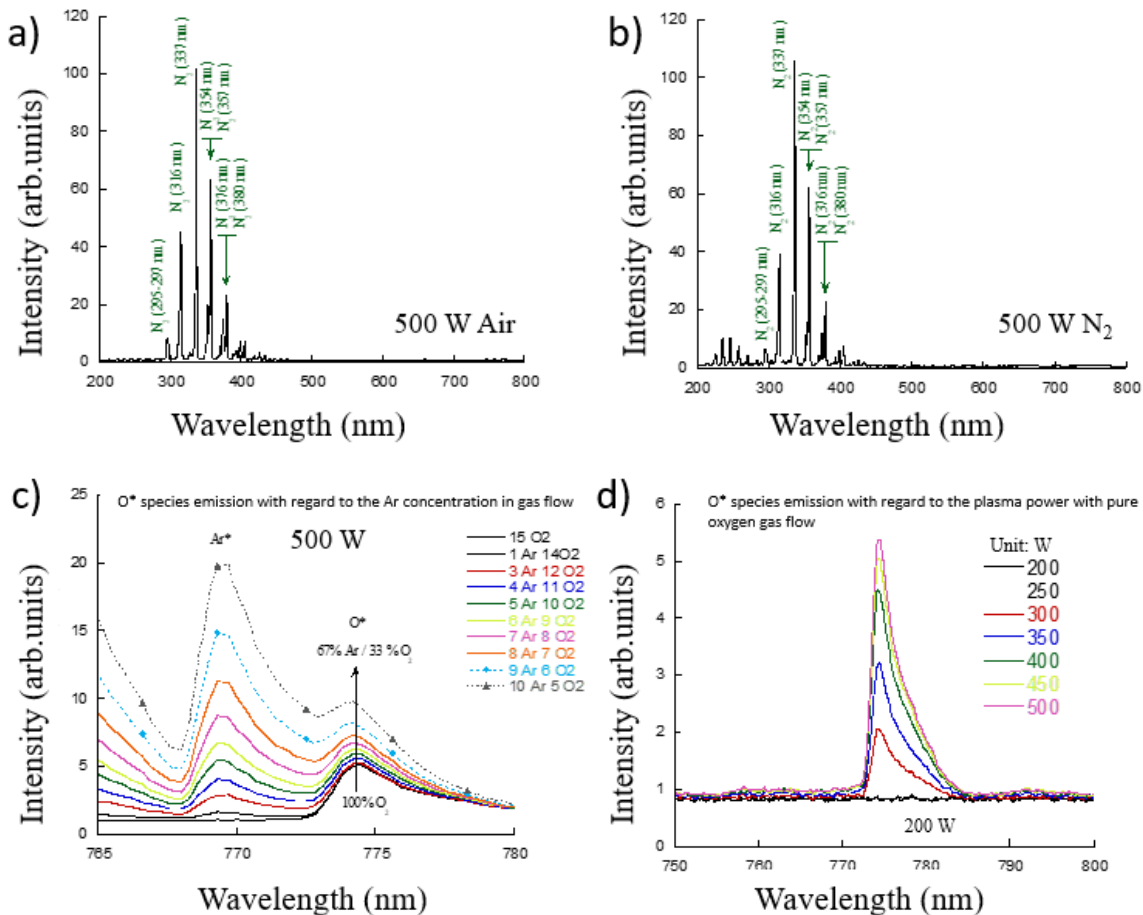


Figure III-27. Atmospheric plasma analyzed by ICP-OES with different gas source and voltages. a) 500 V with air inlet gas. b) 500 V with N<sub>2</sub> inlet gas. c) O<sub>2</sub> as inlet gas with voltage from 200 V to 500 V. d) at 500 V, different concentration of O<sub>2</sub> combining with Ar.

Thus, to make sure ozone is generated through atmospheric plasma, pure oxygen as gas source is preferred and a minimum power of 300 W is required. In addition, when oxidizing the Ag films, one thing to keep in mind is that radicals generated in the plasma can be very aggressive and thus corrosive for the Ag films. To minimize the erosion from radicals, the oxidation process was conducted with a humid environment (created by injecting water mist flow from a separate inlet into the chamber) and with minimum power (with 300 W).

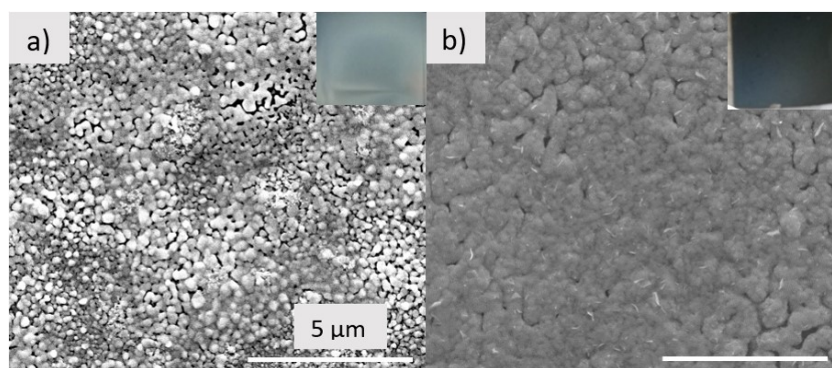


Figure III-28. SEM images of Ag films a) before and b) after oxygen plasma oxidation for 3 min with 300 W at 70 °C.

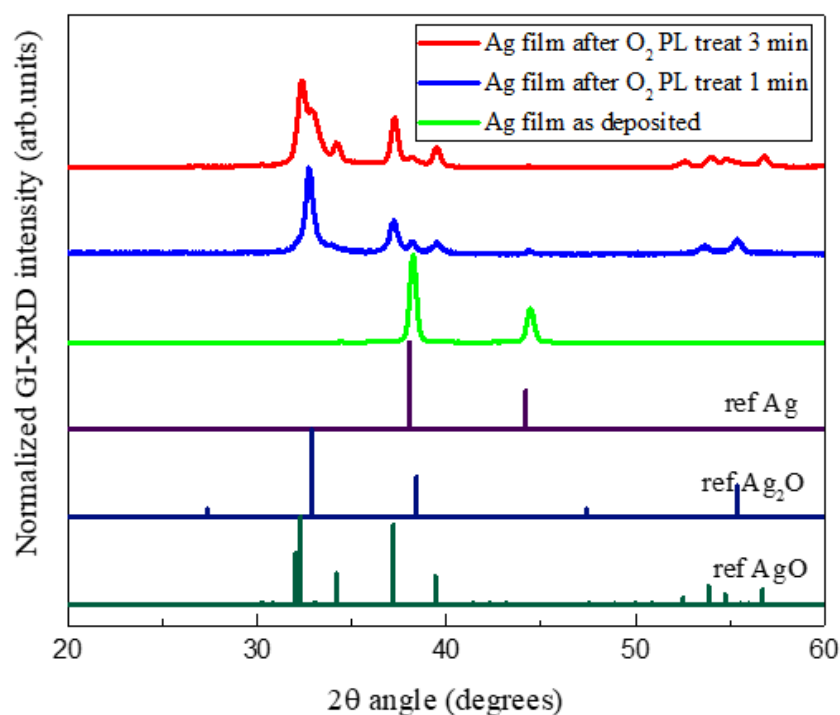


Figure III-29. Phase evolution of Ag films oxidized by oxygen plasma under power 300 W and 70 °C with different durations. Dark line represents as deposited Ag film, red represent Ag film under plasma 1 min and blue refers to Ag film under oxidation for 3 min. All samples used are cut from the same Ag film.

The 100 nm thick silver film was deposited on corning glass via PI-MOCVD at 330 °C with AgAc as precursor, with concentration 0.02 M and 25 ml volume consumption. To avoid the

silver oxide phase decomposing, the plasma treatment were conducted at near room temperature (70 °C).

After exposing the Ag film to the oxygen plasma, the Ag film rapidly changed from silver white color to dark color. The morphology of Ag films before and after (3 min) oxygen plasma treatment are shown in Figure III-28, in which figure a) shows the as deposited Ag film and figure b) presents the morphology of the film after treatment exhibiting a smoother surface and being denser. The resistivity of the oxidized film was measured by home made four point probe as described in experimental Chapter II, obtaining a value about 100  $\Omega$ .cm. The phase change before and after the oxygen plasma were characterized by GIXRD, results are shown in Figure III-29. Initially, the as deposited film only presented a strong reflection intensity from silver phase, as shown in the green curve. After the treatment for only 1 minute, the reflection peaks from Ag<sub>2</sub>O phase emerged, while the reflection intensity from metallic silver phase were largely reduced, as shown in the blue curve. With further plasma treatment duration up to 3 minutes, reflections corresponding to both AgO and Ag<sub>2</sub>O were presented, as shown in the red curve.

Therefore, oxygen plasma has shown several advantages comparing with electrochemical oxidations, including no requirements on substrate conductivity, smooth surface morphology and very efficient, thus it's a useful information to support further work on silver copper oxide compound. Conversely, achieving a phase pure coating may result difficult by this approach.

### **III.4 Chapter summary**

Silver coatings have been obtained through both PI-MOCVD and AA-MOCVD. During the process, 5 types of silver precursors have been tested, from which 3 precursors (including the cheap and commercially available AgAc and two new designed and synthesized precursors, AgT and AgP) allowed the deposition of Ag coatings. The silver coating obtained from AgAc is reported here for the first time and the effect of the dispersant molecules has been discussed, which gives the conclusion that with ethanolamine as dispersant more volatile silver acetate ammine complex can be formed, thus facilitating the precursor transport in PI-MOCVD vacuum condition and thus the high deposition rate. In addition, two new silver metal organic precursors have been synthesized using less expensive and toxic

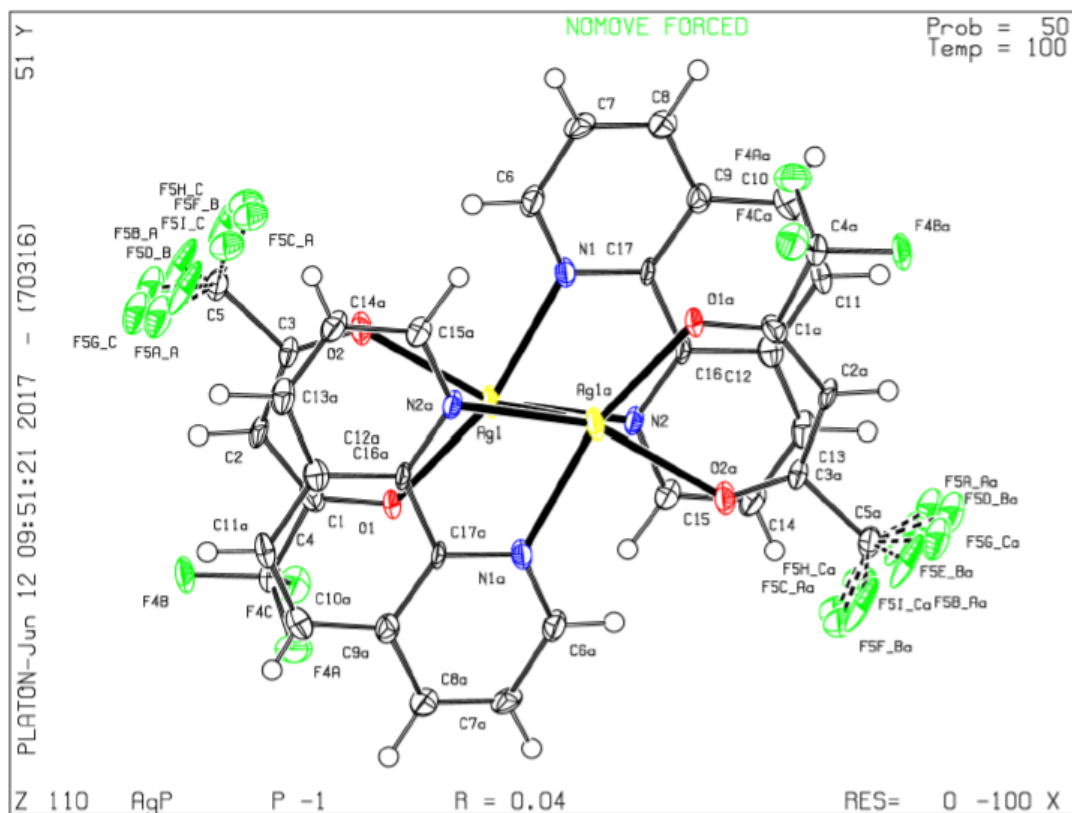
ligands, namely, [Ag(hfac)phen] (**AgP**) and [Ag(triglyme)<sub>2</sub>]<sup>+</sup>[Ag(hfac)<sub>2</sub>]<sup>-</sup> (**AgT**). FTIR spectroscopy has confirmed the formation of such molecular complexes. Furthermore, the

crystal structures of both precursors were solved by means of single crystal X-ray diffraction. TGA analyses have shown that AgT is a precursor with a more rapid and clean decomposition than AgP. The new precursors present a good solubility in ethanol and have been tested in an Aerosol Assisted CVD system. Depositions by AA-MOCVD revealed that the two precursors, used under similar CVD parameters, produced coatings with different surface morphologies. Coatings deposited from AgP are made of Ag nanoparticles presenting a carbonaceous shell. Conversely, Ag coatings from AgT consist of pure Ag nanoparticles and present high crystallinity. In conclusion, our results show that the new AgT adduct is a good precursor for depositing metallic Ag coatings via AA-MOCVD using alcohol solvents.

Secondly, different approaches have been adopted to obtain silver oxide films to lay a foundation for further work of AgCuO<sub>2</sub> phase synthesis. Direct deposition of silver oxide films coupling with the atmospheric plasma system were tested. Due to the relatively high deposition temperatures (at least 270 °C) for all the precursors available to us, silver oxide phase couldn't exist at such temperature. Thus, a two-step process to achieve silver oxide film was used, which was pre-deposition of Ag coatings by MOCVD and after-treatment with oxidation techniques (electrochemical oxidation and oxygen plasma). With both oxidation techniques, AgO phase was obtained, but there are still several issues to be solved. For silver oxide films obtained from electrochemical oxidation, they presented a rough surface and conductive substrate is necessary for a full oxidation. Meanwhile for oxygen plasma treatment, even though it is a rapid oxidation technique and gives smoother and denser silver oxide films as compared with the previous technique, the corrosion from the radicals in plasma is difficult to control and minimize. In both cases, silver oxide films with pure phase composition are rather difficult to obtain.



Datablock AgP- ellipsoid plot:



check CIF/PLATON report for AgT:

### Datablock: AgT

---

Bond precision: C-C = 0.0147 Å                      Wavelength=0.71073  
Cell:                    a=11.4965(6)                    b=12.9561(7)                    c=13.0344(9)  
                          alpha=96.821(5)                beta=91.795(5)                gamma=92.350(4)  
Temperature:        250 K

	Calculated	Reported
Volume	1924.8(2)	1924.8(2)
Space group	P -1	P -1
Hall group	-P 1	-P 1
Moiety formula	C10 H2 Ag F12 O4, C16 H36 Ag O8	?
Sum formula	C26 H38 Ag2 F12 O12	C26 H38 Ag2 F12 O12
Mr	986.30	986.30
Dx, g cm-3	1.702	1.702
Z	2	2
Mu (mm-1)	1.127	1.127
F000	984.0	984.0
F000'	981.18	
h,k,lmax	15,17,17	15,15,17
Nref	10613	7438
Tmin,Tmax	0.737,0.807	0.933,1.000
Tmin'	0.722	

Correction method= # Reported T Limits: Tmin=0.933 Tmax=1.000  
AbsCorr = MULTI-SCAN

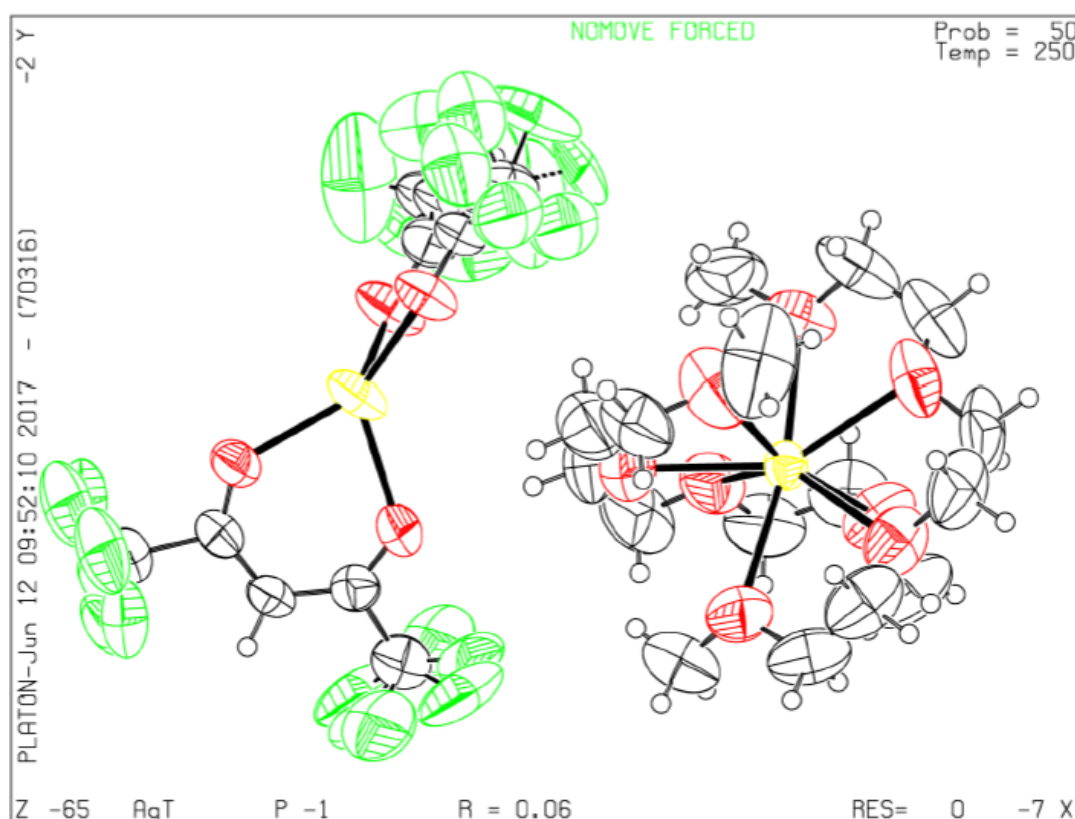
Data completeness= 0.701                      Theta(max)= 29.400

R(reflections)= 0.0637( 5378)                wR2(reflections)= 0.1942( 7438)

S = 1.061                                      Npar= 519

---

Datablock AgP- ellipsoid plot:



### III.6 References

1. Jiang, L., You, T., Yin, P., Shang, Y., Zhang, D., Guo, L. & Yang, S. Surface-enhanced Raman scattering spectra of adsorbates on Cu<sub>2</sub>O nanospheres: charge-transfer and electromagnetic enhancement. *Nanoscale* **5**, 2784–9 (2013).
2. Hsieh, J. H., Chiu, C. H., Li, C., Wu, W. & Chang, S. Y. Development of anti-wear and anti-bacteria TaN-(Ag,Cu) thin films - A review. *Surf. Coatings Technol.* **233**, 159–168 (2013).
3. Janunts, N. A., Baghdasaryan, K. S., Nerkararyan, K. V. & Hecht, B. Excitation and superfocusing of surface plasmon polaritons on a silver-coated optical fiber tip. *Opt. Commun.* **253**, 118–124 (2005).
4. Xu, C., Zhou, R., Chen, H., Hou, X., Liu, G. & Liu, Y. Silver-coated glass fibers prepared by a simple electroless plating technique. *J. Mater. Sci. Mater. Electron.* **25**, 4638–4642 (2014).
5. Chen, Y. H., Hsu, C. C. & He, J. L. Antibacterial silver coating on poly(ethylene terephthalate) fabric by using high power impulse magnetron sputtering. *Surf. Coatings Technol.* **232**, 868–875 (2013).
6. Sarkar, S., Biswas, P. K. & Jana, S. Nano silver coated patterned silica thin film by sol-gel based soft lithography technique. *J. Sol-Gel Sci. Technol.* **61**, 577–584 (2012).



7. Melorose, J., Perroy, R. & Careas, S. *Chemical Vapor Deposition Book. Statewide Agricultural Land Use Baseline 2015* **1**, (Springer Science+Business media, LLC, 2015).
8. Marchand, P., Hassan, I. A., Parkin, I. P. & Carmalt, C. J. Aerosol-assisted delivery of precursors for chemical vapour deposition: expanding the scope of CVD for materials fabrication. *Dalton Trans.* **42**, 9406–22 (2013).
9. Knapp, C. E. & Carmalt, C. J. Solution based CVD of main group materials. *Chem. Soc. Rev.* **45**, 1036–1064 (2016).
10. Ponja, S. D., Sehmi, S. K., Allan, E., Macrobert, A. J., Parkin, I. P. & Carmalt, C. J. Enhanced Bactericidal Activity of Silver Thin Films Deposited via Aerosol-Assisted Chemical Vapor Deposition. *ACS Appl. Mater. Interfaces* **7**, 28616–28623 (2015).
11. Bahlawane, N., Premkumar, P. A., Brechling, A., Reiss, G. & Kohse-Höinghaus, K. Alcohol-assisted CVD of silver using commercially available precursors. *Chem. Vap. Depos.* **13**, 401–407 (2007).
12. Ritala, M., Leskela, M., Hämäläinen, J., Ritala, M. & Leskelä, M. Atomic Layer Deposition of Noble Metals and Their Oxides. *Chem. Mater.* **26**, 786–801 (2013).
13. Niskanen, A., Hatanpää, T., Arstila, K., Leskelä, M. & Ritala, M. Radical-enhanced atomic layer deposition of silver thin films using phosphine-adducted silver carboxylates. *Chem. Vap. Depos.* **13**, 408–413 (2007).
14. Kariniemi, M., Niinistö, J., Hatanpää, T., Kemell, M., Sajavaara, T., Ritala, M. & Leskelä, M. Plasma-Enhanced Atomic Layer Deposition of Silver Thin Films. *Chem. Mater.* **23**, 2901–2907 (2011).
15. Liang, Y. C., Wang, C. C., Kei, C. C., Hsueh, Y. C., Cho, W. H. & Perng, T. P. Photocatalysis of Ag-loaded TiO<sub>2</sub> nanotube arrays formed by atomic layer deposition. *J. Phys. Chem. C* **115**, 9498–9502 (2011).
16. Sivakov, V. A., Höflich, K., Becker, M., Berger, A., Stelzner, T., Eilers, K. E., Pore, V., Ritala, M. & Christiansen, S. H. Silver coated platinum core-shell nanostructures on etched Si nanowires: Atomic layer deposition (ALD) processing and application in SERS. *ChemPhysChem* **11**, 1995–2000 (2010).
17. Edwards, D. A., Mahon, M. F., Molloy, K. C. & Ogorodnik, V. Aerosol-assisted chemical vapour deposition of silver films from adducts of functionalised silver carboxylates. *J. Mater. Chem.* **13**, 563–570 (2003).
18. Xu, C., Hampden-smith, M. J., Kodas, T. T., Dueslert, E. N., Rheingold, A. L. & Yap, G. Pd(hfac-C)(hfac-O,O)(SEt<sub>2</sub>). *Inorg. Chem.* **34**, 4767–4773 (1995).
19. Edwards, D. A., Harker, R. M., Mahon, M. F. & Molloy, K. C. Aerosol-assisted chemical vapour deposition ( AACVD ) of silver films from triorganophosphine adducts of silver carboxylates , including the structure of [ Ag ( O<sub>2</sub>CC<sub>3</sub>F<sub>7</sub> )( PPh<sub>3</sub> )<sub>2</sub> ]. *Inorganica Chim.*

- Acta* **328**, 134–146 (2002).
20. Fragalà, M. E., Malandrino, G., Puglisi, O. & Benelli, C. Synthesis, X-ray structure, and characterization of Ag(hfa)·tetraglyme [hfa = hexafluoroacetylacetonate]: A novel adduct for the fabrication of metallic silver based films via in situ self reduction. *Chem. Mater.* **12**, 290–293 (2000).
  21. Szłyk, E., Piszczek, P., Grodzicki, A., Chaberski, M., Goliński, A., Szatkowski, J. & Błaszczyk, T. CVD of AgI complexes with tertiary phosphines and perfluorinated carboxylates - A new class of silver precursors. *Chem. Vap. Depos.* **7**, 111–116 (2001).
  22. Chi, B. K. & Lu, Y. MOCVD of Silver Thin Films from the (1,1,1,5,5,5-Hexafluoro-2,4-pentanedionato)silver[bis(trimethylsilyl)acetylene] Complex. *Chem. Vap. Depos.* **7**, 117–120 (2001).
  23. Kim, H.-K., Jeong, H.-C., Kim, K. S., Yoon, S. H., Lee, S. S., Seo, K. W. & Shim, I.-W. Preparation of silver thin films using liquid-phase precursors by metal organic chemical vapor deposition and their conversion to silver selenide films by selenium vapor deposition. *Thin Solid Films* **478**, 72–76 (2005).
  24. Gao, L., Härter, P., Linsmeier, C., Gstöttner, J., Emling, R. & Schmitt-Landsiedel, D. Metalorganic chemical vapor deposition of silver thin films for future interconnects by direct liquid injection system. *Mater. Sci. Semicond. Process.* **7**, 331–335 (2004).
  25. Gao, L., Härter, P., Linsmeier, C., Wiltner, a., Emling, R. & Schmitt-Landsiedel, D. Silver metal organic chemical vapor deposition for advanced silver metallization. *Microelectron. Eng.* **82**, 296–300 (2005).
  26. Piszczek, P., Szłyk, E., Chaberski, M., Taeschner, C., Leonhardt, A., Bała, W. & Bartkiewicz, K. Characterization of silver trimethylacetate complexes with tertiary phosphines as CVD precursors of thin silver films. *Chem. Vap. Depos.* **11**, 53–59 (2005).
  27. Abourida, M., Guillon, H., Jiménez, C., Decams, J. M., Weiss, F., Valet, O. & Doppel, P. Silver thin films deposited by Injection MOCVD. *Electrochem. Soc. Proceeding*, 938–945 (2003).
  28. Schneider, C. a, Rasband, W. S. & Eliceiri, K. W. NIH Image to ImageJ: 25 years of image analysis. *Nat. Methods* **9**, 671–675 (2012).
  29. Massai, L., Cirri, D., Michelucci, E., Bartoli, G., Guerri, A., Cinellu, M. A., Cocco, F., Gabbiani, C. & Messori, L. Organogold(III) compounds as experimental anticancer agents: chemical and biological profiles. *BioMetals* **29**, 863–872 (2016).
  30. Burla, M. C., Caliandro, R., Camalli, M., Carrozzini, B., Cascarano, G. L., De Caro, L., Giacovazzo, C., Polidori, G. & Spagna, R. *SIR2004*: an improved tool for crystal structure determination and refinement. *J. Appl. Crystallogr.* **38**, 381–388 (2005).
  31. Sheldrick, G. M. Crystal structure refinement with SHELXL. *Acta Crystallogr. Sect. C Struct.*

- Chem.* **71**, 3–8 (2015).
32. Nardelli, M. a system of Fortran routines for calculating molecular structure parameters from the results of crystal structure analyses. *J. Appl. Crystallogr.* **28**, 659 (1995).
  33. Macrae, C. F., Bruno, I. J., Chisholm, J. A., Edgington, P. R., McCabe, P., Pidcock, E., Rodriguez-Monge, L., Taylor, R., van de Streek, J. & Wood, P. A. new features for the visualization and investigation of crystal structures. *J. Appl. Crystallogr.* **41**, 466–470 (2008).
  34. Young, A. G. & Hanton, L. R. Square planar silver(I) complexes: A rare but increasingly observed stereochemistry for silver(I). *Coord. Chem. Rev.* **252**, 1346–1386 (2008).
  35. Jakob, A., Ruffer, T., Schmidt, H., Djiele, P., Körbitz, K., Ecorchard, P., Haase, T., Kohse-Höinghaus, K., Frühauf, S., Wächtler, T., Schulz, S., Gessner, T. & Lang, H. Disilver(I) coordination complexes: Synthesis, reaction chemistry, and their potential use in CVD and spin-coating processes for silver deposition. *Eur. J. Inorg. Chem.* **5**, 2975–2986 (2010).
  36. Pointillart, F., Herson, P., Boubekeur, K. & Train, C. Square-planar and trigonal prismatic silver(I) in bipyrimidine and oxalate bridged tetranuclear complexes and one-dimensional compounds: Synthesis and crystal structures. *Inorganica Chim. Acta* **361**, 373–379 (2008).
  37. Allen, F. H. The Cambridge Structural Database: a quarter of a million crystal structures and rising. *Acta Crystallogr. Sect. B* **58**, 380–388 (2002).
  38. Zanotto, L., Benetollo, F., Natali, M., Rossetto, G., Zanella, P., Kaciulis, S. & Mezzi, A. Facile Synthesis and Characterization of New  $\beta$ -Diketonate Silver Complexes. Single-Crystal Structures of (1,1,1,5,5,5-Hexafluoro-2,4-pentadionato)(2,2'-bipyridine)silver(I) and (1,1,1,5,5,5-Hexafluoro-2,4-pentadionato)(N,N,N',N'-tetramethylethylenediamine). *Chem. Vap. Depos.* **10**, 207–213 (2004).
  39. *International Tables for X-ray Crystallography.* **3**, (Kynoch Press, Birmingham, 1962).
  40. Griffith, P. W., KOH, T. Y., White, A. J. P. & Williams, D. J. Two new complexes of 1,8-naphthyridine (napy): The X-ray crystal structures of [OSO<sub>4</sub>(napy)] (1) and of [Ag<sub>2</sub>(u-NaPy)<sub>2</sub>(NO<sub>3</sub>)<sub>2</sub>] (2). *Polyhedron* **14**, 2019–2025 (1995).
  41. Venkatalakshmi, N. & Rajasekharan, M. V. bipyridine ) silver ( I ). A dimer held by stacking and silver-silver interactions. *Transit. Met. Chem* **17**, 455–457 (1992).
  42. Edited by W. M. Haynes. *CRC Handbook of Chemistry and Physics, 94th Edition.* (2013).
  43. Groom, C. R., Bruno, I. J., Lightfoot, M. P. & Ward, S. C. The Cambridge Structural Database. *Acta Crystallogr. Sect. B* **72**, 171–179 (2016).
  44. Darr, J. A., Poliakoff, M., Li, W. & Blake, A. J. Salt Species Soluble in Supercritical Carbon Dioxide †. *Dalt. Trans.* **1**, 2869–2874 (1997).
  45. Frechette, M., Butler, I. R., Hynes, R. & Detellier, C. Structures in Solution and in the Solid State of the Complexes of Lanthanum(III) with 1,10-Phenanthroline - X- Ray Crystallographic and H-1, C-13, O-17, and La-139 Solution NMR Studies. *Inorg. Chem.* **31**,

- 1650–1656 (1992).
46. Thornton, L., Dixit, V., Assad, L. O. N., Ribeiro, T. P., Queiroz, D. D., Kellett, A., Casey, A., Colleran, J., Pereira, M. D., Rochford, G., McCann, M., O’Shea, D., Dempsey, R., McClean, S., Kia, A. F.-A., Walsh, M., Creaven, B., Howe, O. & Devereux, M. No Title. *J. Inorg. Biochem.* **159**, 120–132 (2016).
  47. Abu-Zied, B. M. & Asiri, A. M. An investigation of the thermal decomposition of silver acetate as a precursor for nano-sized Ag-catalyst. *Thermochim. Acta* **581**, 110–117 (2014).
  48. Tao, Y., Wang, L., Tao, Y., Wang, B. & Tai, Y. A facile approach to a silver conductive ink with high performance for macroelectronics. *Nanoscale Res. Lett.* **8**, 296 (2013).
  49. Ohtaki, H. & Yoshiakiito. COMPLEX FORMATION OF SILVER ION WITH ETHYLENEDIAMINE AND 1,2-PROPANEDIAMINE. *J. Coord. Chem.* **3**, 131–144 (1973).
  50. Fox, B. S., Beyer, M. K. & Bondybey, V. E. Coordination chemistry of silver cations. *J. Am. Chem. Soc.* **124**, 13613–13623 (2002).
  51. G.Newman & D.B.Powell. The Infrared Spectra and structures of some Silver-Ethylenediamine complexes. *J. Chem. Soc.* 3447–3450 (1962).
  52. Peng, S., McMahon, J. M., Schatz, G. C., Gray, S. K. & Sun, Y. Reversing the size-dependence of surface plasmon resonances. *Proc. Natl. Acad. Sci.* **107**, 14530–14534 (2010).
  53. Mogensen, K. B. & Kneipp, K. Size-dependent shifts of plasmon resonance in silver nanoparticle films using controlled dissolution: Monitoring the onset of surface screening effects. *J. Phys. Chem. C* **118**, 28075–28083 (2014).
  54. Abd El Rehim, S. S., Hassan, H. H., Ibrahim, M. a. M. & Amin, M. a. Electrochemical Behaviour of a Silver Electrode in NaOH Solutions. *Monatshhefte fuer Chemie/Chemical Mon.* **129**, 1103–1117 (1998).
  55. J.Turner. Electrolytic studies on the system Ag / Ag<sub>2</sub>O / AgO in alkaline chloride solutions. *J. Appl. Electrochem.* **7**, 369–378 (1977).
  56. Munoz-Rojas, D., Fraxedas, J., Oró, J., Gómez-Romero, P. & Casañ-Pastor, N. Structural study of electrochemically-synthesized Ag<sub>2</sub>Cu<sub>2</sub>O<sub>4</sub>. A novel oxide sensitive to irradiation. *Cryst. Eng.* **5**, 459–467 (2002).
  57. Wang, F., Eylem, C., Nanjundaswamy, K. & Ilchev, N. Determination of AgCuO<sub>2</sub> Discharge Mechanism in Alkaline Electrolyte. *Electrochem. Solid-State Lett.* **7**, A346 (2004).
  58. Muñoz-Rojas, D., G.Subias, J.Fraxedas, P.Gomez-Romero & N.Casañ-Pastor. Electronic Structure of Ag<sub>2</sub>Cu<sub>2</sub>O<sub>4</sub>. Evidence of Oxidized Silver and Copper and Internal Charge Delocalization. *J. Phys. Chem. B* **109**, 6193–6203 (2005).
  59. Waterhouse, G. I. N., Bowmaker, G. A. & Metson, J. B. Oxidation of a polycrystalline silver foil by reaction with ozone. *Appl. Surf. Sci.* **183**, 191–204 (2001).

60. Waterhouse, G. I. N., Bowmaker, G. A. & Metson, J. B. Interaction of a polycrystalline silver powder with ozone. *Surf. Interface Anal.* **33**, 401–409 (2002).
61. NISHIMURA, T. & HOSHODA, S. SEPARATION OF SILVER BY OZONE OXIDATION OF SILVER NITRATE SOLUTION. *Canadian Metallurgical Quarterly* **47**, 27–36 (2008).
62. Muñoz-Rojas, D., Fraxedas, J., Gómez-Romero, P. & Casañ-Pastor, N. Room temperature solid-state transformation from to by ozone oxidation. *J. Solid State Chem.* **178**, 295–305 (2005).



<i>Chapter IV Deposition of Highly crystalline Cu<sub>2</sub>O films via AA-MOCVD</i>	<i>- 110 -</i>
<i>IV.1 Optimization of deposition system and reaction parameters</i>	<i>- 111 -</i>
<i>IV.1.1 Deposition system configuration</i>	<i>- 111 -</i>
<i>IV.1.2 Choice of precursors</i>	<i>- 114 -</i>
<i>IV.1.2.1 Effects of oxygen ratio during deposition with Cu(AcAc)<sub>2</sub> precursor</i>	<i>- 114 -</i>
<i>IV.1.2.2 Deposition under oxidizing conditions using plasma with Cu(AcAc)<sub>2</sub> precursor</i>	<i>- 116 -</i>
<i>IV.1.3 Depositions of Cu<sub>2</sub>O films using CuF as precursor</i>	<i>- 118 -</i>
<i>IV.1.3.1 Optimization of uniformity</i>	<i>- 118 -</i>
<i>IV.1.3.2 Optimization for oxygen ratio</i>	<i>- 119 -</i>
<i>IV.2 Tuning the texture of Cu<sub>2</sub>O thin films</i>	<i>- 121 -</i>
<i>IV.2.1 Effect of the presence of Ag particles on film growth and morphology</i>	<i>- 122 -</i>
<i>IV.2.2 Effects of humidity on thin film orientation, morphology and electronic properties</i>	<i>- 125 -</i>
<i>IV.3 Studies on the reaction mechanism</i>	<i>- 140 -</i>
<i>IV.3.1 Study of the initial stages of thin film growth.</i>	<i>- 140 -</i>
<i>IV.3.2 Thermodynamic model</i>	<i>- 142 -</i>
<i>IV.4 Chapter IV conclusions</i>	<i>- 145 -</i>
<i>IV.5 References</i>	<i>- 147 -</i>

*Chapter IV Deposition of Highly crystalline Cu<sub>2</sub>O  
films via AA-MOCVD*

In Chapter III, the deposition of metallic silver and further oxidation to its oxides by MOCVD and post treatments have been detailed. To obtain the AgCuO<sub>2</sub> phase by MOCVD, the parameters and setup optimization for the deposition of copper oxide thin films was also carried out. Given that oxidizing conditions are needed to obtain AgCuO<sub>2</sub> and that plasma was only available in our AA-MOCVD system, we only studied the deposition of Cu oxides by AA-MOCVD. In this chapter of work, in order to overcome several issues, optimizations of our deposition system will be described. The effect of different parameters, such as oxygen ratio, presence of Ag and humidity, on the morphology of the Cu<sub>2</sub>O films will be

discussed. By adjusting the different deposition parameter,  $\text{Cu}_2\text{O}$  films with controlled texture have been achieved. High quality textured  $\text{Cu}_2\text{O}$  films have been characterized and implemented in diodes, obtaining on-off ratios exceeding  $10^4$ . To further study the electrical properties of the of (111) textured  $\text{Cu}_2\text{O}$  films, they were characterized by Conductivity Atomic Force Microscope (CAFM) and automatic crystal orientation and phase mapping technique (ASTAR), the correlation between conductivity and phases will be revealed. Lastly, to understand the formation mechanism of larger size grains with the different deposition conditions, short duration depositions have been conducted and different thin film growth modes have been discovered. Furthermore, from the point view of thermodynamics, the formation mechanism has been explained by applying the classical nucleation theory.

## IV.1 Optimization of deposition system and reaction parameters

### IV.1.1 Deposition system configuration

The original AA-MOCVD system has been presented in Chapter II (Figure II-3), with precursor flow coming from the bottom to the top and reacting on the hot plate above (which faces down). While conducting the initial depositions with such configuration, it was very hard to obtain good homogeneity of the deposited  $\text{Cu}_2\text{O}$  films. As it's well-known, in MOCVD, a stable laminar precursor flow is crucial to obtain homogeneous depositions. Under such configuration, the precursor flow needs to go from bottom to the top, against gravity. Even though the large particles and droplets can be avoided in this case, it's rather challenging to obtain a homogeneous flow, as shown in Figure IV-1 a).

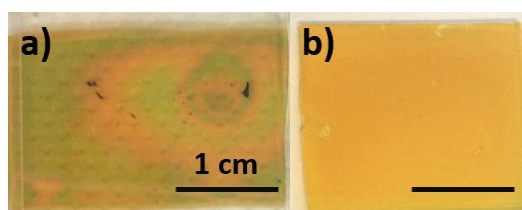


Figure IV-1. Depositions of  $\text{Cu}_2\text{O}$  via AA-MOCVD using our homemade system at  $330\text{ }^\circ\text{C}$  for 1 hour a) in its initial configuration, roughly 60 nm thick; b) in the optimized configuration with thickness about 100 nm.

Comparing to the  $\text{Cu}_2\text{O}$  films deposited with the same conditions using the later optimized case (figure b, see details below), the color gradient due to the uneven thickness is rather clear in figure a). Even worse, with the same precursor consumption rate in the original configuration, the  $\text{Cu}_2\text{O}$  thin film deposition rate is much lower than in the optimized case, indicating a higher percentage of precursor waste. In general, under such configuration in



our AA-MOCVD system, it was rather difficult to obtain optimized and reproducible samples.

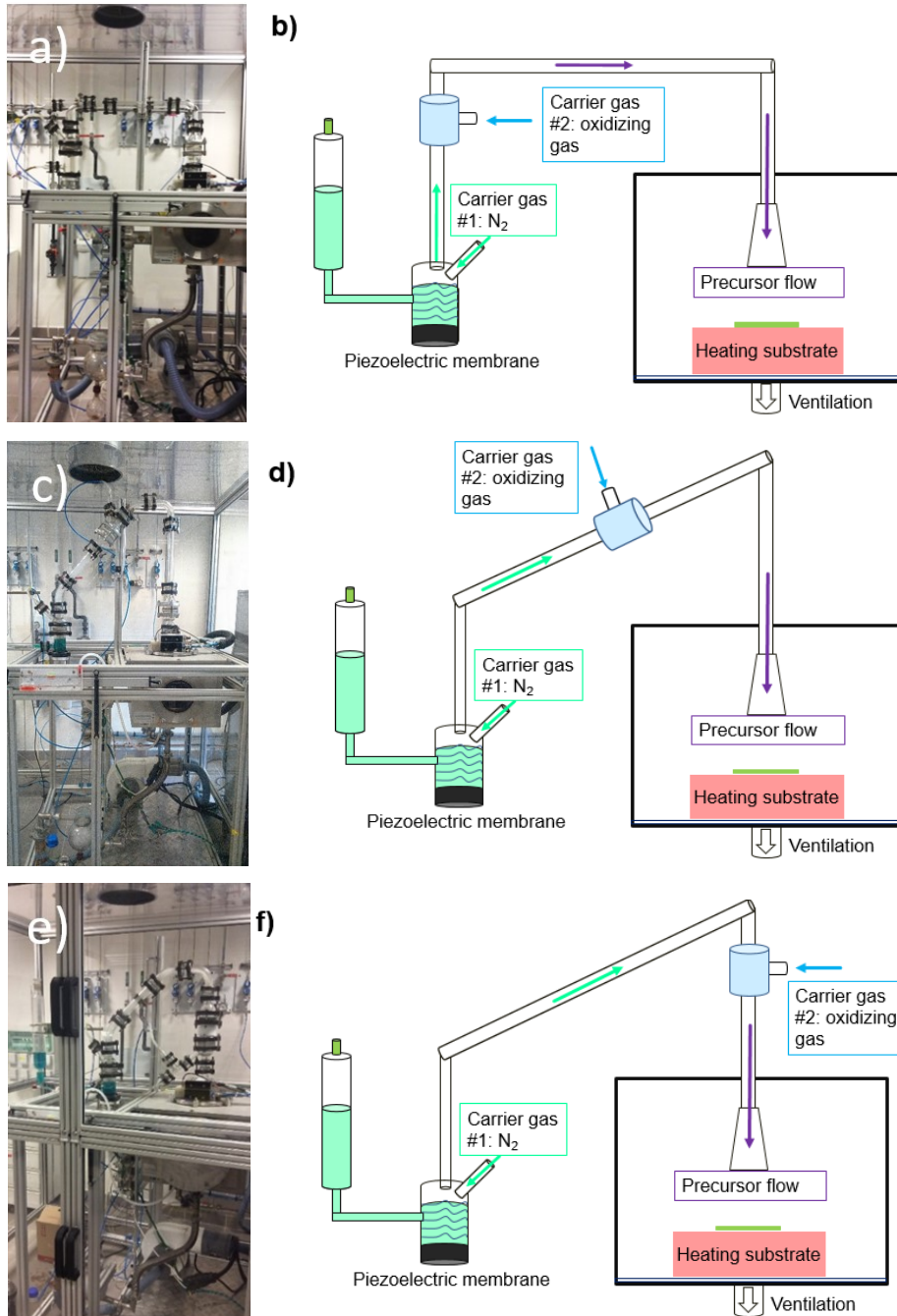


Figure IV-2. Different configurations in the process of AA-MOCVD optimization

To avoid some of these issues, the first modification was to reverse the orientation of the deposition chamber, turning it by  $180^\circ$ . In this configuration, the entrance of the flow into the deposition chamber is located at the top of the chamber, the heating plate staying at the bottom, facing up. The ventilation outlet was also placed at the bottom, to the right, below the hot plate (Figure IV-2 a).

As it is shown in Figure IV-2 a) and b), initially there was a part of the system in which the flow was horizontal before entering the chamber. When tests were performed with such configuration, due to the gravity, a separation between the precursor and the carrier gas was observed (i.e. a layer of precursor solution formed on the horizontal tube). Thus when the flow entered the deposition chamber, it wasn't laminar, and it even carried big droplets from the condensation on the glass tube. Thus, in order to avoid this carrier gas and flow separation, this section of glass tubing was tilted from  $0^\circ$  to approximately  $45^\circ$  with respect to the horizontal (Figure IV-2 b). With such a tilt, it also largely reduced the chance for the condensed solution droplets in the tube to end falling into the deposition chamber. The tilt also enabled a smooth and homogeneous introduction of aerosol droplets into the deposition chamber, while avoiding bigger size droplets that form following condensation in the tube walls.

Lastly, the location of the carrier gas #2 (CG#2) inlet was also carefully optimized: at the beginning of the tube (Figure IV-2 a), in the middle of the tube (Figure IV-2 b) and at the end of the tube (Figure IV-2 c). Placing it at a bigger distance away from the CG#1 inlet, the bigger droplets in the flow have more time to condense and return back to the solution chamber instead of reaching the hot substrate. In addition, it's more safe to separate the oxidizing gas far from the aerosol chamber, where hot flammable solvent is present.

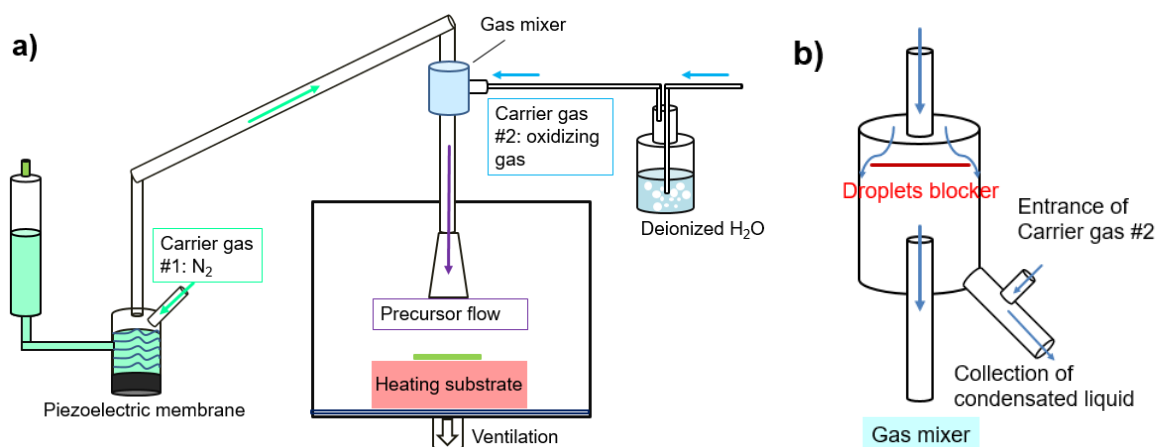


Figure IV-3. Details of the final optimized AA-MOCVD configuration.

Despite the improvement observed with the optimized system configuration, i.e. a homogeneous precursor flow was obtained with majority of the bigger droplets avoided, from time to time, several holes of small size (about 0.5 mm in diameter) were still visible. Even after a careful cleaning of the glass substrate and the deposition chamber, the problem wasn't solved. Thus in order to collect the condensed liquid and further reduce big size droplets, minimizing the chances of having bigger droplets reaching the substrate, a simple

gas mixer was designed fulfill two functions: introducing CG#2 and collecting condensed droplets.

As shown in **Figure II-4**, a square Si substrate was cut to precisely fit into the bigger round gas tube, just beneath the arrival of the flow through the main thinner tube. As the solution mist comes down from the top, the heavier, faster droplets impacted on the Si substrate, falling along its edges to be finally collected at the bottom of the large tube. CG#2 was introduced from the bottom and well mixed inside the bigger gas tube with the solution mix before reaching the deposition chamber through the thinner tube at the bottom (see Figure II-4 b). Thus with such gas mixer, hole free samples with better homogeneity were obtained, with good reproducibility. As a result, nice and homogeneous  $\text{Cu}_2\text{O}$  films could be deposited as shown in Figure IV-1 b.

## IV.1.2 Choice of precursors

Besides the MOCVD system optimization, the choice of precursor used in MOCVD also plays an important role in the final quality and properties of the deposited films. For the deposition of copper oxides, there are several commercial metalorganic precursors available. By taking into account both precursor cost and deposition quality, mainly  $\text{Cu}(\text{AcAc})_2$  (Copper (II) acetylacetonate, STREM Chemicals 98%) and  $\text{CuF}$  (Copper (II) trifluoroacetylacetonate hydrate, STREM Chemicals 99%) were used in this work.

### IV.1.2.1 Effects of oxygen ratio during deposition with $\text{Cu}(\text{AcAc})_2$ precursor

$\text{Cu}(\text{AcAc})_2$  was firstly tested for  $\text{Cu}_2\text{O}$  thin film deposition with various oxygen/nitrogen ratios and deposition temperatures, as shown in Table IV-1. Precursor solutions with a 0.02 M concentration were prepared by mixing 2.62 g of precursor with 500 ml butanol and 1.5 ml of ethylenediamine. With magnetic bar stirring for 10 more min, a crystal clear blue solution was obtained. (More detailed information can be found in Chapter II). The samples were deposited on glass substrate at temperatures ranging from 350 to 375 °C for 1 h with a total carrier gas (CG) flow of 10 L/min (composed of nitrogen and oxygen).

Table IV-1. Deposition parameters using  $\text{Cu}(\text{AcAc})_2$  as precursor.

O <sub>2</sub> ratio in CG	25%	40%	60%	80%
Temperature (°C)				
350 °C	A01	A02	A03	A04
375 °C	B01	B02	B03	B04

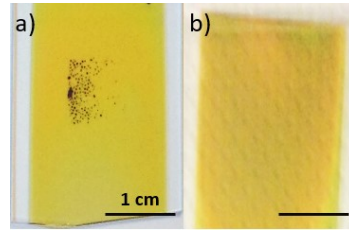


Figure IV-4.  $\text{Cu}_2\text{O}$  films deposited at 320 °C a) and 370 °C b) with  $\text{Cu}(\text{AcAc})_2$  0.01 M concentration for 1 hour in AA-MOCVD. (The black dots on the  $\text{Cu}_2\text{O}$  films are carbon tape residues)

With different oxygen ratio during deposition at 350 °C, the morphology of the samples was rather smooth and similar, as presented in Figure IV-5. The deposited  $\text{Cu}_2\text{O}$  films had thickness around 100 nm. The grain size was very small (about 20 nm) but with dense structure. Samples deposited at 375 °C looked very similar to samples deposited at 320 °C, as shown in Figure IV-4 a) and b). With Raman Spectroscopy, the deposition quality of all samples was further examined, and the results are shown in Figure IV-6.

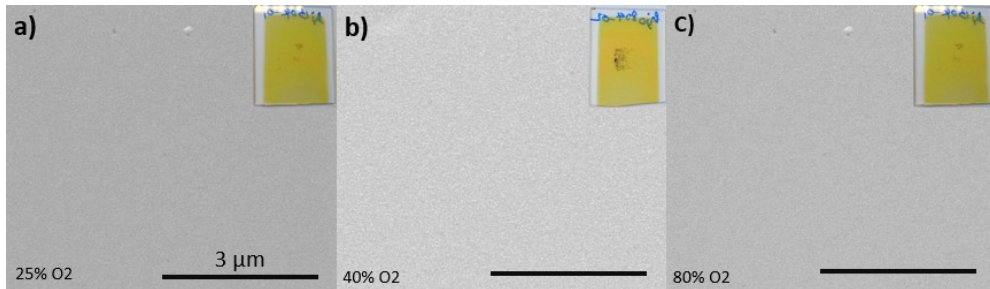


Figure IV-5. SEM images of  $\text{Cu}_2\text{O}$  samples deposited with various oxygen ratios (total flow 10 L/min made of oxygen and nitrogen) at 350 °C. a) 25% of  $\text{O}_2$ . b) 40% of  $\text{O}_2$ . c) 80 % of  $\text{O}_2$ .

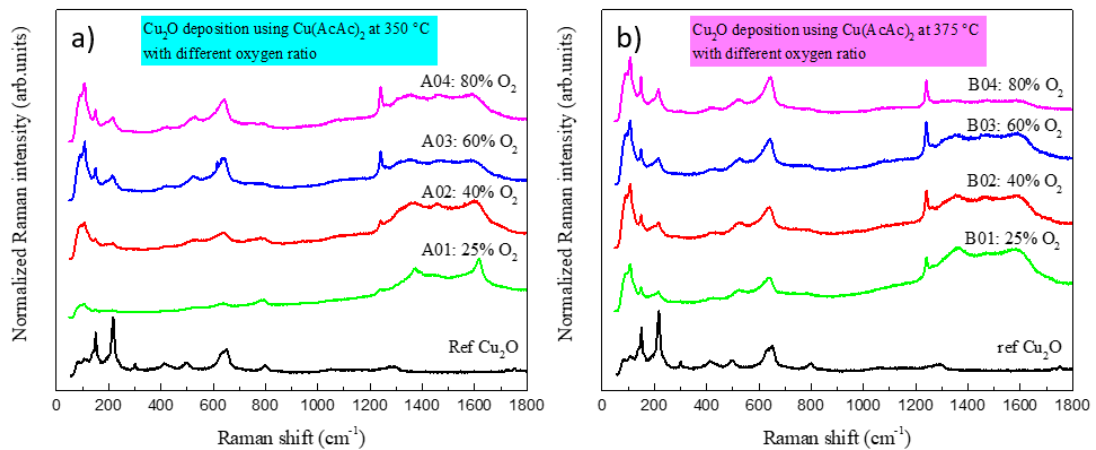


Figure IV-6. Raman spectroscopy curves of a)  $\text{Cu}_2\text{O}$  samples deposited at 350 °C and b) deposited at 375 °C for 1 hour, with oxygen ratio ranging from 25% to 80% using  $\text{Cu}(\text{AcAc})_2$  as precursor.

As shown in Figure IV-6 a),  $\text{Cu}_2\text{O}$  samples deposited at 350 °C present several bands over 1200  $\text{cm}^{-1}$  that correspond to carbon group contaminations in the films. With higher oxygen ratio used during the deposition process, the signal of carbon contamination decreased, which can be attributed to the higher oxygen ratio facilitating precursor decomposition.

But even at the maximum oxygen ratio 80% used, the carbon group signal is still rather visible. At higher deposition temperature 375 °C, similar carbon contamination and trend with oxygen ratio can be found in Figure IV-6 b). In any case, even with the presence of carbon contamination, no peaks corresponding to CuO phase were observed.

#### **IV.1.2.2 Deposition under oxidizing conditions using plasma with Cu(AcAc)<sub>2</sub> precursor**

Due to the high oxidation environment requirement to form AgCuO<sub>2</sub> phase, we explored the use of the atmospheric plasma system coupled to the AA-MOCVD deposition system (see in Chapter II). In addition to providing highly oxidizing conditions, the plasma system was expected to facilitate precursor decomposition, to enhance film crystallinity and to reduce carbon contamination.<sup>1,2,3</sup> The emission characteristics of the plasma head have been reported in Chapter III, showing that a minimum power of 300 W is necessary to obtain ozone species when using pure O<sub>2</sub> as gas source. Before using the plasma for copper oxide film deposition, two types of glass substrates (Frost microscope slide and Corning glass) were tested under oxygen plasma with power of 500 W for 30 min. The glasses were then characterized by Raman spectroscopy. Figure IV-7 shows the Raman spectra of the glasses before and after the treatment are shown. For the frost glass, several extra peaks originally not existing at 101 and 187 cm<sup>-1</sup> can be observed after the plasma treatment, as shown in Figure IV-7 a). As shown in the inserted photo, a white layer was observed on the glass substrate which might correspond to the several new emerged peaks. When the deposition of copper oxide with plasma was tested on this type of glass substrates, no copper oxide films could be coated on top. Conversely, for corning glass, the Raman curves present no difference before and after the oxygen plasma treatment under the same conditions. In addition, copper oxide films could be obtained on corning glass when using the plasma (as detailed below). Thus, corning glass showed better stability than normal microscope glass slide under oxygen plasma and was used as the substrate for the optimization of the deposition of copper oxide films with plasma.

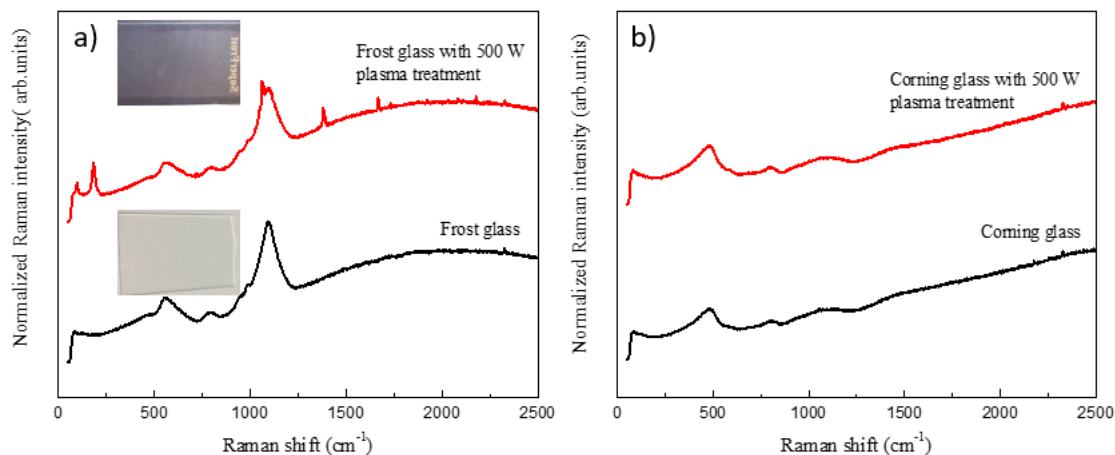


Figure IV-7. Raman spectroscopy curves of a) Frost microscope glass slide (Inset: optical image of the substrate before and after plasma treatment) and b) corning glass slide before and after 30 min 500 W oxygen plasma treatment.

Due to the highly reactive radicals emitted by the oxygen plasma, precursor molecules can react/decompose before reaching the substrate which leads to less reaction taking place on the substrate. As a consequence, higher precursor concentration is required (minimum 0.05 M). The copper oxide films were deposited under different oxygen ratio plasma (30% and 60%) using a plasma power of 350 W, and a deposition temperature of 300 °C, for 1 hour. Since the purpose of using plasma during deposition was mostly focusing on the investigation of precursor decomposition at low temperature (so that the conditions remain compatible with the deposition of Ag oxides), thus tests at higher temperatures were not conducted. The films obtained were characterized by Raman spectroscopy. As shown in Figure IV-8, in both deposition conditions, and despite the use of plasma, the deposited copper oxide films exhibited strong signal of carbon contamination as previously observed, even though the signal slightly decreased with higher oxygen ratio. As shown by the optical images in the figure, the coatings showed a dark brown color. No peaks from CuO or  $\text{Cu}_2\text{O}$  phase could be observed in the Raman spectra, possibly due to a low crystallinity at this low deposition temperature. Therefore, the deposition of carbon free  $\text{Cu}_2\text{O}$  films using  $\text{Cu}(\text{AcAc})_2$  as precursors were rather difficult in our AA-MOCVD system, better copper precursor with clean decomposition was needed.

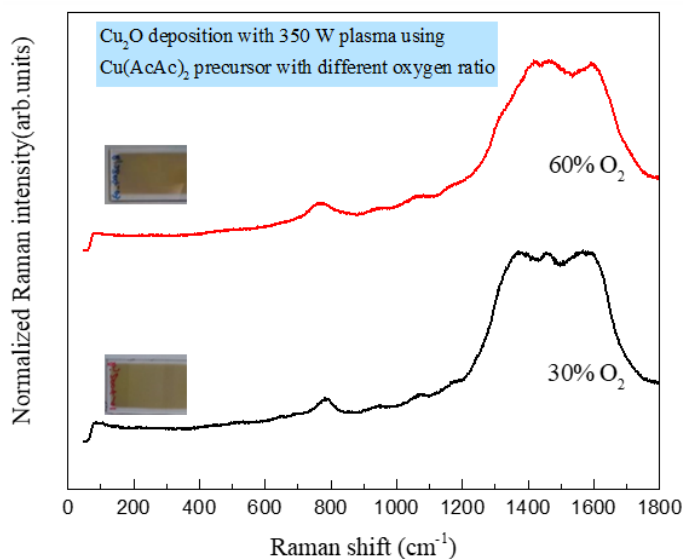


Figure IV-8. Raman spectra of copper oxide films deposited with 0.6 (black) and 0.3 (red) oxygen ratio as gas source (total flow 15 L/min with  $\text{N}_2$  and  $\text{O}_2$ ). Precursor  $\text{Cu}(\text{AcAc})_2$  concentration 0.05 M with 1 hour deposition at 300 °C.

### IV.1.3 Depositions of $\text{Cu}_2\text{O}$ films using $\text{CuF}$ as precursor

Due to the carbon contamination problems with  $\text{Cu}(\text{AcAc})_2$  as precursor, thus for later  $\text{Cu}_2\text{O}$  depositions Copper (II) trifluoro acetylacetonate ( $\text{CuF}$ , 99%, Strem Chemical) was tested in the final optimized AA-MOCVD configuration.

#### IV.1.3.1 Optimization of uniformity

The initial depositions were conducted with 0.01 M  $\text{CuF}$  precursor solution at 330 °C for 1 hour on two type of well cleaned glasses, Frost glass and Corning glass. The deposited  $\text{Cu}_2\text{O}$  films are shown in Figure IV-9, in which figure a) presents the  $\text{Cu}_2\text{O}$  coating deposited on Frost glass (typically with scattered  $\text{Cu}_2\text{O}$  grains on surface) and b) shows the  $\text{Cu}_2\text{O}$  deposition on Corning glass (typical  $\text{Cu}_2\text{O}$  thin film, but need optimization). On Frost glass it was very difficult to obtain dense and continuous  $\text{Cu}_2\text{O}$  films.

Even with the MOCVD system optimized and the correct precursor, clean substrate being chosen, the  $\text{Cu}_2\text{O}$  deposition shown in Figure IV-9 b) is still covered with lots of strange traces. Those marks were thought to be due to the rough surface of the heating plate, thus a flat Si substrate (with diameter about 7.5 cm) was inserted between the glass substrate and the rough heating plate. Under the same deposition condition, the  $\text{Cu}_2\text{O}$  film, as shown in Figure IV-9 c), presented a rather good homogeneity free out those marks on surface. Further characterizations of the  $\text{Cu}_2\text{O}$  films can be found in Figure IV-10 below.

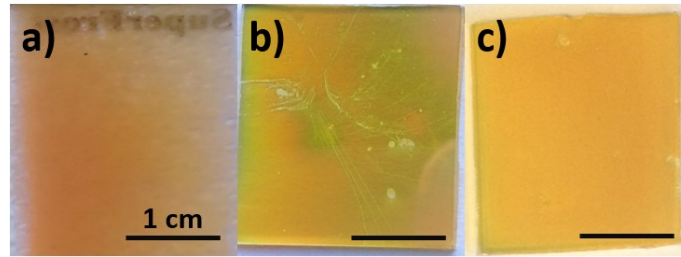


Figure IV-9.  $\text{Cu}_2\text{O}$  coatings using  $\text{CuF}$  as precursor at  $330^\circ\text{C}$  deposited on a) Frost glass and b) Corning glass. c) Optimized  $\text{Cu}_2\text{O}$  film on Corning glass.

#### IV.1.3.2 Optimization for oxygen ratio

It is well known that oxygen plays an important role during the MOCVD process, especially for metal oxide thin film deposition.<sup>4-6</sup> In this work, experiments were carried out with various oxygen ratios during deposition, as shown in Table IV-2, namely D1 (12.5%  $\text{O}_2$ ), D2 (13.75%  $\text{O}_2$ ) and D3 (15%  $\text{O}_2$ ). Precursor solutions using  $\text{CuF}$  with concentration of 0.01 M were prepared based on the description in Chapter II. To compare with  $\text{Cu}_2\text{O}$  films deposited with  $\text{Cu}(\text{AcAc})_2$ , samples were deposited at  $335^\circ\text{C}$  for 1 hour on cleaned Corning glass substrates, with  $\text{CuF}$  precursor solution consumption rate of about 1.5 ml/min and total carrier gas flow of 10 L/min (using nitrogen and oxygen).

Table IV-2.  $\text{Cu}_2\text{O}$  depositions with  $\text{CuF}$  precursor under different oxygen ratios for 1 hour.

Sample names	D1	D2	D3
Oxygen ratio (%)	12.5	13.75	15
Thickness (nm)	100	165	Not a thin film
Resistivity ( $\Omega\cdot\text{cm}$ )	220	215	~250

Figure IV-10 presents the SEM images and Raman spectra of coatings obtained with different oxygen ratio. For 12.5%  $\text{O}_2$  ratio (D1), a dense film with smooth surface and small sized grains was obtained (Figure IV-10 a)). By slightly rising the oxygen ratio in the flow to 13.75% (D2), the surface of the deposited films was rather similar, being still dense and continuous, as shown in Figure IV-10 b). When the oxygen ratio was further increased to 15% (D3), Figure IV-10 c), the films presented a non-continuous, rough surface with clear cubic  $\text{Cu}_2\text{O}$  grains. All those cubic like grains were stacked together with only the corner of the cube pointing above. Those films were characterized by Raman spectroscopy which confirmed the only existence of  $\text{Cu}_2\text{O}$ , as shown in Figure IV-10 d) below. As shown, the intensities of the peaks were rather similar in all cases, with no extra peak at higher oxygen partial pressure, thus eliminating the presence of significant amounts of  $\text{CuO}$  phase in the films. As well, the intensity of the peak around  $200\text{ cm}^{-1}$  presented a rather big difference between the deposited  $\text{Cu}_2\text{O}$  films and the reference curve, which was possibly due to certain



orientation of the polycrystalline grains in the films. Even though the XRD characterizations were also conducted, due to the low thickness of those films, the reflections were full of noise and difficult to distinguish useful information, they are not presented here.

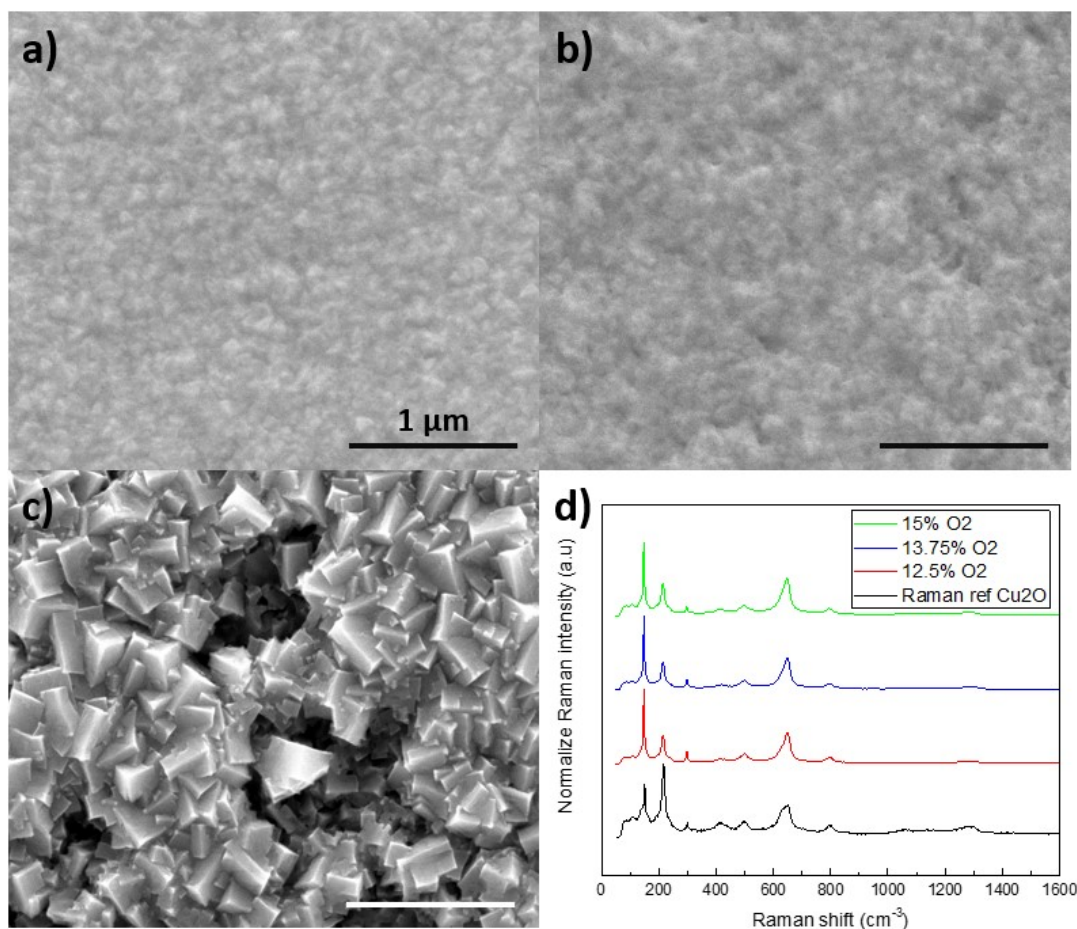


Figure IV-10. SEM of  $\text{Cu}_2\text{O}$  samples deposited at  $335\text{ }^\circ\text{C}$ , for 1 hour with different oxygen ratio: a).  $12.5\% \text{O}_2$ ; b).  $13.75\% \text{O}_2$ ; c).  $15\% \text{O}_2$ . With increasing of oxygen ratio during deposition, more cubes of  $\text{Cu}_2\text{O}$  were formed. d) Raman spectra for  $\text{Cu}_2\text{O}$  films deposited with different oxygen ratio.

Comparing with the Raman curves from  $\text{Cu}_2\text{O}$  samples deposited with  $\text{Cu}(\text{AcAc})_2$  precursor (in Figure IV-6), the Raman spectra from  $\text{Cu}_2\text{O}$  depositions with  $\text{CuF}$  precursor did not show a measurable quantity of carbon contamination. The resistivity of the different films was measured using four point probe and all gave values between  $215$  and  $250\ \Omega\cdot\text{cm}$ , as indicated in Table IV-2. In addition, as shown in the same table, the deposition rate has the trend of enhancing with higher oxygen ratio during deposition, even though the thickness for Figure IV-10 c) is a range between  $120$  and  $197\ \text{nm}$  due to the discontinuity and roughness of the film, which is in accordance with the work of *G.G. Condorelli et al.*<sup>4</sup> To summarize, oxygen ratio in the carrier gas presented a huge impact on the surface morphology of  $\text{Cu}_2\text{O}$  films deposited by MOCVD. A slight increase of oxygen ratio during the MOCVD process yielded  $\text{Cu}_2\text{O}$  films with clear cubic shape grains, while at the same time the surface became rougher

and discontinuous. Comparing the deposition results and optimization process with both precursors, it's much easier to achieve good quality, carbon free and homogeneous Cu<sub>2</sub>O films with CuF as the precursor. The later described Cu<sub>2</sub>O films were thus all deposited with CuF precursor.

## IV.2 Tuning the texture of Cu<sub>2</sub>O thin films

In addition to obtaining thin film depositions with good homogeneity, we managed to tune the texture of the Cu<sub>2</sub>O films by modifying and optimizing the deposition conditions. Textured Cu<sub>2</sub>O films have been mostly obtained by electrochemical deposition.<sup>7,8</sup> In MOCVD, it is well known that adding water vapor to the reaction can facilitate precursor decomposition, enhancing crystallinity and reducing carbon contamination.<sup>9,10</sup> *J-Y Kim et al*<sup>11</sup> reported that Cu metallic films were deposited through MOCVD using a humid flow. In their work, different deposition rates were achieved by controlling the humidity. In another work by *A. Jain et al.*<sup>10</sup>, a detailed explanation was given on the mechanism by which the presence of H<sub>2</sub>O facilitates copper precursor decomposition, involving a proton transfer between H<sub>2</sub>O and the organic precursor. But the effects of humidity on the deposition of Cu<sub>2</sub>O thin films in terms of morphology, grain orientation and electronic properties has not been studied in detail.

In this section of work, several approaches have been found to tune the grain structure in Cu<sub>2</sub>O films, namely, presence of Ag nanoparticles and addition of humidity in the carrier gas. Of the two approaches, the addition of humidity in the carrier gas has shown an obvious impact on grain orientation and morphology, and thus on the resulting electronic properties. By adjusting the humidity in the gas flow we were thus able to tune the deposition speed and texture orientation of deposited Cu<sub>2</sub>O films. As well, an evolution of mobility with deposition temperature and carrier gas humidity was observed, reaching a maximum of 17 cm<sup>2</sup>/V.s. In addition, we used optimized Cu<sub>2</sub>O films to form p-n junctions with ZnO, showing an excellent rectification with an on-off ratio exceeding 10<sup>4</sup>. In order to understand the impact of carrier gas humidity on morphology, the initial nucleation process was studied. Finally, we used the classical nucleation theory and thermodynamics of film growth to explain the results obtained. All the above are shown and discussed in detail in the following sections.

## IV.2.1 Effect of the presence of Ag particles on film growth and morphology

The effects of noble metal on the formation of Cu oxides have been discussed in the work by *L. Wang et al.*<sup>12</sup>, in which the Cu<sub>2</sub>O cubic grain formation by oxidizing a Cu<sub>0.5</sub>-Au<sub>0.5</sub> alloy substrate was studied. Also, in another work by *C.C.Tseng et al.*<sup>13</sup>, the optical and electrical properties of Cu<sub>2</sub>O films incorporating Ag deposited by magnetron sputtering was evaluated. Therefore, in this work we have explored the effects of the presence of Ag in Cu<sub>2</sub>O film formation by AA-MOCVD.

To achieve the incorporation of silver, **AgT** was added to the CuF solution. Table IV-3 summarizes the experimental conditions of each sample deposited with different quantity of Ag incorporated. Copper and silver precursors were mixed in the same alcohol solvent and co-deposited at the same time on Corning glass substrate.

Table IV-3. Cu<sub>2</sub>O samples deposited with different quantity of Ag incorporated.

Sample name	L0	L1	L2	L3	L4	L5
Cu : Ag ratio in solution	Pure	10:0.625	10:0.833	10:1	10:1.25	10:2.5
Ag ratio in film (atom ratio)	None	Not detectable			0.3%	1%
Thickness (nm)	462	682	738	742	774	779

Due to the costly nature of silver precursors, the exploration with higher precursor concentration was avoided. Copper precursor concentration was fixed at 10 mM and depositions were carried out at 335 °C for 3.5 hours. The quantity of Ag in the final Cu<sub>2</sub>O films was adjusted by varying the initial silver precursor concentration. The quantity of Ag in the film was estimated by EDS (using potential of 15 kV with a full scan of surface area about 3 μm × 3 μm).

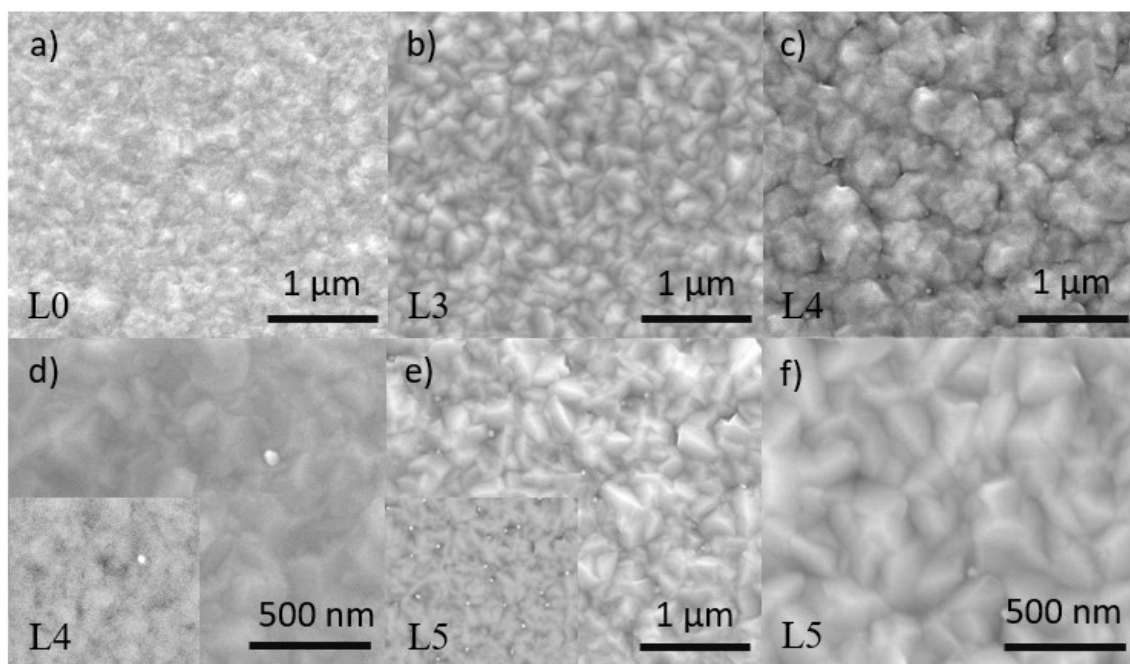


Figure IV-11.  $\text{Cu}_2\text{O}$  film deposited with  $\text{CuF}$  10 mM concentration a) without Ag precursor (L0) at 335 °C for 3.5 hours and samples with various AgT precursor concentration added: b) 10 mM  $\text{CuF}$ : 1 mM AgT (L3); c) and d) 10 mM  $\text{CuF}$ : 1.25 mM AgT (L4), the inserted image is the backscattering electron image; e) and f) 10 mM  $\text{CuF}$ : 2.5 mM AgT (L5), the inserted image is the backscattering electron image.

As presented in Figure IV-11, the morphology of  $\text{Cu}_2\text{O}$  film deposited without adding Ag precursor is shown in figure a), with a rather smooth and dense surface. In figure b), it presents the morphology of  $\text{Cu}_2\text{O}$  film with small quantity of AgT precursor added (sample L3) but the silver content is below the detection limit of EDS. The morphology of samples L1 and L2 is rather similar with L3, in which more clear cubic shape of the  $\text{Cu}_2\text{O}$  grains emerged on the surface. Figure c) and d) show the SEM images of coatings obtained with further increased silver precursor mixed into the deposition solution (detectable Ag atomic ratio 0.3% to Cu). In figure c), a much rougher surface is presented with visible bigger grains. In addition, several nanoparticles scattered across the sample surface and locate at the lower points between the bigger grains. With the inserted backscattering electron image at high magnification in figure d), the nanoparticle was identified as a heavier element than copper, which is most likely to be silver.

With the highest concentration of silver precursor added, the surface of the thin film is also full of scattered silver nanoparticles between the grains, as shown in figure e). It is more clear in the backscattering electron image in the inset. The EDS showed Ag ratio of 1% in the film. With higher magnification image in figure f), cubic shaped grains with sizes of about 200-300 nm and clear grain boundaries are presented.

Thin film thickness was obtained from SEM cross-section measurement, and is detailed in Table IV-3. It is clear that the addition of Ag precursor yielded higher deposition rates. By calculating the average deposition rate as a function of the concentration of Ag precursor (see Figure IV-12), we observed that the deposition rate was enhanced from 2.1 nm/min to 3.5 nm/min.

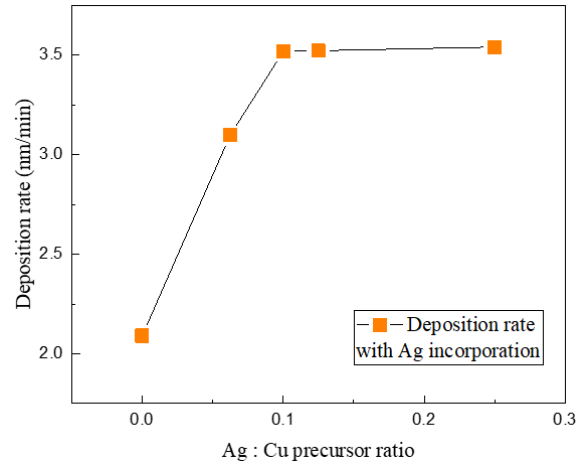


Figure IV-12. The average deposition rate with different silver quantity incorporated.

To check the crystallinity evolution of  $\text{Cu}_2\text{O}$  with the amount of silver, Raman Spectroscopy characterization was conducted. As presented in Figure IV-13 a), Raman curves show that all films deposited with Ag incorporation are still composed of  $\text{Cu}_2\text{O}$  phase without any trace of  $\text{CuO}$ . Interestingly, with more Ag used, a change in peak intensity has been found for the strongest peak  $165\text{ cm}^{-1}$  and the second strongest one at  $210\text{ cm}^{-1}$ , which can be attributed to a change in grain orientation or an increase in film crystallinity.

In Figure IV-13 b), the XRD patterns of these samples also confirmed the orientation shift. Without adding Ag precursor (sample L0), the main orientations obtained were assigned to (1,1,0) and (1,1,1). While as more silver precursor were mixed into the deposition solution, thus more Ag particles were incorporated, the intensity of the reflection corresponding to (1,1,0) decreased while the reflection corresponding to (1,1,1) increased, especially obvious in sample L5.

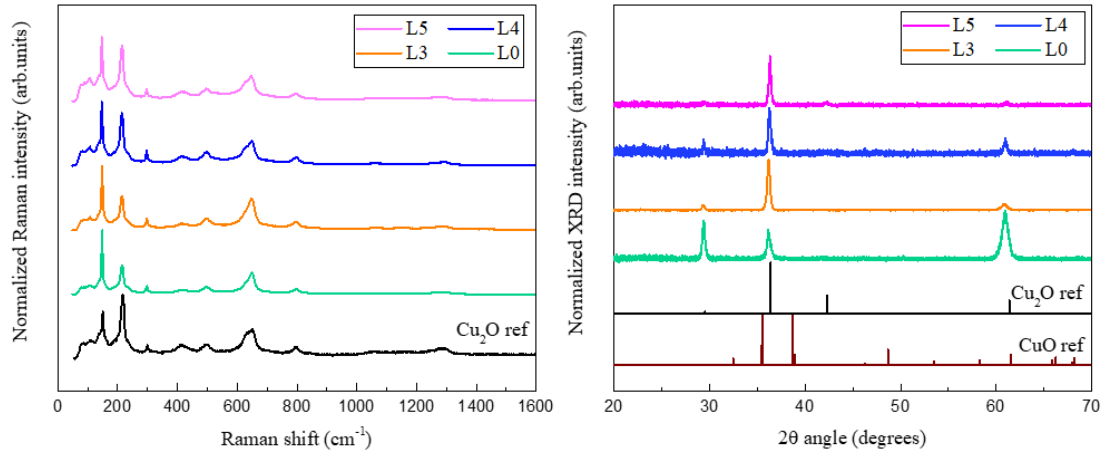


Figure IV-13.  $\text{Cu}_2\text{O}$  films deposited with various quantity of silver precursor mixed: a) Raman spectra, and b) normalized XRD patterns.

In all these samples, the small quantity of metallic Ag in the film could not be detected by XRD. Electronic properties, such as carrier concentration or mobility, of those films were not investigated due to that the sheet resistance of the Ag incorporated  $\text{Cu}_2\text{O}$  films were so resistive that they exceeded the measurable range for the Hall effect equipment we have (sheet resistance maximum up to  $10 \text{ M } \Omega/\square$ ). Thus only resistivity was able to be measured by four probe measurement, giving lowest resistivity value from pure  $\text{Cu}_2\text{O}$  film, about  $200 \text{ } \Omega\cdot\text{cm}$ . Surprisingly, with more silver incorporated in the  $\text{Cu}_2\text{O}$  film, the resistivity tended to increase, the reason behind is not clear yet.

## IV.2.2 Effects of humidity on thin film orientation, morphology and electronic properties

In addition to the study of the effect of Ag incorporation on the growth and morphology of  $\text{Cu}_2\text{O}$  films, the effect of carrier gas humidity was also systematically studied, including the morphology, crystalline structure and electronic properties. During the deposition, the solution consumption rate was controlled by the CG1 flow ( $2 \text{ L/min N}_2$ ) and was maintained around  $1.5 \text{ ml/min}$ . CG2 was then introduced as oxidizing gas ( $5 \text{ L/min air} + 3 \text{ L/min N}_2$ ) through the gas mixer mentioned in Chapter II (Figure II-4). The deposition chamber was slightly below atmospheric pressure due to the ventilation with the liquid pressure gauge reaching about  $3 \text{ cm}$ . The substrates were heated at temperatures ranging between  $290$  and  $365 \text{ }^\circ\text{C}$ . Glass (Corning) substrates were used for the depositions. Standard deposition duration was  $220 \text{ min}$ . Shorter deposition times ( $< 60 \text{ min}$ ) were also used to evaluate the initial nucleation mode.

To introduce the humidity into the carrier gas, a bubbler containing deionized water at room temperature was added to the CG2 line, as shown in Figure IV-14. Reference source not found.. The CG2 flow was thus divided in two separate lines, including i) CG2a gas going directly to the reactor; and ii) CG2b bubbling through water (50 ml) during deposition process. The glass bubbler is a glass bottle with inner diameter about 6 cm. Both flow speed were adjusted to maintain a total CG2 flow rate of 8 L/min with the certain gas composition. By increasing the flow rate through CG2b (i.e. by increasing the water consumption rate) we could control the humidity (water molar ratio) in the carrier gas. Thus, water consumption and the water molar ratio in the flow during deposition was controlled and measured. The study was based on the samples deposited under different conditions, as shown in Table IV-4, with various deposition temperatures and water molar ratios.

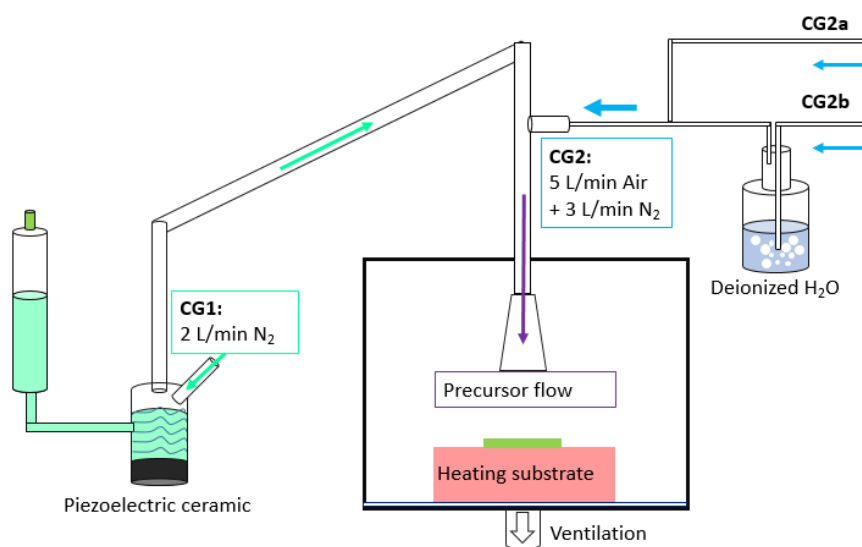


Figure IV-14. Scheme of the modified AA-MOCVD system allowing the introduction of humidity in the carrier gas flow.

To observe the effects of temperature on  $\text{Cu}_2\text{O}$  deposition with both dry and wet carrier gas, parallel experiments were conducted with temperature ranging from 290 °C to 365 °C, as presented in Table IV-4. A constant carrier gas flow of 8 L/min was passed through the bubbler. To estimate the water molar ratio introduced in the total gas flow, we assumed that the water vapor originally present in the carrier gas was 0. The water consumption was 0.11 ml/min, which corresponds to a molar ratio of 1.37 %.

Table IV-4. Sample deposition parameters and samples identification. Original water molecule in carrier gas set as constant zero.

CG2b (L/min)	Temperature (°C)	290	305	320	335	350	365
	Introduced H <sub>2</sub> O molar ratio in total gas flow (%)						
0	0	D290	D305	D320	D-335	D-350	D-365
2	0.38				W02		
4	0.75				W04		
6	1.12				W06		
8	1.37	W290	W305	W320	W335 (= W08)	W-350	W-365

The morphology of the  $\text{Cu}_2\text{O}$  films are presented in Figure IV-15. At lower deposition temperatures, namely 290 °C, and both in dry and wet conditions, discontinuous films were obtained in which cubic crystals were found scattered on the substrate along with a thin  $\text{Cu}_2\text{O}$  layer below, as shown in Figure IV-15 a) and e). The only difference was that in wet deposition condition, the size of cubic grains were much bigger, with edge lengths reaching about 300 nm, as compared with 50 nm for grains in dry deposition condition.

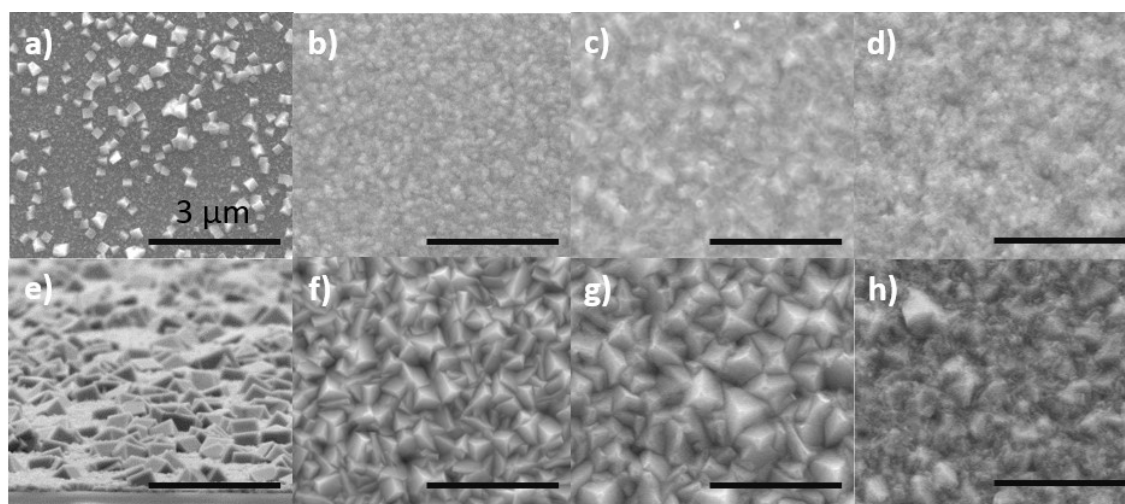


Figure IV-15. Scanning Electron Microscopy images of films deposited at different temperatures in dry and wet conditions. a) 290 °C (D290); b) 305 °C (D305); c) 350 °C (D350); d) 365 °C (D365) and with humid carrier gas with temperatures: e) 290 °C (W290, titled surface); f) 305 °C (W305); g) 350 °C (W350); h) 365 °C (W365).

In the deposition series with dry CG at temperature ranging from 305 °C to 365 °C, the morphology of the  $\text{Cu}_2\text{O}$  films is shown from Figure IV-15 b) to d). Upon increasing the deposition temperature above 290 °C, continuous films were formed at 305 °C and the cubic feature of  $\text{Cu}_2\text{O}$  was not obvious above the surface, shown in Figure IV-15 b). As deposition



temperature increased, in Figure IV-15 c), the  $\text{Cu}_2\text{O}$  film obtained presented bigger grains on the thin film surface (about 200 nm). Finally, at 365 °C, the thin film surface presented small particles forming on the surface of the film, as shown in Figure IV-15 d).

On the other hand, under wet deposition condition, continuous films were obtained containing big  $\text{Cu}_2\text{O}$  crystals such as those in Figure IV-15 e), and thus presenting 'pyramid-like' surface (Figure IV-15 f) and g)). Increasing deposition temperature induced the growth of the cubic grain size. But, similarly to the dry depositions,  $\text{Cu}_2\text{O}$  films deposited at 365 °C with humid carrier gas also resulted in the formation of smaller particles on top of the big cubic crystals, as shown in Figure IV-15 h).

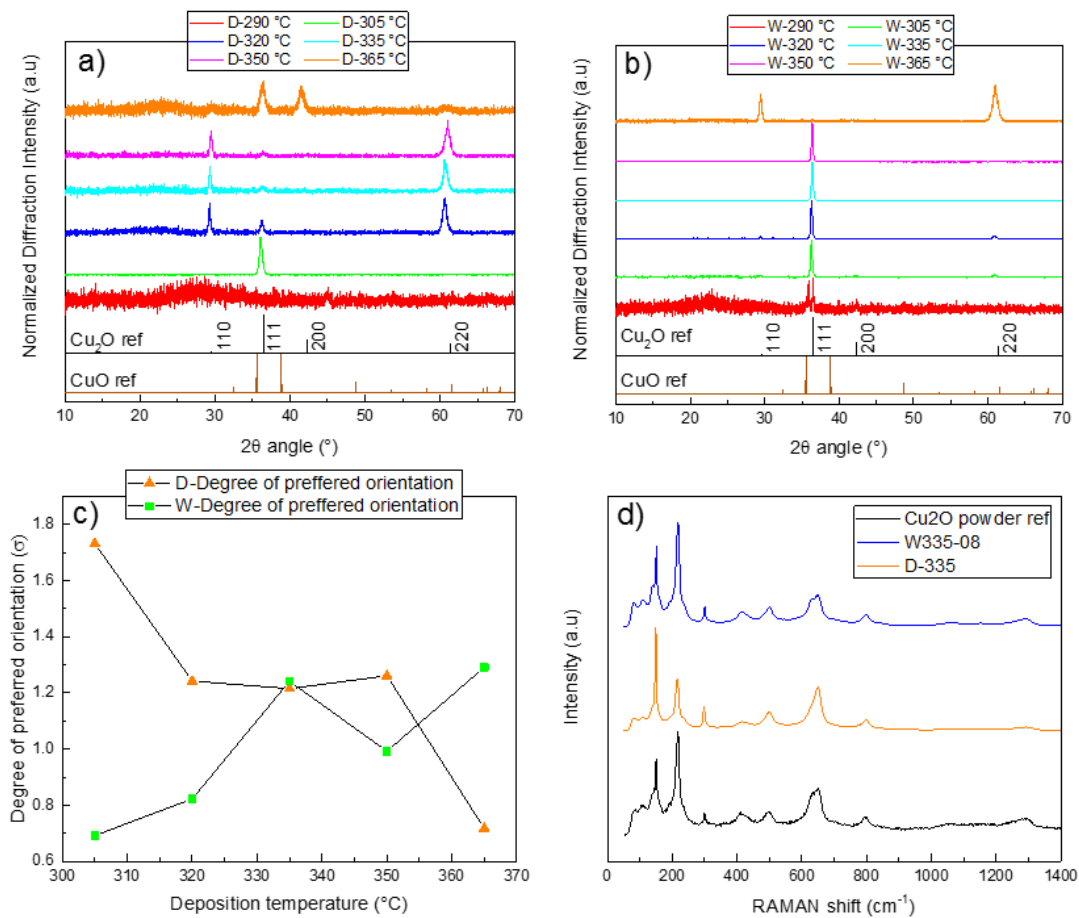


Figure IV-16. XRD patterns of samples deposited at different temperatures with a) dry CG and b) humid CG; c). Evolution of texture coefficient with deposition temperature for both dry and wet CG; d). Raman spectra of samples deposited with dry and humid CG.

To further characterize thin film quality and phase composition, Raman spectroscopy and XRD were used. The results are given in Figure IV-16, in which figure a) shows the XRD patterns of samples deposited with dry CG at different temperatures. At 290 °C, no reflection peaks were obtained, thus indicating a low degree of crystallization. At 305 °C, the film was already crystalline and a unique reflection corresponding to the (111) index could be

observed. As the temperature increased to 320 °C, the intensity of the (111) reflection clearly diminished. Meanwhile, new reflections corresponding to the (110) and (220) indexes appeared, which indicated a change in preferential orientation. Films deposited at 335 and 350 °C presented similar XRD patterns, with even lower (111) peak intensity. Finally, films deposited at 365 °C presented noisier XRD patterns with broad reflections with similar intensities as those obtained for reference bulk samples (reference entry 04-007-9767). This is in agreement with the small particles observed by SEM for such samples.

XRD patterns for the samples deposited with wet CG are presented in Figure IV-16 b). As it is shown, at low deposition temperature (290 °C), reflections corresponding to both Cu<sub>2</sub>O and CuO phases were obtained. Thus, the cubic structures on surface could be associated with Cu<sub>2</sub>O phase shown in Figure IV-15, while CuO could possibly exist in the bottom thin layer. The appearance of the CuO at low deposition temperature was expected concerning the decomposition mechanism of the CuF precursor (will be introduced in detail in section IV.3). With higher deposition temperature, an intense and narrow (111) reflection of Cu<sub>2</sub>O was observed, confirming the preferential orientation along (111) index, in agreement with the "pyramids-like" surfaces from SEM. As well, Cu<sub>2</sub>O films deposited at 305 °C and 320 °C presented weak (110), (220) reflections with a slightly noisy background. Conversely, for films deposited at 335 °C and 350 °C, only the (111) reflection peak was present in the XRD pattern, implying a higher degree of texture with increased temperature. Then, at even higher deposition temperature (365 °C), the (111) reflection no more appeared but only the reflections corresponding to (110) and (220) indexes were presented, indicating that in addition to a change in crystal size and morphology (see in Figure IV-15 above), a change in texture also took place.

We used the texture coefficient<sup>14</sup> to have a qualitative evaluation of the degree of orientation in the different samples, the results are presented in Figure IV-16 c). To conduct the calculation, four reference reflections which are (110), (111), (200) and (220), were taken into account. As it is shown, for the samples deposited with dry CG the texture coefficient decreased with higher deposition temperatures. While for samples deposited with humid CG, the texture coefficient was generally in the trend of rising with higher deposition temperatures, even for different textures as was the case here. Lastly, comparisons of the Raman spectra for the thin films deposited with dry and humid CGs are shown in Figure IV-16 d). In both cases, sharp and intense peaks representing a high crystallinity were observed. While no fluorescence signals corresponding to carbon contamination were

observed above  $1000\text{ cm}^{-1}$ . In addition to that, the strongest peak for sample D335 located at around  $170\text{ cm}^{-1}$ , while for W335 the strongest peak position stayed at  $210\text{ cm}^{-1}$ , again in agreement with the different texture of each sample.

To further study the effects of carrier gas humidity, besides varying the deposition temperature, the humidity was also tuned while fixing the deposition temperature at  $335\text{ }^\circ\text{C}$ . The morphologies of  $\text{Cu}_2\text{O}$  evolved as shown in the SEM images in Figure IV-17. Figure a) shows the surface of a normal  $\text{Cu}_2\text{O}$  film deposited at  $335\text{ }^\circ\text{C}$  with dry carrier gas. It presented a dense and smooth surface, grain size was around  $150\text{ nm}$ . When  $2\text{ L/min}$  gas bubbled through water (with  $0.38\%$  water, W02), the morphology is shown in figure b), the surface of  $\text{Cu}_2\text{O}$  film formed more visible grains out of the plain. Each grain had a wider size on bottom and smaller on the top with a triangle shaped plateau. The bubbler flow was further tuned up to  $4\text{ L/min}$  (with  $0.75\%$  water, W04),  $6\text{ L/min}$  (with  $1.12\%$  water, W06) and  $8\text{ L/min}$  (with  $1.37\%$  water, W08). The morphology was rather similar in those conditions, thus presented in figure c). In the figure, the triangle plateau shrank to a point, thus surfaces with pyramids structure were formed. In addition, bigger cubic grains emerged with maximum size up to  $400\text{ nm}$ .

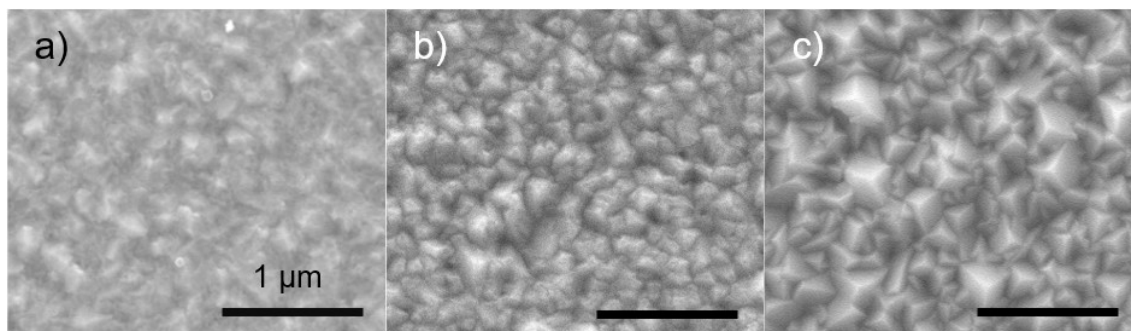


Figure IV-17.  $\text{Cu}_2\text{O}$  films deposited by AA-MOCVD at  $335\text{ }^\circ\text{C}$  with different amount of introduced water molar ratio: a).  $0\%$  (dry, D335), b).  $0.38\%$  (W335-02) and c).  $1.37\%$  (W335-08).

The crystallinity of those samples was also checked by Raman Spectroscopy and X-Ray Diffraction. The patterns are given in Figure IV-18, in which the figure a) shows an evolution of Raman peaks with regarding to the water molar ratio in gas flow. The very bottom Raman spectrum is a normal  $\text{Cu}_2\text{O}$  thin film deposited with dry CG (Sample D335). As we can see, in a normal  $\text{Cu}_2\text{O}$  sample deposited by AA-MOCVD, the first and second strongest peaks located at  $170$  and  $210\text{ cm}^{-1}$  separately, both peaks were intense and sharp, indicating a high crystallinity. While moving to the curves above, more humidity was incorporated during the sample deposition process, with several changes worth noticing. First of all, intensity of the two tiny peaks located at around  $150\text{ cm}^{-1}$  was enhanced. Other than that, an obvious peak

intensity shift happened between the strongest and second strongest ones, which could be associated with the grain orientation change. Lastly, we could also observe that the peak at  $300\text{ cm}^{-1}$  and  $650\text{ cm}^{-1}$  decreased slightly, the later one even splitting into two visible peaks, both associated to  $\text{Cu}_2\text{O}$  phase.

In Figure IV-18 b), the XRD patterns confirmed the sample grain orientation change. The major reflection for the normal  $\text{Cu}_2\text{O}$  sample (D335) corresponded to the (110) orientation (in plain). While with more humidity added during deposition, the main reflection peaks were shifted to the (111) index. In all, with a more humid CG during AA-MOCVD deposition, the morphology of resulting  $\text{Cu}_2\text{O}$  films evolved from flat surface corresponding to (110) orientation to "pyramids-like" rough surface with cubic grains aligned to (111) orientation, meanwhile they still remained as dense and continuous films.

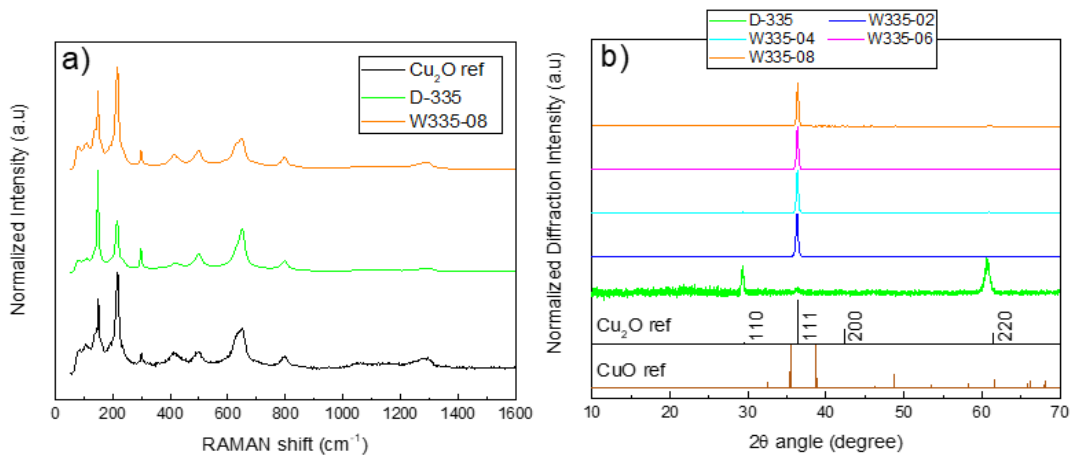


Figure IV-18. a).Raman spectra and b) XRD patterns of samples deposited with different amount of water molar ratio.

In order to give a direct view of different grain orientation on the surface, samples were characterized by EBSD on an area of about  $2 \times 5\ \mu\text{m}^2$  (Figure IV-19). Samples deposited in dry CG condition, exhibited a general surface grain preferential orientation along (101) (plane equivalent to (110)). The alignment of cubic grains on the surface is illustrated in figure a), with a diagonal facet pointing out of the plane. In the SEM image in figure b) and the reconstructed EBSD mapping in figure c), the grains corresponding to (101) were marked in green color, while the white spots were due to the lack of signal from such a rough surface. Such (101) orientation was also confirmed by the inverse pole figure shown in Figure IV-19 d), which showed a broad circle at the center of the diagram (implying an wide orientation distribution around (101)).

On the other hand, deposition with humid CG yielded crystals mostly oriented along (111), as illustrated in Figure IV-19 e), with the corner of the cubic structure pointing out of the

plane. The SEM image and reconstructed EBSD mapping are shown in figure f) and g), in which the grains with (111) orientation are colored in blue. In this case, a smaller orientation distribution was found, as evidenced by the inverse pole figure (Figure IV-19 h)). In conclusion, apart from the difference in morphology observed in SEM, EBSD analyses clearly presented a shift in texture from (101) to (111), as water vapor was added into the gas flow during the deposition process.

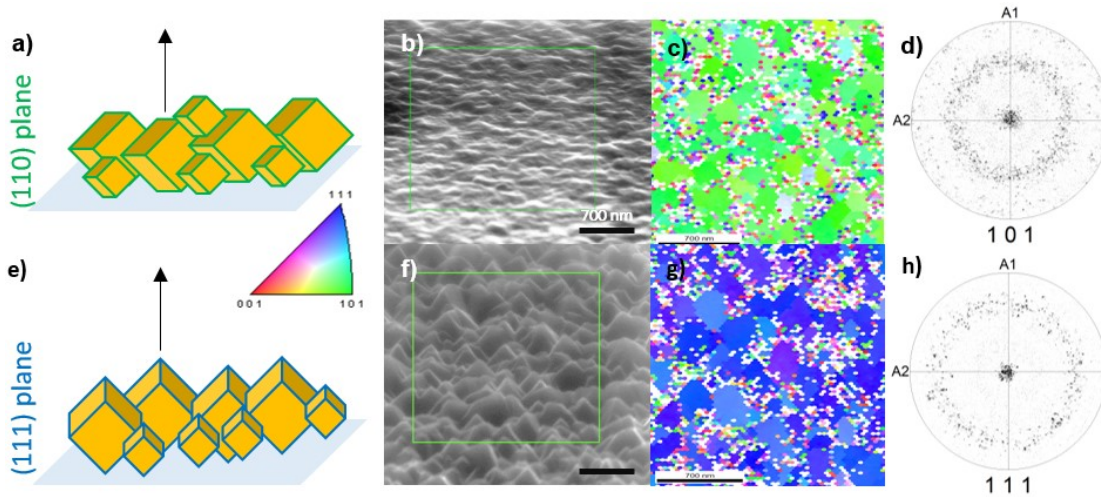


Figure IV-19. EBSD characterization of  $\text{Cu}_2\text{O}$  samples deposited without (D335) and with (W335) humid carrier gas at 335 °C for 220 mins. Deposition with dry carrier gas: a). Secondary electron image of D335 with tilted angle of 70°; b). Recreated image based on EBSD characterization, grains oriented along (110) are marked in green; c). Orientation distribution of D335 in inverse pole figure. Sample deposited with humid carrier gas: d). Secondary electron image of W335 tilted 70°; e). Recreated EBSD image, grains oriented along (111) marked in blue; f). Orientation distribution of W335 in inverse pole figure.

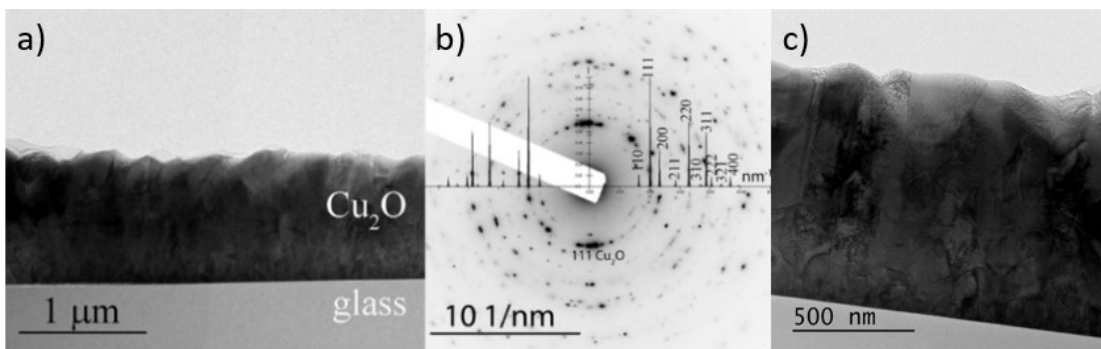


Figure IV-20. a) Low magnification TEM cross-section image of a  $\text{Cu}_2\text{O}$  film with (111) texture deposited at 335 °C on corning glass. b) Corresponding SAED pattern. c) Close up image showing a columnar growth developing from smaller crystals at the interface.

Transmission Electron Microscopy (TEM) was also used to evaluate  $\text{Cu}_2\text{O}$  film quality and morphology evolution along the thickness of the films. The results are presented in Figure IV-20, in which the cross-section and SAED pattern of sample W335 are presented. Figure IV-20 a) and b) present a low magnification cross-section image of the film and the corresponding electron diffraction pattern, respectively.

As it can be observed, the film was dense with no apparent cracks and presented a clean interface with the glass substrate. The SAED pattern showed a general texture along (111), in agreement with EBSD and XRD results. Figure IV-20 c) shows a close up view of the film, in which in the perpendicular to the surface direction, large columns of grains on top of a thinner layer made of smaller crystals were observed. Such a phenomena has been also reported for (111) textured  $\text{Cu}_2\text{O}$  films deposited by electrochemical deposition.<sup>7</sup>

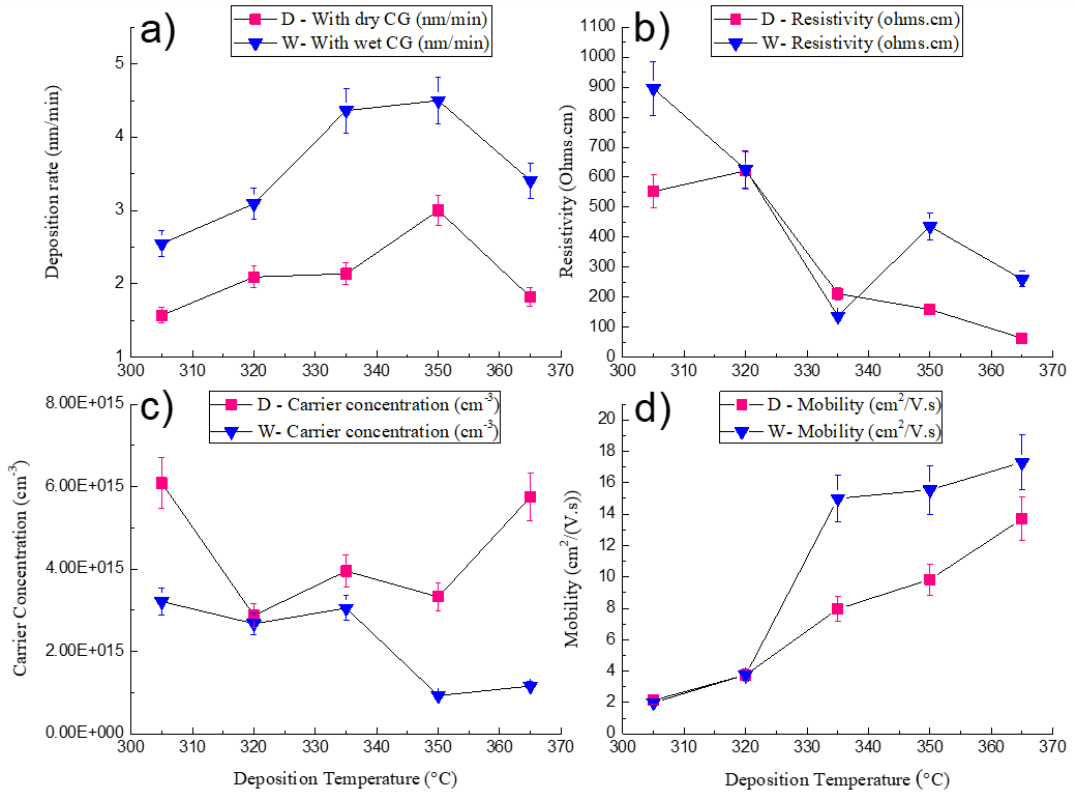


Figure IV-21. Effects of deposition temperature using dry and humid CG on the properties of  $\text{Cu}_2\text{O}$  thin films. a) deposition rate; b). Resistivity; c). Carrier concentration and d). Carrier mobility. (Samples deposited with dry CG are represented with red squares and samples deposited with wet CG are marked with blue triangles.)

Besides the effects of carrier gas humidity on morphology and grain orientation, the evolution of deposition rate and electronic properties with different deposition temperatures in dry and humid conditions were also compared, as presented in Figure IV-21. As shown in Figure IV-21 a), by dividing the thickness over deposition duration, the obtained deposition rate increased with deposition temperature rising from 305 to 350 °C. This was likely due to a more efficient precursor decomposition thanks to enhanced thermal activation of the reaction. At 365 °C the deposition rate decreased, most likely due to a partial pre-decomposition of the precursor before reaching on the substrate.<sup>15,16</sup> In all cases, the deposition rate of  $\text{Cu}_2\text{O}$  films was always faster with wet CG than in dry deposition condition. Thus, water seemed to effectively activate the precursor reaction at the substrate but not its

decomposition at the highest temperature used. The trend of deposition rate versus temperature was rather similar in both cases.

In Figure IV-21 b), the resistivity of Cu<sub>2</sub>O films deposited in both dry and wet conditions at different temperatures is presented. Samples deposited at 290 °C could not be characterized due to the high resistivity presented as a result of the discontinued nature of the film. As it is shown, in both cases resistivity decreased with higher deposition temperatures. Thin films deposited with humid CG presented higher resistivity than the equivalent films deposited with dry CG. The minimum resistivity was obtained with the deposition with dry carrier gas at 365 °C, about 60 Ω.cm. The lowest resistivity for Cu<sub>2</sub>O thin films deposited with humid carrier gas was around 110 Ω.cm.

As shown in Figure IV-21 c), the charge carrier concentrations for Cu<sub>2</sub>O films deposited with dry and wet carrier gas were compared. For Cu<sub>2</sub>O films deposited in dry condition, the carrier concentration stabilized at about  $4 \times 10^{15} \text{ cm}^{-3}$ . While for samples synthesized in humid condition, slightly lower carrier concentrations of about  $1.7 \times 10^{15} \text{ cm}^{-3}$  were obtained for all the temperatures. Furthermore, the evolution of mobility in both deposition conditions are presented in Figure IV-21 d). The figure showed, as expected from film morphology, an increase in mobility with increasing deposition temperature. With dry CG, the mobility of Cu<sub>2</sub>O films was enhanced from 2 cm<sup>2</sup>/V.s up to 13.7 cm<sup>2</sup>/V.s when deposition temperature increased from 305 °C to 365 °C. Similar trend was also observed in the case of humid CG deposition condition, carrier mobility being improved from 5 cm<sup>2</sup>/V.s to 17 cm<sup>2</sup>/V.s. As previously introduced in Chapter I, for pure Cu<sub>2</sub>O films deposited with MOCVD, the mobility was generally about 1 ~ 5 cm<sup>2</sup>/V.s, thus this value was rather good comparing to previous works using similar fabrication techniques<sup>17-19</sup>. This enhancement of mobility could be attribute to the bigger grain size obtained with humid CG deposition condition (maximum 300 nm measuring along the cubic edge). However, the sample with lowest resistivity was not the one deposited at highest temperature, which is attributed to the carrier concentration decrease over 350 °C, as shown in figure c).

In addition, for Cu<sub>2</sub>O films deposited with various water molar ratio at 335 °C, deposition rate and electronic properties were also studied. As shown in Figure IV-22 a), along with higher water molar ratio from 0 % to 1.12 %, an increase in deposition rate from 2.2 nm/min to 4.6 nm/min was observed. From there, growth rate became almost constant. The electronic properties of those films were again evaluated by Hall-effect measurement with Van de Paul four probe configuration. For water molar ratio from 0 % to 1.12 %, the resistivity values

increased from 180  $\Omega\cdot\text{cm}$  to 900  $\Omega\cdot\text{cm}$ . A further increase in water molar ratio in carrier gas produced a resistivity drop back to 160  $\Omega\cdot\text{cm}$  with water consumption of 0.11 ml/min.

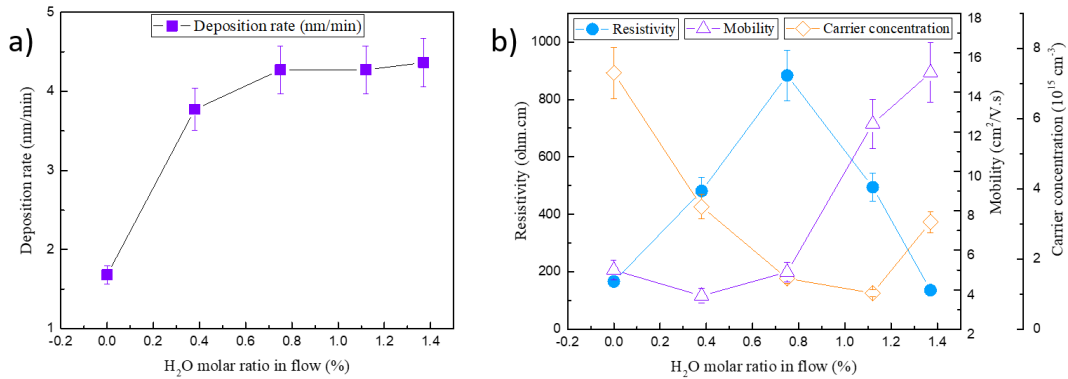


Figure IV-22. Effect of humidity incorporation on  $\text{Cu}_2\text{O}$  thin film a) growth rate and b) on the electronic properties at 335 °C.

Conversely, carrier concentration showed a decreasing trend from  $7.7 \times 10^{15} \text{ cm}^{-3}$  for 0 % to  $1.1 \times 10^{15} \text{ cm}^{-3}$  for 1.37 % water molar ratio. Since the origin of the p type conductivity of  $\text{Cu}_2\text{O}$  film relies on the presence of copper vacancies, carrier concentration in the films is very sensitive to the oxygen ratio change during MOCVD.<sup>20,21</sup> The oxygen introduced in the flow was fixed while the concentration of water vapor varied. Thus, the decrease of carrier concentration with increasing humidity could be explained due to the fact that in presence of water, precursor decomposition was largely accelerated. Thus, this increased supply of copper atoms created an oxygen deficient environment during the deposition process. Since the number of oxygen vacancies in  $\text{Cu}_2\text{O}$  largely rely on the oxygen/copper ratio during the deposition,<sup>21–24</sup> thus the oxygen deficient environment led to a decrease of carrier concentration. However, with a further increase of the water ratio from 1.12 % to 1.37 %, a slight increase of carrier concentration from  $1.1 \times 10^{15} \text{ cm}^{-3}$  to about  $3 \times 10^{15} \text{ cm}^{-3}$  was observed. Meanwhile, by reproducing two more samples at the same conditions we obtained lower concentration around  $1.1 \times 10^{15} \text{ cm}^{-3}$  (with mobility around 13  $\text{cm}^2/\text{V}\cdot\text{s}$ ). This would mean that other factors may be affecting the carrier concentration of the films and that a more detailed study would be necessary to fine tune this parameter. On the other hand, the effect of water facilitated on precursor decomposition was rather saturated over 1.12 % water molar ratio, as shown in Figure IV-22 a). Meanwhile, with higher water molar ratio during MOCVD deposition, the carrier mobility of the produced  $\text{Cu}_2\text{O}$  thin films was largely enhanced from 4  $\text{cm}^2/\text{V}\cdot\text{s}$  to 17  $\text{cm}^2/\text{V}\cdot\text{s}$ , which could be attributed to the bigger grains observed in Figure IV-17.



To further explore the conducting behavior of the (111) oriented  $\text{Cu}_2\text{O}$  films, Conductivity Atomic Force Microscope (CAFM) characterizations were conducted, as previously introduced in Chapter II.3.2.2. Before the characterization, (111) oriented  $\text{Cu}_2\text{O}$  films were deposited on cleaned ITO coated glass substrate at both 305 °C and 335 °C with 0.11 ml/min water consumption (sample W305-08 and W335-08) for 220 minutes.

The AFM images and conductivity mapping of the  $\text{Cu}_2\text{O}$  samples are presented in Figure IV-23. In figure a) and c), the AFM images show the "pyramid-like" surfaces of sample W335-08 with different magnifications, with image size 500 nm and 5  $\mu\text{m}$  separately. This is in agreement with the previous SEM images of (111) oriented  $\text{Cu}_2\text{O}$  films (such as in Figure IV-21). Meanwhile, in Figure IV-23 b) and d) are the conductivity mapping of the corresponding surface areas, in which the darker color represents higher current measured, thus better conductivity. Comparing the AFM image and the correspondent electrical mapping, it's rather clear to point out that the grains have less conductivity than the grain boundaries, as most of the dark points are located between the grains.

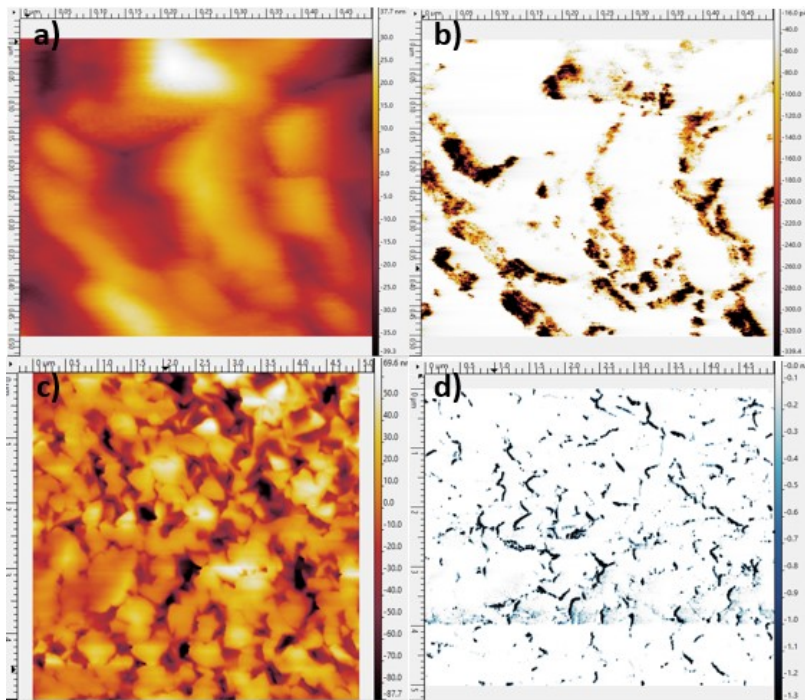


Figure IV-23. AFM images of (111) textured  $\text{Cu}_2\text{O}$  film (W335-08) a) with scan size of 500 nm c) with scan size of 5  $\mu\text{m}$  and corresponding conductivity mapping b) and d).

In addition to the area conductivity mapping, the electrical behavior on certain points was also conducted. To improve the reliability of the results, both  $\text{Cu}_2\text{O}$  films deposited at 305 °C (W305-08) and 335 °C (W335-08) were characterized. Full conductivity scans were firstly conducted over a surface area of  $0.5 \times 0.5 \mu\text{m}^2$  on both  $\text{Cu}_2\text{O}$  films, as shown in Figure IV-24 a) and c) for W305-08 and Figure IV-24 b) and d) for W335-08. The dark red areas

correspond to the parts with higher current measured, thus indicating better conductivity. The conductive areas are mostly located along the grain boundaries, as the area shown with red marks in figure a) and b). By selecting the spots on grain and grain boundary, the AFM tip moved to the positions as marked in blue cross. At each spot, the applied potential varied from -5 V to +5 V and the current was recorded, thus the I-V curve for W305-08 is shown in Figure IV-24 e) while for W335-08 is presented in Figure IV-24 f).

In both Figure IV-24 e) and f), weak rectification behaviors were observed on the  $\text{Cu}_2\text{O}$  grains, while on the grain boundary, current could pass through either directions thus without showing any rectification. The resistivity in the grain boundaries was again much lower than in the grain. To verify the overall rectifying behavior,  $9 \text{ mm}^2$  size Au contacts were deposited directly above the  $\text{Cu}_2\text{O}$  films. By measuring the I-V curve, no overall rectification was found as expected.

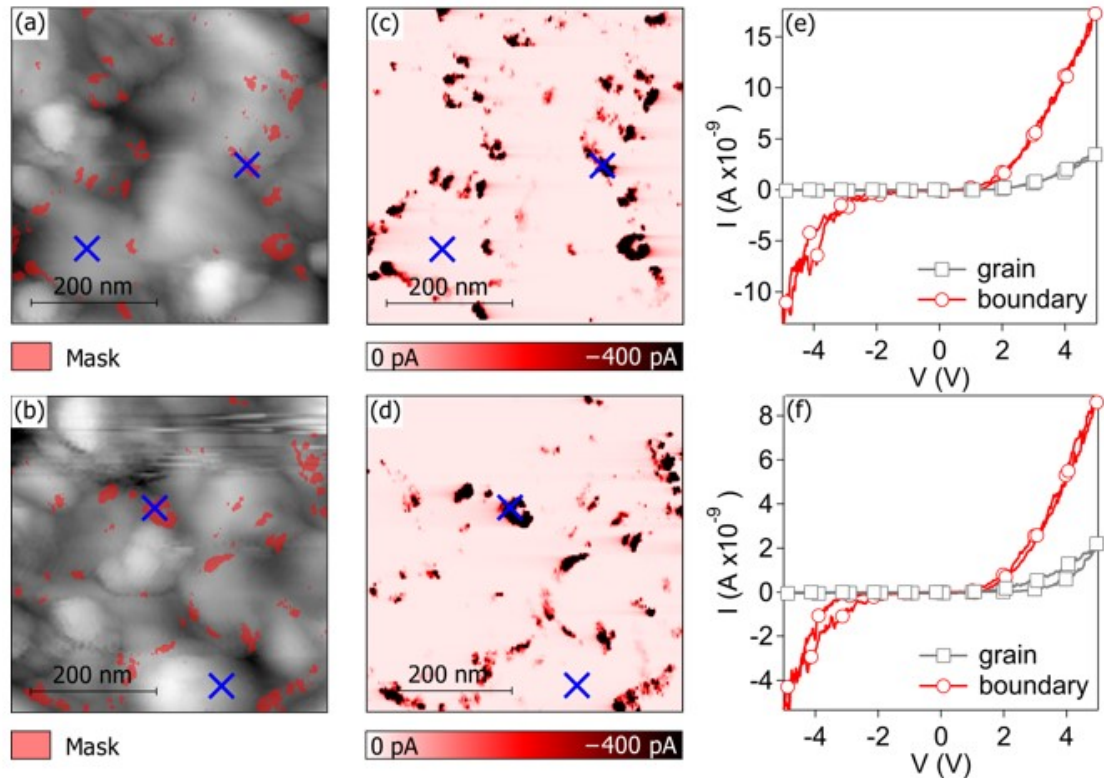


Figure IV-24. a) and b) are AFM images of (111) textured w305 and w335, with 60 nm total height difference; red marks show areas of high conductance; c) and d) are the current mapping with voltage bias -2 V. Blue crosses indicate where IV shown in (e) and (f) were obtained.

To further understand the mechanism behind the high conductivity observed in the grain boundaries, the cross-section of the (111) oriented  $\text{Cu}_2\text{O}$  film (on Si substrate, for the sake of easier sample preparation) was characterized with the ASTAR technique, a TEM-EBSD like phase mapping characterization tool with ultra resolution as introduced in Chapter II.3.2.3.

In previously mentioned  $\text{Cu}_2\text{O}$  films characterized by TEM SAED and XRD (Figure IV-20 and Figure IV-18), the quantity of  $\text{CuO}$  phase was below the detection limit.

Meanwhile with the ultra-fine resolution from the ASTAR technique,  $\text{CuO}$  phase was observed, as presented in Figure IV-25. In figure a), the reconstructed correlation index map is rather similar to the cross-section image shown in Figure IV-25, showing the columnar growth of the films. The gray scale map as presented was obtained by plotting the value of the correlation index for the succession of the electron diffraction patterns at each location. In figure b), a phase mapping of the  $\text{Cu}_2\text{O}$  cross-section is given. The map confirms that the film is mainly composed of  $\text{Cu}_2\text{O}$  phase (colored in red). Meanwhile, the blue colored  $\text{CuO}$  phase was found and mostly located between the column  $\text{Cu}_2\text{O}$  grains. The existence of  $\text{CuO}$  phase in grain boundary has previously been confirmed by XPS in the work of *J. Deuermeier et al.*<sup>25</sup> Especially at the interface between substrate and the  $\text{Cu}_2\text{O}$  film, where lots of smaller  $\text{Cu}_2\text{O}$  grains have been reported in TEM image, more traces of  $\text{CuO}$  phase are observed.

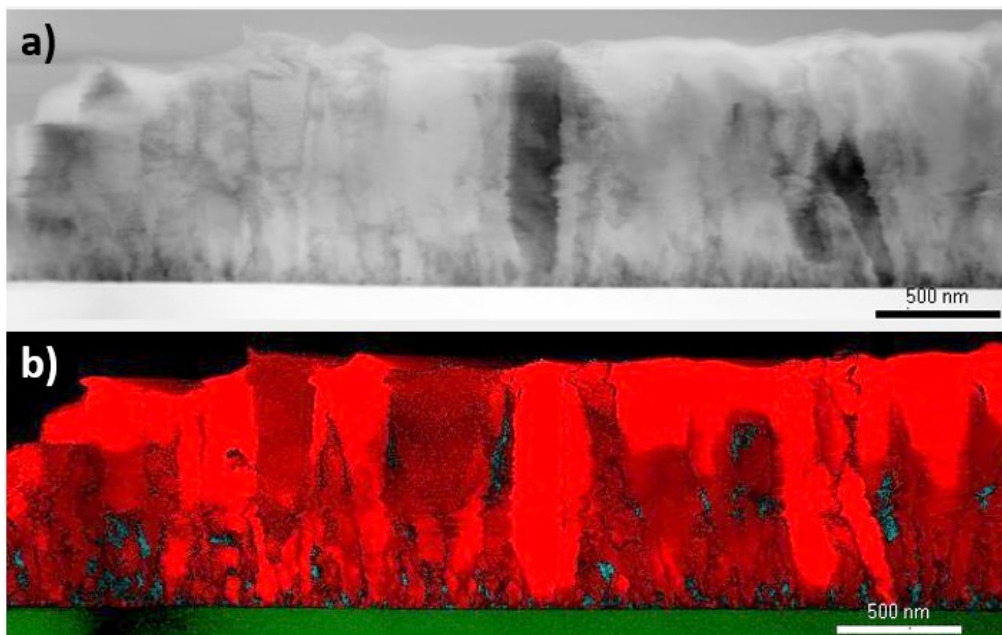


Figure IV-25. ASTAR (TEM-EBSD like technique) Automatic crystal orientation/phase mapping of  $\text{Cu}_2\text{O}$  sample (W335-08) crosssection with orientation (111). a). Reconstructed correlation grey scale index map. b). Phase map (with index-reliability). The red color corresponds to  $\text{Cu}_2\text{O}$  phase, the blue color represents  $\text{CuO}$  phase and the green color refers to the Si substrate.

Taking into account that  $\text{CuO}$  has a better conductivity than  $\text{Cu}_2\text{O}$  and the position where the majority of the  $\text{CuO}$  phase located, it's rather straight forward to associate the existence of  $\text{CuO}$  in grain boundary with the better conductivity that has been observed. The possible effects from the shape of the AFM tip on contact area has been taken into consideration, but the radius of the AFM tip was merely 25 nm. This, together with the rather high resistivity of the  $\text{Cu}_2\text{O}$  films, allow to consider the effects from the tip shape almost negligible.

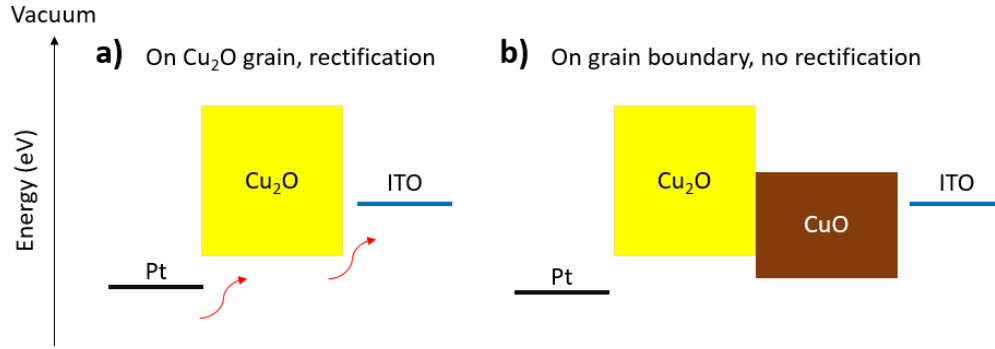


Figure IV-26. The possible origin of rectifying behavior in electrical AFM measurements of  $\text{Cu}_2\text{O}$  films a) on grains with rectification and b) on grain boundary without rectification.

In order to explain the different rectifying behavior when the Pt coated AFM tip was located on grains and grain boundaries, the corresponding energy diagrams of these two different locations of the film are drawn in Figure IV-26. Since  $\text{Cu}_2\text{O}$  is a p type semiconducting material, thus the conductivity is mainly dominated by the hole conductivity in the Valence Band (VB). According to energy diagrams<sup>26,27</sup>, when the AFM tip was pointing above the  $\text{Cu}_2\text{O}$  grains, a typical rectifying junction was formed between Pt/ $\text{Cu}_2\text{O}$ /ITO, as shown in figure a). Thus, it allowed the easy pass of current along one direction while no current was presented with reverse bias. This would be the explanation of the weak rectifying curves shown in Figure IV-24 e) and f) on  $\text{Cu}_2\text{O}$  grains.

Meanwhile, due to the presence of  $\text{CuO}$  between the grain boundaries, figure b), when the AFM moved above the grain boundary, current was running through both  $\text{Cu}_2\text{O}$  and  $\text{CuO}$ . Thus, no rectifying behavior was observed on the grain boundary as shown in Figure IV-24 e) and f). However due to the presence of  $\text{CuO}$  phase (lower resistivity than  $\text{Cu}_2\text{O}$ ), a higher conductivity was observed on grain boundaries.

Optimized  $\text{Cu}_2\text{O}$  films presenting low resistivity and high carrier mobility were combined with ZnO to form p-n junctions. n type ZnO ~70 nm thick layers were deposited on top of the  $\text{Cu}_2\text{O}$  films at 60 °C using a home made Spatial Atomic Layer Deposition (SALD) system (AP-SALD) system,<sup>20,28,29</sup> in collaboration with *Mr. V. Nguyen* from LMGP. In this approach, precursors were continuously injected in different locations of the reactor while the substrate oscillated at very short distance (50 - 200  $\mu\text{m}$ ) from the head. Inert gas barriers located alternatively between precursor flows acted as effective barriers to keep precursor gases chemically isolated, thus conventional ALD cycles were replicated but with up to two orders of magnitude faster. Diethyl zinc ( $(\text{C}_2\text{H}_5)_2\text{Zn}$ ; DEZ) and water vapor ( $\text{H}_2\text{O}$ ) were used as precursors for zinc and oxygen, respectively.. More details can be found in the publication by N. Nguyen et al.<sup>20</sup>

Diodes were made using the  $\text{Cu}_2\text{O}$  films deposited with humidity condition at  $335\text{ }^\circ\text{C}$  (sample W335-08, see Table IV-4). A p-n junction was fabricated following the structure of ITO/ $\text{Cu}_2\text{O}$ / $\text{ZnO}$ /Ag contact, as shown in Figure IV-27 (Ag contact not in the image). Figure IV-27 a) and b) present the top and cross-section view of the p-n junction. The top  $\text{ZnO}$  layer is about  $70\text{ nm}$  thick with good conformity. The dense  $\text{Cu}_2\text{O}$  film is about  $900\text{ nm}$  thick. Between the  $\text{ZnO}$  and  $\text{Cu}_2\text{O}$  layer, no cracks were observed, thus it indicated a good adhesion. The rectified behavior of the p-n junction is presented in Figure IV-27 c). In the I-V curve, the voltage bias was scanned from  $-1\text{ V}$  to  $+1\text{ V}$  and it showed an excellent rectifying shape. The leakage current was merely  $2.2 \times 10^{-6}\text{ mA}$  at  $-1\text{ V}$ , with on current reaching almost  $6 \times 10^{-2}\text{ mA}$  at  $+1\text{ V}$ , thus giving an on-off ratio exceeding  $10^4$ . This indicates that with SALD, even at low deposition temperature ( $60\text{ }^\circ\text{C}$ ), a good p-n junction can be formed between  $\text{ZnO}$  and our optimized  $\text{Cu}_2\text{O}$  layers.

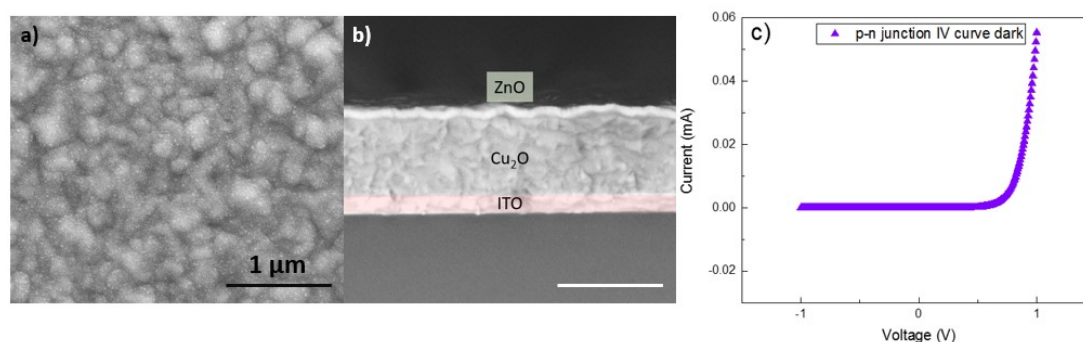


Figure IV-27. p-n junction with structure Ag/ $\text{ZnO}$  ( $60\text{ }^\circ\text{C}$ ,  $70\text{ nm}$ ) /  $\text{Cu}_2\text{O}$  ( $111$ )/ITO. a) SEM images of top and b) cross-section view of the p-n junction; c). Rectifying I-V curve. (Scale bars in images correspond to  $1\text{ }\mu\text{m}$ ).

### IV.3 Studies on the reaction mechanism

#### IV.3.1 Study of the initial stages of thin film growth.

In order to explore the effect of humidity in the reaction mechanism and texture development, depositions were performed with short durations (10 to 50 min). The morphology, mainly the roughness of the different samples, was characterized by Atomic Force Microscopy (AFM), the results are presented in Figure IV-28. The same deposition conditions for samples D335 and W335 in Table IV-4 were used for this study.

Figure IV-28 a), b) and c), presents the morphology of  $\text{Cu}_2\text{O}$  films deposited for 10 min, 20 min and 50 min with dry carrier gas. Meanwhile, in figure d), e) and f) are depositions under humid condition with the three different durations. By comparing the morphology of the depositions under dry and wet conditions, we can see that with dry CG the growth of initial

layers presented more nucleation sites, smaller grain size and smoother surfaces. After 50 min, the films deposited with dry CG didn't show a clear increase in grain size and instead more small grains were present. Conversely,  $\text{Cu}_2\text{O}$  films deposited with wet CG presented a clear increase in grain size with longer deposition duration, and there were much less smaller grains that for the films deposited with dry CG.

In MOCVD there are three well-known growth modes at the initial stages,<sup>30,31</sup> namely, layer-by-layer growth, island growth and layer plus island growth. In the majority cases of thin film depositions by MOCVD, the last mixed growth mode is the most commonly seen, which is also called the *Stranski-Krastanov* (SK) growth. In this case, AFM results have shown that for dry CG deposition condition, a layer-by-layer growth mode took place, in which each layer was made of many small particles that presented a moderate growth in size upon longer deposition duration.

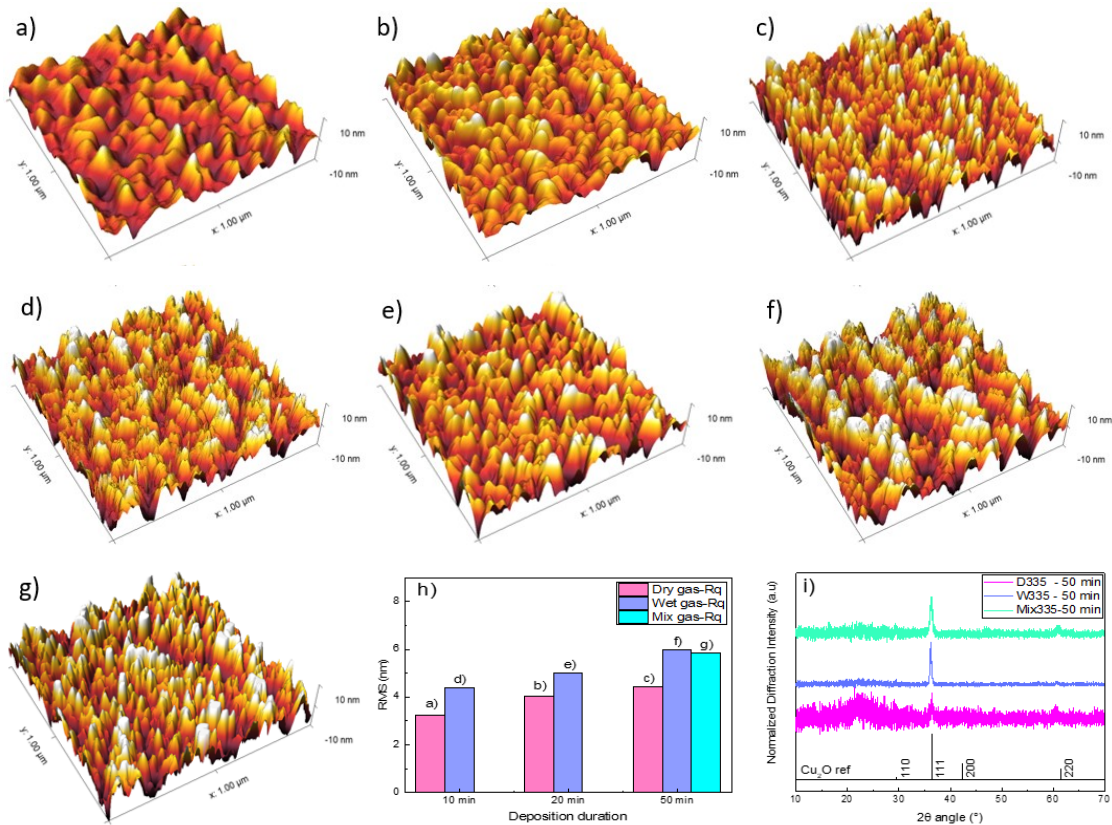


Figure IV-28. AFM 3D images  $1 \times 1 \mu\text{m}^2$  of samples deposited at dry carrier gas condition with different duration: a) 10 min; b) 20 min; c) 50 min. Samples with wet carrier gas and different duration: d) 10 min; e) 20 min; f) 50 min. g) sample was deposited with 10 min humid gas and the switching to dry deposition for 1 h. h) Roughness of samples deposited with different durations in wet and dry carrier gas conditions; i) X-Ray Diffraction patterns of samples with dry, wet carrier gas and sample starting with 10 min humid gas and followed by 40 min dry gas deposition.

Conversely, films deposited under wet CG seemed to develop a SK growth mode, considering bigger grains as the crystallization islands. Especially after 50 min where big

crystals are formed within a matrix of smaller crystals. The addition of water thus seemed to favor the growth of initially formed small nuclei as deposition proceeded, rather than forming new nuclei, as was the case for dry CG condition. This hypothesis is supported by the surface roughness measured for the different films (Figure IV-28 h).

Additionally, to further understand if such a texture orientation change is mainly due to the initial crystallization difference, a sample was deposited using humid CG during the initial 10 min and followed by 40 min deposition using dry CG (in total 50 min deposition). The morphology of this sample is presented in Figure IV-28 g). Its surface is rather similar to the film deposited with humid CG for 50 min (Figure IV-28 f), with big crystals being clearly observed (the same applies for the roughness value obtained, see Figure IV-28 h). XRD was also performed for the different samples (Figure IV-28 i), and the results confirmed that the presence of humidity induced the existence of a different and clear texture for such thin samples (thickness around 80 nm). XRD patterns also revealed the crucial role of water in the initial stages of thin film growth, showing that the preferential orientation of the sample obtained from humid-then-dry CGs was textured along (111), similarly to the sample deposited with humid CG, even though the intensity of reflections was slightly lower.

This implies that with 10 min of deposition under humid CG condition, it is enough to induce a different texture. Thus, these results suggest that once the first few nanometers of films were deposited, by following the principle of surface energy minimization, the later growth was compelled to be stacked in a similar manner by keeping the same orientation. It would also imply that growth along the crystallographic faces in humid conditions is more favorable than nucleation of new grains, even when water is not present anymore. Thus, the addition of humidity in the CG has key effects on the initial stage of reactions and through the water assisted precursor hydrolysis and reaction, favoring growth along the (111) direction, which in turn favored the formation of large crystals.

### **IV.3.2 Thermodynamic explanation**

This section aims to explain the grain growth mechanism from the point of view of a non-quantitative thermodynamic approach. During MOCVD there are several processes taking place. To simplify the problem the assumption that processes occurring before precursor decomposition are relatively similar in all the cases has been made. This includes precursor transport, surface diffusion and precursor adsorption during MOCVD deposition of Cu<sub>2</sub>O. Therefore only precursor decomposition and Cu<sub>2</sub>O nucleation and growth are discussed in our thermodynamic model.

In order to apply the classic thermodynamic nucleation theory, the process from CuF to Cu<sub>2</sub>O has been divided into two stages in our case. Firstly CuF is decomposed (thermally) and reduced into Cu metal atom (by its own reducing organic ligand). Then the metal Cu atoms are oxidized (by reaction with oxidizing reactants during deposition). Therefore, in this case, the thin film deposition rate mainly relies on the precursor decomposition rate on substrate (the first stage CuF decomposition), meanwhile the grain size of the obtained thin films depends on the nucleation and grain growth process (the second stage Cu atoms oxidization). Even though the process does most likely not follow this separate and distinct steps, we can use this approach in our model since the Gibbs free energy change between CuF and copper oxide does not depend on the process, but only on the beginning and final states.

In the Cu<sub>2</sub>O thin film deposition process, we can thus define  $\Delta G$  as the total Gibbs free energy from CuF precursor to form one mole of Cu<sub>2</sub>O in the MOCVD process. Thus, it equals to the Gibbs free energy of precursor decomposition into copper atom ( $\Delta G^R$ ) plus copper atom oxidization with oxygen ( $\Delta G^O$ ) to form Cu<sub>2</sub>O, as shown in Equation IV 22.

$$\Delta G = 2\Delta G^R + \Delta G^O \quad (22)$$

Since  $\Delta G^R$  is related to the reactivity of the precursor, thus it's the dominant factor for deposition rate during MOCVD process. While  $\Delta G^O$  is associated with copper atom oxidation, thus it's the major impact on Cu<sub>2</sub>O grain nucleation and enlargement, which can be applied into classic nucleation theory as shown in Equation IV 23,<sup>32</sup>

$$N_s \sim \exp^{(-\Delta G^O/kT)} \quad (23)$$

where  $N_s$  is the nucleation rate and  $k$  is the Plank constant and  $T$  is the temperature (in Kelvin).

To begin with, several terms and definitions need to be clarified. Firstly, in this work there is two terms related to oxygen ratio,  $P_{O_2}$  and  $P_{O_2}^*$ , which corresponds to oxygen ratio in deposition chamber and oxygen ratio regarding to copper atoms separately. Thus, it's defined that  $P_{O_2}^* = P_{O_2}/M_{Cu}$ , where  $M_{Cu}$  is the quantity of copper atoms decomposed from the CuF precursor per unit time. In the majority of cases, when the supplying of copper atoms for oxidization is constant, those two terms are equal and both constant when they are applied in thermodynamic equations, such as in the work of *L. Wang et al.*<sup>12</sup> But in this work, since in MOCVD process the Cu atom supply can be largely altered and dependent on the precursor reactivity, thus those two terms need to be differentiated for the sake of clarity, therefore the oxygen ratio in Equation IV 25 should be  $P_{O_2}^*$ .



For  $\Delta G^R$ , if we don't consider the decomposition of the ligand here, based on the reaction  $\text{CuF} \rightarrow \text{Cu} + \text{Ligand}$  (volatile), thus Equation IV 24 is given.  $[\text{CuF}]$  is the precursor decomposition rate at standard condition.  $[\text{Ligand}]$  is thus the reactivity of the ligand as a constant here. Also, since the reaction to obtain one mole of  $\text{Cu}_2\text{O}$  is  $2\text{Cu} + 1/2 \text{O}_2 \rightarrow \text{Cu}_2\text{O}$ , thus Equation IV 25 is obtained. This is mainly a description of the crystallization and morphology process, in which  $\ln[\text{CuF}]$  is the reactivity of copper metal organic precursor and it's directly related to copper atom supply, thus growth speed.  $\ln[\text{Cu}]$  is the reactivity of copper atoms.

$$\Delta G^R = \Delta G_0^R - RT\ln[\text{CuF}] + RT\ln[\text{Ligand}] \quad (24)$$

(Governs growth speed)

$$\Delta G^O = \Delta G_0^O - 2RT\ln[\text{Cu}] - 1/2 RT\ln\left[\frac{P_{\text{O}_2}}{M_{\text{Cu}}}\right] \quad (25)$$

(Governs grain size)

Using Equation IV 3 and 4, the deposited  $\text{Cu}_2\text{O}$  films with water vapor and Ag incorporation are explained as following.

**Effects from H<sub>2</sub>O vapor:** It is known that during a MOCVD deposition the presence of water vapor can facilitate the decomposition of metal organic precursor, especially in the case of metal oxide deposition.<sup>33-35</sup> Therefore, in our case humid gas led to a higher precursor reactivity, the term  $[\text{CuF}]$  increased, thus  $\Delta G^R$  was more negative indicating a faster deposition rate. Meanwhile, more copper atoms were supplied during oxidization and nucleation process, while the oxygen partial pressure in chamber  $P_{\text{O}_2}$  was maintained, thus the oxygen/copper atom ratio term  $P_{\text{O}_2}/M_{\text{Cu}}$  became smaller and thus  $\Delta G^O$  was less negative. Based on the nucleation theory, with less negative Gibbs free energy, the nucleation is less favored than grain growth, as confirmed by the results shown in Figure IV-17 and Figure IV-22. With more water vapor incorporated during deposition, the average deposition rate was enhanced and the grain size was increased.

**Copper atom reactivity:** With higher Ag precursor concentration during deposition, more Ag atoms were incorporated into the  $\text{Cu}_2\text{O}$  film. As a result, bigger grains of  $\text{Cu}_2\text{O}$  appeared also with a pyramid-like surface, as shown in Figure IV-11. In the reference work<sup>12</sup>, the effects of a noble metal on reducing the reactivity of copper atoms during oxidation process is presented. Therefore, as shown in Equation IV 4, the total Gibbs free energy was less negative. Thus, the nucleation rate was slowed down due to the lower Gibbs free energy,

and growing big grains was favored. Eventually, with the Ag incorporation, thin films with larger grains were formed. A catalytic effect of Ag in the decomposition of the precursor is also possible but has not been considered in this discussion.

#### **IV.4 Chapter IV conclusions**

In this chapter, first of all the configuration of AA-MOCVD system in LMGP was optimized. Based on that, the deposition parameters, including precursor choice, substrate and the use of plasma, were also adjusted to deliver homogeneous and carbon contamination free Cu<sub>2</sub>O thin films. In the process, CuF was chosen as the precursor instead of Cu(AcAc)<sub>2</sub> due to a cleaner decomposition. With the optimized MOCVD system and Cu<sub>2</sub>O deposition condition, the studies on the effects of oxygen ratio, noble metal incorporation (Ag nanoparticles in this case) and carrier gas humidity were conducted. The results revealed that, during the deposition of Cu<sub>2</sub>O films in AA-MOCVD, a slight higher oxygen ratio, silver nanoparticles and higher humidity all could have huge impacts on the morphology and lead to an increase to grain size. As well, the cubic shape Cu<sub>2</sub>O grains emerged more clearly on the surface. Later on, the effects of humid CG on initial thin film growth mode were explored, identifying the layer-by-layer growth mode for thin films deposited in dry CG while island like growth mode for depositions in wet CG. To better understand the results from those three factors, a simplified thermodynamic model was established and discussed. Based on that, the reason for the emergence of big grains at each condition was explained.

Among those three factors, the effects of carrier gas humidity on morphology, grain orientation and electronic properties were investigated in detail. With the wet CG during deposition, the deposition rate was largely enhanced and the Cu<sub>2</sub>O films with "pyramid-like" surface were obtained, with large grains of 300 nm on the cubic edge. Those types of thin films have been confirmed by EBSD, XRD and TEM to be well textured along the (111) index. In addition, through observing the cross-section of (111) oriented Cu<sub>2</sub>O film by TEM, it was discovered that those films were made of stacks of columnar grains. Furthermore, the electronic properties of deposited Cu<sub>2</sub>O films have been studied, in which higher mobility was found on average on (111) textured samples and maximum mobility reached 17 cm<sup>2</sup>/V.s. In addition, the investigation of the conductivity of the Cu<sub>2</sub>O films was also carried out. With the assistance of electrical AFM, the current mapping of the Cu<sub>2</sub>O surfaces was obtained, indicating a higher current on the grain boundaries. Taking advantage of the ASTAR technique, we were able to scan the cross-section of the Cu<sub>2</sub>O sample with ultra high resolution. As a result, tiny amounts of CuO phase were discovered in the grain boundaries,

especially in the bottom part of the film, which helped to explain the electrical characteristics observed in the electrical AFM mapping. With optimized Cu<sub>2</sub>O (111) films, a p-n junction was also fabricated with structure of ITO/Cu<sub>2</sub>O/ZnO/Ag contact, and an excellent rectifying curve was obtained with on-off ratio exceeding 10<sup>4</sup>.

## IV.5 References

1. Chryssou, C. E. & Pitt, C. W. Al<sub>2</sub>O<sub>3</sub> thin films by plasma-enhanced chemical vapour deposition using trimethyl-amine alane (TMAA) as the Al precursor. *Appl. Phys.* **475**, 469–475 (1997).
2. Lee, J. H., Cho, Y. J., Min, Y. S. & Rhee, D. K. W. Plasma enhanced atomic layer deposition of SrTiO<sub>3</sub> thin films with Sr(tmhd)<sub>2</sub> and Ti(i-OPr)<sub>4</sub>. *J. Vac. Sci. Technol. A Vacuum, Surfaces, Film.* **1828**, 1–4 (2002).
3. Battiston, G. A. *et al.* PECVD of amorphous TiO<sub>2</sub> thin films: effect of growth temperature and plasma gas composition. *Thin Solid Films* **371**, 126–131 (2000).
4. Condorelli, G. G., Malandrino, G. & Fragala, I. Metal-Organic Chemical Vapor Deposition of Copper-Containing Phases : Kinetics and Reaction Mechanisms. *Chem. Mater.* 1861–1866 (1994). doi:10.1021/cm00046a048
5. Sénateur, J.-P., Dubourdieu, C., Weiss, F., Rosina, M. & Abrutis, A. Pulsed injection MOCVD of functional electronic oxides. *Adv. Mater. Opt. Electron.* **10**, 155–161 (2000).
6. Tsuji, T. & Hirohashi, M. Influence of oxygen partial pressure on transparency and conductivity of RF sputtered Al-doped ZnO thin films. *Appl. Surf. Sci.* **157**, 47–51 (2000).
7. Lee, Y. H., Leu, I. C., Liao, C. L. & Fung, K. Z. The structural evolution and electrochemical properties of the textured Cu<sub>2</sub>O thin films. *J. Alloys Compd.* **436**, 241–246 (2007).
8. Golden, T. D. *et al.* Electrochemical Deposition of Copper(I) Oxide Films. *Chem. Mater.* **8**, 2499–2504 (1996).
9. Salhi, R. *et al.* Effect of humidity and UV assistance on the properties of erbium doped yttrium oxide films prepared by aerosol-MOCVD. *Chem. Vap. Depos.* **17**, 93–97 (2011).
10. Pinkas, J., Huffman, J. C., Baxter, D. V, Chisholm, M. H. & Caulton, K. G. Mechanistic Role of H<sub>2</sub>O and the Ligand in the Chemical. *Chem. Mater.* **7**, 1589–1596 (1995).
11. J., H.-S. M. Chemical Vapor Deposition of Copper from (hfac)CuL (L = VTMS and 2-Butyne) in the Presence of Water, Methanol, and Dimethyl Ether. *Chem. Mater.* **8**, 1119 (1996).
12. Wang, L. & Yang, J. C. Enhanced Nucleation and Decreased Growth Rates of Cu<sub>2</sub>O in Cu<sub>0.5</sub>Au<sub>0.5</sub> (001) Thin Films During in situ Oxidation. *J. Mater. Res.* **20**, 1902–1909 (2011).
13. Tseng, C. C., Hsieh, J. H., Liu, S. J. & Wu, W. Effects of Ag contents and deposition temperatures on the electrical and optical behaviors of Ag-doped Cu<sub>2</sub>O thin films. *Thin Solid*

- Films* **518**, 1407–1410 (2009).
14. Márquez, J. A. R. *et al.* Effect of Surface Morphology of ZnO Electrodeposited on Photocatalytic Oxidation of Methylene Blue Dye Part I: Analytical Study. *Int. J. Electrochem. Sci.* **6**, 4059–4069 (2011).
  15. Hou, X. & Choy, K.-L. Processing and Applications of Aerosol-Assisted Chemical Vapor Deposition. *Chem. Vap. Depos.* **12**, 583–596 (2006).
  16. Roger, C., Corbitt, T. S., Hampden-Smith, M. J. & Kodas, T. T. Aerosol-assisted chemical vapor deposition of copper: A liquid delivery approach to metal thin films. *Appl. Phys. Lett.* **65**, 1021–1023 (1994).
  17. Ikenoue, T., Sakamoto, S. & Inui, Y. Fabrication and characteristics of p-type Cu<sub>2</sub>O thin films by ultrasonic spray-assisted mist CVD method. *Jpn. J. Appl. Phys.* **53**, 4–7 (2014).
  18. Brochen, S. *et al.* Effect of Strontium Incorporation on the p-Type Conductivity of Cu<sub>2</sub>O Thin Films Deposited by Metal–Organic Chemical Vapor Deposition. *J. Phys. Chem. C* **120**, 17261–17267 (2016).
  19. Resende, J., Jiménez, C., Nguyen, N. D. & Deschanvres, J.-L. Magnesium-doped cuprous oxide (Mg:Cu<sub>2</sub>O) thin films as a transparent p-type semiconductor. *Phys. Status Solidi* **7**, 1–7 (2016).
  20. Nguyen, V. H. *et al.* Deposition of ZnO based thin films by atmospheric pressure spatial atomic layer deposition for application in solar cells. *J. Renew. Sustain. Energy* **9**, 21203 (2017).
  21. Nandy, S. *et al.* Efficient Field Emission from Vertically Aligned Cu<sub>2</sub>O 1- $\delta$  (111) Nanostructure Influenced by Oxygen Vacancy. *Adv. Funct. Mater.* n/a-n/a (2014). doi:10.1002/adfm.201402910
  22. Biccari, F. Defects and Doping in Cu<sub>2</sub>O. (2009). doi:10.1016/0038-1098(70)90325-X
  23. Fortunato, E., Barquinha, P. & Martins, R. Oxide semiconductor thin-film transistors: a review of recent advances. *Adv. Mater.* **24**, 2945–86 (2012).
  24. Li, J. *et al.* Probing defects in nitrogen-doped Cu<sub>2</sub>O. *Sci. Rep.* **4**, 7240 (2014).
  25. Deuermeier, J. *et al.* Highly conductive grain boundaries in copper oxide thin films. *J. Appl. Phys.* **119**, (2016).
  26. Wilson, S. S. *et al.* Interface stoichiometry control to improve device voltage and modify band alignment in ZnO/Cu<sub>2</sub>O heterojunction solar cells. *Energy Environ. Sci.* **7**, 3606–3610 (2014).
  27. Mageshwari, K., Han, S. & Park, J. Fabrication and characterization of a CuO/ITO heterojunction with a graphene transparent electrode. *Semicond. Sci. Technol.* **31**, 55004 (2016).
  28. Marin, A. T. *et al.* Novel Atmospheric Growth Technique to Improve Both Light Absorption

- and Charge Collection in ZnO/Cu<sub>2</sub>O Thin Film Solar Cells. *Adv. Funct. Mater.* **23**, 3413–3419 (2013).
29. Muñoz-Rojas, D. & MacManus-Driscoll, J. Spatial atmospheric atomic layer deposition: a new laboratory and industrial tool for low-cost photovoltaics. *Mater. Horizons* **1**, 314 (2014).
  30. Fuks, D., Dorfman, S., Zhukovskii, Y. F., Kotomin, E. A. & Stoneham, A. M. Theory of the growth mode for a thin metallic film on an insulating substrate. *Surf. Sci. J.* **499**, 24–40 (2002).
  31. Grabow, M. H. & Gilmer, G. H. Thin film growth modes, wetting and cluster nucleation. *Surf. Sci.* **194**, 333–346 (1988).
  32. Karthika, S., Radhakrishnan, T. K. & Kalaichelvi, P. A Review of Classical and Nonclassical Nucleation Theories. *Cryst. Growth Des.* **16**, 6663–6681 (2016).
  33. Libera, J. A., Hryn, J. N. & Elam, J. W. Indium oxide atomic layer deposition facilitated by the synergy between oxygen and water. *Chem. Mater.* **23**, 2150–2158 (2011).
  34. Reinke, M., Kuzminykh, Y. & Hoffmann, P. Low temperature chemical vapor deposition using atomic layer deposition chemistry. *Chem. Mater.* **27**, 1604–1611 (2015).
  35. Selvaraj, S. K., Jursich, G. & Takoudis, C. G. Design and implementation of a novel portable atomic layer deposition/chemical vapor deposition hybrid reactor. *Rev. Sci. Instrum.* **84**, (2013).



<i>Chapter V Deposition and characterization of AgCuO<sub>2</sub> thin films</i>	<i>- 151 -</i>
<i>V.1 Co-deposition of silver copper oxide via Plasma Enhanced AA-MOCVD</i>	<i>- 152 -</i>
<i>V.2 Oxidation of Ag-Cu metal alloy film</i>	<i>- 156 -</i>
<i>V.2.1 Deposition of Ag<sub>0.5</sub>Cu<sub>0.5</sub> alloy films</i>	<i>- 156 -</i>
<i>V.2.2 Electrochemical oxidation</i>	<i>- 158 -</i>
<i>V.2.3 Oxygen plasma treatment</i>	<i>- 164 -</i>
<i>V.3 Deposition of AgCuO<sub>2</sub> thin films by Successive Ionic Layer Adsorption and Reaction (SILAR)</i>	<i>- 166 -</i>
<i>V.3.1 Experimental setup and parameters</i>	<i>- 167 -</i>
<i>V.3.2 Substrate preparation</i>	<i>- 168 -</i>
<i>D. Cu<sub>2</sub>O/glass substrate preparation:</i>	<i>- 168 -</i>
<i>E. ZnO/glass substrate preparation:</i>	<i>- 168 -</i>
<i>F. TiO<sub>2</sub>/glass substrate preparation:</i>	<i>- 168 -</i>
<i>V.3.3 SILAR deposition parameters</i>	<i>- 169 -</i>
<i>V.3.4 Optimization of deposition condition</i>	<i>- 169 -</i>
<i>V.3.5 Understanding the mechanism of AgCuO<sub>2</sub> thin film coating by SILAR process.</i>	<i>- 177 -</i>
<i>V.3.6 Optical and electronic property of AgCuO<sub>2</sub> films obtained by SILAR</i>	<i>- 182 -</i>
<i>V.4 Chapter VI conclusions</i>	<i>- 185 -</i>
<i>V.5 References</i>	<i>- 187 -</i>

## *Chapter V Deposition and characterization of AgCuO<sub>2</sub> thin films*

As presented in Chapter I, AgCuO<sub>2</sub> has shown to have potential to be an excellent p type small bandgap (about 1 eV) semiconductor material. The first discovery of this phase was through solution reaction and resulting in powder form<sup>1</sup>. Although several works have reported its crystal structure<sup>2</sup>, single crystal resistivity measurement<sup>3</sup> and its electronic structure<sup>4</sup>, the optical properties (eg. transmittance, bandgap) and further electrical characterizations (e.g. Hall Effect measurement) have not yet been conducted. The lack of related reports is due to the difficulty of AgCuO<sub>2</sub> thin films synthesis. To achieve such phase,

the synthesis condition has to consider both the thermal instability inherent of Ag compounds and the high oxidation states in this metal oxide. Only recently a few studies have reported attempts to synthesizing AgCuO<sub>2</sub> in thin film through electrochemical deposition, pulsed laser deposition or sputtering.<sup>5-7</sup> The electrochemical deposition method yielded rather rough, discontinuous films containing micron sized nanoplates of AgCuO<sub>2</sub>, on ITO substrate.<sup>5</sup> With the reported work with the PLD technique, the deposited thin film was not well crystallized due to the relatively lower deposition temperature (room temperature).<sup>8</sup> Sputtering films were usually not pure and presented very low crystallinity.<sup>7,9,10</sup>

With the working experiences on silver and copper oxides in MOCVD as introduced previously, this chapter will introduce the work on exploring new approaches to obtain better quality AgCuO<sub>2</sub> thin films in terms of morphology and crystallinity. There are several thin film coating techniques that have been tested in this work, including initially planned co-deposition of silver copper oxide film with Plasma Enhanced MOCVD. Other approaches explored in this work include oxygen plasma treatment of Ag-Cu alloy films deposited by MOCVD, electrochemical oxidation of Ag-Cu alloy films or by the solution method Successive Ionic Layer Adsorption and Reaction (SILAR). Finally, optical and electrical characterizations of AgCuO<sub>2</sub> films are reported for the first time.

## **V.1 Co-deposition of silver copper oxide via Plasma Enhanced AA-MOCVD**

As previously mentioned, the initial attempt was trying to use both silver and copper precursors in solution to achieve AgCuO<sub>2</sub> phase by AA-MOCVD at relatively low deposition temperatures (less than 270 °C, to avoid decomposition of Ag-Cu mixed phases). With the foundation of the previous work, by comparing the lowest decomposition temperature of the precursors available, Ag(hfac)triglyme (AgT) and Cu trifluoro acetylacetonate (CuF) were chosen as the precursors. The lowest possible deposition temperature from both precursors is at least 270 °C. Even though the temperature is still too high concerning the phase stability, there is still possibility to achieve AgCuO<sub>2</sub> thin films at such temperature in an oxidizing environment generated by oxygen plasma (containing ozone and radical species).


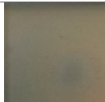
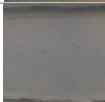



Due to the limited availability of AgT precursor (also due to the high price of Ag), the maximum mixed precursor solution concentration used was 0.02 M, which was prepared by mixing 4.9 g of AgT and 3.69 g of CuF in 500 ml of ethanol and stirring for 10 minutes at



room temperature. A crystal clear green-blue solution was achieved. A plasma power of 350 W was used with mixture of oxygen and argon as gas source. Corning glass was used as substrate for the deposition. Several depositions were performed at 250 °C and 270 °C for 1 hour, as shown in Table V-1. The obtained coatings were characterized by SEM and EDS analyses. Although XRD characterization was also used for phase identification, due to the low thickness and crystallinity of the films obtained at such deposition temperature, no reflections were obtained in the XRD patterns.

Samples were deposited with and without oxygen plasma at the same conditions. Table V-1 details the deposition parameters and the images of the deposited thin films. Judging from the intensity of the color, when using plasma during depositions the resulting samples were lighter, indicating thinner coatings (sample C1). Even though the oxygen ratio in plasma gas source was decreased, attempting to reduce the corrosion ability of the radicals, the deposited films were still rather thin (sample C2 and C3). Despite SEM characterization was attempted, the strong charging effect did not allow to obtain topographical information on the sample.

Table V-1. Co-deposition details in Plasma Enhanced AA-MOCVD, with precursor ratio AgT: CuF = 1:1 for 1 h.

Sample name	Picture of sample	Deposition temperature (°C)	Plasma power (W)	Oxygen ratio in plasma gas source
C1		270	350	50%
C2		270	350	20%
C3		270	350	10%
C4		270	300	50%
C5		250	0	
C6		270	0	

By slightly tuning down the plasma power to 300 W, at the same deposition temperature for 1 hour coating, the sample obtained (C4) showed a much more intense dark color, thus indicating a probably thicker deposition. Conversely, with further increasing the plasma

power with those deposition conditions, coatings were barely visible on the glass substrate. In addition, for the sake of comparison, two samples were also coated at 250 °C and 270 °C without plasma, as shown in Table V-1 (samples C5, C6). Without oxygen plasma, even at 250 °C, a yellow colored deposition was observed. At 270 °C, the 1 hour duration deposition without plasma resulted in a much darker colored thin film. Thus, once again the corrosive effect from the radicals in high power oxygen plasma was rather obviously evidenced.

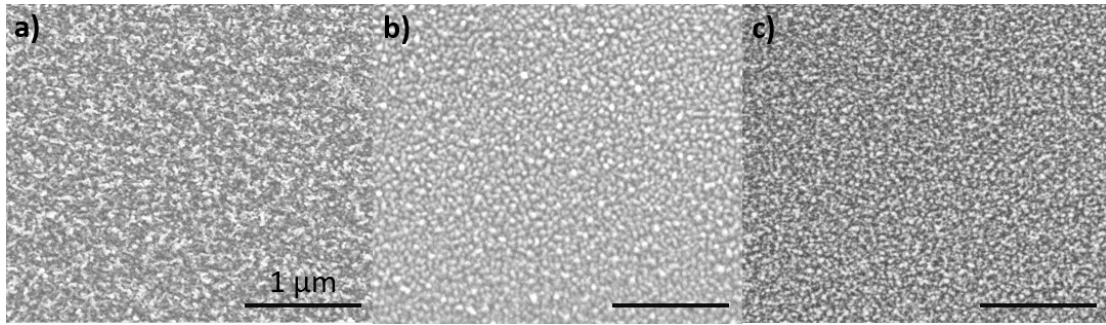
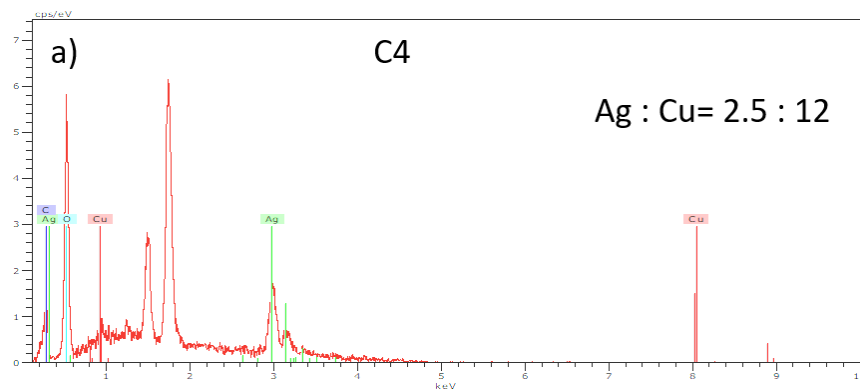


Figure V-1. SEM images of co-deposition samples in Plasma Enhanced AA-MOCVD for samples a) C4, b) C5 and C6.

SEM images of samples C4, C5 and C6, are presented in Figure V-1. The three samples presented smooth surfaces with small grains. The conductivity of sample C6 (about 40 ~ 50 nm thick) was close to metallic films with sheet resistance  $0.03 \Omega/\square$ , while the other two were rather resistive. The EDS analyses of those samples were conducted with 10 kV voltage and the results are presented in Figure V-2. Comparing all EDS analyses in figure a), b) and c), an excessive of Cu was always found in the deposited samples. Comparing figure a) and c), the 300 W plasma didn't significantly change the element ratio in the resulted thin films (at 270 °C roughly about Ag: Cu= 1: 4). At even lower deposition temperature, less copper precursors were decomposed thus an increase of silver atomic ratio was observed in Figure V-2 b).



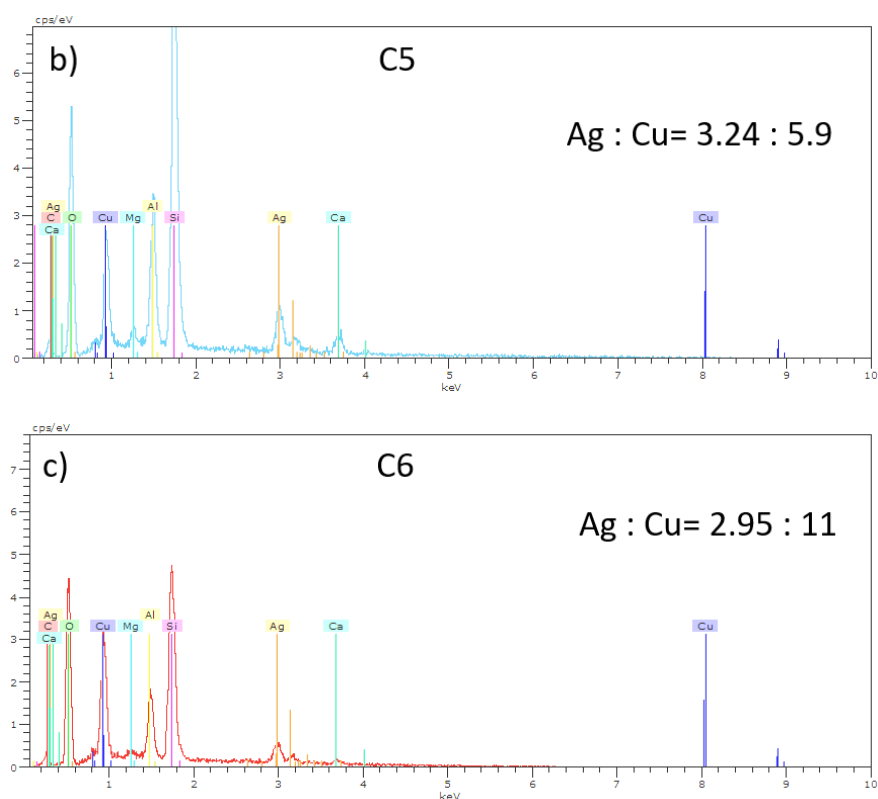


Figure V-2. EDS analyses of co-deposited samples of samples a) C4, b) C5 and c) C6.

Further tests to co-deposit silver copper oxide thin films were not conducted, due to the following several problems. First of all, to meet the temperature gap between the  $\text{AgCuO}_2$  phase stability window and precursor decomposition in MOCVD, precursors with much lower decomposition temperature (at least lower than  $200\text{ }^\circ\text{C}$ ) would be required. Due to the fact that all commercialized precursors with such low decomposition temperature, especially for silver precursors, are extremely expensive (more than 100 euro/g). Meanwhile, in AA-MOCVD, large quantity of precursors are required for each deposition (at least 1 g of precursor per deposition). Furthermore, the corrosive radicals from the oxygen plasma even bring more difficulty for the deposition process. Thus, higher precursor consumption per deposition is needed, making such co-deposition approach economically unaffordable for us. Therefore, even though it's theoretically achievable, co-deposition of  $\text{AgCuO}_2$  is not easy or affordable through Plasma Enhanced AA-MOCVD method with the current experimental conditions. For future work, an ozone generator is suggested to replace the role of oxygen plasma, so that only ozone species are produced without corrosive radicals. In addition, designing/finding new precursors with even lower decomposition temperature is necessary and the deposition temperature is suggested not exceeding  $200\text{ }^\circ\text{C}$ . Thus, other more convenient approaches to obtain  $\text{AgCuO}_2$  thin films were adopted in this work.

## V.2 Oxidation of Ag-Cu metal alloy film

Due to the difficulty of co-depositing AgCuO<sub>2</sub> with our AA-MOCVD system and the precursors available, a two-step process to achieve AgCuO<sub>2</sub> was explored, as was done for Ag (see Chapter III). As it has been reported in the work of *D. Muñoz-Rojas et al.*,<sup>11,12</sup> the AgCuO<sub>2</sub> phase can be transformed through oxidation of Ag<sub>2</sub>Cu<sub>2</sub>O<sub>3</sub> power either electrochemically or by ozone. Thanks to the high diffusion mobility of Ag atoms<sup>13-16</sup>, the oxidization of Ag<sub>0.5</sub>Cu<sub>0.5</sub> alloy films was tested to obtain the AgCuO<sub>2</sub> phase. Thus, in this work, Ag-Cu alloy films were firstly co-deposited by PI-MOCVD system (since less precursor is consumed than with AA-MOCVD) with an adjusted atomic ratio close to 1:1, and then further oxidized.

### V.2.1 Deposition of Ag<sub>0.5</sub>Cu<sub>0.5</sub> alloy films

The metallic alloy films were deposited at 320 °C with pressure 0.01 mbar and 1000 injection pulses (25 ml solution consumption) on corning glass substrates. During the deposition, the carrier gas for precursor transportation was 1 L/min Ar while the oxidizing gas was 1 L/min of oxygen. To obtain Ag<sub>0.5</sub>Cu<sub>0.5</sub>, the precursor solutions were initially prepared by mixing an equimolar amount of both precursors (0.0835 g of AgAc and 0.185 g of CuF, 0.5 mmol) in 25 ml ethanol solvent with 5 minutes of stirring. Again, to facilitate the precursor dissolution, 2.5 mmol of ethanolamine were added as dispersant. By varying the precursor concentration of the copper precursor solution, the element ratio in the films was tuned, as shown in Table V-2.

Table V-2. Detail parameters for optimization of AgCu alloy film deposition in PI-MOCVD.

Sample name	M1	M2	M3
AgAc : CuF concentration ratio	1:1	1:1.2	1:1.7
EDS analyses atomic ratio Ag: Cu	1:0.31	1:0.55	1:0.91

The EDS analyses of the films were conducted with 10 kV voltage and the results are presented in Figure V-3. As it's shown in figure a), with a 1:1 silver copper precursor ratio in solution, the deposited alloy film contained more silver than copper, with ratio 1:0.31 (sample M1). Therefore, the copper precursor concentration was increased from 0.02 M to 0.024 M, while silver precursor remained as 0.02 M. The composition of sample M2 is presented in figure b), with a slight increase of copper ratio, Ag:Cu was about 1:0.55. With

further increase of copper precursor concentration to 0.034 M, the Ag:Cu ratio in the alloy film was rather close to 1:1 ( actual value 1:0.91), as shown in figure c).

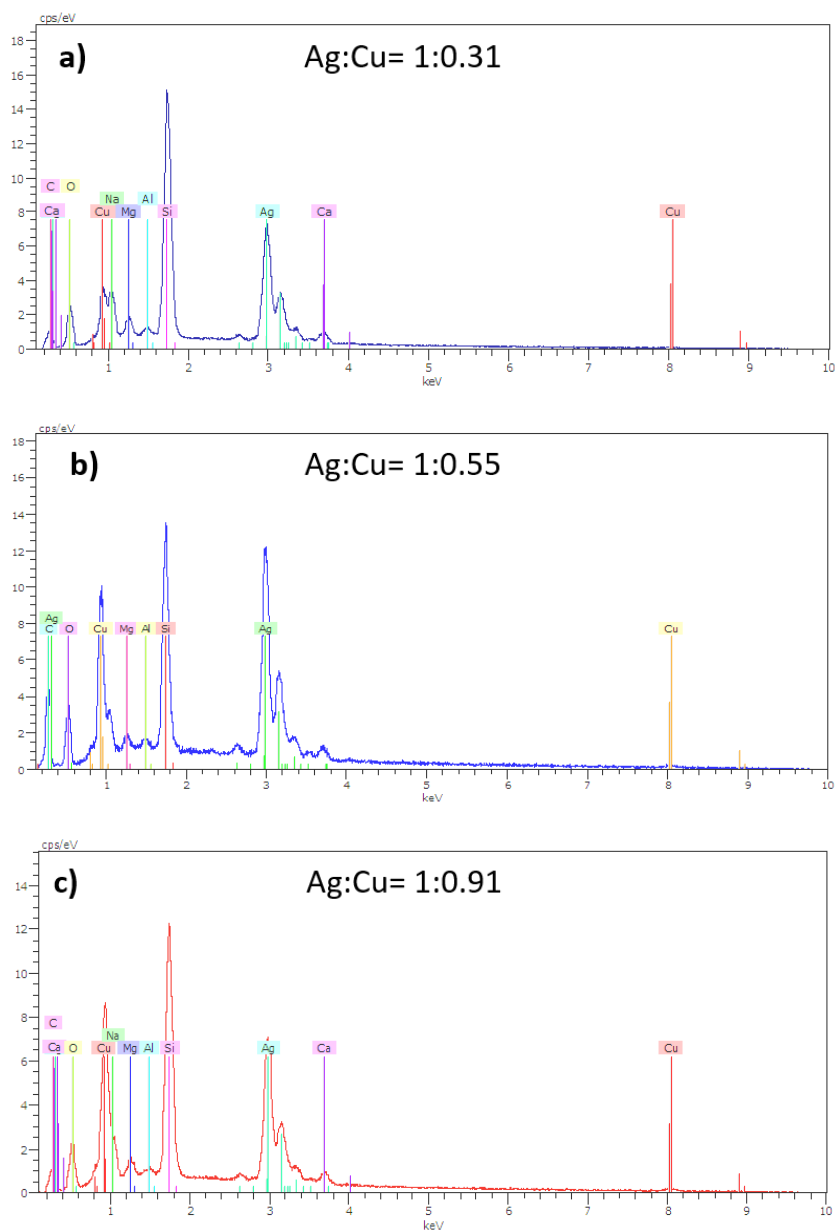


Figure V-3. EDS analyses of samples a) M1, b) M2 and c) M3.

The morphology of the optimized  $\text{Ag}_{0.5}\text{Cu}_{0.5}$  films is shown in Figure V-4, in which figure a) is the secondary electron image and figure b) is the backscattering electron image of sample M3. They show continuous AgCu metal alloy films with rather homogeneous element distributions. It's difficult to judge the elemental distribution from the backscattering electron image with the particles on surface from figure b), thus further EDS element mapping for both Cu and Ag atoms was conducted. The results are shown in Figure V-4 c) and d), an overall homogeneous element distribution was thus confirmed. These  $\text{Ag}_{0.5}\text{Cu}_{0.5}$  metallic alloy thin films were then used for further oxidation tests to obtain the  $\text{AgCuO}_2$

phase. We used two techniques to oxidize the AgCu alloy film, namely, electrochemical oxidation and oxygen plasma treatment. Those are presented in the following sections.

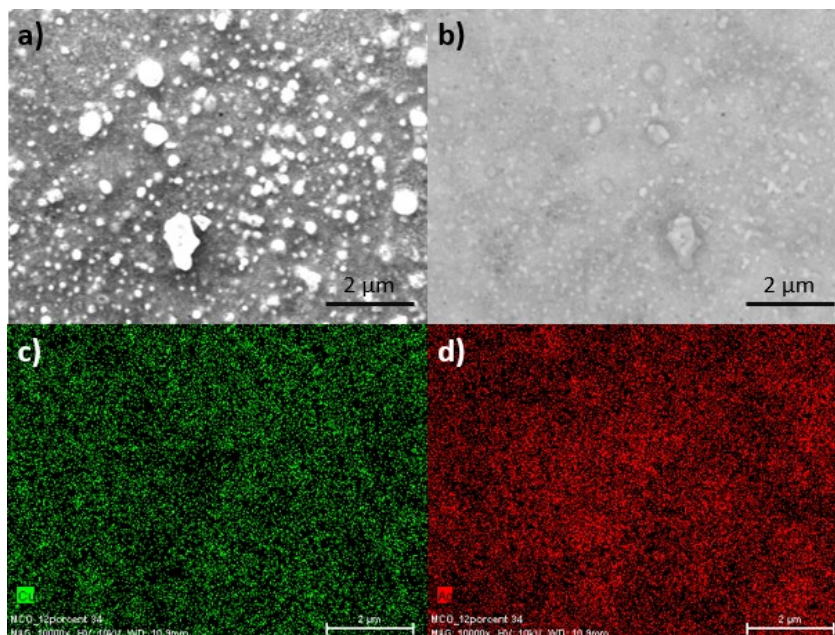


Figure V-4. a) Secondary electron image and b) Back scattering electron (BSE) image of an AgCu alloy film (sample M3) with homogeneous Cu, Ag element distribution in c) and d).

## V.2.2 Electrochemical oxidation

In Chapter III, it has been shown that silver (I, II) oxide films can be achieved through electrochemical oxidation of conductive Ag films. Therefore, a similar approach was applied for the oxidation of AgCu alloys. As usual, the initial step was to perform a cyclic voltammetry on the samples to detect the different electrochemical processes taking place and the voltages at which those occur.

Similar as for Ag films, a 3 electrode cell was used with Pt foil (size about  $1 \text{ cm}^2$ ) as counter electrode, Ag/AgCl 3.5 M KCl as reference electrode and AgCu alloy films as working electrode in 1 M NaOH electrolyte solution. The cyclic voltammetry of AgCu alloy film was obtained in the potential window  $0 \text{ V} \rightarrow 1 \text{ V} \rightarrow -1 \text{ V} \rightarrow 0 \text{ V}$  with a scanning speed of 10 mV/s. The obtained voltammogram is presented in Figure V-5.

However, the cyclic voltammetry presented in Figure V-5 does not show any clear oxidation peak from 0 V to 1 V. From 1 V to -1 V, two reduction peaks were observed at -0.82 V and -0.95 V. From -1 V to 0 V, two oxidation peaks were observed at -0.43 V and -0.16 V. Therefore, only two reversible processes seemed to appear after a first oxidation of the sample that are hard to assign.

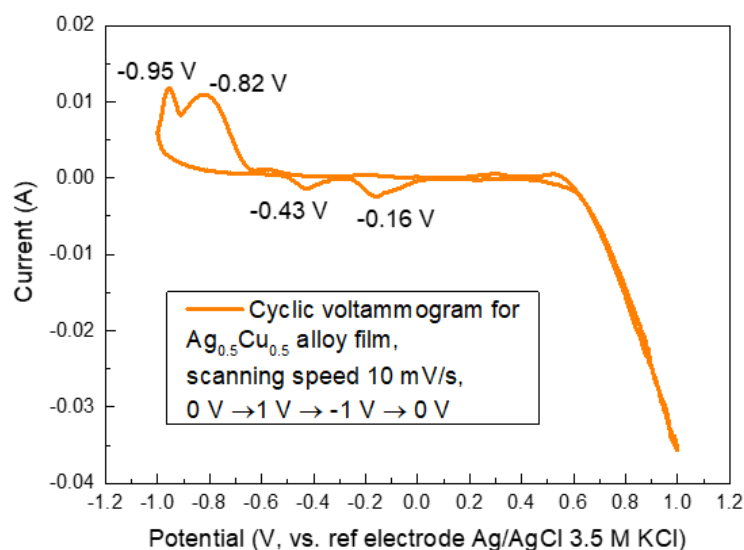


Figure V-5. Cyclic voltammetry of  $\text{AgCu}$  alloy film with scanning speed of  $1 \text{ mV/s}$ , from  $0 \rightarrow 1 \rightarrow -1 \rightarrow 0 \text{ V}$ . Scanning was conducted with  $\text{Pt}$  as counter electrode and  $0.35 \text{ M AgCl/KCl}$  as reference electrode in  $1 \text{ M NaOH}$  solution.

Thus, we used previously reported electrochemical works of D. Muñoz-Rojas *et al.*,<sup>12</sup> and several electrochemical oxidation experiments were designed with parameters as shown in Table V-3. The electrochemical oxidation of  $\text{AgCu}$  films was conducted under different potentials ranging from  $+0.5 \text{ V}$  to  $+0.7 \text{ V}$ . Besides, the effect of electrolyte concentration ( $\text{NaOH}$  solution) was also studied. As for the  $\text{AgCu}$  alloy thin film samples, even though the deposition parameters to obtain  $\text{Ag}_{0.5}\text{Cu}_{0.5}$  composition films were optimized, unfortunately, due to the reproducibility problem of the PI-MOCVD system, the later deposited  $\text{AgCu}$  films have less copper element incorporated.

Table V-3. Electrochemical oxidation of  $\text{AgCu}$  film parameters.

Sample names	Electrolyte NaOH concentration (M)	Potential for oxidation (V)	Oxidation duration (min)	Obtained phases
EA01	0.2	0.5	17	$\text{Ag}_2\text{O}$ , Cu
EA02		0.6		Ag, Cu
EA03		0.7		$\text{Ag}_2\text{O}$ , Cu
EA03b		0.7	34	Ag, Cu
EB01	0.5	0.5	17	$\text{Ag}_2\text{O}$ , Cu
EB02		0.6		$\text{Ag}_2\text{O}$ , Cu
EB03		0.7		$\text{Ag}_2\text{O}$ , Cu
EB03b		0.7	34	$\text{Ag}_2\text{O}$ , Cu
EC01	1	0.5	17	$\text{Ag}_2\text{O}$ , Cu
EC02		0.7		$\text{Ag}_2\text{O}$ , Cu

The morphologies of the electrochemically oxidized  $\text{AgCu}$  samples in  $0.2 \text{ M NaOH}$  solution at various potentials are shown in Figure V-6. In figure a),  $0.5 \text{ V}$  was applied for  $17 \text{ min}$  (sample EA01), on the surface both big cubic and needle like structures were observed. With

higher potential, 0.6 and 0.7 V (sample EA02 and EA03), the needle-like particles became more prominent as shown in Figure V-6 b) and c). In figure d), with longer oxidation time at 0.7 V (sample EA03b), the sample surface was mostly covered by needle structured grains.

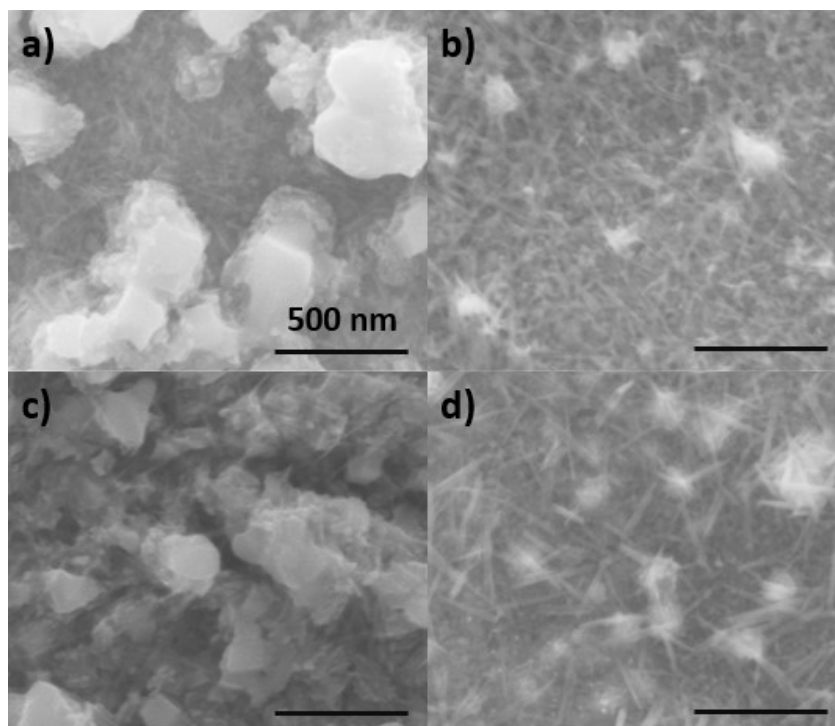


Figure V-6. SEM of electrochemically oxidized AgCu film in 0.2 M NaOH solution with different potentials: a) 0.5 V (sample EA01), b) 0.6 V (sample EA02), c) 0.7 V (sample EA03) for 17 min and d) 0.7 V (sample EA03b) for 34 min.

In addition to the morphology characterization, the GIXRD patterns of the different samples were recorded and are shown in Figure V-7. Since those electrochemically oxidized samples were silver rich films, in the XRD of the original AgCu alloy film, only a weak peak reflection corresponding to Cu phase was obtained. In all XRD patterns, the reflection with the strongest intensity corresponds to metallic Ag, indicating a majority of Ag phase in all these samples. When 0.5 V were applied for the oxidation (EA01), a reflection corresponding to  $\text{Ag}_2\text{O}$  phase appeared. Similar XRD peaks corresponding to CuO were also observed with 0.7 V potential (sample EA03). Meanwhile, in the other two cases, the XRD patterns didn't show any change comparing with the original XRD reflections. In addition, no peak reflections corresponding to  $\text{Ag}_2\text{Cu}_2\text{O}_3$  or  $\text{AgCuO}_2$  phase was observed in these oxidation conditions.



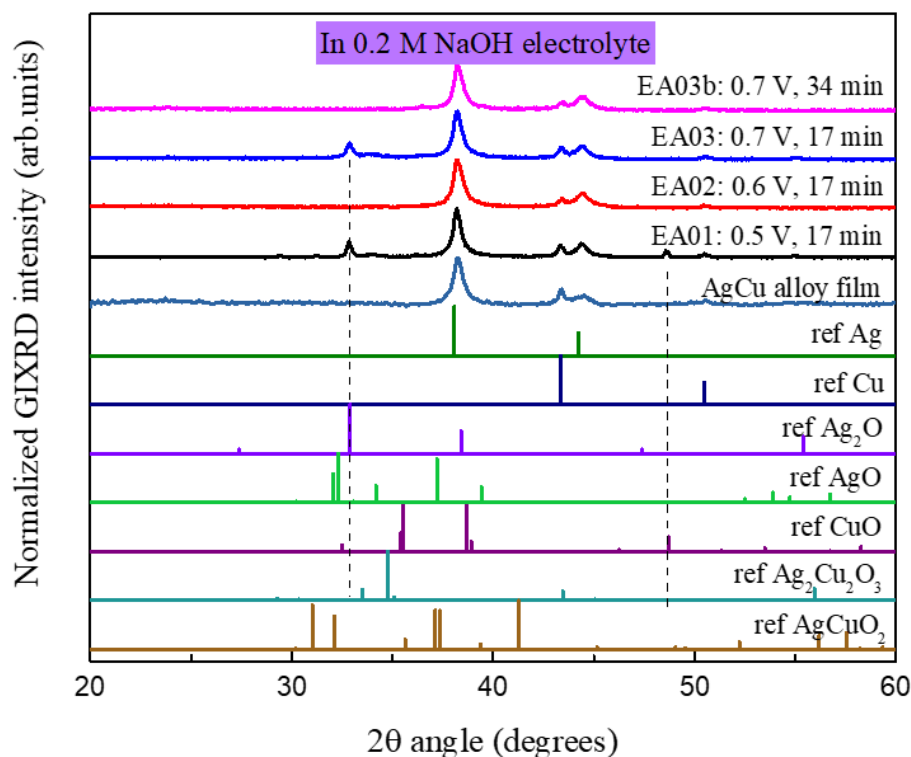


Figure V-7. GIXRD patterns of electrochemically oxidized AgCu film in 0.2 M NaOH solution at different potentials ranging from 0.5 to 0.7 V.

In addition to the oxidation of AgCu in 0.2 M NaOH solution, oxidations were also carried out with higher electrolyte concentration, namely, 0.5 and 1 M. The morphology of the samples obtained in 0.5 M NaOH solutions are presented in Figure V-8, in which at lower potentials, 0.5 and 0.6 V, both cubic and needle like particles are visible on the surface as shown in figure a) and b). With increased potential to 0.7 V, the needle-like grain structure became prominent on the surface, as presented in Figure V-8 c). In Figure V-8 d), at 0.7 V with longer oxidation duration (34 min), the needle like grains didn't appear on the surface, which could be because of reproducibility issues with our oxidation setup.

Concerning the phase change during the electrochemical oxidation process, Figure V-9 presents the emergence of a reflection at about  $32^\circ$  for  $\text{Ag}_2\text{O}$  in all cases. With longer duration, the reflection peak intensity corresponding to  $\text{Ag}_2\text{O}$  increased. Thus, comparing with previous works on CuO nano structures,<sup>17-19</sup> those needle like grains are more likely CuO grains. Meanwhile, considering the cubic structure of  $\text{Ag}_2\text{O}$  grains, those cubic grains on surface are more likely to be the  $\text{Ag}_2\text{O}$  identified in XRD.

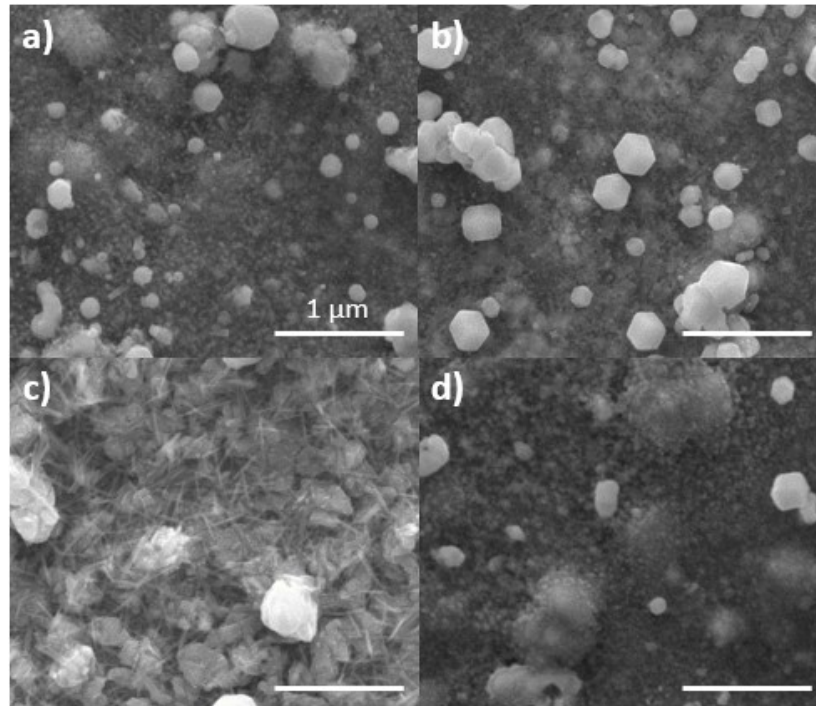


Figure V-8.  $\text{AgCu}$  films electrochemically oxidized in 0.5 M  $\text{NaOH}$  solution with potentials, a) 0.5 V (EB01), b) 0.6 V (EB02), c) 0.7 V for 17 min (EB03) and d) 0.7 V for 34 min (EB03b).

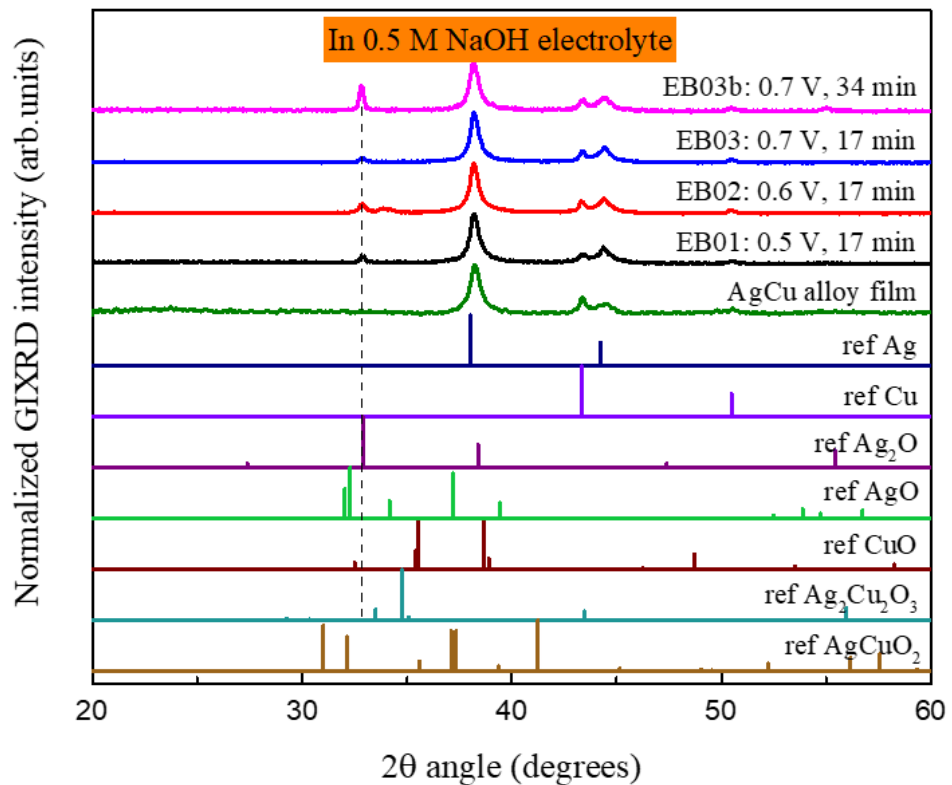


Figure V-9. GIXRD of  $\text{AgCu}$  films electrochemically oxidized in 0.5 M  $\text{NaOH}$  solution with various potentials. Similar experimental setups were used as introduced before.

Finally, with even higher electrolyte concentration ( $\text{NaOH}$  1 M), oxidation of  $\text{AgCu}$  films were conducted by applying 0.5 V and 0.7 V for 17 min. The morphology of the oxidized samples is presented in Figure V-10. At lower oxidation potential 0.5 V, clusters made with nanoplates like structures emerged out of the surface. Similar clusters can also be found on the surface of the sample oxidized at 0.7 V. Thus, even if the desired  $\text{AgCuO}_2$  phase is able to be formed through such oxidizing technique, the morphology of the obtained films will be rather rough and not homogeneous, which is not ideal neither for thin film property characterizations nor for device fabrication.

The GIXRD patterns of those samples are shown in Figure V-11, in which reflections corresponding to  $\text{Ag}_2\text{O}$  phase appeared, similar to the previous results. Since in SEM, only the nanoplates clusters are observed, thus inform the XRD data, these structures can be associated with the  $\text{Ag}_2\text{O}$  phase. The change of the grain shape is more like due to a higher electrolyte concentration.

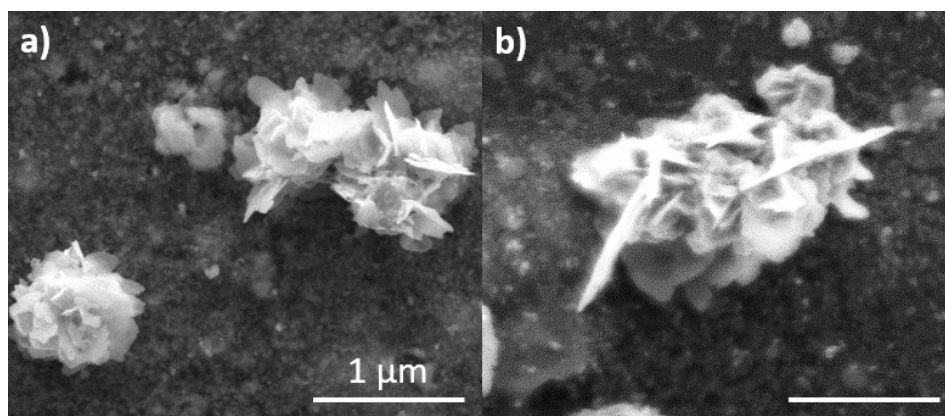


Figure V-10. Morphology of  $\text{AgCu}$  film oxidized electrochemically in 1 M  $\text{NaOH}$  solution by applying potential a) 0.5 V (EC01) and 0.7 V (EC02) for 17 min.

So as shown, the oxidation of  $\text{AgCu}$  films through electrochemical approach was tested in different concentration of  $\text{NaOH}$  solution electrolyte with potential ranging from 0.5 to 0.7 V. The treated samples were characterized by GIXRD and no reflections were found corresponding to the desired silver copper mixed oxide phase. In addition, the oxidized samples presented quite rough morphology, which is in accordance with the results of the electrochemical oxidation of  $\text{Ag}$  films presented in Chapter III. Conversely, as previously reported, the oxygen plasma treatment was able to oxidize 100 nm  $\text{Ag}$  films rapidly, the morphology of the oxidized films presented a smooth and continuous manner. Therefore, the same oxidation technique, oxygen plasma treatment, was adopted and the results are presented in the next section.

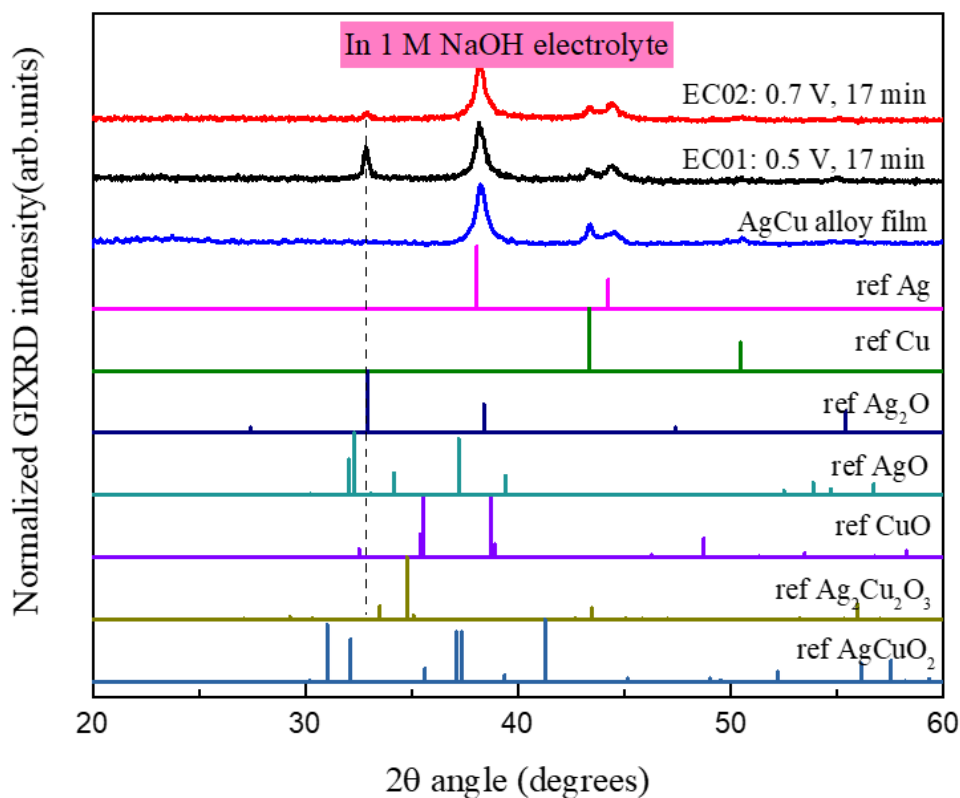


Figure V-11. GIXRD of AgCu film oxidized electrochemically in 1 M NaOH solution by applying potential a) 0.5 V and 0.7 V for 15 min.

### V.2.3 Oxygen plasma treatment

In addition to the electrochemically oxidation, there are several other approaches that can be applied to oxidize the AgCu film. In this work, oxygen plasma treatment was also tested. As previously introduced with oxygen plasma treatment of Ag films, such oxidation technique is rapid and it doesn't have the requirement for a conductive substrate.

The oxygen plasma treatments were conducted with different plasma power (ozone intensity) and substrate temperatures. The morphology of the as-deposited and oxidized films is presented in in Figure V-12. Figure V-12 a) shows the the surface morphology of the as-deposited AgCu alloy film. By applying 300 W power of pure oxygen plasma on heated substrate (at 75 °C) for 3 min, the morphology did not change much, as shown in Figure V-13 b). With increased plasma power to 400 W, after 3 min treatment (at 75 °C), hollow structures were visible on the sample surface, as presented in Figure V-12 c). Figure V-12 d) shows the morphology obtained after treating the alloy for 3 min with a plasma of 300 W, as shown in Figure V-13 b), but at higher temperature (200 °C). In this case, there is a significant change in film morphology, with big particles visible on top of the film.

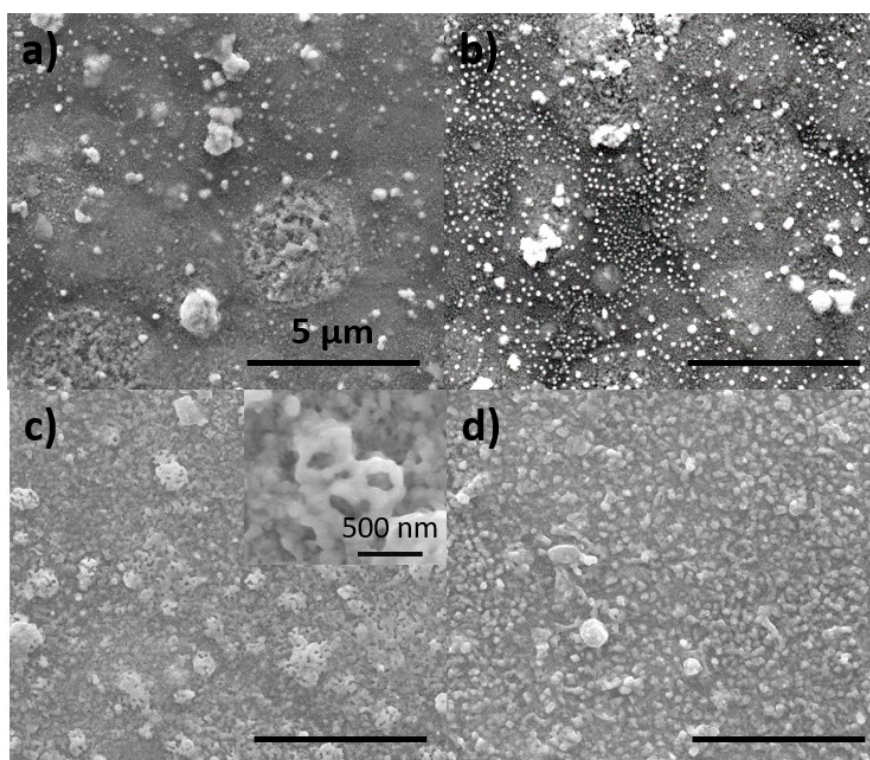


Figure V-12. SEM images of a) as-deposited AgCu film, and films oxidized at 75 °C for 3 min using a 300 W (b) and 400 W (c) plasma (PL1 and PL2). d) Film oxidized at 200 °C for 3 min using 300 W plasma (PL3).

The GIXRD patterns of these samples are shown in Figure V-13. Similar with previous case, the intensity of reflections corresponding to Cu was rather weak. By comparing the phase change between different plasma power and treatment temperature, the latter seems to play a more critical role for increasing the reactivity of the metal atoms thus obtaining a strong signal from  $\text{Ag}_2\text{O}$ , as shown by the sky blue curve. But unlike the simple case with Ag film only (introduced on Chapter III), except the  $\text{Ag}_2\text{O}$  phase no other phases were obtained. Thus, no reflections corresponding to silver copper mixed oxide phase was observed. In a work of D. Muñoz-Rojas *et al.*,<sup>11</sup> the solid phase transformation from  $\text{Ag}_2\text{Cu}_2\text{O}_3$  powders to  $\text{AgCuO}_2$  was conducted in ozone environment at room temperature and lasting for more than 10 hours. In addition, the ozone treatment of a mixture of metallic copper and silver powder with 1:1 ratio was reported. The ozone treated powders only resulted in small amount of  $\text{AgCuO}_2$  phase. The major obtained phase was silver oxide but without copper oxide. In addition, the ozone oxidation of AgCu alloy films were also tested, and the results showed that it was mostly silver that was oxidized, in agreement with the results here. In our work, because of the thin film form of the alloy instead of the powders, less areas were exposed to the ozone species, which further increases the difficulty to achieve the full oxidation of the alloy film. In addition, in this work, due to the corrosive radicals from the oxygen plasma, long duration exposure of samples to ozone species were not possible. Combining all those reasons, the

oxygen plasma treatment of  $\text{AgCu}$  alloy films was not suitable to obtain  $\text{AgCuO}_2$  thin films neither.

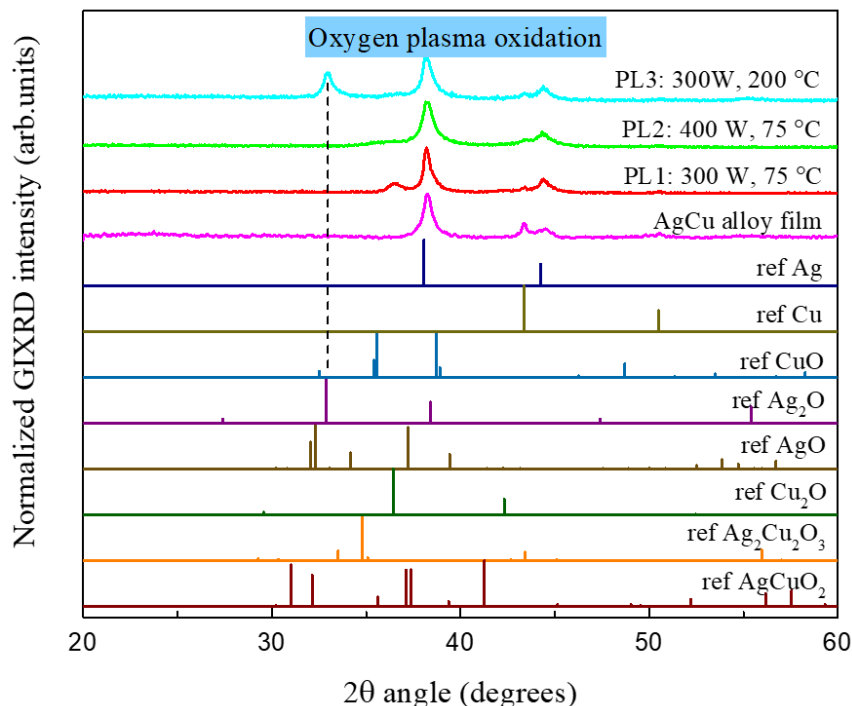


Figure V-13. GIXRD patterns of  $\text{AgCu}$  film as deposited and treated by oxygen plasma with different power and temperatures.

### V.3 Deposition of $\text{AgCuO}_2$ thin films by Successive Ionic Layer Adsorption and Reaction (SILAR)

As previously introduced, several approaches have been tested to synthesize  $\text{AgCuO}_2$  thin films. Initially, the direct co-depositions were attempted via Plasma coupled AA-CVD. Then, the oxidation of the  $\text{AgCu}$  alloy films was also tested. Unfortunately, none of those methods was able to yield  $\text{AgCuO}_2$  thin films. As previously introduced, to obtain  $\text{AgCuO}_2$  phase, there are mainly two criteria, low deposition temperature and highly oxidizing environment. Those two requirements can be easily satisfied in solution-based deposition techniques. Therefore, to obtain  $\text{AgCuO}_2$  thin films, the possibility of using solution based coating techniques was investigated.

Successive Ionic Layer Adsorption and Reaction (SILAR) has been widely used for the deposition of high quality binary/ternary compound thin film coatings.<sup>20-22</sup> The reaction mechanism of SILAR, which relies on the adsorption and reaction of metal cations and negative anions, has been introduced in Chapter II. Since SILAR is a low temperature deposition technique, thus the concerns about  $\text{AgCuO}_2$  thermal stability can be eliminated.

The high oxidizing reaction environment in SILAR process can be easily created by adding oxidizing chemical reagents, such as  $\text{H}_2\text{O}_2$ ,  $\text{Na}_2\text{S}_2\text{O}_8$ , etc. Thus, this part of work will introduce the experimental setup and parameters used for the deposition of  $\text{AgCuO}_2$  thin films by SILAR method. In addition, the electronic and optical properties of the obtained  $\text{AgCuO}_2$  thin films will be reported for the first time in literature.

### V.3.1 Experimental setup and parameters

The metal oxide thin film coating process known as SILAR is shown in Figure V-14. A specifically chosen substrate is immersed in metal and cation ion solutions in sequence, and buffer solution in between to rinse away the excessive ions on the surface. Different concentrations of  $\text{AgNO}_3$  (99%, Sigma Aldrich), and  $\text{Cu}(\text{NO}_3)_2 \cdot 3\text{H}_2\text{O}$  (98%, Sigma Aldrich) were used as the metal precursors in the metal ion solution to meet the stoichiometry in  $\text{AgCuO}_2$  in the final films. Pure deionized water was used as buffer solution. To deposit metal oxide,  $\text{NaOH}$  was introduced as the anion solution. According to previous works about solution synthesis of  $\text{AgCuO}_2$  powders, the concentration of  $\text{NaOH}$  solution was chosen as 1 M.<sup>1,2</sup> Due to the high oxidation states in  $\text{AgCuO}_2$ , sodium persulfate ( $\text{Na}_2\text{S}_2\text{O}_8$ , 98%, Sigma Aldrich), was also mixed into the anion solution as a strong oxidizer.<sup>3,23</sup> During the deposition process, the immersion speed was set to 60 mm/s and withdrawal speed was fixed at 5 mm/s. The moving distance on Z axis and rotation angles of the different motors in the X-Y plane were adjusted and controlled through a central server connecting with a PC using Perfect Motion V.02 software.

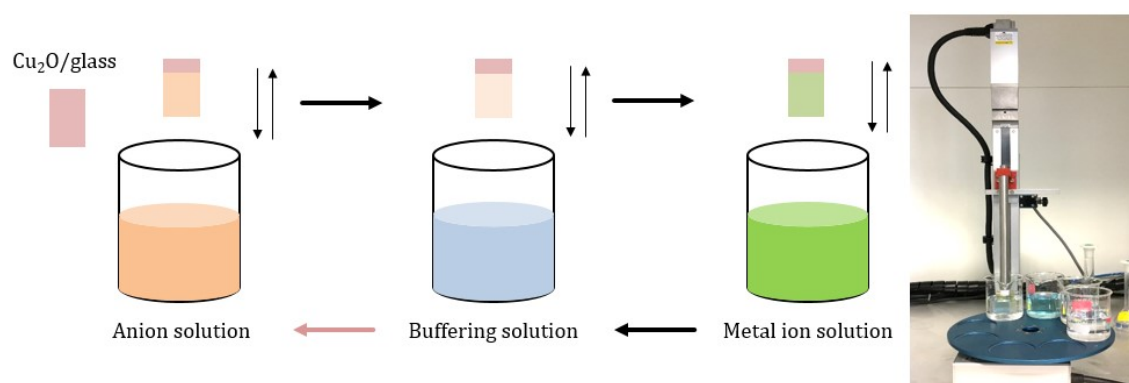


Figure V-14. Schematic presentation of the SILAR process for the deposition of metal oxides thin films. The image to the left shows the actual setup used.

### V.3.2 Substrate preparation

The substrate is crucial for a successive SILAR deposition, thus different substrates were tested, including Corning glass, Si substrate and metal oxide thin films ( $Cu_2O$ ,  $ZnO$  and  $TiO_2$ ). Among these substrates,  $Cu_2O$ /glass,  $ZnO$ /glass and  $TiO_2$ /glass were prepared in LMGP. Below, the substrate preparation for SILAR deposition is described for each case.

#### D. $Cu_2O$ /glass substrate preparation:

The  $Cu_2O$  films were coated on cleaned Corning glasses (with size about  $2.5\text{ cm} \times 3.75\text{ cm}$ ). The depositions were conducted in AA-CVD as introduced in Chapter IV. During the deposition, aerosol were formed with 0.01 M  $CuF$  precursor solution and they were carried into deposition chamber by CG1 (2 L/min) and CG2 (3 L/min) plus 5 L/min air. The ventilation value was set to 250, corresponding to 3 cm of liquid length in the pressure gauge. The depositions were carried out at  $335\text{ }^\circ\text{C}$  with dry carrier gas for 40 min, reaching a thickness of approximately 70 nm.

#### E. $ZnO$ /glass substrate preparation:

The  $ZnO$  layers were deposited by Atmospheric Pressure Spatial Atomic Layer Deposition (AP-SALD) with the help of *Mr. V.H.Nguyen* in LMGP, as in Chapter IV. Diethyl zinc ( $(C_2H_5)_2Zn$ ; DEZ) and water vapor ( $H_2O$ ) were used as precursors for zinc and oxygen, respectively. The flowrate for  $N_2$  bubbling through the DEZ and  $H_2O$  bubbler were 30 sccm and 100 sccm, then diluted with  $N_2$  flow rates of 270 sccm and 350 sccm, respectively.. The sample oscillated under the injection head at a travelling speed of 10 cm/s. The depositions were conducted at  $220\text{ }^\circ\text{C}$  for 200 cycles on cleaned corning glass substrate, reaching a thickness of about 300 nm. Before using them for SILAR coating, the substrates were cut in pieces  $2.5\text{ cm} \times 3.75\text{ cm}$  in size.

#### F. $TiO_2$ /glass substrate preparation:

With the help of *Mr. R.Parize* in LMGP, the  $TiO_2$  thin layers were prepared by Atomic Layer Deposition (ALD) (F200 Fiji reactor from Cambridge Nanotech). The deposition parameters have been reported.<sup>24</sup> Sequential pulses of tetrakis dimethylamino titanium (TDMAT) and  $H_2O$  of 0.1 s followed by a purge of 10 s after each pulse were used to alternately inject titanium and oxygen precursors, respectively. The TDMAT chemical precursor was heated at  $75\text{ }^\circ\text{C}$ . The deposition chamber was maintained at  $200\text{ }^\circ\text{C}$  during the whole deposition,



and its pressure was set to 11 mTorr. 500 cycles of deposition were employed to grow about 30 nm thick TiO<sub>2</sub> layers on Si substrate. The samples were annealed in air in an oven kept at 300 °C for 3 h for crystallizing the amorphous TiO<sub>2</sub> layer into the anatase-TiO<sub>2</sub> phase.

With the prepared substrate, before being employed in SILAR process, 10 min of acetone and 10 min of isopropanol ultrasonic bath were required. Then, the substrates were dried by nitrogen purges and thus ready for deposition.

### **V.3.3 SILAR deposition parameters**

The metal precursor solution was prepared by mixing 0.42 g of AgNO<sub>3</sub> (0.0025 mol) and different amounts ( $m_{Cu}$ ) of Cu(NO<sub>3</sub>)<sub>2</sub>.3H<sub>2</sub>O in 50 ml D.I. water and followed by 5 minutes magnetic bar stirring. The cation solution was prepared by adding 2 g of NaOH (0.05 mol) and 1 g of Na<sub>2</sub>S<sub>2</sub>O<sub>8</sub> (0.0042 mol) in 50 ml of D.I. water and the mixture was stirred for 10 minutes. The two buffer solutions used were 50 ml of D.I. water. To achieve the same liquid level, all those solutions were kept in glass beakers with the same size (total volume of 80 ml). The moving down range for the substrate was set to 77 mm. To be immersed in solution, the substrates were moved down with speed of 5 mm/s. To remove the substrate from the solutions, they were withdrawn at a speed of 60 mm/s. One cycle of SILAR deposition normally began with substrate immersion in cation ion solution for  $t_1$  s, then the position of the substrate was changed to the buffer solution 1 for  $t_2$  s. Thirdly, the cation ion covered substrate was taken out of buffer solution 1 and immersed in metal ion precursor solution and maintained for  $t_3$  s. Lastly, the substrate was rinsed in buffer solution 2 for  $t_4$  s. By repeating the cycles, the coating of AgCuO<sub>2</sub> were achieved.  $m_{Cu}$  represents the mass of added Cu(NO<sub>3</sub>)<sub>2</sub>.3H<sub>2</sub>O precursor,  $t_1$ ,  $t_2$ ,  $t_3$  and  $t_4$  are the duration in each solution. The deposited films were dried by nitrogen purge and then in 100 °C oven for 1 hour. With other parameters remaining the same, those parameters were chosen to be optimized and the results are presented in the following sections.

### **V.3.4 Optimization of deposition condition**

The first SILAR deposition was conducted adding 0.47 g (0.0025 mol) of Cu(NO<sub>3</sub>)<sub>2</sub>.3H<sub>2</sub>O in the mixture precursor solution.  $t_1$ ,  $t_2$ ,  $t_3$  and  $t_4$  were set to be 15 s, 10 s, 5 s and 10 s. Under this deposition conditions, different substrates including corning glass, Si substrate, TiO<sub>2</sub>/glass, ZnO/glass and Cu<sub>2</sub>O/glass were tested with 70 deposition cycles. Due to a low adhesion between the metal ions and most of the mentioned substrates, the coated layers on surface tend to fall back in the solutions. Only ZnO/glass and Cu<sub>2</sub>O/glass could give

successive SILAR coatings. Especially with  $\text{Cu}_2\text{O}$  layer, the deposition rate was much faster than with any other substrate. Thus, the optimization of  $\text{AgCuO}_2$  film deposition was mainly conducted with  $\text{Cu}_2\text{O}$ /glass substrate. The depositions on  $\text{ZnO}$ /glass by SILAR will be presented in the section dealing with reaction mechanism below.

Using these deposition parameters, sample A0 was coated on  $\text{Cu}_2\text{O}$ /glass substrate. The morphology of the coating is presented in Figure V-15 a) and b). The secondary electron image in figure a) shows a sample with big grains scattered on the surface. The grain size reaches 300 nm, as shown in the inserted close-up image.

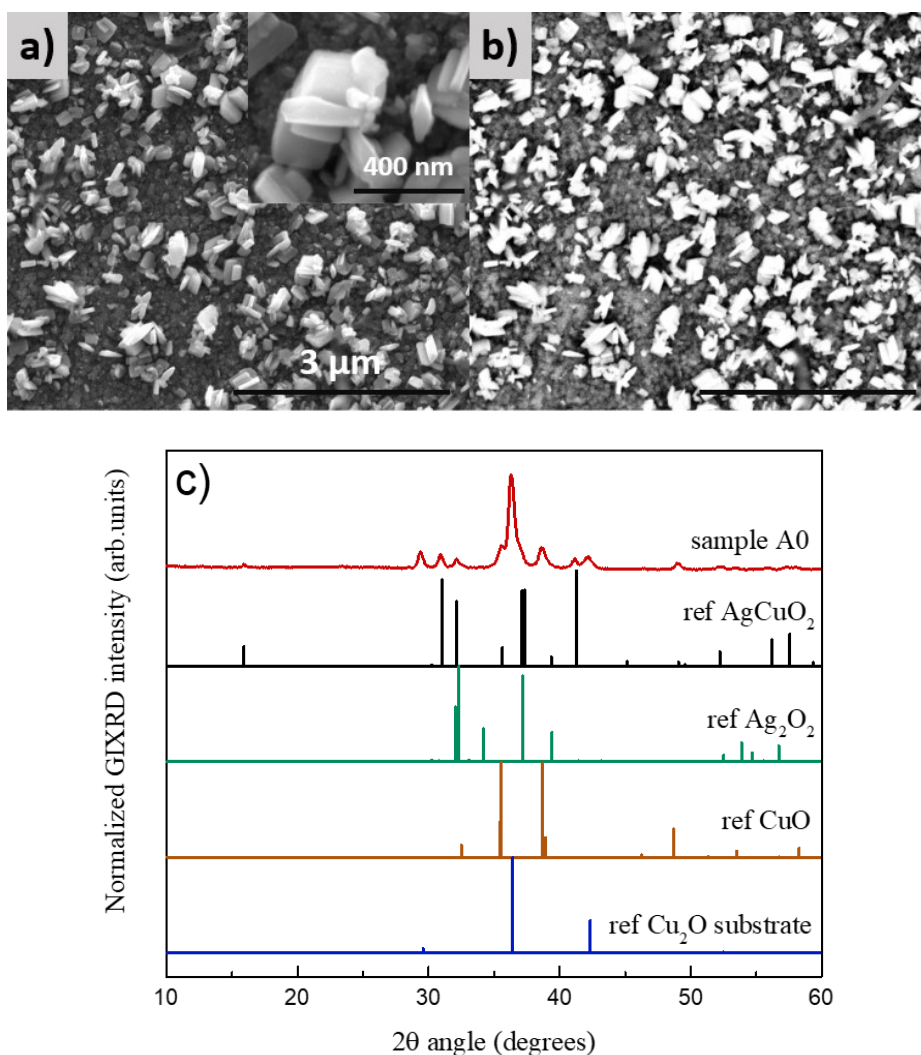


Figure V-15. Characterizations of first synthesized  $\text{AgCuO}_2$  film by SILAR deposition (sample A0): a) SEM secondary electron image and corresponding b) SEM backscattering image. c) GIXRD pattern.

In figure b), the BSE image presents a rather clear element contrast between grains and substrate. On those grains, the electron intensity is much brighter than the surrounding substrate, which could be either due to a loose connection between these grains and the

substrate (thus inducing charging effects) or the to the heavier elements being more concentrated in those scattered particles.

The GIXRD pattern of sample A0 is presented in Figure V-15. As it is shown, the strongest reflection corresponds to the Cu<sub>2</sub>O phase (from the substrate). Besides that, several unique reflections corresponding to AgCuO<sub>2</sub> phase were observed. Those unique reflections are locating around 16 °, 31.5 °, 32.3 ° and 41.5 °. Thus, AgCuO<sub>2</sub> phase could be successfully synthesized through the SILAR approach. Meanwhile, in addition to the desired phase, rather clear reflections associated with CuO phase were also observed in the XRD pattern. Thus, the optimization of AgCuO<sub>2</sub> thin film deposition in SILAR was carried out from two aspects, morphology and phase purity.

The discontinuity of the deposited particles on substrate could be possibly due to the insufficient time for metal ions to cover the substrate surface evenly during immersion. Therefore, increasing the immersion duration in the metal ion solution was used to try to improve that. To optimize the morphology of AgCuO<sub>2</sub> thin films (on Cu<sub>2</sub>O/glass substrate), the immersion duration (**t**<sub>3</sub>) in metal ion precursor was increased from 10 s to 27 s, as shown in Table V-4.

Table V-4. Parameters of AgCuO<sub>2</sub> surface morphology optimization.

Sample names	A0	A1	A2	A3
Immersion duration in metal ion precursor <b>t</b> <sub>3</sub> (s)	5	10	20	27

Note: Ag<sup>1+</sup> and Cu<sup>2+</sup> ion concentration were fixed to 0.05 M. **t**<sub>1</sub>, **t**<sub>2</sub>, **t**<sub>4</sub> remained the same with values 10 s, 15 s, and 10 s.

The evolution of thin film morphology regarding to the immersion duration in the metal cations solution is presented in Figure V-16. As it is shown, with less immersion time in, due to the incomplete covering of the surface by ions, the resulting deposition is more island-like (sample A1), as shown in Figure V-16 a). With more time in metal cation solution, a 90 nm thick thin film with better continuity was obtained (sample A2, morphology shown in Figure V-16 b) and cross section in d)). In addition to that, the inserted back scattering image shows a uniform element composition on the surface. With even longer duration, the surface still remained continuous but the BSE image showed rather clear contrast, which is more likely due to the rough morphology in this case (sample A3), as shown in Figure V-16 c).

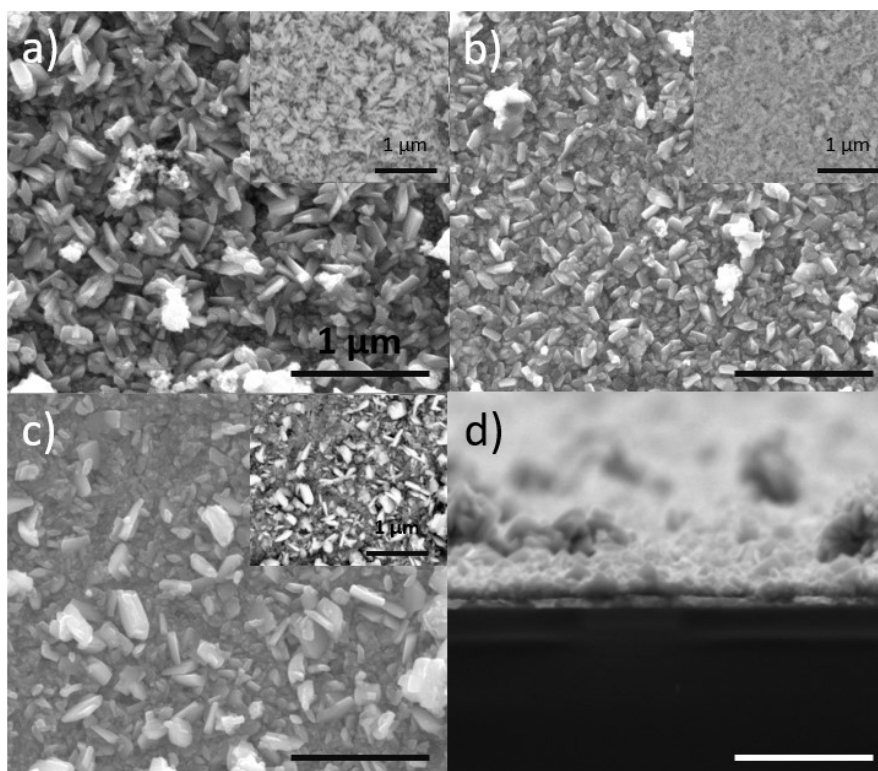


Figure V-16. SEM images of  $\text{AgCuO}_2$  samples deposited by SILAR with different immersion times in metal precursor solution. a) 10 s (A1), b) 20 s (A2), c) 27 s (A3) and d) cross section of b).

On the other hand, in order to reduce the impurity in the  $\text{AgCuO}_2$  film, the copper ion concentration was decreased gradually while the silver ion concentration was kept constant at 0.05 M. The immersion duration in metal precursor solution ( $t_3$ ) was thus set to 20 s. With all other deposition conditions remaining the same, several depositions were conducted as shown in Table V-5. Due to the special condition of the samples (both substrate and the deposited  $\text{AgCuO}_2$  films contain copper), the EDS analyses can possibly penetrate the deposited sample layers thus the copper element from the substrate can be taken into account as well. Therefore, the EDS analyses of the element composition of the films is not reliable. To evaluate the deposited phase, GIXRD was the most appropriate available technique for phase identification in our case.

Table V-5. Phase purity optimization by adjusting the concentration of copper ions in solution.

Sample names	B5	B4	B3	B2	B1
Phase optimization: $\text{Ag}^{1+}$ fixed at 0.05 M, $\text{Cu}^{2+}$ precursor concentrations (M)	0.028 M	0.03 M	0.035 M	0.04 M	0.05 M

The morphology of the samples deposited with different copper metal ion concentrations were characterized by SEM and the images are presented in Figure V-17. As it is shown, figure a) is the SEM image of the film deposited with equal ratio of copper and silver ion concentration in solution, presenting a dense surface with small grains (size about 100 nm). Similar to the grains presented in Figure V-15, they have a platelet-like shape but with much small grain size (about 70 nm in length).

Due to the vertical geometry of the SILAR deposition system, any particles in the solution could have the possibility to attach on the substrate surface, thus there are several bigger clusters remaining on the deposited film. The corresponding BSE image is placed on the top-right corner, in which a rather uniform element distribution across the surface is observed. The slight white and black contrast in the backscattering electron image is more likely attributed to the morphology of the sample.

With slightly decreased copper ion concentration down to 0.4 M, the surface morphology of the deposited film (sample B2) has a more flat surface as shown in figure b). The shape of the grains changed from platelet-like to more cubic-like particles, with length around 80 nm. Meanwhile, the inserted BSE image shows a rather homogeneous element distribution. With a further decrease in the the copper ion concentration (sample B3) is presented in figure c), similar platelet-like structures were also observed on the sample surface, but with a much bigger size (with length up to 200 nm). The film still showed a dense and continuous aspect. The inserted BSE image also shows a homogeneous element distribution. Lastly, with further lowering the copper ion concentration, a smooth thin film surface was obtained, as presented in figure d). In this case the film is made up of much smaller particles (about 70 nm) than for samples deposited with higher Cu concentration (sample B4). The backscattering electron image also shows an even element distribution between silver and copper on the surface. Due to a smoother surface morphology, less contrast is present in the image.

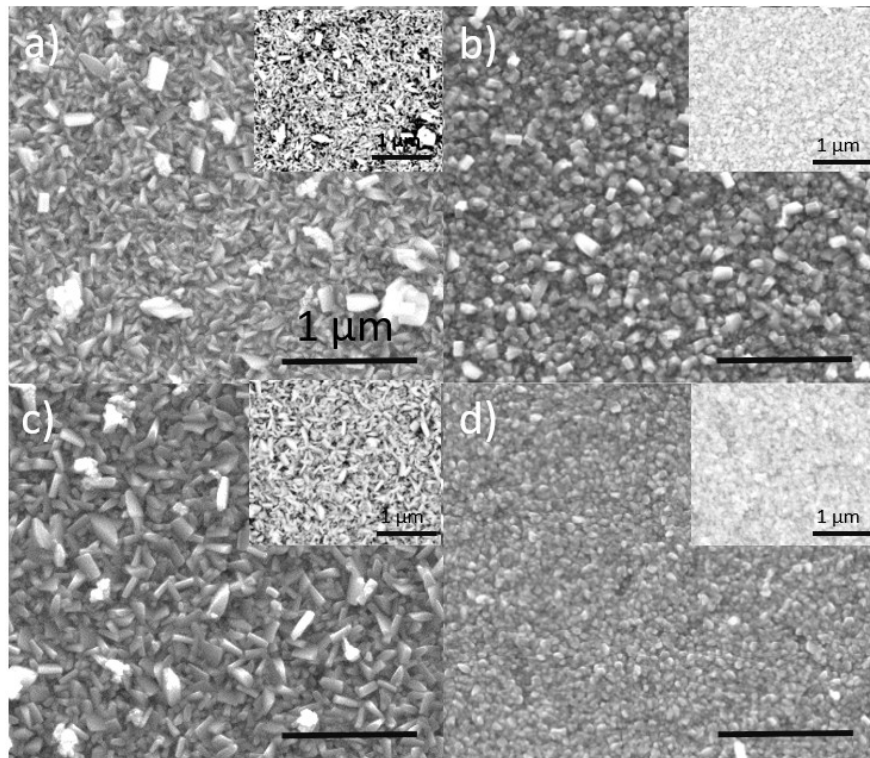


Figure V-17. SEM images of  $\text{AgCuO}_2$  films deposited by SILAR with different copper ion concentrations. a) 0.04 M (B2), b) 0.035 M (B3), c) 0.03 M (B4) and d) 0.028 M (B5).

In addition to SEM, the surface of sample B5, being the most continuous and smooth, was also characterized by AFM, as shown in Figure V-18, in which the recreated 3D morphology is presented. As it is shown the grain is rather dense and continuous with surface roughness RMS about 8 nm.

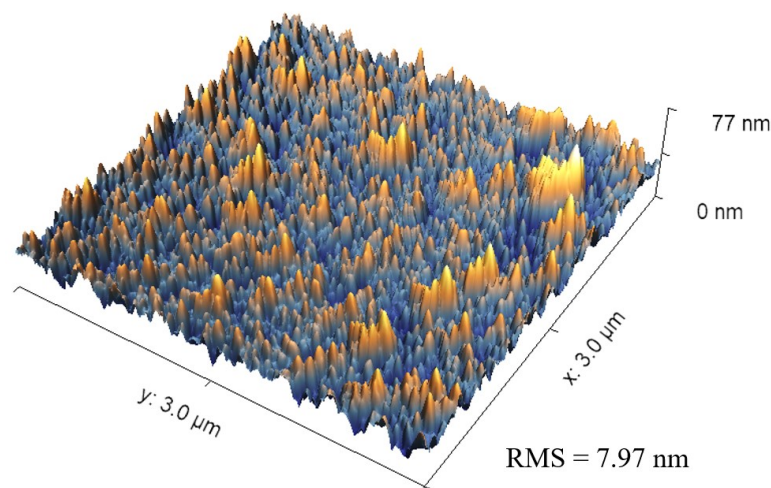


Figure V-18. Reconstructed 3D AFM images of  $\text{AgCuO}_2$  films deposited by SILAR using optimized conditions (Sample B5) with RMS value about 8 nm.

To identify the phases deposited, GIXRD characterizations were again conducted and the results are shown in Figure V-19. In all the XRD patterns, reflection corresponding to  $\text{AgCuO}_2$  can be easily distinguished and they present the strongest peak intensity at about

31.5 °. The two possible impurities in the deposited films are CuO and AgO. There are several peaks overlaying with the desired  $\text{AgCuO}_2$  phase, thus for CuO its unique and strong intensity peak is located at 38 °, as marked by the blue dashed line in the figure. Meanwhile for AgO phase, the easiest peak for identification is located at around 34 °, marked by a red dashed line in the figure. Thus, the major impurity presented by GIXRD in all cases was CuO phase.

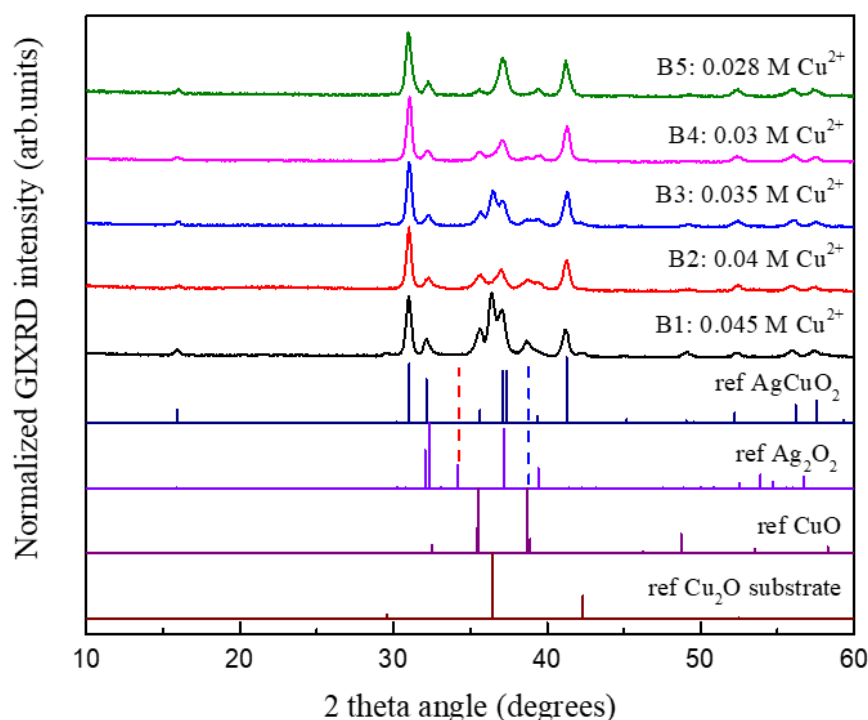


Figure V-19. GIXRD patterns of process of optimization the purity of  $\text{AgCuO}_2$  films by reducing the copper ion concentration.

Even though, in GIXRD the accurate composition of each phase can't be obtained from GIXRD patterns, by comparing the intensity of the reflections corresponding to impurity phase with the peak intensity of  $\text{AgCuO}_2$ , the trend of the amount of impurities in the films can be presented relatively. As shown in Figure V-19, with gradually decreasing the copper ion concentration in solution, the peak reflection intensity corresponding to CuO decreases until fully disappears for the samples deposited with 0.03 M (sample B4) and 0.028 M (sample B5) copper ion concentration. But again, this pure phase  $\text{AgCuO}_2$  film was rather difficult to be reproduced. Even if no CuO phase appears on the XRD patterns, the existence of such impurity phase inside the  $\text{AgCuO}_2$  is still believed to be below the detection limit. While by checking the reference peaks corresponding to AgO phase, no clear evidence proves the existence of detectable amount of AgO impurity in the  $\text{AgCuO}_2$  films.

Besides the XRD analyses, Raman characterizations were also conducted.  $\text{AgCuO}_2$  powder obtained in previous work by d. Muñoz-Rojas et al.<sup>3</sup>, was used as reference for Raman. The  $\text{AgO}$  powder was bought from Sigma Aldrich (99.5%), thus allowing the Raman characterization in LMGP. The  $\text{Cu}_2\text{O}$  reference curve was taken from reference<sup>25</sup> and  $\text{CuO}$  reference peaks were taken from the reference<sup>26</sup>. The characterizations were conducted with a blue laser (448 nm wavelength as excitation line),  $\times 100$  objective and acquisition time of 400 s using 2 cycles.

The obtained Raman spectra for samples B1 and B4 are presented in Figure V-20. As it is shown, the Raman spectra of  $\text{AgCuO}_2$  films deposited by SILAR have only three major peaks located at 220.2, 439 and 521.4  $\text{cm}^{-1}$ , which is in agreement with the reference curve obtained from pure  $\text{AgCuO}_2$  powders. In the Raman spectra of sample B1, a peak at around 150  $\text{cm}^{-1}$  was observed which is associated with the  $\text{Cu}_2\text{O}$  phase.

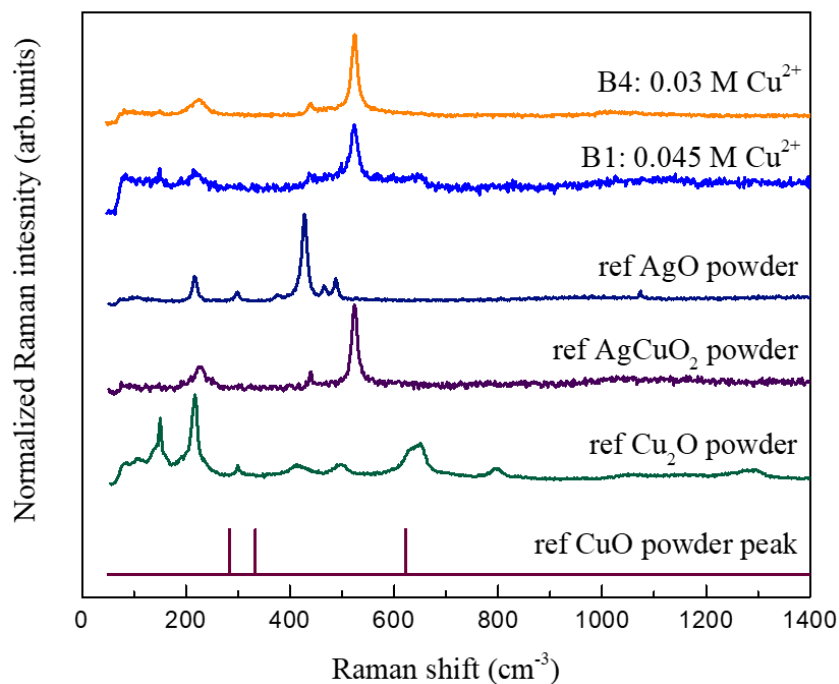


Figure V-20. RAMAN spectra of the synthesized  $\text{AgCuO}_2$  with comparison to the powder references.

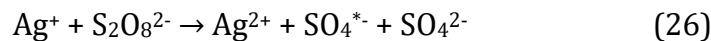
Meanwhile, the similar peak didn't emerge in B4 Raman spectra. Combining their morphologies presented in Figure V-17 a) and c), sample B4 possibly had a denser or thicker film than B1. By comparing Raman spectra from the thin films with the  $\text{AgO}$ ,  $\text{CuO}$  reference spectra, no visible peaks were observed corresponding to the two impurity phases, indicating a lower sensitivity of Raman characterization as compared with GIXRD. For both samples, the Raman spectra are rather flat at higher wavenumbers (more than 1000  $\text{cm}^{-3}$ ), indicating high quality depositions without significant amount of carbon contamination.



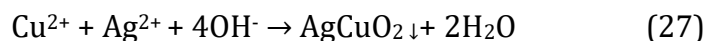
Therefore, combining all the optimized parameters, the deposition of continuous and almost pure phase AgCuO<sub>2</sub> films in SILAR could be achieved with the following parameters. The precursor solution contained 0.05 M Ag<sup>1+</sup> and 0.03 M Cu<sup>2+</sup>. The cation solution is composed of 1 M NaOH and 0.08 M Na<sub>2</sub>S<sub>2</sub>O<sub>8</sub>. The immersion and withdraw speed in Z axis are set to 4 mm/s and 60 mm/s. The immersion duration in cation solution (t<sub>1</sub>), buffer solution 1 (t<sub>2</sub>), metal ion solution (t<sub>3</sub>) and buffer solution 2 (t<sub>4</sub>) is 15 s, 10 s, 20 s, 10 s, respectively. To obtain a 100 nm thick AgCuO<sub>2</sub> film, 70 cycles of deposition are required.

### V.3.5 Understanding the mechanism of AgCuO<sub>2</sub> thin film coating by SILAR process.

The reaction mechanism for the deposition of AgCuO<sub>2</sub> phase in SILAR process is discussed here. During the SILAR process, the substrate and the oxidizer played important roles. The oxidizer used in this work was Na<sub>2</sub>S<sub>2</sub>O<sub>8</sub>, which was added into the anion high pH NaOH solution. As it is reported in the work of D.Zhao *et al.*,<sup>27</sup> Na<sub>2</sub>S<sub>2</sub>O<sub>8</sub> is a very strong oxidant which can be activated through several means, thermally (over 60 °C), metal ion or by base activation. The oxidation of Ag<sup>1+</sup> ions with Na<sub>2</sub>S<sub>2</sub>O<sub>8</sub> has been reported in the work of G.P. Anipsitakis *et al.*<sup>28</sup> In their work, they pointed out that the Ag<sup>1+</sup> ions can be oxidized by the S<sub>2</sub>O<sub>8</sub><sup>2-</sup> anions into Ag<sup>2+</sup> state, as shown in Equation V 26.



Even though it has been reported that Cu<sup>2+</sup> ions can be also oxidized by persulfate anions into Cu<sup>3+</sup>,<sup>29,30</sup> this oxidation state is not stable in solution and the oxidizing rate is slow. Thus, in our case, we considered that only silver cations were oxidized. Therefore, during the SILAR process when the Ag<sup>1+</sup> and Cu<sup>2+</sup> ions adsorbed to the substrate surface were immersed into the NaOH solutions containing persulphate, the oxidation and co-precipitating in such basic solution occurred, thus yielding the formation of AgCuO<sub>2</sub>, as shown in Equation V 27,



Due to the highly oxidizing environment, the first few layers of Cu<sub>2</sub>O could be oxidized into CuO. Thus, besides the origin of CuO impurity phase from excessive copper ion concentration, this could be an inevitable source. To understand the role of substrate and oxidizer during the SILAR deposition of AgCuO<sub>2</sub> films, coatings with the following parameters in Table V-6 were conducted. Two substrates were tested under similar conditions, with cation solution only containing silver or both silver and copper ions, and

with and without oxidizer. The Ag<sup>1+</sup> ion precursor concentration was 0.05 M in all cases and the concentration of Cu<sup>2+</sup> was 0.03 M. For all of those samples, 70 cycles were used.

*Table V-6. Effects of seed layer on final coating products by SILAR.*

Substrate	Precursors	Oxidizer (Y/N)	Product	Sample names
Cu <sub>2</sub> O	Ag <sup>1+</sup>	N	Ag <sub>2</sub> O	C1
		Y	AgCuO <sub>2</sub> +Ag <sub>2</sub> O and possible AgO	C2
	Ag <sup>1+</sup> , Cu <sup>2+</sup>	N	Cu(OH) <sub>2</sub>	C3
		Y	AgCuO <sub>2</sub>	C4
ZnO	Ag <sup>1+</sup>	N	Ag <sub>2</sub> O	Z1
		Y	Ag <sub>2</sub> O	Z2
	Ag <sup>1+</sup> , Cu <sup>2+</sup>	N	Cu(OH) <sub>2</sub>	Z3
		Y	Ag <sub>2</sub> Cu <sub>2</sub> O <sub>3</sub>	Z4

The morphology of some of the samples is presented in Figure V-21. The morphology of samples coated on Cu<sub>2</sub>O/glass substrate are firstly introduced. In Figure V-21 a), the morphology of sample C1, deposited with only Ag<sup>1+</sup> solution without oxidizer, is presented. Porous discontinuous structures are found on the substrate. The morphology of sample C2, deposited with only Ag<sup>1+</sup> and with oxidizer, is shown in Figure V-21 b), in which cuboid shape grains with length about 200 nm are dispersed. The inserted BSE image presents a clear contrast of element distribution, but again such contrast can be also due to the rough morphology. The morphology of the sample C3, coated with both metal ion precursors but without oxidizer, is presented in figure c). The surface is in this case covered by nanowire structures with length about 1 μm. The inserted BSE image shows a homogeneous element distribution on the sample surface. However, with EDS analyses, small amount of silver were still found on the surface. For comparison, the image of sample C4, which was deposited under standard conditions, is presented in in figure d). It shows a dense and continuous surface with small plate like grains, similar to the previous thin film coatings by SILAR. Then the morphology of samples deposited on ZnO/glass substrate are presented.

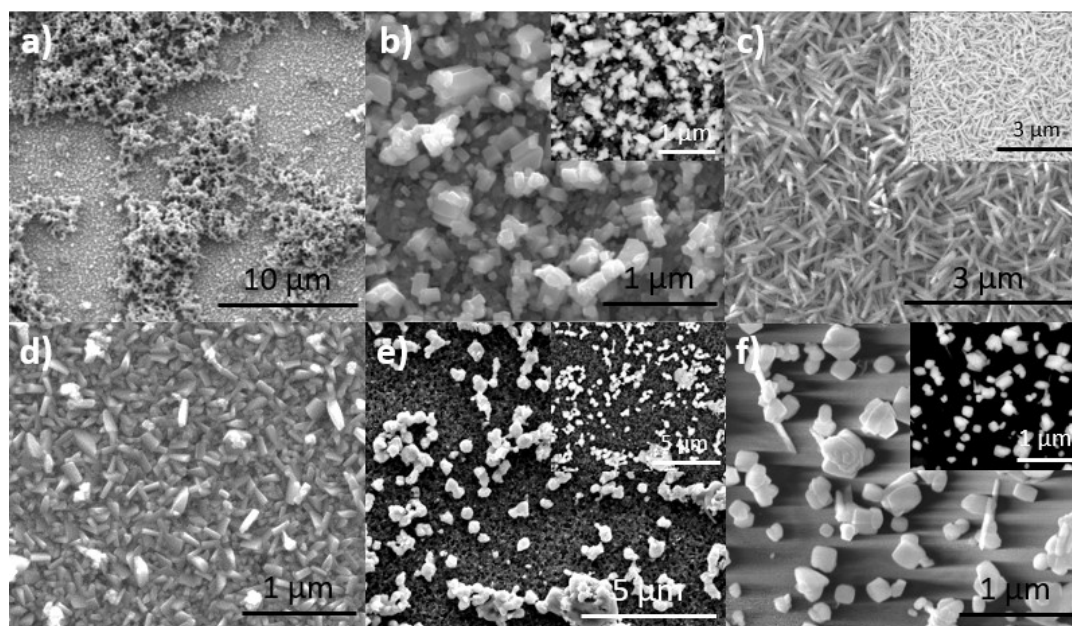


Figure V-21. Morphology of coated samples by SILAR on  $\text{Cu}_2\text{O}/\text{glass}$  substrate: a) deposition with only  $\text{Ag}^{1+}$  ion precursor, without oxidizer (sample C1); b) deposition with only  $\text{Ag}^{1+}$  ion precursor with oxidizer (sample C2); c) coatings with both metal ion precursors, without oxidizer (sample C3); d) standard thin film coatings for comparison (sample C4). The morphology of coatings on  $\text{ZnO}/\text{glass}$  substrate: e) deposited with only  $\text{Ag}^{1+}$  ion precursor without oxidizer (sample Z1); f) deposited with both metal ion precursor with oxidizer (sample Z4).

In Figure V-21 e), the morphology of sample Z1 is shown. The sample was deposited with only  $\text{Ag}^{1+}$  precursor and without oxidizer. On the surface, the bottom ZnO layer has been largely etched away by the strong basic environment, thus the porous structures left behind. On top of the porous layer, the coated grain particles scatter on the surface. In the corresponding BSE image, much higher intensity is observed on these grains. Lastly, Figure V-21 f) presents the morphology of sample Z4, which was deposited with both ion precursors and oxidizer. On the sample surface, big plate like grains (size about 300 nm) are dispersed on the substrate. Unlike in figure e), no porous structures were obtained in the bottom layer. By further checking the BSE image, a very weak electron signal is presented on the substrate, while grains appear very bright, which indicates that the ZnO layer was possibly totally dissolved in this case. Since the substrate was ZnO, the EDS analyses of the deposited grains presented Ag:Cu atomic ratio very close to 1:1.

To obtain the information of the phase composition of those samples, GIXRD was conducted and the results are shown in Figure V-22. The XRD of SILAR coatings on  $\text{Cu}_2\text{O}/\text{glass}$  substrate are presented in Figure V-22 a). As it is shown, for sample C1, the major reflections correspond to  $\text{Ag}_2\text{O}$  phase, which is rather reasonable since the sample was deposited without oxidizer. Meanwhile, and quite surprisingly, the XRD reflections for sample C2

were mainly related to  $\text{AgCuO}_2$  phase, with a weak reflection from  $\text{Ag}_2\text{O}$  being also observed.

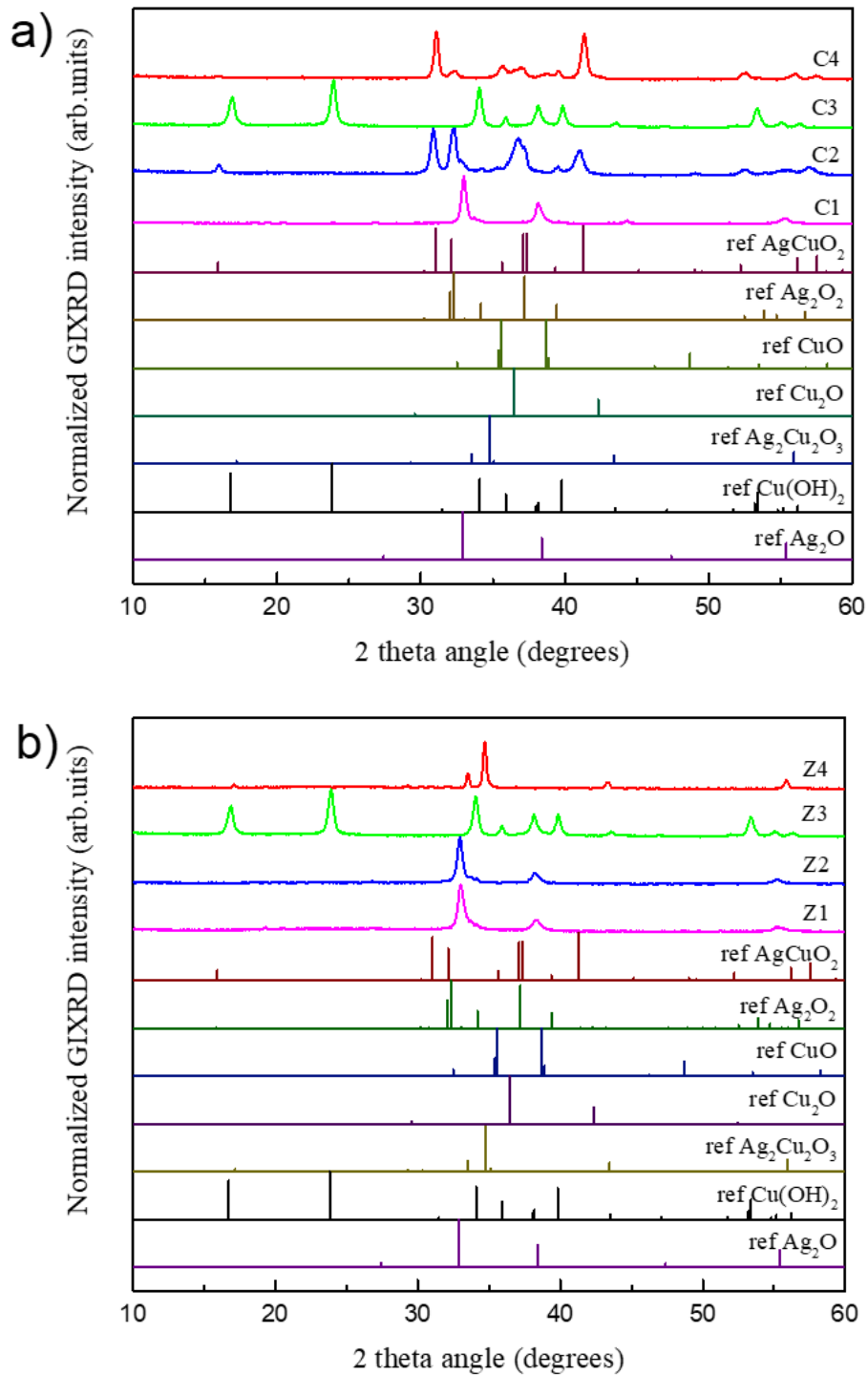


Figure V-22. GIXRD patterns of SILAR coatings on a)  $\text{Cu}_2\text{O}/\text{glass}$  and b)  $\text{ZnO}/\text{glass}$  substrate with different conditions.

Since this sample C2 was coated without  $\text{Cu}^{2+}$  ion precursor, the formation of  $\text{AgCuO}_2$  indicates that part of  $\text{Cu}_2\text{O}$  on the substrate was also participating in the SILAR reaction, which might explain the difficulty to reproduce pure  $\text{AgCuO}_2$  phase thin films with no  $\text{CuO}$  contamination. For sample C3

it's quite surprising to find that even though a cation solution containing the two metal ions was used, the majority of the as-deposited phase is identified as Cu(OH)<sub>2</sub>, corresponding to the needle like structures showing in Figure V-21 c). No trace of silver oxides or other silver containing crystalline compound are presented in the XRD.

During the SILAR deposition process for sample C3, lots of dark precipitates were observed in the NaOH solution, thus The absence of Ag<sub>2</sub>O is possibly due to a low adhesion between the Ag<sup>1+</sup> ions and the deposited Cu(OH)<sub>2</sub> needle structures. However, under the deposition condition of C1, even though the precipitation in NaOH solution was also observed, the Ag<sup>1+</sup> ions could have stronger adhesion with the Cu<sub>2</sub>O thin film, thus Ag<sub>2</sub>O was coated on the substrate.

As for sample C4, the reflections obtained mainly correspond to AgCuO<sub>2</sub> phase and a weak reflection is related to the CuO impurity phase. Comparing the XRD of C2, the intensity of the peak located at 33 ° is much stronger than that in sample C4. This difference in this reflection intensity could possibly be due to several reasons. The first reason can be the different morphology between sample C2 (shown in Figure V-21 b) and sample C4 (Figure V-21 d). Other than that, the presence of impurity AgO phase is also possible, since the major reflection of AgO overlaps with this stronger reflection from sample C2.

For samples deposited on ZnO/glass substrate, the GIXRD patterns are presented in Figure V-22 b). Similar to sample C1, under the same deposition conditions, the reflections of sample Z1 correspond to Ag<sub>2</sub>O phase as well. In the XRD pattern of sample Z2, which was deposited with the same conditions of sample C2 (with oxidizer, with only Ag ions), the reflections correspond to Ag<sub>2</sub>O phase, as opposed to C2, where AgCuO<sub>2</sub> was mostly obtained. For sample Z3, due to the extremely thin coatings, no reflection peaks were observed from the GIXRD pattern, thus it's not presented here. Lastly, under the same deposition conditions as used for sample C4, the XRD reflections for Z4 are associated with Ag<sub>2</sub>Cu<sub>2</sub>O<sub>3</sub> phase, as the image presented in Figure V-21 f). Combining the results from sample Z2 and Z4, the oxidizer seems to have limited effect on silver ions coated on the ZnO/glass substrate, only depositions with Ag<sup>1+</sup> state were obtained. Therefore, in sample Z4, the Ag in the deposited silver copper oxide phase is also 1+, thus the co-precipitation is Ag<sub>2</sub>Cu<sub>2</sub>O<sub>3</sub> grains. During the deposition, lots of dark precipitates were also observed in NaOH solution. In addition, as shown in Figure V-21 e) and f), the deposited grains were rather dispersed and rare on the ZnO surface. Unlike samples deposited on Cu<sub>2</sub>O/glass substrate (C2, C4), the deposited silver oxide was in 1+ charge state, thus this could be due to a low adhesion between the oxidized Ag<sup>2+</sup> ions and the ZnO/glass substrate.

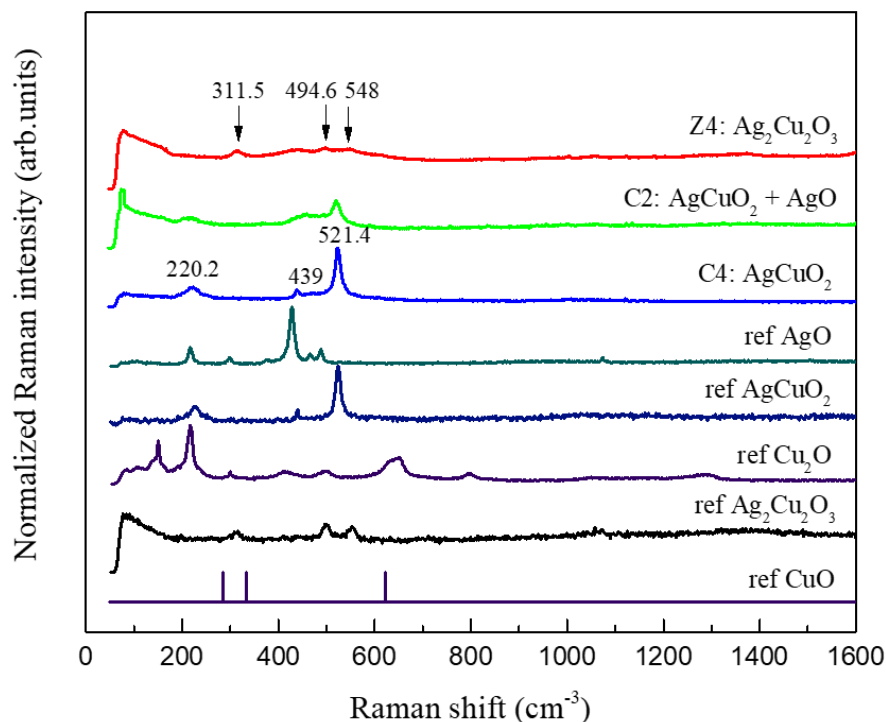


Figure V-23. Comparing Raman spectra of SILAR coated  $\text{AgCuO}_2$ ,  $\text{Ag}_2\text{Cu}_2\text{O}_3$  with powders synthesized through hydrothermal reactions from reference work.

To further confirm the phase of those SILAR coated thin films, sample Z4 ( $\text{Ag}_2\text{Cu}_2\text{O}_3$  identified by GIXRD), C4 ( $\text{AgCuO}_2$  identified by GIXRD) and C2 ( $\text{AgO}+\text{AgCuO}_2$ ) were characterized by Raman spectroscopy, the results are presented in Figure V-23. In this Raman characterization, a green laser (with wavelength 514.5 nm) was applied with integration duration  $600 \text{ s} \times 2$  cycles. For  $\text{AgCuO}_2$  sample (C4), comparing with the Raman spectra shown in Figure V-20, with green laser, stronger signal and less noise were presented and the same three peaks at the same positions were observed. The reference Raman curve for  $\text{Ag}_2\text{Cu}_2\text{O}_3$  was obtained by characterizing the powders synthesized based on reference work<sup>31</sup>. The Raman signals from  $\text{Ag}_2\text{Cu}_2\text{O}_3$  powder or SILAR coating were much weaker and less visible. However, three peaks at 311.5, 494.6 and  $548 \text{ cm}^{-1}$  were found in both the reference powder and SILAR coating. For sample C2, the Raman spectra presented peaks from both  $\text{AgCuO}_2$  and  $\text{AgO}$  phases, confirming the formation of  $\text{AgCuO}_2$  on the  $\text{Cu}_2\text{O}$  substrate (with only silver precursor).

### V.3.6 Optical and electronic property of $\text{AgCuO}_2$ films obtained by SILAR

The transmittance and reflectance of the films deposited with different copper ion concentrations were characterized by UV-Vis spectroscopy. All samples were deposited for 70 cycles and measured by SEM cross-section, they had rather similar thickness around 100

nm. The results of the UV-Vis characterizations are presented in Figure V-24, in which figure a) shows the transmittance and figure b) presents the reflectance of the deposited films. The  $\text{Cu}_2\text{O}$  seed layer below presents a maximum 80% transmittance for light with 600 nm wavelength. While with the SILAR deposited films, they have generally lower transmittance in all wavelengths especially at the visible range, down to 20%.

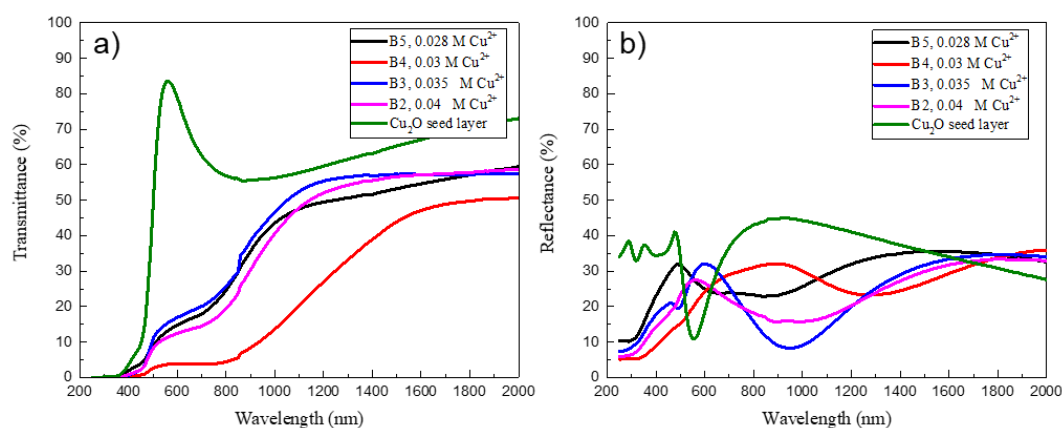


Figure V-24. Optical characterizations of  $\text{AgCuO}_2$  films coated with various copper ion concentration by SILAR process: a) Transmittance curve and b) reflectance curve.

The red transmittance curve corresponding to sample B4 presents the lowest transmittance in visible range, but the onset of transmittance starts at the same wavelength as the other samples, about 420 nm. Since the thickness of all the deposited film is almost the same, the most possible reason is due to a rougher surface (as presented in Figure V-17 c) above). Besides the transmittance, the reflectance curves of those samples are given in Figure V-24 b). The  $\text{Cu}_2\text{O}$  seed layer gives an average 35% to 40% reflectance throughout the whole spectrum but reaches down to a minimum at about 10% at 590 nm. Meanwhile, the  $\text{AgCuO}_2$  films coated by SILAR exhibit higher reflection in the visible light range, ranging from 20% to 30%.

In addition to those characterizations, the Tauc formula (assuming both direct and indirect bandgap) was applied on the transmittance curve in order to estimate the bandgap of  $\text{AgCuO}_2$ , as shown in Figure V-25. In figure Figure V-25 a), the Tauc plot was obtained assuming a direct bandgap. The curve with black empty diamond represents the Tauc plot for the  $\text{Cu}_2\text{O}$  seed layer used in this work, with direct bandgap about 2.5 eV. With the layers coated on top of  $\text{Cu}_2\text{O}$  by SILAR, the onset of absorption was largely decreased. By following the linear part and plotting their interception with the X axis, these curves all yielded a bandgap of about 1.2 eV, regardless of the adjustment of the copper ion concentration. Meanwhile, figure b) presents the Tauc plot assuming an indirect bandgap. As it is shown, the absorption coefficient versus the photon energy is not a straight line. Therefore, the SILAR deposited

$\text{AgCuO}_2$  is more likely to be a material with about 1.2 eV direct optical bandgap, in agreement with previous theoretical calculations in which 1 eV was predicted<sup>32</sup>.

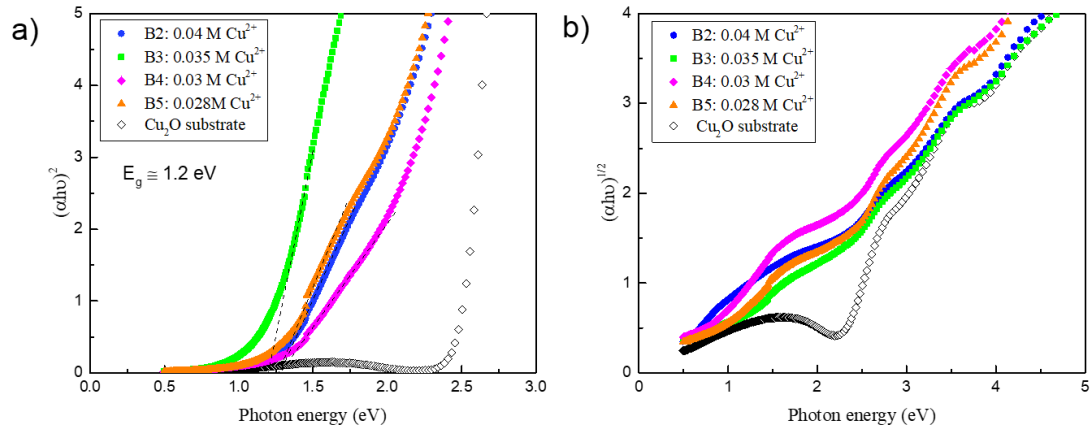


Figure V-25. Optical bandgap of  $\text{AgCuO}_2$  film deposited by SILAR using Tauc formula with different copper ion concentration used: a) plot as direct bandgap and b) as indirect bandgap.

In addition to the optical characterizations, the deposited  $\text{AgCuO}_2$  films were also characterized by Hall effect measurement. Before the characterization, the Pt tips were directly placed on top of the deposited films, the I-V plot presented a straight linear correlation, indicating an excellent ohmic contact between the tip and the  $\text{AgCuO}_2$  film. Thus, in this work no metal contacts were pre-deposited before characterization. Even though the  $\text{AgCuO}_2$  films were characterized above thin  $\text{Cu}_2\text{O}$  layers (about 60 nm thick), due to its high resistivity (see Chapter IV), the contribution from the bottom  $\text{Cu}_2\text{O}$  layer was negligible.

With the Hall effect measurement, p type conductivity of such phase was confirmed and the results of electrical measurements are presented in Figure V-26. In the figure, it shows a trend of decreasing resistivity with decreasing copper ion concentration, from 1.6  $\Omega\cdot\text{cm}$  down to a minimum of 0.2  $\Omega\cdot\text{cm}$  (with copper ion concentration 0.03 M, sample B4). In addition, with lower copper ion concentration, the carrier concentration of the deposited sample decreased from  $1.7 \times 10^{18}$  to  $2.5 \times 10^{17}$   $\text{cm}^{-3}$ . Meanwhile, the mobility was enhanced from 0.2 to more than 10  $\text{cm}^2/\text{V}\cdot\text{s}$ . Each data point has been repeated twice (sample deposition and characterizations), the value presented is the minimum value obtained and 10% error bar was added for all values. With copper ion concentration of 0.05 M, equal to the silver ions, the carrier concentration reached as high as  $1.7 \times 10^{18}$   $\text{cm}^{-3}$ , but very low mobility of 0.2  $\text{cm}^2/\text{V}\cdot\text{s}$  was observed. With reduced copper ion concentration, the carrier concentration gradually decreased down to the order of  $10^{17}$   $\text{cm}^{-3}$  while the mobility was enhanced, up to more than 10  $\text{cm}^2/\text{V}\cdot\text{s}$ . With copper ion concentration at 0.03 M, both the



carrier concentration and mobility reached an optimal value, namely,  $1.55 \times 10^{18} \text{ cm}^{-3}$  for carrier concentration and  $24 \text{ cm}^2/\text{V.s}$  for the mobility. This increase in electrical conductivity can be related with a higher purity AgCuO<sub>2</sub> phase, as previously reported in Figure V-19. With even lower copper ion concentration, rather high mobility (around  $10 \text{ cm}^2/\text{V.s}$ ) with carrier concentration in the order of  $10^{17} \text{ cm}^{-3}$  still can be found.

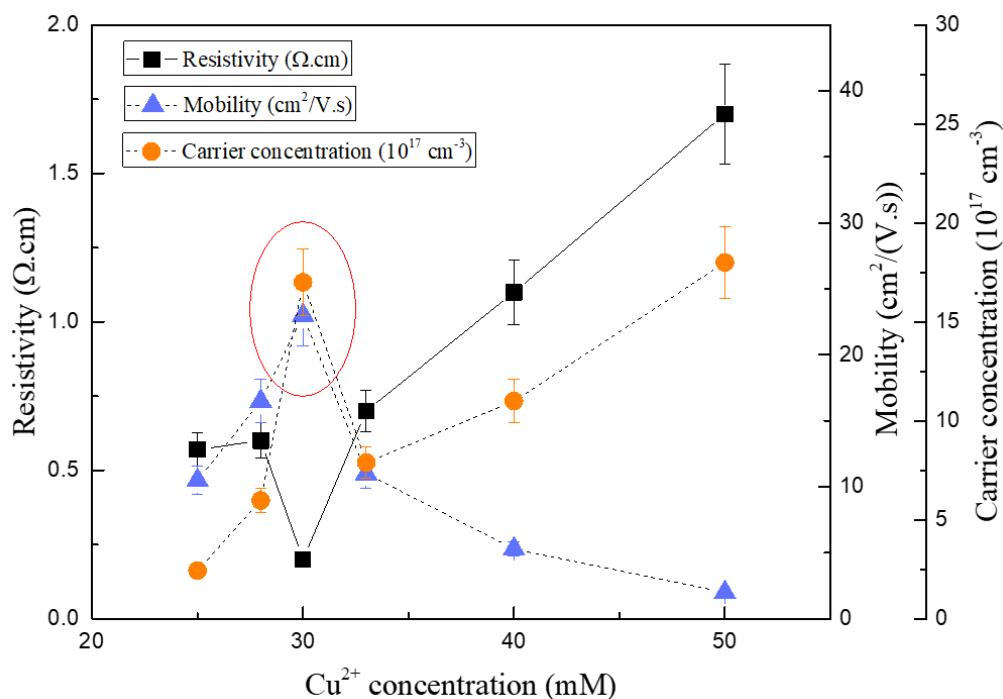


Figure V-26. Electronic properties of AgCuO<sub>2</sub> film deposited by SILAR using Hall effect measurement with different copper ion concentration used. Values with 10% error bar.

Depending on the copper ion concentration, the carrier concentrations were in the range of  $10^{17}$  and  $10^{18} \text{ cm}^{-3}$  and mobility reached a maximum of  $24 \text{ cm}^2/\text{V.s}$ . The resistivity of those SILAR deposition AgCuO<sub>2</sub> films varied from 0.1 to  $2 \text{ } \Omega.\text{cm}$ . Comparing with the previously reported CuMO<sub>2</sub> (M= Al, Cr, Ca, etc) ternary compounds, AgCuO<sub>2</sub> films exhibited rather low resistivity (See in Chapter I, Table.I.1).<sup>33-37</sup> Such low resistivity could be associate with the delocalized charge and mix valence state reported.<sup>38</sup> In addition, comparing with those compounds, much higher mobility and lower bandgap were found with AgCuO<sub>2</sub>, which expands its potential application in both thin film transistors and photovoltaics.

#### V.4 Chapter VI conclusions

To summarize, in this part of the work we were aiming at the synthesis of AgCuO<sub>2</sub> thin films. To achieve that, co-deposition by AA-MOCVD with silver and copper precursors with oxygen plasma was tested. Due to the corrosive nature of the radicals contained in the oxygen

plasma, depositions could be hardly obtained. In addition, AgCuO<sub>2</sub> phase is thermally unstable over 200 °C in air, thus precursors for both copper and silver with lower decomposition temperatures are required (better to be less than 200 °C). Combining all the difficulties, another approach was adopted. Thus alternatively, oxidation of AgCu metal alloy films (deposited by MOCVD with Ag and Cu ratio 1:1) was tested by two approaches, electrochemical oxidation and oxygen plasma treatment. From both oxidation results, only AgO, CuO phases were obtained. The formation of AgCuO<sub>2</sub> phase during oxidation was also extremely difficult with the experimental conditions available.

Therefore, the last alternative tested was synthesizing AgCuO<sub>2</sub> films through solution based deposition techniques. As a widely used thin film coating methods, Successive Ionic Layer Adsorption and Reaction (SILAR) process was adopted. To achieve dense and continuous thin film deposition, different substrates were tested and Cu<sub>2</sub>O/glass gave the best deposition results. With the optimized condition, dense and continuous AgCuO<sub>2</sub> thin films can be coated (about 100 nm thick), with surface roughness RMS about 8 nm. Besides that, by comparing the deposition results on Cu<sub>2</sub>O/glass and ZnO/glass, the SILAR reaction mechanisms for AgCuO<sub>2</sub> were also investigated, but more work is needed to completely elucidate the reactions taking place.

The optical bandgap of the deposited layer was determined using the Tauc formula, and a value of 1.2 eV was obtained assuming a direct bandgap. By comparing the Tauc plots with both direct and indirect bandgap, AgCuO<sub>2</sub> is more likely to be a direct optical bandgap material. In addition to that, through Hall effect characterizations, p type conductivity of such AgCuO<sub>2</sub> films was confirmed and the films presented rather low resistivity reaching down to 0.2 Ω.cm. Majority of the samples could have carrier concentration in the range of 10<sup>17</sup> to 10<sup>18</sup> cm<sup>-3</sup> and giving mobility over 10 cm<sup>2</sup>/V.s. Comparing with previously reported ternary copper based oxide compounds, AgCuO<sub>2</sub> has lower resistivity, higher mobility and lower bandgap.

## V.5 References

1. Munoz-Rojas, D., Fraxedas, J., Oró, J., Gómez-Romero, P. & Casañ-Pastor, N. Structural study of electrochemically-synthesized Ag<sub>2</sub>Cu<sub>2</sub>O<sub>4</sub>. A novel oxide sensitive to irradiation. *Cryst. Eng.* **5**, 459–467 (2002).
2. Curda, J., Klein, W. & Jansen, M. AgCuO<sub>2</sub>—Synthesis, Crystal Structure, and Structural Relationships with CuO and AgI<sub>2</sub>Ag<sub>2</sub>O<sub>3</sub>. *J. Solid State Chem.* **162**, 220–224 (2001).
3. Muñoz-Rojas, D., Córdoba, R., Fernández-Pacheco, A., De Teresa, J. M., Sauthier, G., Fraxedas, J., Walton, R. I. & Casañ-Pastor, N. High conductivity in hydrothermally grown AgCuO<sub>2</sub> single crystals verified using focused-ion-beam-deposited nanocontacts. *Inorg. Chem.* **49**, 10977–10983 (2010).
4. Sauvage, F., Muñoz-Rojas, D., Poeppelmeier, K. R. & Casañ-Pastor, N. Transport properties and lithium insertion study in the p-type semi-conductors AgCuO<sub>2</sub> and AgCu<sub>0.5</sub>Mn<sub>0.5</sub>O<sub>2</sub>. *J. Solid State Chem.* **182**, 374–380 (2009).
5. Lu, Q., Lu, K., Zhang, L., Gong, J. & Liu, R. Electrodeposition of AgCuO<sub>2</sub> Nanoplates. *J. Electrochem. Soc.* **164**, D130–D134 (2017).
6. Pierson, J. F., Rolin, E., Clément-Gendarme, C., Petitjean, C. & Horwat, D. Effect of the oxygen flow rate on the structure and the properties of Ag-Cu-O sputtered films deposited using a Ag/Cu target with eutectic composition. *Appl. Surf. Sci.* **254**, 6590–6594 (2008).
7. Reddy, P. N., Sreedhar, a., Prasad Reddy, M. H., Uthanna, S. & Pierson, J. F. Process-Parameter-Dependent Structural, Electrical, and Optical Properties of Reactive Magnetron Sputtered Ag-Cu-O Films. *J. Nanotechnol.* **2011**, 1–8 (2011).
8. Naji, I. S. & Abdulwahe, S. H. EFFECT OF SINTERING TEMPERATURE ON THE PHYSICAL PROPERTIES OF THIN Ag<sub>2</sub>Cu<sub>2</sub>O<sub>3</sub> FILMS PREPARED BY PULSED LASER DEPOSITION. *Dig. J. Nanomater. biostructures* **12**, 507–521 (2017).
9. Pierson, J. F., Wiederkehr, D., Chappé, J. M. & Martin, N. Reactive sputtering: A method to modify the metallic ratio in the novel silver-copper oxides. *Appl. Surf. Sci.* **253**, 1484–1488 (2006).
10. Hari Prasad Reddy, M., Narayana Reddy, P., Sreedhar, B., Pierson, J. F. & Uthanna, S. Effect of substrate temperature on the structural, electrical and optical behaviour of reactively sputtered Ag–Cu–O films. *Phys. Scr.* **84**, 45602 (2011).
11. Muñoz-Rojas, D., Fraxedas, J., Gómez-Romero, P. & Casañ-Pastor, N. Room temperature solid-state transformation from to by ozone oxidation. *J. Solid State Chem.* **178**, 295–305 (2005).
12. Fraxedas, J. & Casa, N. Electrochemically induced reversible solid state transformations : electrosynthesis of Ag<sub>2</sub>Cu<sub>2</sub>O<sub>4</sub> by room temperature. *Electrochem. commun.* **4**, 684–689 (2002).

13. Pacchioni, G. *First Principles Calculations on the Diffusion of Cu, Ag and Au Atoms or Aggregates on the Bulk and Surface of Titania*. (2011).
14. Williams, P. L., Mishin, Y. & Hamilton, J. C. An embedded-atom potential for the Cu–Ag system. *Model. Simul. Mater. Sci. Eng.* **14**, 817–833 (2006).
15. Boisvert, G. & Lewis, L. J. Self-diffusion on low-index metallic surfaces: Ag and Au (100) and (111). *Phys. Rev. B* **54**, 2880–2889 (1996).
16. Liu, C. L., Cohen, J. M., Adams, J. B. & Voter, A. F. EAM study of surface self-diffusion of single adatoms of fcc metals Ni, Cu, Al, Ag, Au, Pd, and Pt. *Surf. Sci.* **253**, 334–344 (1991).
17. Xia, X., Zhang, Y., Chao, D., Guan, C., Zhang, Y., Li, L., Ge, X., Bacho, I. M., Tu, J. & Fan, H. J. Solution synthesis of metal oxides for electrochemical energy storage applications. *Nanoscale* **6**, 5008–48 (2014).
18. Chen, X., Zhang, N. & Sun, K. Facile fabrication of CuO 1D pine-needle-like arrays for super-rate lithium storage. *J. Mater. Chem.* **22**, 15080–15084 (2012).
19. Bayansal, F., Cetinkara, H. A., Kahraman, S., Cakmak, H. M. & Güder, H. S. Nano-structured CuO films prepared by simple solution methods: Plate-like, needle-like and network-like architectures. *Ceram. Int.* **38**, 1859–1866 (2012).
20. Ghosh, A., Deshpande, N. G., Gudage, Y. G., Joshi, R. A., Sagade, A. A., Phase, D. M. & Sharma, R. Effect of annealing on structural and optical properties of zinc oxide thin film deposited by successive ionic layer adsorption and reaction technique. *J. Alloys Compd.* **469**, 56–60 (2009).
21. Lee, H., Wang, M., Chen, P., Gamelin, D. R., Zakeeruddin, S. M. & Gra, M. Efficient CdSe Quantum Dot-Sensitized Solar Cells Prepared by an Improved Successive Ionic Layer Adsorption and Reaction Process. *Nano Lett.* **9**, 4221–4227 (2009).
22. Nair, M. T. ., Guerrero, L., Arenas, O. L. & Nair, P. . Chemically deposited copper oxide thin films: structural, optical and electrical characteristics. *Appl. Surf. Sci.* **150**, 143–151 (1999).
23. Curda, J., Klein, W., Liu, H. & Jansen, M. Structure redetermination and high pressure behaviour of AgCuO<sub>2</sub>. *J. Alloys Compd.* **338**, 99–103 (2002).
24. Parize, R., Katerski, A., Gromyko, I., Rapenne, L., Roussel, H., Kärber, E., Appert, E., Krunk, M. & Consonni, V. ZnO/TiO<sub>2</sub>/Sb<sub>2</sub>S<sub>3</sub> Core-Shell Nanowire Heterostructure for Extremely Thin Absorber Solar Cells. *J. Phys. Chem. C* **121**, 9672–9680 (2017).
25. Bergerot, L., Jiménez, C., Chaix-Pluchery, O., Rapenne, L. & Deschanvres, J.-L. Growth and characterization of Sr-doped Cu<sub>2</sub>O thin films deposited by metalorganic chemical vapor deposition. *Phys. Status Solidi* **212**, 1735–1741 (2015).
26. Volanti, D. P., Keyson, D., Cavalcante, L. S., Simões, A. Z., Joya, M. R., Longo, E., Varela, J. A., Pizani, P. S. & Souza, A. G. Synthesis and characterization of CuO flower-nanostructure processing by a domestic hydrothermal microwave. *J. Alloys Compd.* **459**, 537–

- 542 (2008).
27. Zhao, D., Liao, X., Yan, X. & Huling, S. G. Effect and mechanism of persulfate activated by different methods for PAHs removal in soil. *J. Hazard. Mater.* **254–255**, 228–235 (2013).
  28. Anipsitakis, G. P. & Dionysiou, D. D. Radical Generation by the Interaction of Transition Metals with Common Oxidants Radical Generation by the Interaction of Transition Metals with Common Oxidants. *Environ. Sci. Technol.* **38**, 3705–3712 (2004).
  29. Liu, C. S., Shih, K., Sun, C. X. & Wang, F. Oxidative degradation of propachlor by ferrous and copper ion activated persulfate. *Sci. Total Environ.* **416**, 507–512 (2012).
  30. Xu, X., Ye, Q., Tang, T. & Wang, D. Hg<sup>0</sup> oxidative absorption by K<sub>2</sub>S<sub>2</sub>O<sub>8</sub> solution catalyzed by Ag<sup>+</sup> and Cu<sup>2+</sup>. *J. Hazard. Mater.* **158**, 410–416 (2008).
  31. Tejada-rosales, E. M., Rodri, J., Casan, N., Bellaterra, E.-, Brillouin, L. L. & Etudes, C. Room-Temperature Synthesis and Crystal, Magnetic, and Electronic Structure of the First Silver Copper Oxide. *Society* **41**, 103–108 (2002).
  32. Feng, J., Xiao, B., Chen, J. C., Zhou, C. T., Du, Y. P. & Zhou, R. Optical properties of new photovoltaic materials: AgCuO<sub>2</sub> and Ag<sub>2</sub>Cu<sub>2</sub>O<sub>3</sub>. *Solid State Commun.* **149**, 1569–1573 (2009).
  33. Kudo, A., Yanagi, H., Hosono, H. & Kawazoe, H. SrCu<sub>2</sub>O<sub>2</sub>: A p-type conductive oxide with wide band gap. *Appl. Phys. Lett.* **73**, 220–222 (1998).
  34. Ueda, K., Hase, T., Yanagi, H., Kawazoe, H., Hosono, H., Ohta, H., Orita, M. & Hirano, M. Epitaxial growth of transparent p-type conducting CuGaO<sub>2</sub> thin films on sapphire (001) substrates by pulsed laser deposition. *J. Appl. Phys.* **89**, 1790–1793 (2001).
  35. Tripathi, T. S., Niemelä, J.-P. & Karppinen, M. Atomic layer deposition of transparent semiconducting oxide CuCrO<sub>2</sub> thin films. *J. Mater. Chem. C* **3**, 8364–8371 (2015).
  36. Lim, S. H., Desu, S. & Rastogi, A. C. Chemical spray pyrolysis deposition and characterization of p-type CuCr<sub>1-x</sub>Mg<sub>x</sub>O<sub>2</sub> transparent oxide semiconductor thin films. *Journal of Physics and Chemistry of Solids* **69**, 2047–2056 (2008).
  37. Gong, H., Wang, Y. & Luo, Y. Nanocrystalline p-type transparent Cu–Al–O semiconductor prepared by chemical-vapor deposition with Cu(acac)<sub>2</sub> and Al(acac)<sub>3</sub> precursors. *Appl. Phys. Lett.* **76**, 3959–3961 (2000).
  38. Muñoz-Rojas, D., G.Subias, J.Fraxedas, P.Gomez-Romero & N.Casañ-Pastor. Electronic Structure of Ag<sub>2</sub>Cu<sub>2</sub>O<sub>4</sub>. Evidence of Oxidized Silver and Copper and Internal Charge Delocalization. *J. Phys. Chem. B* **109**, 6193–6203 (2005).

<i>Chapter VI In situ XRD characterization of formation mechanism of AgCuO<sub>2</sub> phase in hydrothermal reaction</i>	- 190 -
<i>VI.1 Experimental setup</i>	- 191 -
<i>VI.2 Effects of solution pH and reaction mechanism</i>	- 192 -
<i>VI.3 Effects of temperature and calculation of the reaction activation energy</i>	- 203 -
<i>VI.4 Chapter VI conclusions</i>	- 205 -
<i>VI.5 Appendix V: In situ XRD of hydrothermal reactions at different temperatures.</i>	- 206 -
<i>VI.6 References</i>	- 209 -

*Chapter VI In situ XRD characterization of formation mechanism of AgCuO<sub>2</sub> phase in hydrothermal reaction*

Most of the previously reported synthesis techniques for AgCuO<sub>2</sub> phase were through solution reaction routes. The starting materials were mostly stoichiometric mixture of AgNO<sub>3</sub> and Cu(NO<sub>3</sub>)<sub>2</sub> with K<sub>2</sub>S<sub>2</sub>O<sub>8</sub> as oxidizer, in basic media. The starting materials were added into NaOH solution and reacted at 90 °C.<sup>1-4</sup> Under these reaction conditions, the coprecipitation between oxidized Ag<sup>2+</sup> and Cu<sup>2+</sup> were widely believed to be the formation mechanism of AgCuO<sub>2</sub>. Meanwhile, from the work of *D. Muñoz-Rojas et al.*,<sup>5</sup> AgO and CuSO<sub>4</sub> were also reported as starting material. With a hydrothermal reaction at 120 °C in 1 M KOH solution, the desired AgCuO<sub>2</sub> phase was also obtained. Since AgO remains a solid phase during the reaction, this result implied that the reaction mechanism taking place during the hydrothermal reaction might be different from the mechanism of previous coprecipitation approaches.

In this work, through a collaboration with the group of Prof. Mari-Ann Einarsrud from the Norwegian University of Science and Technology (NTNU), we were able to study the reaction process of the hydrothermal synthesis of AgCuO<sub>2</sub> with a more advanced characterization tool. Hydrothermal reactions are chemical bath reactions conducted in an

evenly heated, close environment. With AgO and CuSO<sub>4</sub> as starting materials, the phase transformation process during hydrothermal reaction was studied by *in situ* X-ray diffraction in the ESRF synchrotron, in Grenoble. To understand the reaction process, different factors during the reaction, including pH, temperature and pressure, were studied. Lastly, based on the experimental results, a reaction mechanism for the hydrothermal synthesis of AgCuO<sub>2</sub> is proposed.

## VI.1 Experimental setup

The *in situ* XRD measurements were conducted in the Swiss-Norwegian Beam lines (BM01A) at the European Synchrotron Radiation Facility (ESRF), Grenoble, France. The diffraction data were collected in transmission mode ( $\lambda = 0.6999 \text{ \AA}$ , 17714.56 eV) using the PILATUS@SNBL platform.<sup>6</sup> The reaction cell is illustrated in Figure VI-1 a). The starting solution/suspension (prepared just before the experiment) can be loaded through one end while the other end connects with a pressure controller during the reaction (high-pressure liquid chromatography pump, R128703 Waters 515 Hplc Wat207000). Reaction temperature was calibrated and controlled thanks to a heat blower, as described in previous works<sup>7-9</sup>.

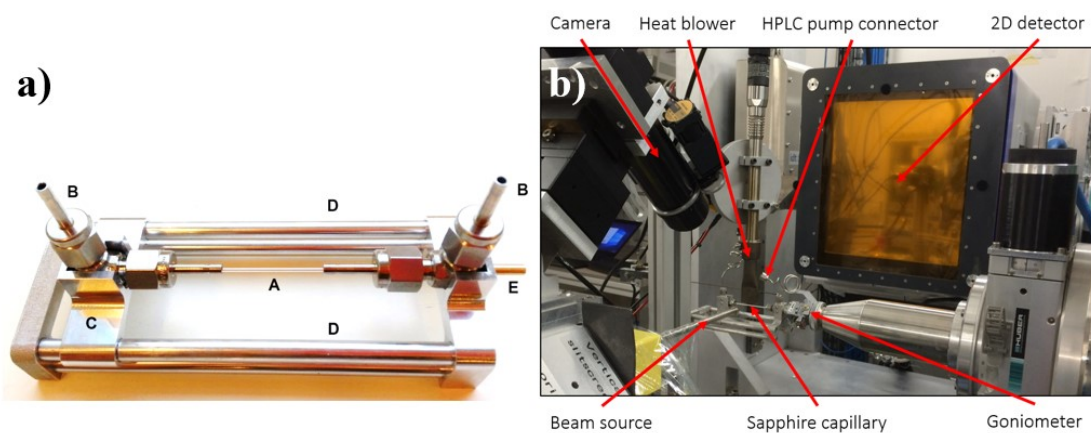


Figure VI-1. a). Image of the capillary in situ reactor used: A: Sapphire capillary. B: Connections for external tubing. C: Sliding end connection. D: Parallel rails for preventing strain on the capillary. E: Goniometer head connection pin.<sup>10</sup> b). *In situ* XRD experimental setup at line BM01A, including X-Ray source, 2D detector, heater, capillary cell, goniometer and CCD camera.

To study the reaction mechanism and activation energy, the hydrothermal synthesis of AgCuO<sub>2</sub> with AgO and CuSO<sub>4</sub> as starting materials was reproduced, as previously reported in the work of *D. Muñoz-Rojas et al.*<sup>5</sup> To prepare the initial slurry (suspension), 0.262 g of AgO and 0.522 g of CuSO<sub>4</sub>.5H<sub>2</sub>O were mixed and stirred in 6 ml of deionized water for 5 min, then certain amount of KOH was added and the suspension was stirred for further 5 min. The slurry was then also grinded in a tender manner (i.e. to avoid clogging the capillary

with big particles) in an agate mortar to facilitate the injection into the single crystal sapphire capillary ( $1.15 \pm 0.1$  and  $0.8 \pm 0.08$  mm outer and inner diameters, respectively, see Figure VI-1). Once the sample was loaded in the cell, it was assembled in the beam line, as shown in Figure VI-1 b), and 250 bar of pressure were applied to the cell thanks to the pump. Then by setting the reaction temperature, the preparation for characterization was ready.

Once the capillary reached the set point temperature (less than 10 s, temperature is calibrated previously by placing a thermocouple inside the capillary), the samples were exposed to the X-ray and the diffracted signals were collected by an Oxford Diffraction Titan CCD detector. In order to eliminate the possible effect of light on the reaction process (Ag compounds being photosensitive), the whole preparation and characterization process was done in the dark. The reflections from the sapphire capillary, shadow of the beam stopper and bad pixels were masked out from the raw data. Then the corrected 2D data were integrated into 1D by Fit2D software.<sup>7</sup> All initial calibrations were performed using a NIST 660a LaB6 standard.

## VI.2 Effects of solution pH and reaction mechanism

The first factor we studied during the reaction was the pH, by modifying the amount of KOH added to the reaction. Before moving to the synchrotron experiments, three comparison synthesis were conducted in the lab with different concentrations of KOH, as shown in Table VI-1. The reactions were conducted with equal molar ratio (0.3 mol) of AgO and  $\text{CuSO}_4$  in 12 ml of KOH solution at 90 °C in sealed hydrothermal Parr reactor for 10 hours. Once the reaction was completed, the suspensions were filtered and the obtained powders were dried in an oven at 60 °C for 1 h.

Table VI-1. Samples synthesized in different concentration of KOH solutions at 90 °C.

Sample names	A1	A2	A3
KOH concentration (M)	1	0.3	0
Reaction temperature (°C)	90	90	25

Thus, the synthesized powders were characterized XRD (Bruker C40 D8) under grazing incidence geometry and the reflections are presented in Figure VI-2. As it's presented, for sample A1 which was synthesized in 1 M KOH solution, the major XRD reflections correspond to the  $\text{AgCuO}_2$  phase. Meanwhile, some reflections with weak intensity are associated with AgO impurity phase. With reduced KOH concentration (0.3 M, sample A2), the XRD reflections correspond to  $\text{Cu}_4(\text{SO}_4)(\text{OH})_6$ . No indication of any silver containing



phases was observed in the XRD patterns. Lastly, for the hydrothermal reaction conducted without any KOH (0 M, sample A3), the XRD reflections of the obtained powder also corresponded to Cu<sub>4</sub>(SO<sub>4</sub>)(OH)<sub>6</sub>. Again, no XRD reflections associated with any silver containing compound were identified.

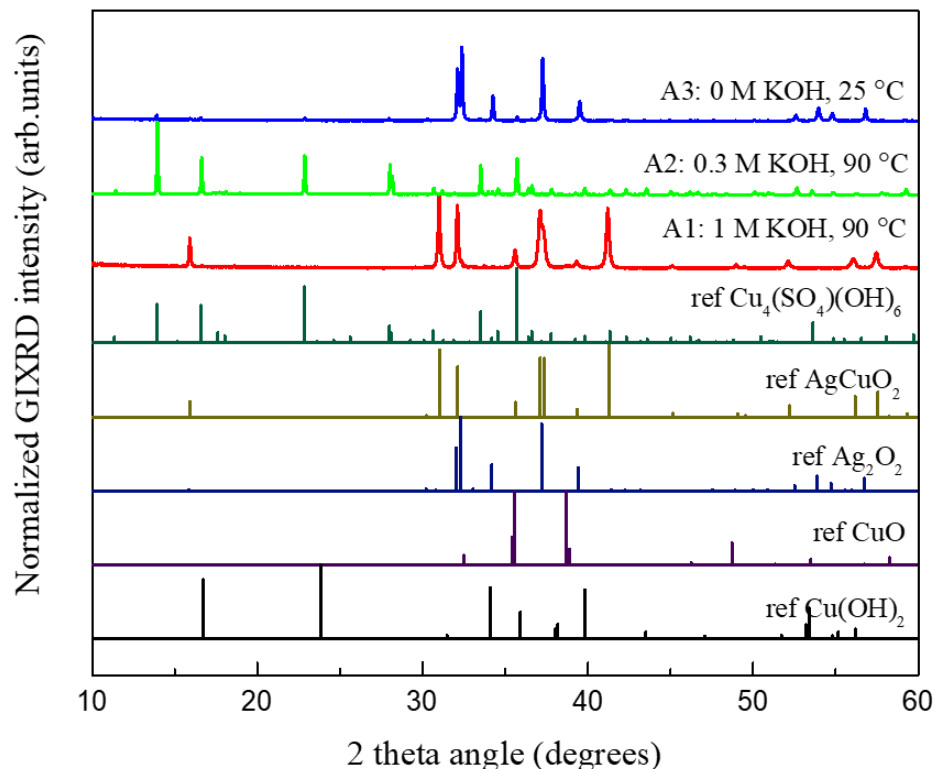


Figure VI-2. Normalized GI-XRD reflections of samples A1, A2 and A3 characterized in the lab.

To understand the hydrothermal reaction process of AgCuO<sub>2</sub>, similar experiments were repeated and characterized by *in situ* XRD in the synchrotron, as shown in detail in Table VI-2. For the sake of simplicity, here we define the standard hydrothermal reaction conditions as the equimolar mixture of Ag and Cu precursors reacting in 1 M KOH solution at 90 °C with 250 bar of pressure. All suspensions were prepared right before the synchrotron characterization, no more than 10 minutes. To study the effect of pH during the hydrothermal reaction process, the same concentrations of KOH solutions than the ones used in the lab were used in sample S1, S2 and S3 in the synchrotron.

Table VI-2. *in situ* XRD of samples under different conditions.

Sample names	temperature (°C)	KOH solution concentration (M)	Pressure (bar)	Obtained phase
S1	90	1	250	AgCuO <sub>2</sub>
S2		0.3		Cu <sub>4</sub> (SO <sub>4</sub> )(OH) <sub>6</sub>
S3		0		Cu <sub>4</sub> (SO <sub>4</sub> )(OH) <sub>6</sub> with intermediate phases
S1b		1	1	AgCuO <sub>2</sub>

The recorded raw diffraction data were treated by Matlab program to obtain 2D and 3D phase transition maps. In addition the treated data with ".xy" format were converted into ".raw" files (with wavelength 0.6999 Å) with DIFFRACTION PLUS V.04. Then phase identification was carried out using the software EVA V.02. The details of data treatment will be presented in the appendix at end of the chapter. All diffraction signal acquisition duration in S1, S2 and S3 are 5 s, thus their reflection intensity are comparable. In the first case we followed the standard reaction parameters (sample S1), which was also defined as standard reaction condition in this work.<sup>5</sup> The phase evolution and identifications are presented in Figure VI-3. In Figure VI-3 a), the 2D the evolution of the patterns versus reaction time (Y axis) is presented in 2D. From the 2D diagram, consistent variations of the intensity of the different reflections were observed. Among all those transitions, the line emerging at low angle (about 7°) marks the formation of AgCuO<sub>2</sub> phase (corresponding to the unique reflection of AgCuO<sub>2</sub> phase at low angle 16.5 ° in Cu Kα wavelength). By extending the reflection intensity in Z axis, the 3D phase transition diagram was obtained, as presented in Figure VI-3 b). From the side view, a clear reflection at low diffraction angle is presented. In addition, a rapid increase of reflection intensity at 13 ° was also observed. In Figure VI-3 c), the identified phases from the reflections are presented. The starting precursors of the reaction were AgO and CuO (obtained from CuSO<sub>4</sub> precipitation in 1 M KOH solution in the starting slurry). The reflection at low diffraction angle (about 7 °) was confirmed to correspond to AgCuO<sub>2</sub> phase. In addition, several other reflections with increasing intensity also matched AgCuO<sub>2</sub>. On the other hand, the intensity of reflections corresponding to Ag<sub>2</sub>O<sub>2</sub> (AgO) and CuO phases rapidly decreased until almost disappeared from the diffraction. Meanwhile, a tiny amount of Ag<sub>2</sub>O phase from AgO reduction was also observed at diffraction angle 14.5 °. With a good solubility in water, the reflections of other chemicals, like Na<sub>2</sub>S<sub>2</sub>O<sub>8</sub> and KOH were not present in the diffraction pattern. Even though the experiment was stopped after 250 seconds, the whole reaction was complete in only about 75 s. In the end, a powder was obtained with a majority of AgCuO<sub>2</sub> phase, in agreement with the XRD patterns from the synthesis in lab shown in Figure VI-2 (sample A1).

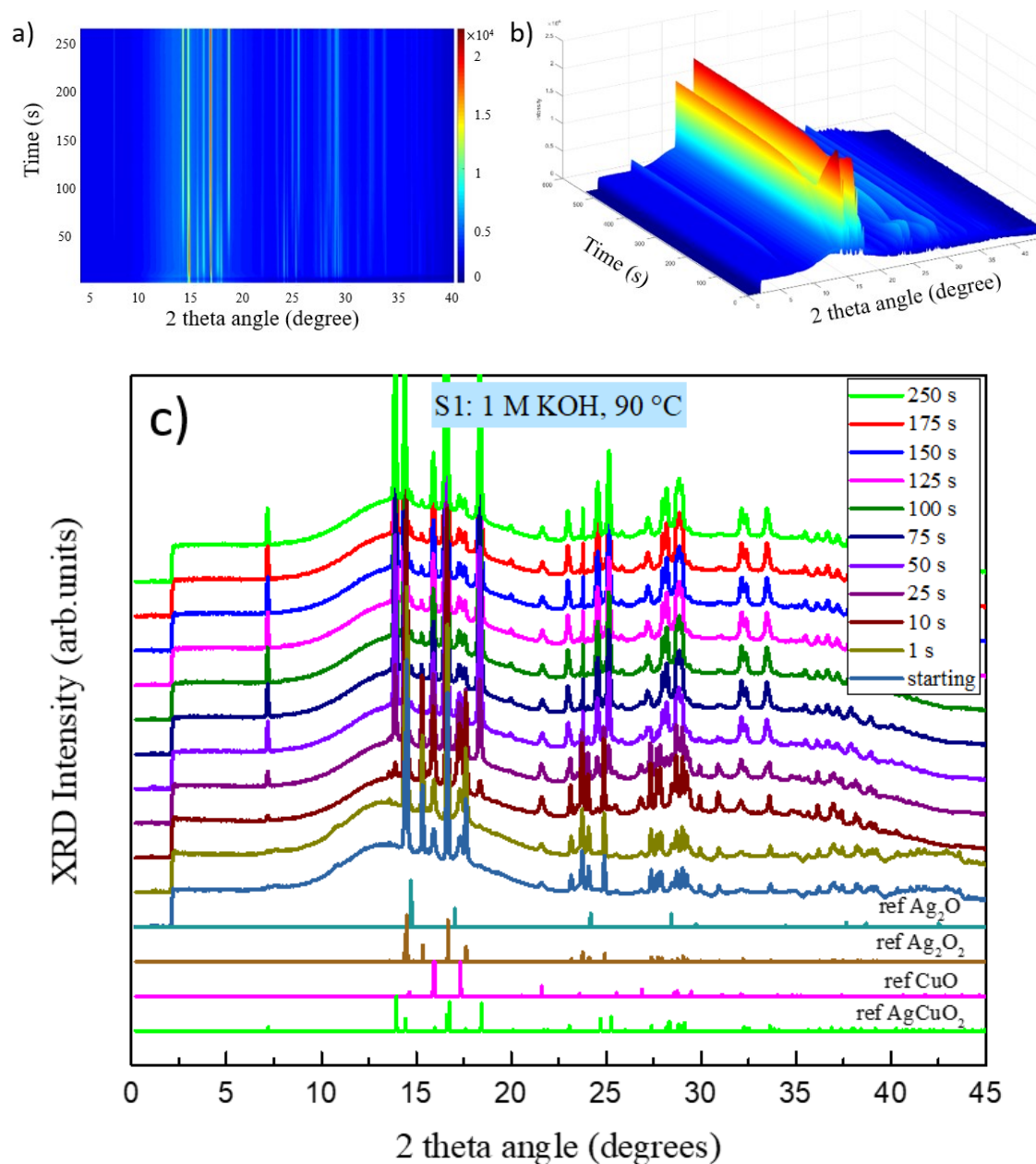


Figure VI-3. Phase evolution of reaction S1, with 1 M KOH solution with 250 bar pressure under 90 °C: a) 2 D, b) 3 D diagram and c) phase identification of selected XRD patterns.

In the XRD characterizations of the sample synthesized in lab, with lower KOH concentration, only Cu<sub>4</sub>(SO<sub>4</sub>)(OH)<sub>6</sub> powder was identified from the XRD pattern, as presented in Figure VI-2 (sample A2). Meanwhile, interestingly reflections corresponding to any silver containing compound were not presented. To understand the reason behind, the experiment was repeated and also followed by *in situ* XRD (sample S2, except that in synchrotron the pressure was much higher, 250 bar, than for lab synthesis in the lab, roughly 3 bar). The corresponding transitions of reflection intensity and identified phases are given in Figure VI-4. The reflection intensity versus time 2D diagram is presented in figure a). Comparing with the standard 1 M KOH concentration, an increase of the background signal

can be observed between 10 and 20 °, indicating a much stronger diffraction background. This stronger background is associated to the X-ray interaction with a higher concentration of dissolved ions in solution. In addition, at lower diffraction angles, at least two clear lines emerged during the reaction, at 5 ° and 7.5 ° separately. As well, similar with sample S1, in the 2D diagram, the evolution of reflected X-ray intensity were continuous and no intermediate phases appeared. The 3D diagram of the reflection intensity transition is presented in Figure VI-4 b). At lower angles, the two reflections at low angles are very clear, increasing in intensity with time, differently to what was observed when using 1 M KOH condition. In Figure VI-4 c), the emerged new phase and consumed reagents were distinguished from the reflections. Comparing the XRD references, the two distinct low angle reflections correspond to Cu<sub>4</sub>(SO<sub>4</sub>)(OH)<sub>6</sub>. Interestingly, when the CuSO<sub>4</sub> was added into 0.3 M KOH, unlike the precipitation of CuO phase as starting precursor in sample S1, the CuSO<sub>4</sub> precipitated as Cu<sub>4</sub>(SO<sub>4</sub>)(OH)<sub>6</sub>. Thus, the reflection signal of this copper compound existed even at the beginning of the hydrothermal reaction, see for instance the reflection at 16 °. The completion of the whole reaction was the total recorded duration of 650 s.

Throughout the characterization, the intensity of AgO phase reflections decreased as the reaction proceeded. However, at the end of this hydrothermal reaction, neither the reflection corresponding to AgCuO<sub>2</sub> nor any silver containing compound was observed. The absence of silver containing phase and the resulting Cu<sub>4</sub>(SO<sub>4</sub>)(OH)<sub>6</sub> crystalline phase in solution were in agreement with the XRD results obtained from sample A2, synthesized in the lab. The explanation for the absence of silver containing phases can be found from the work of *N.N.Lesnykh et al.*<sup>11</sup> As it's know that, metal oxides are partially soluble in basic solution to form metal hydroxide complex in solution. Here is the same for AgO, even though the solubility is rather low. However, in that work, it pointed out due to the presence of SO<sub>4</sub><sup>2-</sup> anions in solution, the formed [AgOH(SO<sub>4</sub>)]<sub>2</sub><sup>-ads</sup> complex was much more soluble than [Ag(OH)<sub>2</sub>]<sub>ads</sub> complex in 0.1 M NaOH solution. In our case, the SO<sub>4</sub><sup>2-</sup> ions were also included in the slurry (from CuSO<sub>4</sub>) and the KOH concentration was also in the same level (0.3 M), thus this could explain the dissolution of AgO. On the other hand, the Cu<sub>4</sub>(SO<sub>4</sub>)(OH)<sub>6</sub> precipitated as the final product, which also confirmed the existence of such metal sulfate hydroxide complex.

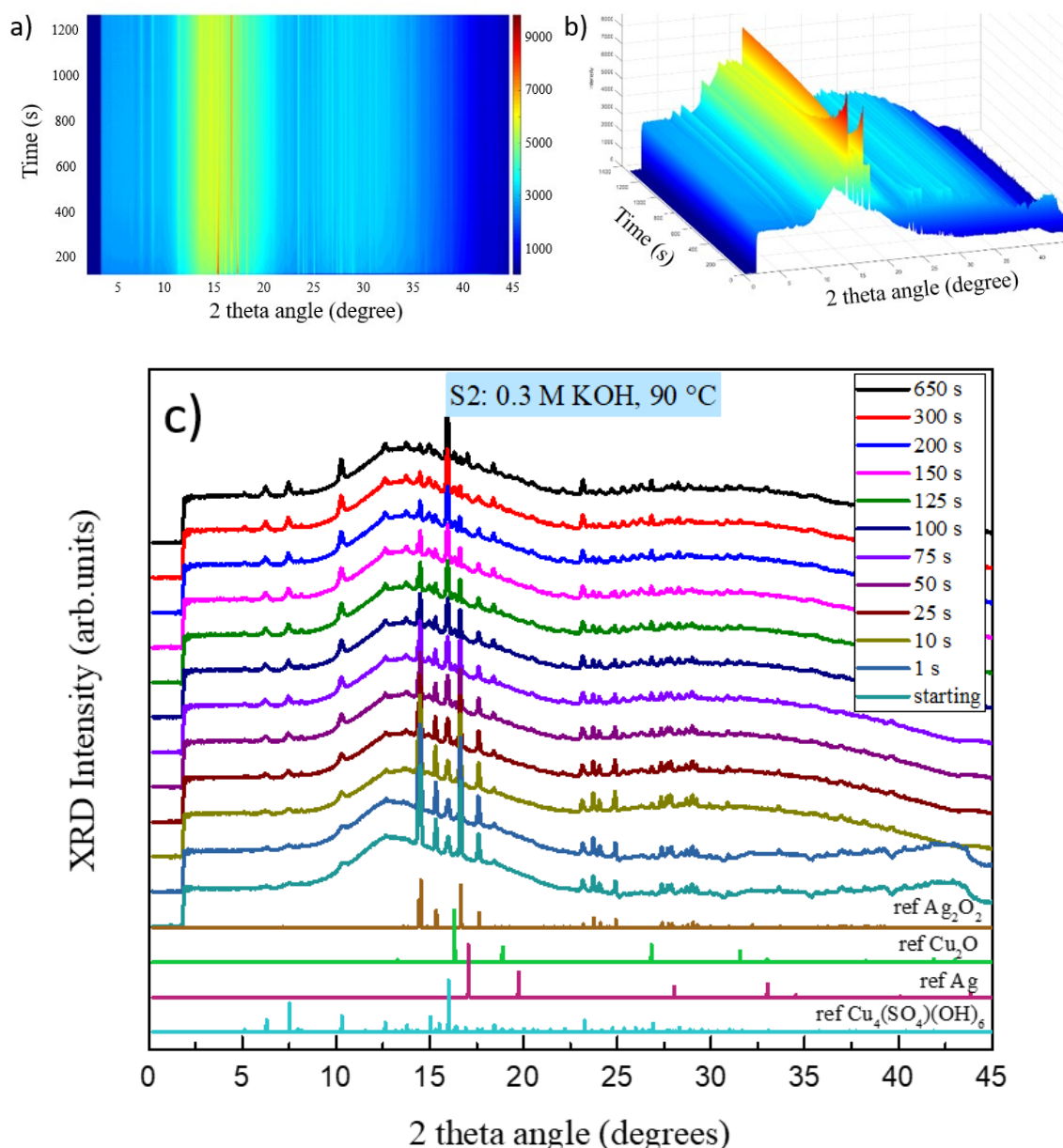


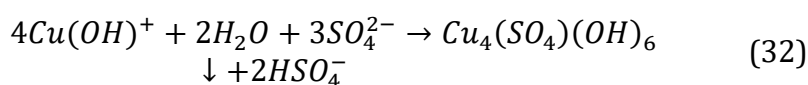
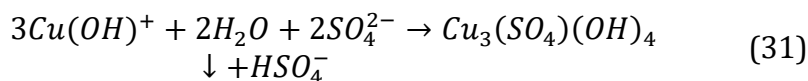
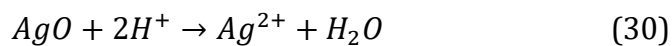
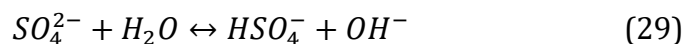
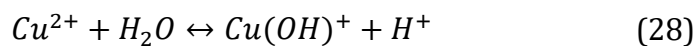
Figure VI-4. Phase evolution of reaction S2, with 0.3 M KOH and 250 bar at 90 °C: a) 2 D, b) 3 D diagram and c) phase identification of selected XRD patterns.

Lastly, in the case of the reaction without no added KOH, the *in situ* XRD characterization was also conducted (sample S3), and the results are shown in Figure VI-5. In figure a), a low background signal was presented in the 2D diagram. In addition, several short lines were observed during the reaction, indicating the existence of intermediate phases during the hydrothermal reaction without KOH added. Similar evidence of intermediate phases can be also found around 23 °. Lastly, the intensity of all the new formed lines were rather weak, which can be attribute a lower quantity of precipitation. Those results are further presented with a more clear view in the 3D diagram, as shown in figure b). At low diffraction angle, a reflection emerged right after the characterization began and then about 100 s afterwards

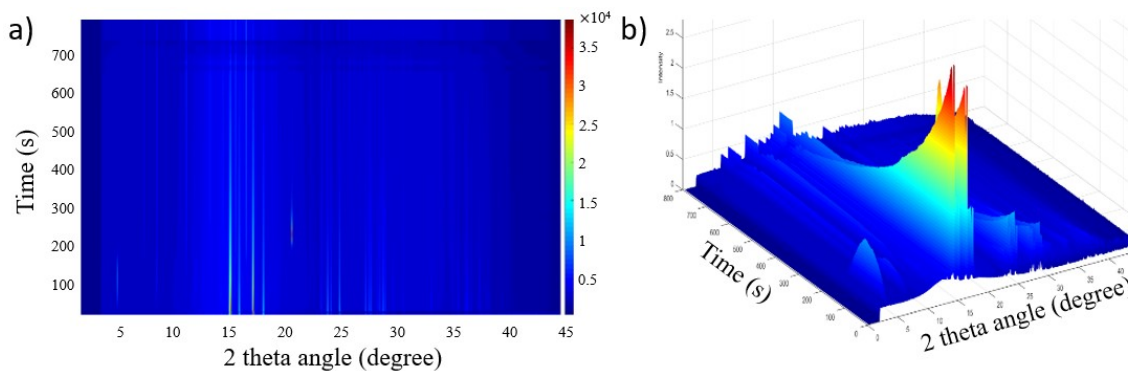
disappeared. Comparing with the strong reflections at the beginning of the reaction, coming from the AgO powder, the intensity of newly emerged reflections was much weaker. In figure c), several selected patterns are presented along with the reference patterns of the identified phases involved in the reaction. The emergence and disappearance of those reflections was actually a phase transition from  $\text{Cu}_{2.5}(\text{SO}_4)_5(\text{OH})_3 \cdot 2\text{H}_2\text{O}$  to  $\text{Cu}_3(\text{SO}_4)(\text{OH})_4$  and finally stabilized as the phase  $\text{Cu}_4(\text{SO}_4)(\text{OH})_6$ . Meanwhile, the reflections corresponding to AgO phase totally disappeared after about 10 min of reaction. The final products of the reaction are the same as for the equivalent sample synthesized in the lab, as previously presented in Figure VI-2.

However, this result was rather surprising, since the initial pH was neutral and thus the AgO powder should remain precipitated. Actually the formation of different types of copper sulfate hydroxide phases were reported from the work of *H.Tanaka et al.*<sup>11</sup> In the publication,  $\text{CuSO}_4$  solution (1 M) was added into NaOH solution (0.01 M, pH 12) by titration. With different quantities of  $\text{CuSO}_4$  solution added, different copper sulfate hydroxide phases were formed. As it is widely known that  $\text{CuSO}_4$  solution presents acidic nature due to its hydrolysis in water, thus the addition of  $\text{CuSO}_4$  solution in a NaOH solution leads to a decrease in pH. In the work, it is also mentioned that when the whole solution reaches neutral pH,  $\text{Cu}_4(\text{SO}_4)(\text{OH})_6$  phase formed. By adding more  $\text{CuSO}_4$  solution, the pH of the solution even dropped from 12 to 4. In our case, only AgO powder and 0.25 M  $\text{CuSO}_4$  solution were present in the initial reaction solution.

As shown in Equation VI 1 and 2, both  $\text{Cu}^{2+}$  and  $\text{SO}_4^{2-}$  ions are able to hydrolysis with water, however since  $\text{H}_2\text{SO}_4$  is a strong acid, thus its  $\text{SO}_4^{2-}$  ion is a weak basic, thus the overall  $\text{CuSO}_4$  solution presents acidic pH. In the reaction slurry, AgO was also added as reactant, thus it was dissolved in the acidic solution as shown in Equation VI 3. Therefore, the  $\text{H}^+$  ions were consumed and balance in Equation VI 1 shifted to the  $\text{Cu}(\text{OH})^+$  complex. Thus, combining the  $\text{SO}_4^{2-}$  ions and  $\text{H}_2\text{O}$ , this complex was precipitated into  $\text{Cu}_3(\text{SO}_4)(\text{OH})_4$ , as reaction shown in Equation VI 4. As the reaction proceeded, thus more protons were consumed by AgO, the more supplying of  $\text{Cu}(\text{OH})^+$  complex, thus the  $\text{Cu}_4(\text{SO}_4)(\text{OH})_6$  precipitation was observed, as the reaction shown in Equation VI 5. During the reaction, the water hydrolysis could even be accelerated by the applied 90 °C temperature, thus acceleration of the precipitation process. Meanwhile, since there was always excessive  $\text{CuSO}_4$  in solution, the formed intermediate phases, such as  $\text{Cu}_3(\text{SO}_4)(\text{OH})_4$ , possibly re-dissolved in acidic solution.



Therefore, to conclude, the pH of the solution plays a critical role in AgCuO<sub>2</sub> phase formation. Different pH during reaction can lead to the different reaction mechanism between CuSO<sub>4</sub> and AgO thus resulting in different final products. From the absence of intermediate phase or shifting of peaks during the formation of AgCuO<sub>2</sub> in 1 M KOH solution, possibility of solid phase transformation as the AgCuO<sub>2</sub> formation mechanism in the alkaline solution is thus excluded.



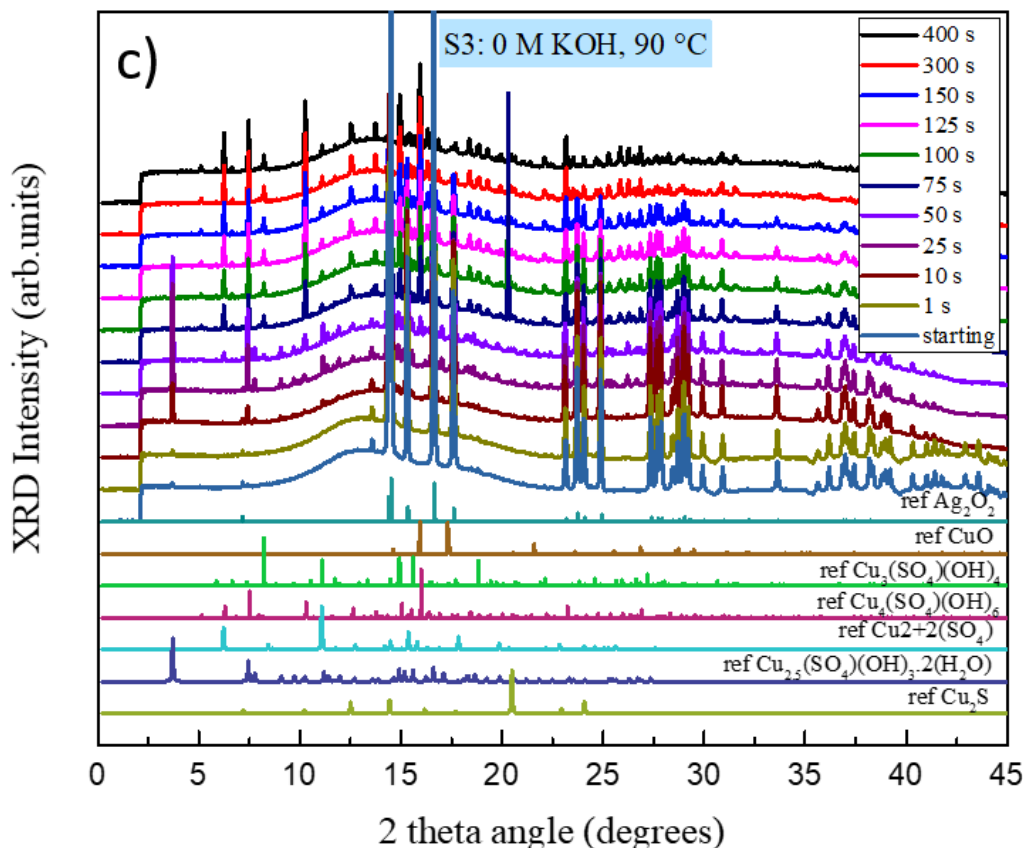


Figure VI-5. Phase evolution of reaction S3, with no KOH with 250 bar pressure under 90 °C: a) 2 D, b) 3 D diagrams and c) phase identification of selected XRD patterns.

In order to compare the results obtained in lab (with pressure close to 3 bar) and in synchrotron (with pressure of 250 bar), the *in situ* XRD characterization was also conducted for reaction in 1 M KOH solution at 90 °C with 3 bar pressure (sample S1b), as the result shown in Figure VI-6. The evolution of the reflections were compared with sample S1 with 250 bar of pressure (shown in Figure VI-3). In this reaction with 1 bar pressure, similar trend of reflection intensity was observed. Reflections corresponding to AgCuO<sub>2</sub> increased while the reflections for initial AgO, CuO precursors decreased until fully disappeared. Comparing the reflections corresponding to AgCuO<sub>2</sub> in Figure VI-3 and Figure VI-6, no apparent shift of peaks or intensity changes were observed due to different pressures used. Therefore, the applied 250 bar pressure had negligible effect on the AgCuO<sub>2</sub> hydrothermal reaction. Thus, we can consider that the samples synthesized in lab (with 1 bar pressure) and in synchrotron (with 250 bar pressure) are comparable.



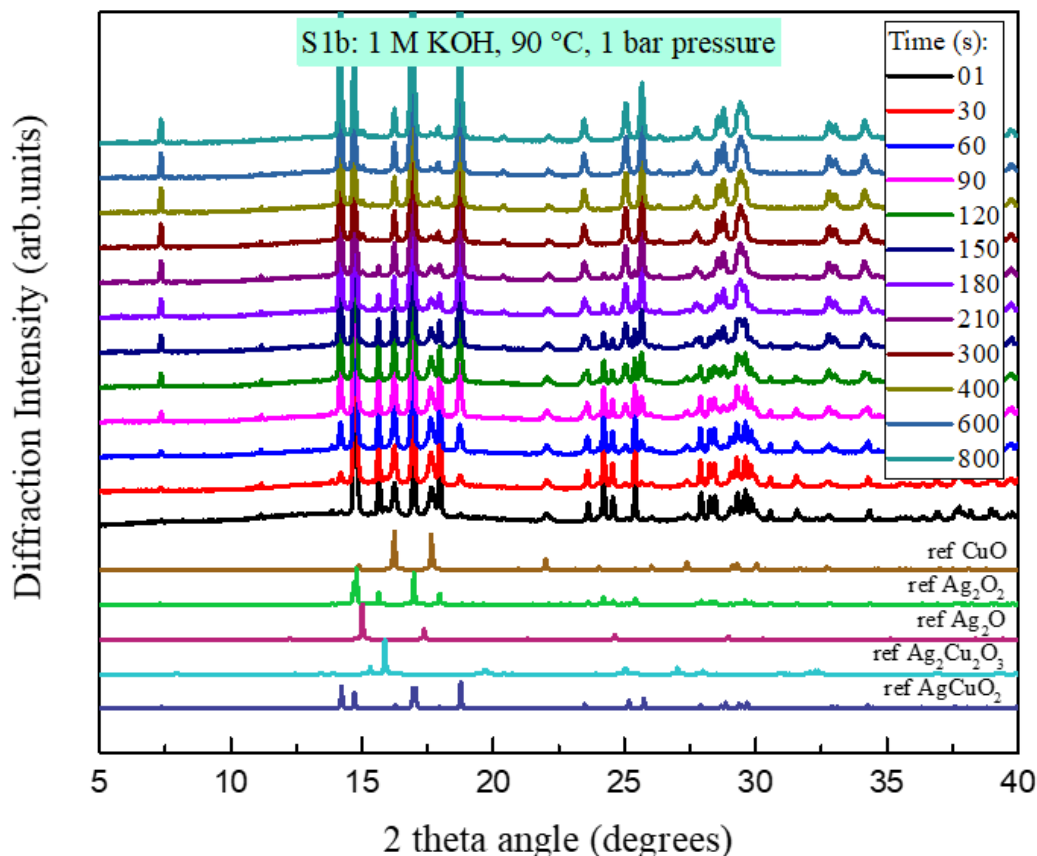
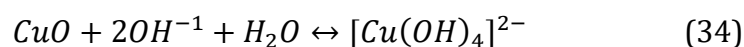
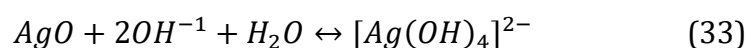
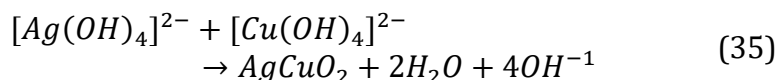


Figure VI-6. Extracted 2D XRD patterns from reaction (sample S1b) in 1 M KOH solution at 90 °C with 3 bar pressure.

Combining the results obtained from the different reactions discussed so far, we propose the reaction mechanism for the hydrothermal synthesis of  $\text{AgCuO}_2$ , as illustrated in Figure VI-7. At the beginning of the reaction, dissolved  $\text{CuSO}_4$  is mixed with a 1 M KOH solution. At such basic pH,  $\text{CuO}$  precipitates<sup>12</sup>, which was also confirmed by the reflections at the beginning of the characterization as shown in Figure VI-3 c). Therefore, the actual reaction precursors in 1 M KOH solution are  $\text{CuO}$  and  $\text{AgO}$  in suspension.

In this starting slurry, there is always an equilibrium between the metal oxide and the metal hydroxide complex, as shown in Equation VI 6 and 7.<sup>13</sup> Even though, for  $\text{AgO}$ , such solubility is rather low.





Then, since  $\text{AgCuO}_2$  is more stable and thus less soluble in basic solution,<sup>2,14</sup> the co-precipitation between  $[\text{Ag}(\text{OH})_2]^{2-}$  and  $[\text{Cu}(\text{OH})_2]^{2-}$  happens, as shown in Equation VI 7. Therefore, the silver and copper hydroxide complexes in solution are consumed by  $\text{AgCuO}_2$  phase precipitation, displacing the equilibrium between metal oxides and metal hydroxide complex towards the latter. Thus,  $\text{AgO}$  and  $\text{CuO}$  powders were consumed through such hydroxide complex co-precipitation and the  $\text{AgCuO}_2$  phase was formed.

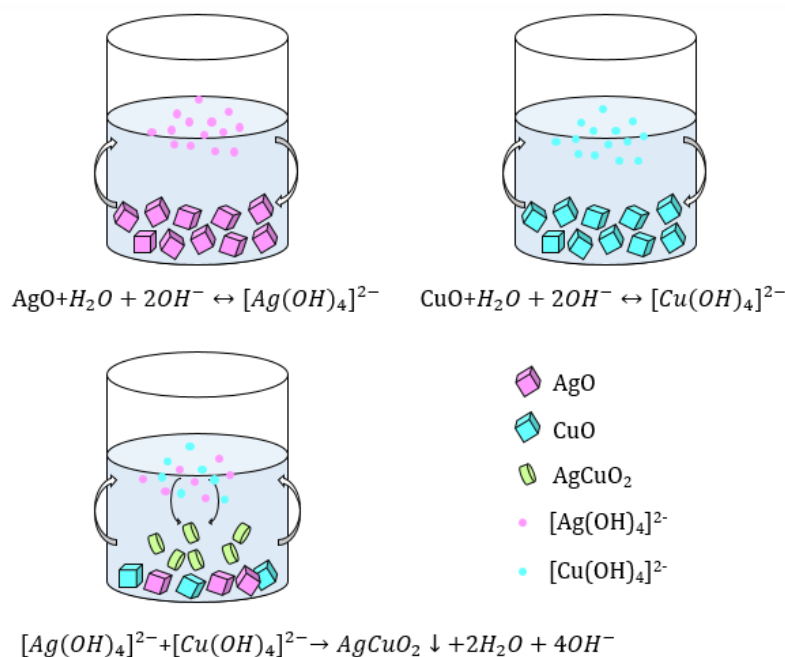


Figure VI-7. Illustration of  $\text{AgCuO}_2$  phase formation mechanism by high pH facilitated co-precipitation.

The rather constant background signal obtained in all patterns supports this view since a change in the total concentration of dissolved species would lead to a change in background. The mechanism of the process is also illustrated in Figure VI-7. With this model, we can predict that with higher reaction temperatures, metal oxides can dissolve faster in the alkaline solution due to the equilibrium with metal hydroxide complex in the solution. Thus, the  $\text{AgCuO}_2$  precipitation speed can be largely enhanced. This was indeed the case, as it is shown in the next section.

### VI.3 Effects of temperature and calculation of the reaction activation energy

In addition to studying the effects of pH on the reaction outcome and mechanism, the activation energy was also estimated by recording the reaction duration at different temperatures. The solution pH was maintained at 1 M with 250 bar pressure and the reaction temperature was varied from 50 °C to 120 °C, as shown in Table VI-3.

Table VI-3. *In situ XRD study of hydrothermal reaction at different temperatures.*

Sample Names	Reaction temperature (°C)	KOH concentration (M)	Pressure (bar)	Reaction duration (s)	Obtained phase
T1	50	1	250	2500	AgCuO <sub>2</sub>
T2	70			600	
T3	80			140	
T4	90			120	
T5	120			20	

Since the slurry used had the same concentration, the quantity of injected reactants in the capillary tube were roughly the same. In all reaction temperatures, AgCuO<sub>2</sub> was obtained as the final product. The full patterns of the *in situ* XRD characterizations are presented at the end of this chapter as appendix. In all cases a similar reaction evolution was observed, with the intensity of reflections corresponding to AgO, CuO decreasing and the reflections for AgCuO<sub>2</sub> increasing.

To have a clear view of the AgCuO<sub>2</sub> phase evolution at different temperatures, reflections corresponding to (111) at 14.22 ° were selected. The evolution of reflection intensity with time at different temperatures are presented in Figure VI-8. Figure a) presents the (111) reflections at 50 °C (sample T1). The intensity of the reflections increased rather slowly and they stabilized at the same time, after about 4000 s. Meanwhile, with increased reaction temperature, the reaction duration was largely reduced, as shown in the patters obtained at 70 °C (Figure VI-8 b)), 80 °C (Figure VI-8 c)) and 90 °C (Figure VI-8 d)).

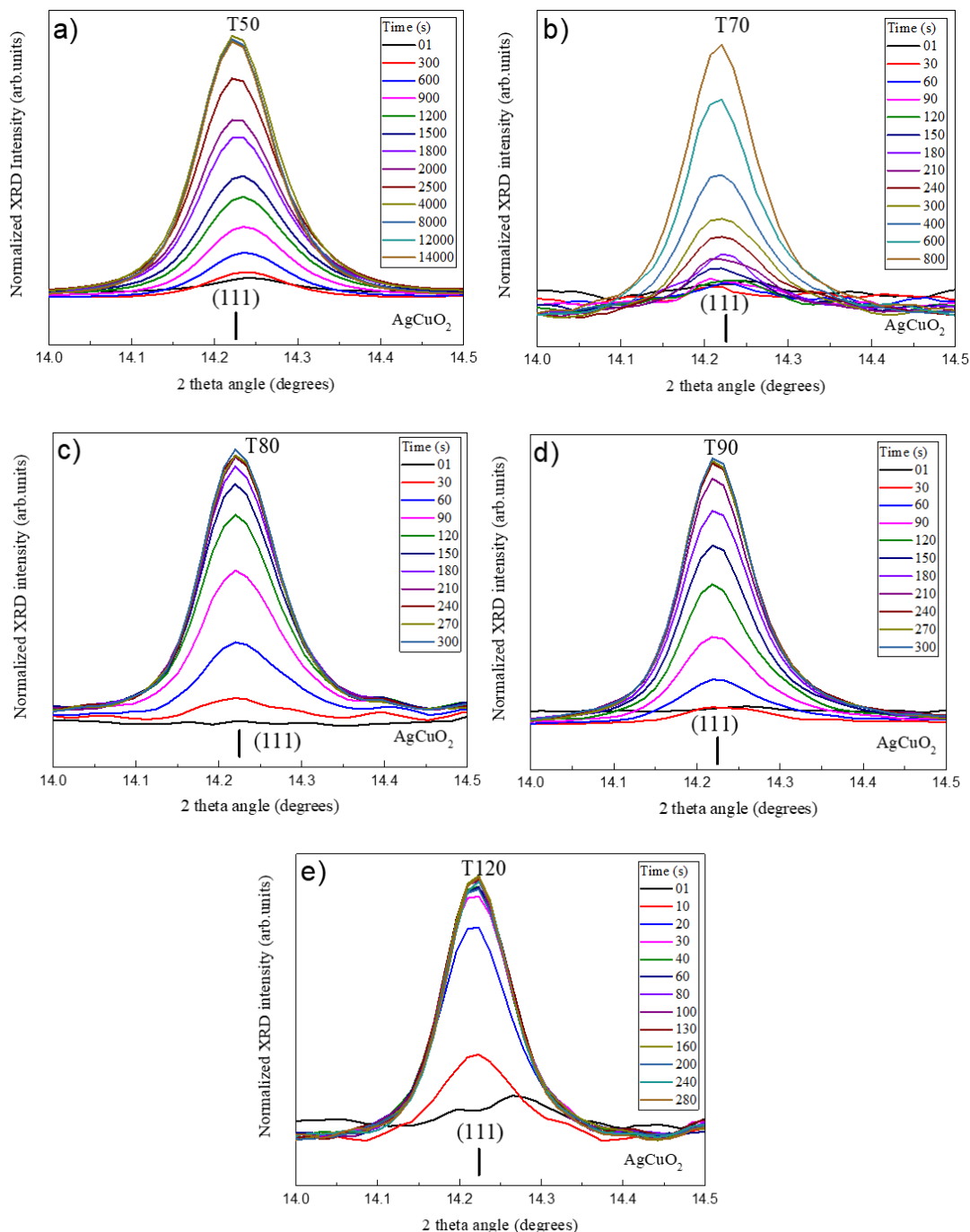


Figure VI-8. Evolution of  $\text{AgCuO}_2$  (111) reflections for reactions made in 1 M KOH solution with 250 bar pressure at a) 50 °C a), b) 70 °C, c) 80 °C, d) 90 °C and e) 120 °C.

At 70 °C (sample T2), by comparing the reflection intensity, the reaction was completed after about 800 s. For reactions at 80 °C (sample T3) and 90 °C (sample T4), the obtained evolution of reflection intensity were rather similar. Reactions at both temperatures were completed after around 180 s. Lastly, Figure VI-8 e) presents the reflections at the highest reaction temperature (120 °C, sample T5) during characterization. By comparing the intensity change, only 30 s were required to complete the reaction. Therefore, since the

quantity of reagents injected in capillary were similar, a much faster reaction speed was observed with increasing temperature.

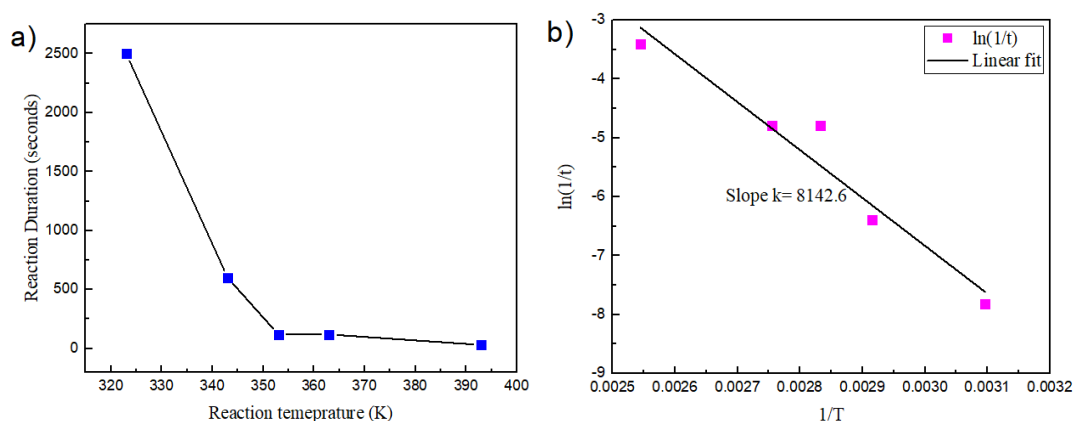


Figure VI-9. With reactions conducted in 1 M KOH solution with 250 bar, a) reaction durations under different temperatures and b) activation energy fitting.

Lastly, based on the experimental data above, the reaction duration was determined for each temperature. In Figure VI-9 a), the relation between reaction duration and temperature is plotted. Since each experiment was loaded with similar amount of starting precursors, thus we suppose there was a rather constant amount of precursors ( $m$  mol, molar ratio between AgO and CuO were 1, giving the same amount of AgCuO<sub>2</sub> in all reactions) reacted.  $t$  being the reaction duration, thus the reaction rate  $k$  can be expressed as  $m/t$ . Thus, based on the Arrhenius activation energy theory, the following calculations were developed:

$$\ln(m/t) = \ln(k) = \ln(A) - E_a/R \times (1/T) = \ln(a) - B \times (1/T)$$

$$\ln(m) + \ln(1/t) = \ln(A) - B \times (1/T)$$

$$\text{Thus, } \ln(1/t) = (\ln(A) - \ln(m)) - B \times (1/T)$$

$$\ln(1/t) = A' - B \times (1/T)$$

To find out the value  $B$ , a linear fitting between  $\ln(1/t)$  and  $(1/T)$  is given in Figure VI-9 b). By linear fitting, we can obtain:  $\ln(1/t) = 17.6 - 8142.6(1/T)$ ,  $E_a = 8.143k \times R = 8.143k \times 8.31446 \text{ J/mol} = 67.7 \text{ kJ/mol}$ . Therefore the activation energy for AgCuO<sub>2</sub> formation in such solution condition is about 67.7 kJ/mol.

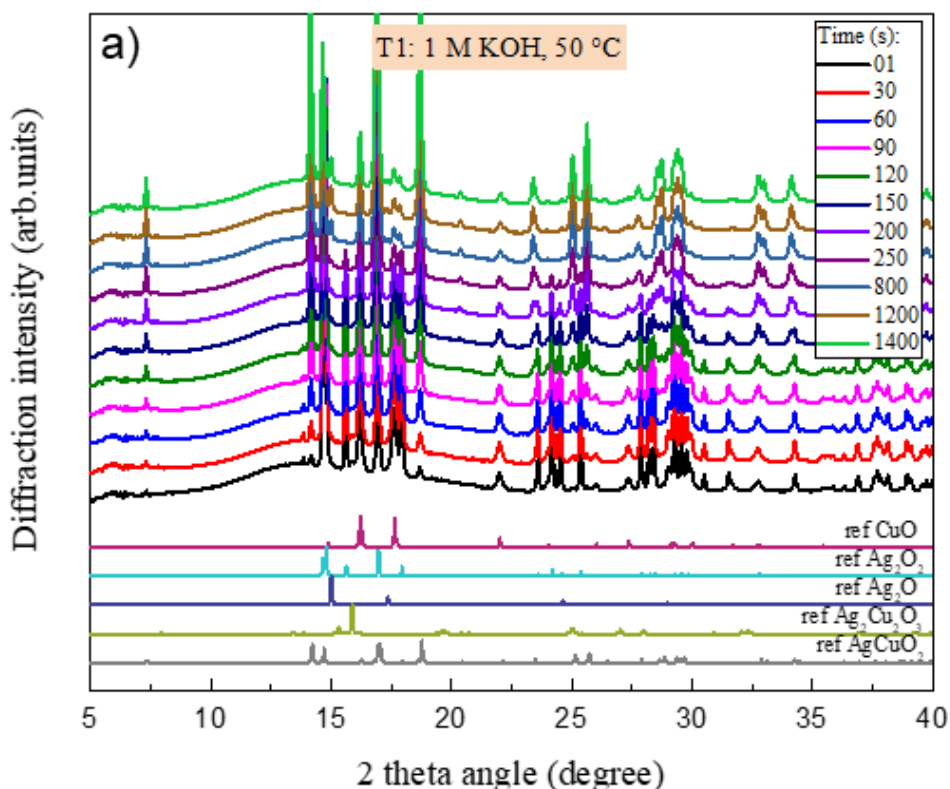
## VI.4 Chapter VI conclusions

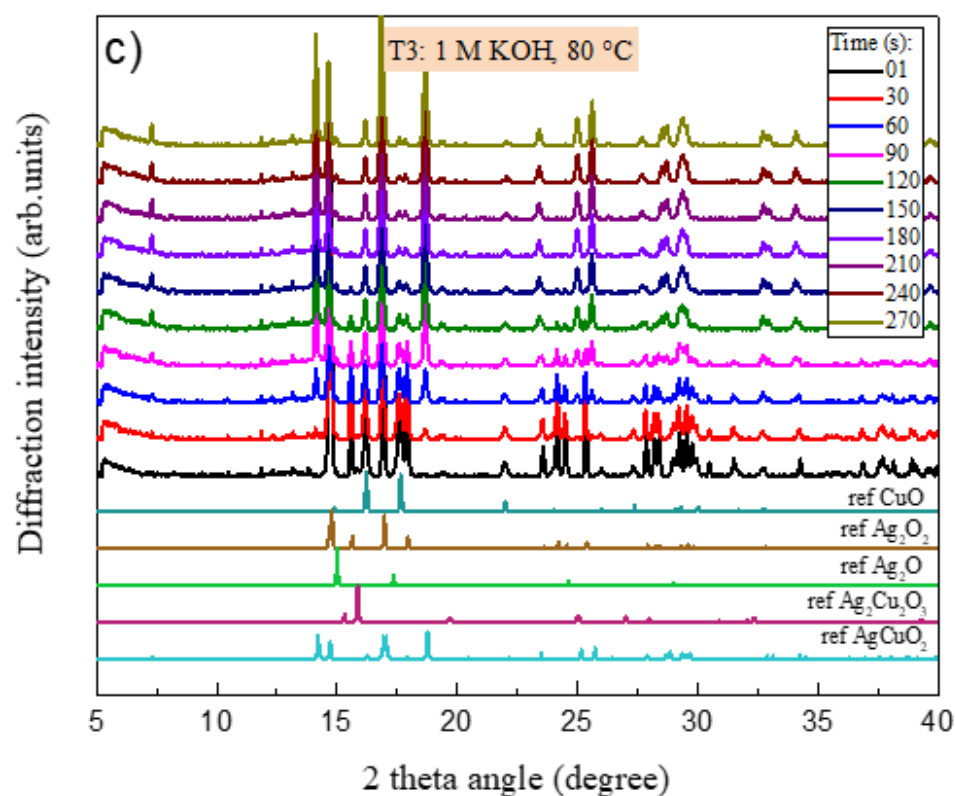
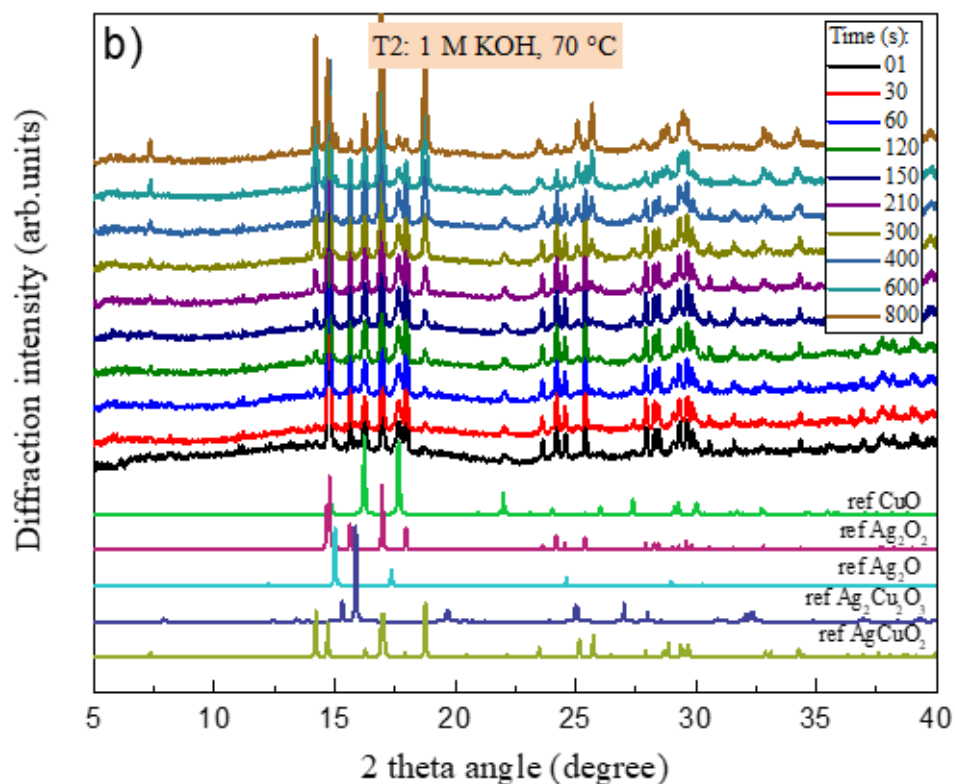
In this chapter, the hydrothermal reactions of AgCuO<sub>2</sub> phase synthesis were studied. Choosing AgO, CuSO<sub>4</sub> and KOH solution as precursors, the reactions were firstly conducted in the laboratory under 1 bar pressure with various KOH concentrations. AgCuO<sub>2</sub> could only be obtained when using 1 M KOH solution, while in the other cases only Cu<sub>4</sub>(SO<sub>4</sub>)(OH)<sub>6</sub> was obtained. To further investigate the effects of solution pH, similar samples were

synthesized and followed by *in situ* XRD in synchrotron. By reviewing the evolution of the reflection intensity for each phase, the reasons for the absence of AgO phase were explained, and why only with enough high KOH concentration the AgCuO<sub>2</sub> phase can be formed.

Besides the *in situ* XRD characterizations with different KOH concentration, the effects of reaction temperature were also studied with 1 M KOH solution and 250 bar pressure. The morphology of the grains synthesized at different temperatures was also studied. With a lower reaction temperature, averagely smaller grain size and anisotropic crystal growth are found. With increasing reaction temperature from 50 °C to 120 °C, the reactions were completed in shorter times. By extracting the reaction durations at each temperature, the Arrhenius equation was used and thus the reaction activation energy was estimated about 67.7 kJ/mol.

### VI.5 Appendix V: *In situ* XRD of hydrothermal reactions at different temperatures.





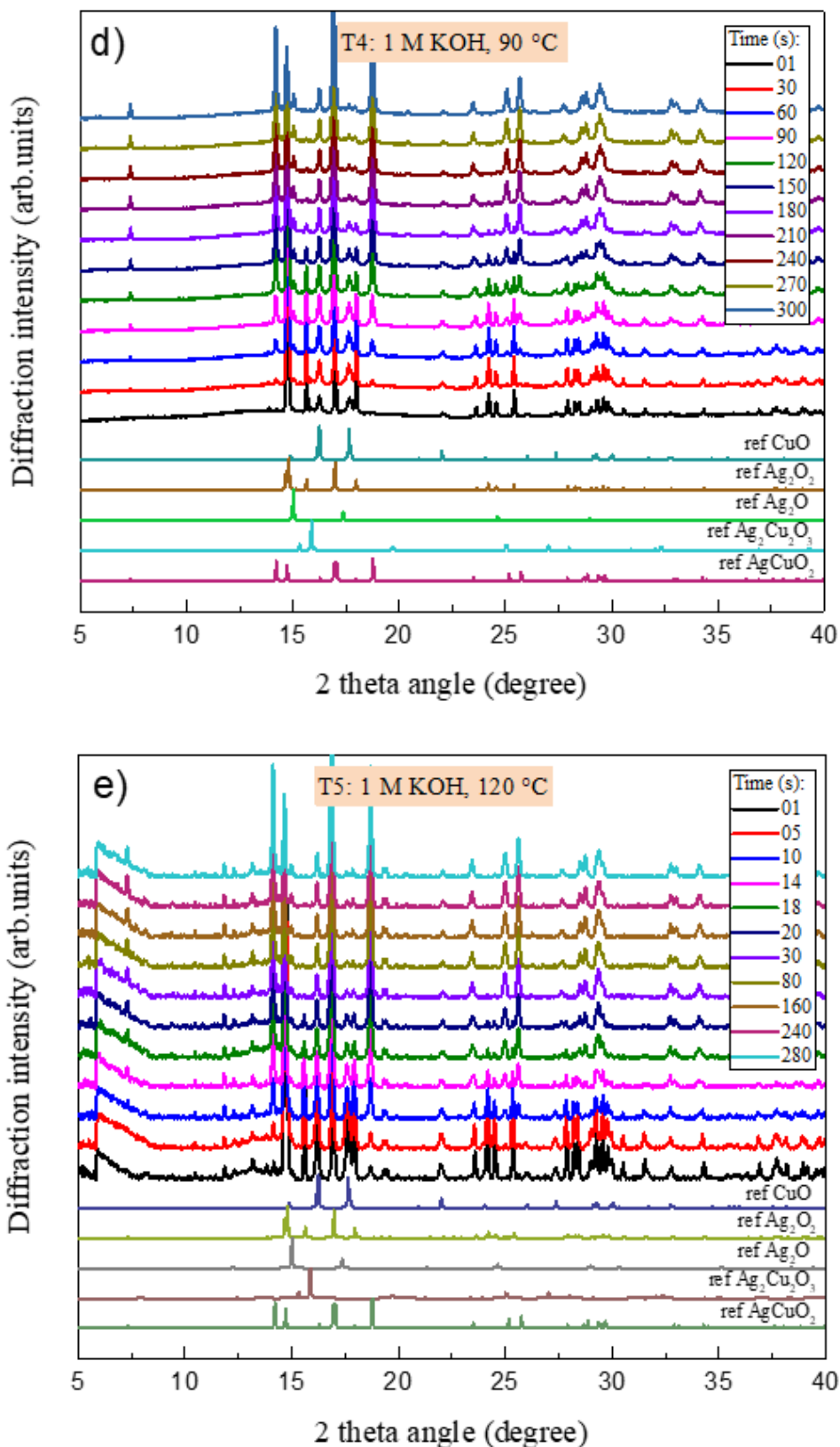


Figure S1. Full *in situ* XRD patterns of samples reacted in 1 M KOH solution with 250 bar pressure at temperature a) 50 °C, b) 70 °C, c) 80 °C, d) 90 °C and e) 120 °C.



## VI.6 References

1. Curda, J., Klein, W., Liu, H. & Jansen, M. Structure redetermination and high pressure behaviour of AgCuO<sub>2</sub>. *J. Alloys Compd.* **338**, 99–103 (2002).
2. Wang, F., Eylem, C., Nanjundaswamy, K. & Ilchev, N. Determination of AgCuO<sub>2</sub> Discharge Mechanism in Alkaline Electrolyte. *Electrochem. Solid-State Lett.* **7**, A346 (2004).
3. Sauvage, F., Muñoz-Rojas, D., Poeppelmeier, K. R. & Casañ-Pastor, N. Transport properties and lithium insertion study in the p-type semi-conductors AgCuO<sub>2</sub> and AgCu<sub>0.5</sub>Mn<sub>0.5</sub>O<sub>2</sub>. *J. Solid State Chem.* **182**, 374–380 (2009).
4. Curda, J., Klein, W. & Jansen, M. AgCuO<sub>2</sub>—Synthesis, Crystal Structure, and Structural Relationships with CuO and AgI<sub>2</sub>Ag<sub>2</sub>O<sub>2</sub>. *J. Solid State Chem.* **162**, 220–224 (2001).
5. Muñoz-Rojas, D. *et al.* High conductivity in hydrothermally grown AgCuO<sub>2</sub> single crystals verified using focused-ion-beam-deposited nanocontacts. *Inorg. Chem.* **49**, 10977–10983 (2010).
6. Dyadkin, V., Pattison, P., Dmitriev, V. & Chernyshov, D. A new multipurpose diffractometer PILATUS@SNBL. *J. Synchrotron Radiat.* **23**, 825–829 (2016).
7. Skjaervø, S. L. *et al.* Formation mechanism and growth of MNbO<sub>3</sub>, M=K, Na by in situ X-ray diffraction. *J. Am. Ceram. Soc.* 1–8 (2017). doi:10.1111/jace.14932
8. Jensen, K. M. Ø. *et al.* Revealing the mechanisms behind SnO<sub>2</sub> nanoparticle formation and growth during hydrothermal synthesis: An in situ total scattering study. *J. Am. Chem. Soc.* **134**, 6785–6792 (2012).
9. Becker, J. *et al.* Experimental setup for in situ X-ray SAXS/WAXS/PDF studies of the formation and growth of nanoparticles in near-and supercritical fluids. *J. Appl. Crystallogr.* **43**, 729–736 (2010).
10. Dalod, A. R. M. *et al.* Controlling Oriented Attachment and in Situ Functionalization of TiO<sub>2</sub> Nanoparticles during Hydrothermal Synthesis with APTES. *J. Phys. Chem. C* **121**, 11897–11906 (2017).
11. N.N.Lesnykh, N.M.Tutukina, I. . M. The Effect of Sulfate and Nitrate Ions on the Passivation and Activation of Silver in Alkaline Solutions. *Prot. Met.* **44**, 437–442 (2008).
12. Yagi, S. in *Thermodynamics - Physical Chemistry of Aqueous Systems* (ed. Moreno-Piraján, J. C.) (InTech, 2011). doi:10.5772/21548
13. Dirkse, T. P. & Wiers, B. The Stability and Solubility of AgO in Alkaline Solutions. *J. Electrochem. Soc.* **106**, 284 (1959).
14. Lu, Q., Lu, K., Zhang, L., Gong, J. & Liu, R. Electrodeposition of AgCuO<sub>2</sub> Nanoplates. *J. Electrochem. Soc.* **164**, D130–D134 (2017).



## *Conclusions and perspectives*

In this thesis work, we have achieved four main results, including silver and its oxide thin film coatings, tuning the  $\text{Cu}_2\text{O}$  films into (111) texture in AA-MOCVD, obtaining dense, continuous  $\text{AgCuO}_2$  thin films with unprecedentedly reported electrical and optical characterizations and studying the solution mechanism of  $\text{AgCuO}_2$  by in-situ XRD in ESRF synchrotron .

### *Deposition of silver and oxidation to silver oxide films.*

Since our initial attempt was depositing  $\text{AgCuO}_2$  films in AA-MOCVD with the oxygen plasma coupling, the work began with silver metallic coatings. During this section of work, with the assistance of ethanolamine as dispersant, low cost silver precursor AgAc was firstly reported for silver coatings in MOCVD. However the silver coatings were not homogeneous due to the low volatility of AgAc. The commercialized silver metal organic precursors are rather expensive concerning the quantity of precursor consumption in AA-MOCVD. Therefore, to obtain affordable silver metalorganic precursors with better volatility and deposition quality, a collaboration with Prof.Graziella Malandrino from University of Catania, Italy was established. Through this, two brand new silver precursors were reported, which were Ag(hfac)phenanthroline (AgP) and Ag(hfac)triglyme (AgT). Both precursors were able to delivery good quality silver coatings. Especially with AgT precursor, carbon free and homogeneous Ag coatings can be achieved. In addition, the two newly designed silver precursors have much lower ligands than commercial products.

After the Ag films were able to be deposited and optimized, the next step was trying to obtain silver oxide films. However, direct deposition of silver oxide films in MOCVD was always very challenging due to the incompatibility of the temperature between the precursors decomposition and the silver oxide phase. Therefore, an after-treatment approach was adopted, i.e. the first step was depositing Ag metallic films and then oxidizing them. To oxidize the silver films, we tested electrochemical oxidation and oxygen plasma treatment. From both methods, AgO films were obtained. With oxygen plasma treatment, the oxidization duration (about 2 min) was much shorter than the electrochemical oxidation (at least 20 min). In addition, the plasma oxidized silver oxide films had less impurities and more homogeneous surfaces.

*Cu<sub>2</sub>O thin film optimization in AA-MOCVD.*

In order to achieve AgCuO<sub>2</sub> thin film deposition in MOCVD, besides the work about silver and silver oxides, the copper oxide thin film optimization was also required. However, thanks to the long working experience in LMGP about copper oxide, the deposition of CuO was already well studied and optimized. Thus, we turned our interests to Cu<sub>2</sub>O thin film optimizations and attempted to achieve Cu<sub>2</sub>O films with better electrical properties.

During this part of work, to achieve Cu<sub>2</sub>O films with better homogeneity, the configuration of the AA-MOCVD system in LMGP was optimized. With a careful choice of the copper precursor (using Cu(II) trifluoroacetylacetonate (CuF)), high crystalline, homogenous and carbon-free Cu<sub>2</sub>O films were deposited. Based on that, the effects of oxygen ratio, silver nanoparticle incorporation and carrier gas humidity were investigated during the MOCVD. With slight higher oxygen ratio (still in the range of Cu<sub>2</sub>O deposition), Cu<sub>2</sub>O films with rougher surfaces and cubic grains were deposited. In addition, to incorporate the Ag nanoparticles in Cu<sub>2</sub>O film, the silver precursor AgT was mixed into CuF solution with various concentrations. With a higher AgT concentration, more Ag nanoparticles were incorporated in the Cu<sub>2</sub>O films. With more Ag nanoparticle incorporation, Cu<sub>2</sub>O films with bigger size, (111) oriented grains and higher deposition rates were observed. Lastly, with a tunable humidity in the carrier gas, depositions were carried out. The incorporation of humid carrier gas during MOCVD had a great impact on the deposited Cu<sub>2</sub>O films. First, the surface of the films presented 'pyramids-like' structure and those types of films were identified with (111) texture by XRD, electron diffraction in TEM and EBSD. In addition, higher deposition rates were observed with more humid carrier gases. By the TEM cross-section view of the sample, big grains (width over 300 nm) with columnar structures were observed. From the point view of electrical properties, Cu<sub>2</sub>O films deposited with humid carrier gas presented high carrier mobility, reaching a maximum of 17 cm<sup>2</sup>/V.s. As well, the conduction characteristics of those (111) oriented Cu<sub>2</sub>O films were further examined by electrical AFM. Through this, a higher conductivity was observed on the grain boundaries than on grains. The ASTAR phase mapping with ultra-fine resolution revealed a higher distribution of CuO phase in the grain boundaries which might be responsible for this abnormally high conductivity.

As the last part of work in this section, the effects of humidity on the initial thin film nucleation were studied. Cu<sub>2</sub>O films deposited for short durations (10 min ~ 50 min ) with and without humidity carrier gas were characterized by AFM. From the characterization,

much higher roughness of  $\text{Cu}_2\text{O}$  films were found when deposited with humid carrier gas, indicating a Stranski–Krastanov growth mode. Meanwhile, without humid carrier gas, the  $\text{Cu}_2\text{O}$  films tended to have layer-by-layer growth. Furthermore, based on the classic nucleation theories, the Gibbs free energy during the deposition process with different conditions (oxygen ratio, silver incorporation and humidity) was discussed. Through the model established, from the point view of thermodynamics, the larger grain sizes and high deposition speed were explained.

*AgCuO<sub>2</sub> thin film coating and electrical and optical property characterizations.*

Finally, with the foundation of the work about silver, silver oxide and copper oxides, we moved towards  $\text{AgCuO}_2$  film deposition. First of all, an attempt to deposit  $\text{AgCuO}_2$  in AA-MOCVD was tested. To conduct such tests, a mixture precursor solution of  $\text{CuF}$  and  $\text{AgT}$  was used for the co-deposition. During the deposition process, the oxygen plasma provided the high oxidizing species. Those co-depositions were tested at the precursor decomposition temperature limit, however similar to the silver oxide deposition, the temperature incompatibility between precursor and  $\text{AgCuO}_2$  phase made such co-deposition extremely difficult. In addition, besides the oxidizing species provided from oxygen plasma, highly corrosive radicals were also emitted and they made the deposition process even more complicated. Considering both the durability and the cost of precursors, a lower cost solution thin film coating technique was adopted instead, namely was Successive Ionic Layer Adsorption and Reaction (SILAR). Metal ion precursor solution was made up with almost equal ratio of  $\text{AgNO}_3$  and  $\text{Cu}(\text{NO}_3)_2$ . The cation solution contained 1 M  $\text{NaOH}$  solution. By adding sodium persulfate in the solution, the strong oxidation ability was provided. Since SILAR deposition is a rather substrate sensitive technique, different substrates with/without seed layers were tested. As a result,  $\text{Cu}_2\text{O}$ /glass substrate was able to deliver a high quality coating. Even though with  $\text{ZnO}$ /glass substrate coatings can also be obtained, continuous films were rarely achieved. The deposited films on  $\text{Cu}_2\text{O}$ /glass were identified by GIXRD to be the  $\text{AgCuO}_2$  phase, even though with a small quantity of  $\text{CuO}$  as impurities. In the optimized case, a continuous and dense 100 nm thick  $\text{AgCuO}_2$  thin film was coated. The RMS value was as low as 8 nm, indicating a rather smooth surface. The deposited  $\text{AgCuO}_2$  films were then characterized by UV-Vis spectroscopy. With the transmittance data, the Tauc plots were used for estimating the bandgap with both direct and indirect formula. By comparing the obtained Tauc plots in those two cases, a 1.2 eV direct bandgap was obtained.

In addition to the bandgap estimation, the AgCuO<sub>2</sub> films were also characterized by Hall Effect measurement. From the Hall Effect measurement, p type conductivity was confirmed. The lowest resistivity obtained was 0.2 Ω.cm, which is even lower than other CuMO<sub>2</sub> (M= Al, Cr, Sr, etc) delafossite compounds. In addition, the general low carrier concentration in those delafossite compounds was not observed in the SILAR coated AgCuO<sub>2</sub> film, which is possibly due to the mixed valence band and charge delocalization in this compound. The maximum carrier mobility obtained was 24 cm<sup>2</sup>/V.s and the carrier concentration was in the order of 10<sup>17</sup> cm<sup>-3</sup> ~ 10<sup>18</sup> cm<sup>-3</sup>. Therefore, AgCuO<sub>2</sub> is an excellent p type metal oxide with low resistivity. With its high carrier mobility and low bandgap, it presents the possibility of applications in both oxide transistor and photovoltaic devices.

*In-situ XRD characterization of AgCuO<sub>2</sub> hydrothermal reaction*

Through a collaboration with Prof. Mari-Ann Einarsrud from NTNU, Norway, the last part of the thesis work was focussed on the study of the hydrothermal reaction mechanism through in-situ XRD characterizations. AgO and CuSO<sub>4</sub> were chosen as the starting precursors. The hydrothermal reaction was studied in different concentrations of KOH solution 0, 0.3 and 1 M. In laboratory synthesis condition, the applied pressure was close to 1 bar and with temperature 90 °C. Only with 1 M KOH solution, the resulted powder was AgCuO<sub>2</sub>, while in the other cases only Cu<sub>4</sub>SO<sub>4</sub> (OH)<sub>6</sub> compound was obtained.

To understand the effects of solution pH, similar reactions were repeated in synchrotron experimental under 250 bars pressure, with various concentration of KOH solution. By checking the evolution of the reflection intensity for each phase, the reasons for the absence of AgO phase at less basic pH were explained. The dissolution of AgO in 0.3 M KOH solution was attributed to the higher solubility of [AgOH(SO<sub>4</sub>)]<sub>ads</sub><sup>2-</sup> complex than [Ag(OH)<sub>2</sub>]<sub>ads</sub> complex in low concentration KOH solution. Meanwhile in the case of 0 M KOH solution, the absence of AgO was due to the acidic pH with CuSO<sub>4</sub> solution. Besides that, by comparing the in-situ characterizations with 250 bar and 1 bar pressure in 1 M KOH solution at 90 °C, any effect of pressure on the AgCuO<sub>2</sub> formation process was barely observed.

Besides the in-situ XRD characterizations with different KOH concentration, the effects of reaction temperature were also studied with 1 M KOH solution and 250 bar pressure. The morphology of the grains synthesized at different temperatures were also studied. With a lower reaction temperature, averagely smaller grain size and anisotropic crystal growth are found. From 50 °C to 120 °C, with higher reaction temperature, the faster the reactions were

### *General conclusion and perspectives*

completed. By extracting the reaction durations at each temperature, the Arrhenius plot was given and thus the activation energy was estimated about 67.7 kJ/mol.

### *Perspectives in future work*

1. Co-deposition of AgCuO<sub>2</sub> in MOCVD/ALD is still doable provided low decomposition temperature precursors. In addition, to avoid the corrosive radicals, ozone generator is suggested for providing oxidizing species instead of oxygen plasma system.
2. Furthermore works are required to study the electronic structure of the AgCuO<sub>2</sub> phase. Especially in order to form a p-n junction for device applications, it's important to know the electron affinity thus to choose a proper n type metal oxide material.
3. XPS is also needed to compare the charge states of silver atom in this deposited thin films and compare it with the AgCuO<sub>2</sub> phase synthesized through other approaches in literatures.
4. When all the electronic structure information are obtained for AgCuO<sub>2</sub> thin films, they should be applied into transistors or photovoltaic devices.